UNIVERSITY OF OKLAHOMA

GRADUATE COLLEGE

ATMOSPHERIC DUST FROM THE UPPER CARBONIFEROUS COPACABANA FORMATION (BOLIVIA): A HIGH-RESOLUTION RECORD OF CLIMATE AND VOLCANISM FROM NORTHWESTERN GONDWANA

A THESIS

SUBMITTED TO THE GRADUATE FACULTY

in partial fulfillment of the requirements for the

Degree of

MASTER OF SCIENCE

By

CARLOS PATRICIO CARVAJAL GARCIA
Norman, Oklahoma
2016

ATMOSPHERIC DUST FROM THE UPPER CARBONIFEROUS COPACABANA FORMATION (BOLIVIA): A HIGH-RESOLUTION RECORD OF CLIMATE AND VOLCANISM FROM NORTHWESTERN GONDWANA

A THESIS APPROVED FOR THE
CONOCO PHILLIPS SCHOOL OF GEOLOGY AND GEOPHYSICS

BY

____
Dr. Gerilyn S. Soreghan, Chair

____
Dr. Peter E. Isaacson

____
Dr. Michael J. Soreghan

____
Dr. Shannon A. Dulin

Acknowledgements

This thesis was funded by the National Science Foundation research fund EAR-1338331 and EAR-1418716. Acknowledgement goes to Dr. Peter Isaacson and Dr. George Grader for offering biostratigraphic framework. Dr. Linda Hinnov who offered crucial platform for collaboration with quantitative cyclostratigraphy analysis and assistance during core description. Dr. Michael Hamilton for assisting with U-Pb dating and dust provenance and Dr. Nicholas Heavens for providing insightful input on climate modeling and wind patterns. Dr. Karin Goldberg and Dr. Vicky Valdez for suggesting sources for diamictite geochemistry of the greater region. Acknowledgement goes to Dr. Kathleen Benison and Dr. Greg Wahlman for their feedback on the petrographic analysis of evaporites and boundstone facies, respectively.

Drs. P. E. Isaacson, M. J. Soreghan, and A. S. Dulin served as committee members and are acknowledged for guidance and thoughtful review of this paper. I have a profound and sincere respect and admiration for my advisor and committee chair, Dr. Lynn Soreghan, who consistently shows creativity, understanding, determination, and mentorship. Her impact has transcended in me and will continue as I pursue my professional career.

A special acknowledgement goes to Amy Bailey for her great assistance in the lab, to Luke (U. Idaho) for staying until 11pm and helping sampling the core, and to Dr. Roger Slatt and Dr. Bryan Turner for his help with the XRF analysis and his input using geochemistry proxies. Acknowledgments go to Dr. Preston Larson, Curtis Smith, and Gerard Heij for their assistance with the SEM instrument and analysis. Special thanks go to Alyssa Wickard for always fixing the microscope camera for me. Special thanks to Benmadi Milad, Katie Garret, Javier Tellez, Carolina Mayorga, Curtis Smith, Cecilia Lopez-Gamundi, Molly Sexton, Kathleen Baczkowski and the rest of graduate student who provided me with their friendship and generosity and shared with me these two years of academic adventures.

Special acknowledgment goes to my family, my mother and stepdad whose sacrifices and guidance have helped me achieve my academic goals, to my dad, stepmom, and little brother whose prayers and thoughts have encourage me to continue working.

Lastly, I want to dedicate this work to Natasha Lewis and Pia Valdiviezo who are now reading this paper from the skies above. Pia gracias por educarme y enseñarme a ser un buen hombre. Natasha, we did it! Thank you for staying by my side and encourage me with your smile.

Table of Contents

List of Tables

List of Figures

Abstract

This study documents the occurrence of atmospheric dust from Pennsylvanian carbonates of the Copacabana Formation, recovered in core (Mobil-Oxy Manuripi X-1) from the Madre de Dios basin (Bolivia), within southern mid-latitudes (~35˚S) of western Gondwana. The Copacabana Formation spans Late Carboniferous-Early Permian time, and thus formed coeval with and in relative proximity to ice centers and associated glacial deposits located at southern paleolatitudes in adjoining regions of Gondwana (e.g. the Paraná, Tarija, and Paganzo basins in Brazil, southeastern Bolivia, and Argentina, respectively). In Late Carboniferous time carbonate deposition of the Copacabana Formation occurred on a ramp isolated from fluvial-deltaic influx, and thus siliciclastic material in this system reflects atmospheric input. The study interval comprises a series of upwardly shallowing successions 1 – 3 m thick ranging from normal marine outer-mid ramp facies to more restricted inner-ramp facies, commonly capped by horizons of microkarsted and/or red mudstone reflecting subaerial exposure of the carbonate ramp. These surface mark abnormal exposure interpreted to record glacial lowstands.

Dust recovered from throughout the study section varies from ~1 – 43 wgt % in carbonate facies and is quartzo-feldspathic. Grain size modes range from <1 to 97 μm, with coarser intervals generally corresponding to peak dust content (wgt %), and high-frequency sequence (glacial-stage) boundaries. However, two discrete sources of atmospheric input occur–a western volcanic arc source and eastern continental source, recording both westerly (zonal) and easterly (katabatic) wind directions. The western (volcanic) source records zonal westerlies expected at this mid-latitude (~35˚S) locality.

In contrast, easterly winds suggest the influence of katabatic winds associated with Gondwanan ice centers. The most likely dust-sourcing regions are the periglacial to proglacial regions of the Gondwanan ice sheets. Non-volcanic peaks occur most commonly associated with subaerial exposure surfaces suggesting peak dustiness that accompanied glacial stages.

Introduction

Dust deposits form robust paleoclimate archives and are an active climate-forcing agent. Late Cenozoic records of eolian dust from both continental and marine environments comprise high-resolution climate archives (e.g., Rea and Bloomstine, 1986; Porter and An, 1995; Kemp, 2001; Scheuvens, et al., 2013; Schatz et al., 2015). Dust can be preserved within a variety of environments, including glaciers, lacustrine and marine systems, and as loess deposits (Smalley, 1966, 1997; Pécsi, 1990; Pye, 1995; Muhs and Bettis, 2000, 2003, 2014). In the Quaternary, for example, the Chinese Loess Plateau constitutes one of the most extensive continental climate archives, as it consists of a succession of loess and paleosols that has been accumulating since ~2.6 Ma, recording variations in atmospheric dustiness through glacial-interglacial phases (Kukla and An, 1989; Spassov et al., 2002).

In the Quaternary, continental dust (loess) deposits form climate archives in both periglacial loess deposits of high- and mid-latitudes and in peridesert loess deposits of subtropical latitudes (Pecsi, 1990; Pye, 1995; Bettis, et al., 2003; Muhs and Bettis, 2003; Muhs, et al., 2014). Dust deposits are less known from Earth's deep-time sedimentary record, but are well recognized from the Upper Carboniferous-Lower Permian record of western equatorial Pangaea (e.g., Soreghan et al., 2002a, 2002b, 2008). Dust can be preserved within carbonate systems otherwise isolated from detrital (fluvio-deltaic) influx and recovered to assess the geologic record of atmospheric dustiness (cf. Sur et al., 2010a). These dust deposits of the Late Paleozoic ice age (LPIA) present an opportunity to examine spatial and temporal variations of atmospheric dust loading during Earth's most recent pre-Cenozoic icehouse and through glacial-interglacial cycles (Soreghan et al., 2008, 2014; Heavens et al., 2015).

Extending previous research that reported apparently high dustiness in the Carboniferous-Permian of western equatorial Pangaea (e.g., Soreghan et al., 2008, 2013; Sur et al., 2010a; Foster et al., 2014), this research examines the amount and temporal variation in atmospheric dust flux to carbonate strata of the Upper Carboniferous (upper Bashkirian) Copacabana Formation in the Madre de Dios basin, Bolivia, which formed in the southern mid-latitude region. For the time interval of interest, this carbonate system formed isolated from fluvial-deltaic influx; thus, detrital silicate material recovered from these carbonate strata should reflect atmospheric input. However, the source of eolian material includes potential volcanic influx in this active arc setting, as well as non-volcanic atmospheric dust. The primary goal of this study is to assess the atmospheric dustiness and temporal variation in dustiness of the southern mid-latitude region of western Gondwana during the study interval of the early Late Carboniferous. Specifically, these data document (1) the sources of atmospheric dust based on mineral and chemical composition, (2) the impact of glacial-interglacial cycles on atmospheric dust variability, and (3) the regional dispersal of the non-volcanic dust fraction determined by the dust provenance and paleo-wind patterns. These data can shed light on temporal shifts in atmospheric circulation and aridity, and provide input to further constrain climate models of the LPIA.

Geological Setting

In the Late Cambrian to Early Ordovician, the western Gondwanan margin along the western part of present-day South America developed into an active margin (Sempere, 1995; Jaillard et al, 2000; Grader, 2003; Sempere et al., 2002). The development of this active margin had two contrasting phases from the Carboniferous (359-299 Ma) to Permian (299-254 Ma) interval in that a retroarc foreland basin formed inboard of the arc along the western Gondwanan margin in early Carboniferous time, but evolved to backarc transtension by the late Carboniferous (Jaillard et al, 2000; Grader 2003; Grader et al, 2003), with arc volcanism persisting from Late Cambrian to Jurassic times (Isaacson and Diaz Martinez, 1993; Sempere, 1995; Jaillard et al, 2000).

Paleomagnetic data from the Madre de Dios basin of western Bolivia indicate a paleolatitude of ~36˚ S for the Early Carboniferous (Fig. 1; Díaz-Martinez, 1995; Sempere, 1995; Grader et al, 2008). The paleolatitude of the region varied considerably during this time as this region drifted northward, from ~35˚S in the Late Carboniferous to ~19˚S by the Late Permian (Tait et al, 2000; Rakotosolofo et al, 2006). A paleolatitude of 28.1˚S was calculated (pers. commun., S. Dulin, 2016) from inclination data reported (Rakotosolofo, et al., 2006) for the Early Permian (Asselian-Sakmarian) Copacabana Formation exposed in Peru. Thus, the paleolatitude of the studied (older) section in Bolivia is constrained to between 36˚S and 28˚S, but likely closer to 36˚S given the age. The strata of the Madre de Dios basin reflect this shift from high-mid-latitude deposition influenced by the near-field effects of Gondwanan glaciation to low-mid-latitude deposition influenced by carbonate- and eolian-influenced systems (Fig. 3; Díaz-Martinez, 1996; Suarez-Suroco, 2000; Grader et al., 2003).

Whereas the LPIA was once cast as a prolonged icehouse characterized by essentially continuous and invariant glaciation of relatively constant extent, more recently several authors have suggested that multiple short-lived ice sheets waxed and waned at the 1-8 My timescale throughout high-latitude Gondwana during the Late Paleozoic Ice Age (~335-260 Ma; Isbell et al., 2003, 2012; Fielding et al., 2008; Montañez and Poulsen, 2013; Limarino et al., 2014). Glacial centers that supplied sediment to the Madre de Dios basin comprised the Brazilian Shield to the east, Arequipa Massif to the west, and the Puna Arc to the south (Fig. 2-B; Caputo, 2008). Limarino et al. (2014) argued that glacial deposits (glacial diamictite, dropstones, and varve deposits) diminished during early Bashkirian (early Late Carboniferous) time in the basins along western Gondwana, whereas glaciation persisted into Early Cisuralian (Early Permian) time in the eastern basins including the Paraná, South Paraná, and Chaco Paraná (Fig. 2-B).

The Copacabana Formation accumulated in the Madre de Dios basin from early Late Carboniferous (Bashkirian, ~323 Ma) time through Early Permian (Artinskian, ~279 Ma) time, and consists of pericratonic marine strata (Grader et al., 2003). The Mobil-Oxy Manuripi X-1 core (recovered in 1991) from the northern margin of the Madre de Dios basin includes the Devonian Tomachi-Toregua formations, the Upper Carboniferous (Bashkirian-Moscovian) interval of the Copacabana Formation, the Cretaceous Beu-Eslabon formations, and the Neogene (Miocene) Bala Formation (Marshall and Sempere, 1991; Mamet, 1995; Isaacson et al., 1995; Mamet and Isaacson, 1997). Grader et al. (2003) and Isaacson et al. (1995) used lithofacies associations of the Copacabana Formation in the Manuripi-X core to infer an open-marine ramp depositional setting with facies varying from intertidal to distal/basin ramp (Diaz-Martinez, 1994; Grader, 2003; Grader et al., 2007, 2008). In this study, we focus on the upper Bashkirian to lower Moscovian carbonate system (870.0 - 897.5 m subsurface) that accumulated isolated from fluvial-deltaic influx; therefore, any siliciclastic material archives eolian input into this system.

Methods

Logging, Core Description, and Well Logs

The Mobil-Occidental Manuripi X-1 core is currently stored at the University of Idaho. The studied interval for analysis was 870.0 - 897.5 m subsurface (27.5 m thick). Previous palynological studies of the Manuripi X-1 suggested a Bashkirian-Moscovian age for this interval (Grader, 2008; Schiappa, 2016). This interval of the studied section consists of carbonate with very minor (< 3%) fine-grained red mudstone horizons and discrete horizons of green siliceous mudstone. Isaacson (1995) and Grader (2003) interpreted the green siliceous material as air fall ash, an interpretation confirmed now with new U-Pb zircon analysis. New U-Pb geochronological analysis of the youngest zircons recovered from a 1-m ash within the study interval revealed an absolute age of 316.15 ± 0.52 Ma (2σ) (Hamilton et al., 2016), which falls within the latest Bashkirian (near the Bashkirian-Moscovian boundary) according to the latest timescale (www.stratigraphy.org, accessed 2016).

The core was logged at cm-scale resolution to assess lithology and initial facies designations. Samples (~35 g) were collected at a vertical resolution of ~20 cm, with tighter spacing around suspected sequence boundaries, for a total of 95 samples. Minor occurrences of macroscopic diagenesis (e.g., chert, calcite spar-filled fractures) and obvious ash layers were avoided during sampling.

The gamma ray (GR) well log was digitized from the Mobil-Occidental integrated stratigraphic composite log of the Manuripi X-1.

Petrography, XRF, ICP-MS analysis

Thin sections (45) of representative facies enabled detailed facies and diagenetic analysis and guided sequence-stratigraphic determinations. Petrographic analyses were supplemented with chemical analyses using a handheld Bruker Trace IV-SD XRF scanner and accompanying software S1PXRF S1 MODE. Major elements were analyzed using an accelerating voltage of 15 kv, current of 30 μA, vacuum of <10 Torr, and a standing time of 90 seconds with no filter. Trace elements were measured using an accelerating voltage of 40 kv, current of 17.1 μA, vacuum of <10 Torr, and a standing time of 60 s with a titanium aluminum filter. A total of 86 samples were analyzed from the target section with 2 samples analyzed every 10 samples to control for any signal drift. In addition, 6 samples of representative facies were powdered for whole-rock geochemical analysis (major, trace, and rare earth elements) by inductively coupled plasma mass spectrometry (ICP-MS) by an outside vendor.

Extraction of the Silicate Mineral (Dust) Fraction

For extraction of the silicate mineral fraction (SMF), 86 samples were cleaned of any external debris and crushed to gravel size (~0.5 cm), washed with distilled water, then subjected to a series of dissolution steps (details in Sur et al., 2010b). This process involved: 1) dissolution of the carbonate with 2N hydrochloric acid (HCl), 2) combustion of the acid-insoluble residue at 500˚C for ~15 hrs to remove organic matter and oxidize any pyrite, and 3) dissolution of iron oxides with a citrate-bicarbonate-dithionite (CBD) treatment. The resultant SMF was weighed and inspected using reflected-light microscopy to assess the presence of diagenetic contamination. If present, diagenetic components (e.g. silicified material) were removed manually and a new sample weight was recorded. Finally, presence of non-detrital components was also addressed using smear-slide analysis; if these analyses confirmed presence of only detrital components material, the sample was taken to represent dust. Out of the total 95 samples, only 4.2 % contained non-detrital components consisting of silicified bioclasts, and invariably occurring in horizons within 4 cm subjacent to an ash horizon. In rare cases (2 samples) wherein authigenic contamination was too pervasive to enable separation of the pure detrital component, the sample was eliminated from further analysis.

Scanning Electron Microscopy

Extracted dust from representative depositional facies was used for additional data on grain mineralogy, grain morphology, and surface microtextures. Dust was sprinkled on an aluminum stub with double-sided carbon tape, and sputter coated with gold-palladium to prevent charging for SEM analysis. A FEI Quanta Scanning Electron Microscope was used in secondary electron mode with the following settings: a spot size of 5 (dimensionless), a working distance of 10 mm, and an accelerating voltage of 20 kV. Grains were analyzed with energy-dispersive X-ray spectroscopy (EDS) to confirm the mineralogy of the grains prior to morphology analysis.

Principal Component Analysis (PCA)

PCA uses correlation statistics to categorize data into uncorrelated linear combinations that can explain the most variance represented in the data set in the least possible combinations (e.g. for a dataset with N variables, a total of N linear combinations will be produced). The top ten elements measured during XRF analysis (Ca, Si, Mg, Na, Fe, K, Al, S, Ti, and Mn) registering the highest concentrations (ppm) were selected as input variables for PCA. Samples (53) with concentrations measured (average 350 ppm or higher) in all selected ten elements were employed for the studied section, with a median sample rate of 0.37 m and mean sample rate of 0.51 m for the PCA analysis. The objective of the analysis is to identify which elements dominate the principle components (PCs), accounting for the most variance.

Shape Characterization of Gamma Ray Log

The first derivative of the Manuripi X-1 gamma ray (GR) curve was determined by calculating the differences between two adjacent (sub/superjacent) log values using the petrophysics software Techlog. The first derivative represents the slopes between consecutive readings and the resulting bi-color image emphasizes high-frequency oscillations, which can help identify possible trends of depositional facies (Collins and Doveton, 1988; Doveton, 1994).

Results

Lithofacies Characterization

The Upper Carboniferous (upper Bashkirian-lower Moscovian) study section of the Copacabana Formation is composed of 9 lithofacies (Table 1, Fig. 5-6), described below. Table 1 also notes common facies associations.

Boundstone Facies—The boundstone facies consists of light pink to grey lime wackestone 20 - 40 cm thick that in thin section exhibits a pervasive clotted micrite texture, and contains brachiopods spines and irregularly laminar red algae (cf. Wahlman, 2002), and brachiopod spines. The siliciclastic fraction in this facies is <5 wgt% (Fig. 6-A).

Interpretation— The clotted micritic fabric suggests a microbial influence (Riding, 2000) that, together with the occurrence of red algae, indicates deposition in a subtidal organically bound buildup (Toomey and Winland, 1973). Presence of brachiopod components suggests deposition in open marine conditions, but possibly below photic zone.

Bryozoan-Foraminiferal Wackestone—The bryozoan-foraminiferal wackestone consists of tan-grey to tan mottled lime wackestone 20 – 80 cm thick exhibiting a siliciclastic fraction of <3 wgt%. This facies contains milliolid forams and peloids, and comminuted skeletal hash comprising bryozoan and crinoidal debris (Fig. 6-B).

Interpretation— The presence of comminuted debris of primarily heterozoans indicates at least periodically moderate energy, within at least storm wave base, and thus a proximal open-marine outer-ramp setting.

Crinoidal-Bryozoan Packstone—The crinoidal-bryozoan packstone consists of grey to tan-pink lime packstone 10 - 65 cm thick, with abundant whole and comminuted heterozoans, especially crinoids, bryozoans, and brachiopods. The siliciclastic fraction varies from <1 to ~23 wgt% (Fig. 6-C).

Interpretation—The predominance of normal-marine heterozoans, and minimal lime mud in this facies record deposition in normal subtidal, moderate-energy conditions. This facies is interpreted to record deposition in a low- to moderate-energy, proximal outer ramp environment, above storm wave base.

Molluscan Packstone—The gastropod packstone facies consists of massive, tan orange to grey lime packstone 10 - 30 cm thick with locally abundant stick bryozoa, and gastropod and ostracod debris. The siliciclastic fraction ranges from ~5-11 wgt% (Fig. 6-D).

Interpretation—The relatively high abundance of components typical of somewhat restricted conditions within a relatively low-mud matrix suggests deposition in a moderate-energy, slightly restricted inner-ramp environment.

Molluscan Mud-Wackestone Facies—The mud-wackestone facies consists of tan orange to grey, massive to bioturbated lime mudstone 20 - 80 cm thick. The only allochems consist of localized concentrations of thin-shelled molluscs (pelecypods, gastropods, ostracods), and peloids or recrystallized ghosts of peloids, and the siliciclastic fraction ranges from ~3-22 wgt% (Fig. 6-E).

Interpretation—The sparse, low-diversity molluscan fauna, and abundant lime mud record deposition in a low energy, restricted inner-ramp environment; this facies could be a lower-energy, more restricted variant of the molluscan packstone facies.

Dolomitic Mudstone—The dolomitic mudstone facies consists of tan orange to grey barren dolomitic mudstone 100 – 190 cm thick, exhibiting <7.5% siliciclastic material. Some examples of this facies contain remnant halite and gypsum within what are now calcitic "snowballs" embedded within a dolomitic matrix (Buck et al., 2010) (Fig. 6-F).

Interpretation—The lack of biota and local presence of displacive evaporite pseudomorphs (and rare preserved remnant evaporite phases) in conjunction with the dolomitic mineralogy indicates low-energy, highly evaporative conditions, reflecting deposition in a highly restricted marginal-marine setting (Smith, 1971; Wilson, 1975; Melvin, 1991; pers. commun., K. Benison, 2015).

Microkarst Facies— Microkarst horizons 10 cm- 40 cm thick consist of angular micritic clasts locally with rare gastropods and ostracod fragments supported within a red siltstone matrix. This red to orange-tan facies exhibits fracture-mosaic to chaotic brecciated fabrics with the siliciclastic fraction of the matrix ranging from ~7 - 38 wgt%. This facies commonly overlies dolomitic mudstone or peloidal packstone facies (Fig. 5-G).

Interpretation—The presence of clasts of barren dolomitic mudstone (inferred as restricted) commonly exhibiting a mosaic fabric, within an oxidized siliciclastic matrix records karstification of restricted facies associated with prolonged subaerial exposure (Esteban and Colin 1983; Kerans, 1991)

Red Mudstone—The red mudstone facies consists of massive to faintly laminated calcareous mudstone (siliciclastic fraction >50 wgt%) to silty carbonate mudstone (siliciclastic fraction <50 to 22 wgt%) in horizons ranging in thickness from

2-12 cm. The grain size modes of the siliciclastic fraction range from ~6-97 μm with the coarser material composed of subangular to angular quartzo-feldspathic grains. This facies commonly grades upward into the peloidal or crinoidal-bryozoan packstone facies. Bryozoan fragments occur rarely (only where subjacent strata consist of the crinoidal-bryozoan packstone), otherwise this facies is barren, and locally exhibits circumgranular cracking of the micritic matrix (Fig. 6-G).

Interpretation—The fine-grained siliciclastic fraction within a (typically) nonfossiliferous micritic matrix is interpreted to record the introduction of abundant eolian material into a very restricted marginal marine or non-marine setting. An eolian origin rather than fluvial origin is supported by the consistently fine grain size, and massive structure lacking lag deposits or sedimentary structures. Moreover, localized circumgranular cracking of the micritic matrix records exposure and incipient pedogenesis (Wright, et al., 1988; Platt, 1989; Zarza, et al., 1992).

Siliceous Claystone— The green-gray claystone intervals are siliceous, and occur randomly in discrete horizons ranging from <1 to 100 cm thick, locally disrupted (at contacts) by bioturbation. Average SiO_2 content is approximately 53.3 wgt% (samples may contain traces of carbonate-bound Ca, hence, this is an approximation). These horizons have been recognized previously in both outcrop and core of the Copacabana Formation, and interpreted as volcanic ash deposited into the shallow marine carbonate system (e.g. Isaacson et al, 1995; Grader, 2003; Grader et al., 2003; Zappettini et al., 2015; Fig. 5). Geochemical and geochronological analyses (presented in other sections) confirm this.

Cyclo- and Sequence Stratigraphy

The studied section of the Copacabana Formation in the Manuripi X-1 contains a range of carbonate facies that record deposition in conditions ranging from normal-marine subtidal to highly restricted marginal marine/continental, and include evidence for prolonged emergence of the marine system sufficient for pedogenic overprints on subtidal facies. The facies form successions 1-3 m thick consisting commonly of the following facies, from base to top although not all facies are present in each succession: boundstone, bryozoan wackestone, crinoidal/bryozoan packstone, gastropod packstone, carbonate mud-wackestone, dolomitic mudstone, microbreccia, and/or red mudstone (Figs. 4, 7). The shifts from carbonate facies upward into red mudstone or microbreccia horizons record subaerial exposure that demonstrate incomplete facies progradation, in that supratidal facies are missing prior to subaerial exposure. Such relationships constitute "abnormal" subaerial exposure that records the influence of an allogenic process, common to icehouse intervals forced by glacioeustasy (e.g. Wright, 1992; Soreghan, 1997; Read, 1998; Rankey et al., 1999; Burgess, 2016). Accordingly, these facies successions are interpreted as high-frequency sequences recording interglacial highstands and glacial lowstands, somewhat analogous to the many examples of such Upper Carboniferous-Lower Permian marine to marginal marine "cyclothems" of low latitudes in both western (e.g., Soreghan, 1994; Rankey et al., 1999; Heckel, 2002; Bishop et al., 2010; Sur et al, 2010a) and eastern (Davies, 2008; Waksmundzka, 2013) Pangaea.

Stratigraphy Distribution and Sedimentology of the Siliciclastic Fraction

In view of the carbonate-ramp setting of the Copacabana Formation for the study interval, and reinforced by the depositional attributes of the mudstone facies, the (non-diagenetic) siliciclastic fraction extracted from this section is taken to record atmospheric dust influx. Figure 4-B shows the distribution of this dust fraction through the study section. Because Figure 4-B excludes samples from the well-recognized ash layers within the section, the fraction depicted here is interpreted to represent predominantly non-volcanic atmospheric input to the section.

As shown in Figure 4-B, the (non-volcanic) dust fraction (hereafter referred to simply as "dust fraction") peaks most commonly coincide with facies associated with high-frequency sequence boundaries (red mudstone and microkarst horizons) and within shallow-water facies (dolomitic mudstone, molluscan packstone, and molluscan mud-wackestone) relative to facies interpreted to record deeper-water deposition (crinoidal-bryozoan packstone, bryozoan wackestone, and boundstone). This relationship is complicated somewhat by a potential data aliasing since sampling was not continuous but represents spots samples at ~20 cm resolution.

Petrographic analysis of smear slides of the dust fraction from the mudstone facies reveals that quartz and clays are the dominant components, followed by feldspar (plagioclase), biotite, and zircon, in order of decreasing abundance. The coarser grains are subangular to angular, and size modes range from ~6 – 97 µm. In contrast, within the carbonate facies, the dust component contains subrounded to subangular grains composed of ~90% quartz and ~10% feldspars and clays (visual qualitative estimate).

Geochemistry of Lithofacies

Table 2 shows results of bulk-rock (ICP-MS-based) geochemical analysis of representative facies (including ash-rich horizons) from this study, along with average loess samples (of Quaternary age) reported in Taylor et al. (1983). A plot (Fig. 8) of La-Th-Sc compositions shows that ash-rich samples exhibit a volcanic-arc signal whereas samples from representative facies plot in the continental margin field similar to loess samples from Taylor et al. (1983). Ash samples identified in the La-Th-Sc ternary diagram were used as a correlation proxy with other identified ash horizons in the studied section to infer their compositional similarities. XRF elemental ratios Na/K and K/(Fe+Mg) were used to identify remaining ash-rich horizons (Sageman and Lyons, 2003).

Enrichment in Th reflects a silicic source, whereas enrichments in Cr and Sc indicate mafic derivation (Totten et al., 2000). Ratios of Th/Sc ≥10 typically indicate a granitic/upper continental crust (UCC) signature whereas Th/Sc <1 indicates mafic sources (Totten et al., 2000). Figure 9 shows the differentiation of ash-rich samples that exhibit an intermediate to mafic composition corresponding to volcanic input from a continental island arc, and more felsic compositions for all depositional facies of the Manuripi X-1. Additionally, cross plots of Zr/TiO_2 and Nb/Y of the ash-rich samples indicate volcanic compositions ranging from trachyte to trachyte-andesite (Winchester and Floyd, 1977), consistent with this volcanic arc setting (Breitkreuz, 1995; López-Gamundí and Breitkreuz, 1997, Zapettini et al, 2015; Coira et al., 2016). Carbonate and red mudstone facies show a relative depletion in Na_2O and K_2O compared with ash-rich horizons. Al_2O_3 values for the ash-rich sections vary from ~9 to ~23 wgt % and K_2O

values vary from ~3 to 5 wgt%, higher than any modern loess sample and higher than the red mudstone facies of the Manuripi X-1.

Figure 10 shows all XRF geochemical data including ash-rich horizons plotted in ternary space with apices of Na/K, (Zr/Al)*100, and K/(Fe+Mg). Higher Na and Fe + Mg are indicative of volcanic ash input relative to indicators of detrital flux from the Upper Continental Crust such as K (Totten et al., 2000; Sageman and Lyons, 2003). Figure 7 shows profiles of Na/K and K/(Fe+Mg) ratios; inverse correlation ("crossover") between these measures marks ash-rich horizons. After all the ash horizons were identified visually and chemically, they were excluded from subsequent Principal Component Analysis.

XRF Results

Figure 11 shows XRF-based elemental chemical profiles of Si, Na, Fe, K, Al, S, and Ti. Owing to the focus on the silicate (dust) component, elements associated (as major or trace phases) with carbonate facies (Ca, Mg, Sr, Fe, Mn) are considered less influential than other elements. Facies associated with near-exposure and exposure (dolomitic mudstone, microbreccia, and red mudstone facies) exhibit peaks in Si; similarly, K, Al, and Ti also peak in red mudstone and microkarst facies, and exhibit more variable concentrations in carbonate facies.

Principal Component Analysis of XRF data

The results of the PCA are summarized in Table 3 and Figure 8. Principal component 1 (PC1) explains 37.26 % of the XRF data variance. The elements K, Al, Ti, and Si contribute strongly to PC1, which shows a major oscillation of 20 m from 895 m to 875 m with additional high (spatial) frequency (2 - 5 m) and lower amplitude oscillations, resembling the trends exhibited in dust content (Fig. 11).

PC2 explains 28.59% of the dataset variance, and is characterized by major contributions from –Mg (note negative sign), Ca, Na and Ti. The two large minima indicate anomalously large contributions from Mg (negative PC value multiplied by -1 Mg), and are most likely associated with dolomite occurrence.

PC3 with 11.06 % of dataset variance has main contributions from Mn, -Fe, and Si, and oscillates in the 2 m range.

PC4 (S, -Na, Mn), PC5 (-Fe, Mg), and PC6 (-Si, Mn, Al) explain most of the remaining ~20% of the XRF dataset variance, and exhibit relatively regular 2.5 m cycles.

GR Shape Characterization

Quantitative characterization of the GR curve using its first derivative helped in the verification of the oscillations ranging from 2 – 2.5 m. Figure 7 D-E shows a graph of the first derivative of the log representing a continuous profile of the log slope, which oscillates between positive and negative values. The zero crossing of this profile describes shifts in the original log from a peak to trough section. The smoothed GR log is averaged by the vertical resolution of the log tool and its first derivative provides information on curve oscillation over extended vertical distances, hence, inferring large-scale cycles.

Discussion

Origin of the Dust Contribution

The paleogeographic setting of the Copacabana Formation implies it records carbonate ramp deposition isolated from fluvio-deltaic input, and facies attributes of the (minor) siliciclastic component further reinforces this interpretation. However, two discrete sources of atmospheric input occur, differentiated initially from macroscopic facies observations, and confirmed with geochemical data. These sources consist of a volcanically derived component, and a non-volcanic (continental) component.

The material of volcanic derivation must reflect transport from the west approximately 650 km from the study area (northern Chile-southern Peru), where arc magmatism was present, as recorded by pyroclastic and lava flow deposits of Devonian through Permian age (Breitkreuz, 1991, 1995; López-Gamundi and Breitkreuz, 1997). The volcanic activity was characterized by two episodes of arc magmatism: (1) the initial formation along an active margin interpreted to be contaminated with metasedimentary crustal components possibly from continental accretion processes, and (2) granitic intrusions with related volcanic activity showing evidence of melting of the early Proterozoic crust (Mpodozis et al, 1992; Jaillard et al., 2000; Grader, 2003). Although the eruptions generating the ash deposits were likely explosive, the presence of these ashes nevertheless records a westerly wind component during these events, which is expected for this mid-latitude location under conditions of zonal circulation.

In contrast, the non-volcanic dust component most likely derives from continental sources located to the east representing eolian deflation of proglacial and periglacial systems that would have emanated from periodically expanding and contracting ice sheets located to the east-southeast (Parana Basin, Chaco-Paranaense, and Southeast Subandean Tarija Basins) of Gondwana (Fig. 1-B) (Starck and del Papa, 2006, Limarino et al., 2013). The study section was located relatively high on the carbonate ramp of the Copacabana system, and approximately 700 km northwest from well-recognized late-Bashkirian-early Moscovian ice centers documented in western Gondwana (Limarino et al., 2002, 2014; Limarino, 2006; Starck and del Papa, 2006; Gulbranson et al., 2015, Fig. 1). Dust input from eastern sources implies wind directions with an easterly component for at least part of the time, although the paleolatitude (36˚ S) implies placement within a westerly wind regime assuming a zonal climate system. This wind pattern requires a reorganization of the regional atmospheric circulation that could be explained by katabatic winds emanating from a glacial anticyclone influenced by nearby LPIA ice sheets (e.g. analogy to Quaternary systems-- Hobbs, 1943; Muhs and Bettis, 2000; Muhs and Budhan 2006; Schaetzl and Attig, 2013)

Timing and Magnitude of Dust Inputs to the Study Section

Variation in the volume of dust contributions to the studied section reflects to some degree temporal variations in atmospheric dustiness. The volcanic contributions would have occurred in a temporally random fashion, but the importance of the continental (non-volcanic) fraction appears to have varied relatively systematically in time at both the glacial-interglacial timescale and possibly higher-frequency ($<10^5$ yr) scales.

High-frequency glacioeustasy and the associated development of cyclothems during the late Paleozoic could reflect a dominant Milankovitch control (e.g., Heckel 1986, 2008; Anderson, 2011; Hinnov, 2013), analogous to the glacial-interglacial oscillations of the Quaternary (Hays et al., 1976). Therefore, a quantitative cyclostratigraphic approach was employed to assess the possible influence of orbitally driven climatic signals in the dust record. Constraining the geological age of the studied section can introduce challenges in determining the periodicity of the rock record (Berger et al. 1991). Frequency-domain minimal tuning method was performed on the gamma-ray (GR) curve of the Manuripi X-1 to assess Milankovitch precession (17-19 kyr), obliquity (32 kyr), short eccentricity (95-130 kyr), and long eccentricity (405 kyr) cycles (Berger and Loutre, 1991).

At the glacial-interglacial timescale, the stratigraphic patterns commonly document highest dust amounts in lowstand/exposure facies suggesting highest atmospheric dustiness during incipient glaciation to full glacial phases (Fig. 12). In the study section, the dust fraction increases in the shallowest-water carbonates (late highstand/incipient glaciation) approaching sequence boundaries and maximizes at microkarst and paleosols (early to full lowstand/full glaciation). Minimal dust input corresponds to the deeper-water carbonate facies (Fig. 12), interpreted to record late transgression to highstand (incipient to full interglacial).

These changes in dust input are interpreted to reflect in part the climate of the dust source regions, with more humid conditions that restricted dust mobility during interglacials. Arid conditions coupled with expansion of regions of eolian deflation associated with significant glacial-stage sea-level fall likely resulted in mobilization of dust near sequence boundaries, as shown on Al/Zr, Ti/Al, and Si/Al values (Fig. 13). The proximity of the study region to major Gondwanan ice centers (Fig. 1) would have resulted in major potential for production of rock flour from glacial grinding, as well as heightened wind action. This timing is a common theme for Quaternary proglacial regions; for example, Last Glacial Maximum (LGM) ice from alpine systems in Peru record heightened dustiness attributed to both aridity and high winds (Thompson et al., 1995), and many others have noted a pattern of glacial dustiness attributable to aridity, exposure of deflation areas (by sea-level change), dust production, and steepened temperature gradients that promote gustiness (e.g. Broecker, 2002; McGee et al., 2010; e.g., Kohfeld et al., 2013; Lamy et al., 2014).

Conclusions

(1) The silicate mineral fraction extracted from shallow marine carbonates of the Pennsylvanian Copacabana Formation (Bolivia) provides a valuable proxy for atmospheric dust during Late Carboniferous time in this region relatively proximal to the Gondwanan glacial region.

(2) In the study section, 15 cycles were identified, many capped by evidence for subaerial exposure, recording glacioeustatic lowstands associated with waxing and waning of nearby icesheets. The dust fraction throughout the study section varies from 1 – 64 wgt%, inferred to record variations in atmospheric dustiness driven by both glacial-interglacial and higher-resolution climate. The general coincidence of inferred lowstands with highest dust content suggests greater atmospheric dustiness during deglaciation to full glacial phases.

(3) Two discrete sources of atmospheric input occur–a western volcanic arc source and eastern continental source, recording both westerly and easterly wind directions, respectively. A dust input from eastern sources implies wind directions with an easterly component for at least part of the time, although the paleolatitude (36˚ S) implies placement within a westerly wind regime within a zonal climate system. The presence of both components suggests the existence of a katabatic wind regime or katabatically enhanced easterlies driven by a glacial anticyclone.

Figure Captions

Figure 1: Paleogeographic map of Gondwana during Late Carboniferous time (323-299 Ma) modified from Blakey (2011) showing the icesheet distributions and the study area.

Figure 2: (A) Present location of the Mobil-Oxy wells in the Madre de Dios Basin in Bolivia. (B) Glacial ice-sheet distribution with paleogeographic features of the western margin of Gondwana during the Middle to Late Carboniferous modified from Limarino et al. (2014). (C) W-E cross-section showing Upper Carboniferous - Permian deposits with paleogeographic features that compose the Copacabana Formation. Also, shown is the relative location of the Mobil-Oxy wells (Manuripi X-1 and Pando X-1) in the Madre de Dios basin (modified from Grader, 2003).

Figure 3: Generalized stratigraphy of the Manuripi X-1 well adapted from Isaacson et al., (1995) and Grader, (2003) showing the time interval of this study with star symbol.

Figure 4: (A) Manuripi X-1 lithologic log annotated with sampling levels and example dust grain-size distributions for (1) red mudstone (MAN 876.77), (2) crinoidal/bryozoan packstone (MAN 886.62), and (3) microkarst facies (MAN 888.86); (B) Dust weight % distribution throughout lithological log; (C) Dust weight % distribution.

Figure 5: Manuripi X-1 core samples (A) Volcanic ash from 883 m, (B) Bryozoan Wackestone, (C) Crinoidal/bryozoan Packstone – note the crinoid fragments (D) Gastropod Packstone – large gastropods present, (E) Carbonate mud-

wackestone, (F) Dolomite Mudstone – note the evaporites, (G) Microbreccia – note the angular interclasts in red mudstone matrix, and (H) Red Siltstone, (1) grey color carbonate micritic mud in a red mudstone (2).

Figure 6: Photomicrographs of facies. (A) Boundstone facies, with poorly preserved red-algae laminae; (B) Bryozoa wackestone facies, with bryozoan fragment in micritic matrix; (C) Crinoidal bryozoan packstone (D) Gastropod packstone facies, with abundant ostracod shells; (E) Carbonate mud wackestone facies exhibiting low diversity bioclasts and mollusc debris; (F) Dolomitic mudstone facies—note "snowballs" interpreted as evaporite pseudomorphs; (G) Microkarst facies exhibiting clast floating in siliciclastic matrix; and (H) Red Mudstone exhibiting root traces as evidence of pedogenesis.

Figure 7: (A) Lithologic log showing location of U-Pb dated horizon, (B) Dust weight % fraction distribution throughout the core, (C) Inferred upwardly shallowing cycles, (D) Gamma ray smoothed 1st derivative curve, (E) Gamma ray 1st derivative curve, highlighting smaller oscillations (F) shows gamma ray smoothed log overlaying digitized gamma ray log. Oscillations between positive and negative values in the derivative curves indicate either an extreme peak or through on the gamma ray log curve, and (G) elemental ratios, ashes occur where XRF K/(Fe+Mg) and Na/K cross-over creating an 'ash effect'.

Figure 8: La-Th-Sc ternary diagram showing Manuripi X-1 samples illustrating chemical composition based on depositional environment environment (Cullers, 1994). Most of the samples group in the continental margins along with loess

samples from Taylor et al. (1983). Ash-rich samples group within the continental island-arc environment.

Figure 9: Geochemical cross-plots of oxides and selected trace elements. (A-B) La/Sc versus Th/Sc and Cr/Th versus Th/Sc plots suggest a more intermediate-composition source for the ash-rich samples (Totten et al, 2000), and a more mixed composition for the other carbonate facies. (C) K_2O + Na_2O vs SiO_2 plot suggests an alkali-siliceous volcanic source for the ash-rich samples. (D) Zr/TiO2 vs Y/Pb indicates the volcanic composition of the ash samples.

Figure 10: Ternary diagram of (Zr/Al)*1000, Na/Al, and K/(Fe+Mg) highlights the alkali-volcanic composition of red mudstones and ashy sections (Circled).

Figure 11: Principal Component Analysis (PCA) showing principal components (PC) and their elements with variance percentages. PC 1 to PC 6 account for 96.95 % of the total variance, and PC1 shares similar trend as the dust % fraction indicating the possible main chemical composition of the dust fraction with minor contribution of other elements from other PC groups.

Figure 12: (A) Timing of dust influx with respect to relative sea level in the study interval. B) Schematic of mudrock and carbonate deposition during various glaciao-eustatic phases.

Figure 13: Dust % fraction plotted along the element ratios of Al/Zr, Ti/Al, and Si/Al to show the possible composition of the dust as aridity presumably increased with the onset of glacial stages.

References

Anderson, R. Y., 2011. Enhanced climate variability in the tropics: a 200,000 yr annual record of monsoon variability from Pangea's equator. Climate of the Past 7, 757-770.

Berger, A., 1991. Long-term history of climate ice ages and Milankovitch periodicity. in Sonett, C. P., Giampapa, M. S., and Matthews, M. S. (Eds.), The Sun in Time, Tucson, AZ, University of Arizona Press, p. 498-510.

Berger, A., and Loutre, M. F., 1991. Insolation values for the climate of the last 10 million years. Quaternary Science Reviews 10, p. 297-317.

Bettis, E. A., Muhs, D. R., Roberts, H. M., Wintle, A. G., 2003. Last Glacial loess in the conterminous USA. Quaternary Science Reviews 22, p. 1907-1946.

Breitkreuz, C., 1995. The Late Permian Peine and Cas Formations at the eastern margin of the Salar de Atacama, Northern Chile: stratigraphy, volcanic facies, and tectonics. Andean Geology 22, p. 3-23.

Breitkreuz, C., 1991. Fluvio-lacustrine sedimentation and volcanism in a Late Carboniferous tensional intra-arc basin, northern Chile. Sedimentary Geology 74, p. 173-187.

Bishop, J. W., Montañez, I. P., & Osleger, D. A., 2010. Dynamic Carboniferous climate change. Arrow Canyon, Nevada, Geosphere 6, p. 1-34.

Blakey, R., 2011. Mollewide Plate Tectonics Maps: Pennsylvanian. Retrieved from < http://cpgeosystems.com/300moll.jpg>.

Broecker, W. S., 2002. Dust: Climate's Rosetta Stone,Proceedings of the American Philosophical Society 146, p. 77-80.

Burgess, P. M., 2016. Identifying ordered strata: evidence, methods, and meaning. Journal of Sedimentary Research 86, p. 148-167.

Buck, B. J., Lawton, T. F., Brock, A. L., 2010. Evaporitic paleosols in continental strata of the Carroza Formation La Popa Basin, Mexico: Record of Paleogene climate and salt tectonics. Geological Society of America Bulletin 122, p. 1011-1026.

Caputo, M. V., de Melo, J. H. G., Streel, M., Isbell, J. L, 2008. Late Devonian and early Carboniferous glacial records of South America. In: Fielding, C. R., Frank, T. T., and Isbell, J. L. (Eds.), Resolving the Late Paleozoic Ice Age in Time and Space, Geological Society America, Special Paper, vol. 441, p. 161-173.

Coira, B., Cisterna, C. E., Ulbrich, H. H., and Cordani, U. G., 2016. Extensional Carboniferous magmatism at the western margin of Gondwana: Las Lozas Valley, Catamarca, Argentina, Andean Geology 43, p. 105-126.

Collins, D. R., and Doveton, J. H., 1988. Colour image transformations of wireline logs as a medium for sedimentary profile analysis. Bulletin of Canadian Petroleum Geology 36, n 2, p. 186-190.

Cullers, R. L., 1994. The chemical signature of source rocks in size fractions of Holocene stream sediment derived from metamorphic rocks in the wet mountains region. Colorado, USA, Chemical Geology 113, n 3, p. 327-343.

Davies, S. J., 2008. The record of Carboniferous sea-level change in low-latitude sedimentary successions from Britain and Ireland during the onset of the late Paleozoic ice age. In: Fielding, C. R., Frank, T. D., and Isbell, J. L., eds., Resolving the Late Paleozoic Ice Age in Time and Space. Geological Society of America Special Paper vol. 441, p. 187–204.

Díaz-Martínez, E. D., 1995. Regional correlations with late Paleozoic events in Bolivia. 2nd Simpósio sobre Cronoestratigrafía da Bacia do Paraná, Porto Alegre-Brazil, Boletim de Resumos Expandidos, p. 98-100.

Diaz Martinez, E. D., 1996. Síntesis estratigráfica y geodinámica del Carbonífero de Bolivia. In: Memorias del 12 Congreso Geologico de Bolivia, Congreso Geologico de Bolivia, 12, Tarija, Bolivia, 1996, p. 355-367.

Doveton, J. H., 1994. Theory and Applications of Time Series Analysis to Wireline Logs. Chapter 5. Geologic Log Analysis Using Computer Methods: American Association of Petroleum Geologists, Computer Applications in Geology 2, p. 97-125.

Esteban, M., and C. F. Klappa, 1983. Subaerial exposure environment. In: Scholle P. A., Bebout, D. G., and Moore, C. H. (Eds.), Carbonate Depositional Environments, Tulsa, OK, American Association of Petroleum Geologists, Memoir 33, p. 1-54.

Fielding, C., Frank, T., Birgenheier, L., Rygel, M., Jones, A., Roberts, J., 2008. Stratigraphic imprint of the Late Palaeozoic Ice Age in eastern Australia: a record of alternating glacial and non-glacial climate regime. Journal of the Geological Society of London 165, p. 129-40.

Foster, T. M., Soreghan, G. S., Soreghan, M. J., Benison, K. C., Elmore, R. D., 2014. Climatic and paleogeographic significance of eolian sediment in the middle Permian Dog Creek Shale (Midcontinent U.S.). Palaeogeography, Palaeoclimatology, Palaeoecology 402, p. 12-29.

Grader, G. W., 2003. Carbonate-siliciclastic sequences of the Pennsylvanian and Permian Copacabana Formation, Titicaca Group, Andes of Bolivia [Ph.D. dissertation]: Moscow, Univeristy of Idaho, 359p.

Grader, G. W., Isaacson, P. E., Arispe, O., Pope, M., Mamet, B., Davydov, V., Díaz-Martínez, E., 2003. Back-Arc Carbonate-Siliciclastic sequences of the

Pennsylvanian and Permian Copacabana Formation, Titicaca Group, Bolivia. Revista Tecnica de YPFB 21, p. 207-227.

Grader, G. W., Díaz-Martínez, E., Davydov, V., Montañez, I., Tait, J., Issacson, P. E., 2007. Late Paleozoic Stratigraphy Framework in Bolivia: Constraints from the Warm Water Cuevo Megasequence. Cuadernos de Museo Geominero 8, p. 181-188.

Grader, G. W., Issacson, P. E., Díaz-Martínez E, Pope, M. C., 2008. Pennsylvanian and Permian sequences in Bolivia: Direct responses to Gondwana glaciation In: Fielding, C. R., Frank, T. D., and Isbell, J. L. (Eds.), Resolving the Late Paleozoic Ice Age in Time and Space: Geological Society of America Special Paper 441, p. 143-159.

Gulbranson, E. L., Montañez, I. P., Tabor, N. J., & Limarino, C. O., 2015. Late Pennsylvanian aridification on the southwestern margin of Gondwana (Paganzo Basin, NW Argentina): a regional expression of a global climate perturbation. Palaeogeography, Palaeoclimatology, Palaeoecology 417, p. 220-235.

Hays, J. D., Imbrie, J., & Shackleton, N. J., 1976. Variations in the Earth's orbit: pacemaker of the ice ages. American Association for the Advancement of Science 194, n 4270, p. 1121-1132.

Hamilton, M. A., Soreghan, G. S., Carvajal, C. P., Isaacson, P. E., Grader, G. W., Di Pasquo, M. M., 2016. A precise U-Pb zircon age from volcanic ash in the Pennsylvanian Copacabana Formation, Bolivia [abstract], in Geological Society of America Rocky Mountain Section – 68th Annual Meeting; 2006 May 18-19, Moscow, Idaho, 2006, Abstract no. 276278.

Heavens, G. H., Mahowald, N. M., Soreghan, G. S., Soreghan, M. J., Shields, A. C., 2015. A model-based evaluation of tropical climate in Pangaea during the late Palaeozoic icehouse. Palaeography, Palaeoclimatology, Palaeoecology 425, n 1, p. 109-127.

Heckel, P. H., 1986. Sea-level curve for Pennsylvanian eustatic marine transgressive-regressive depositional cycles along midcontinent outcrop belt, North America. Geology 14, p. 330-334.

Heckel, P. H. 2002. Overview of Pennsylvanian cyclothems in Midcontinent North America and brief summary of those elsewhere in the world. In: Hills, L. V., Henderson, C. M., and Bamber, E. W. (Eds.), Carboniferous and Permian of the World, XIV International Congress of the Carboniferous and Permian Proceeds. Calgary, Alberta, Canada, Canadian Society of Petroleum Geologists, Memoir 19, p. 79-98.

Heckel, P. H., 2008. Pennsylvanian cyclothems in Midcontinent North America as far-field effects of waxing and waning of Gondwana ice sheets. In: Fielding, Cr. R., Frank, T. D., and Isbell, J. L. (Eds.), Resolving the Late Paleozoic Ice Age in

Time and Space, Boulder, CO, Geological Society of America Special Paper 441, p. 275-289.

Hinnov, L. A., 2013. Cyclostratigraphy and its revolutionizing applications in the earth and planetary sciences. Geological Society of America Bulletin 125 (11-12), p. 1703-1734.

Hobbs, W. H., 1943, The glacial anticyclone and the continental glaciers of North America. Proceedings of the American Philosophical Society 86, p. 368-402.

Isaacson, P. E., Palmer, B. A., Mamet, B. L., Cooke, J. C., & Sanders, D. E., 1995. Devonian-Carboniferous stratigraphy in the Madre de Dios basin, Bolivia: Pando X-1 and Manuripi X-1 wells. In: A. J. Tankard, R. Suárez S., and H. J. Welsink, Petroleum Basins of South America, Tulsa, OK, American Association of Petroleum Geologists Memoir 62, p. 501–509.

Isbell, J. L, Miller, M. F., Wolfe, K. L., Lenaker, P. A., 2003. Timing of late Paleozoic glaciation in Gondwana: Was glaciation responsible for the development of northern hemisphere cyclothems? In: Chan M. A., and Archer, A. W. (Eds.), Extreme Depositional Environments: Mega end Members in Geological Time, Boulder, CO, Geological Society of America Special Papers 340, p. 5-24.

Isbell, J. L., Henry, L. C., Gulbranson, E. L., Limarino, C. O., Fraiser, M. L., Koch, Z. J., Ciccioli, P. L, Dineen, A. A., 2012. Glacial paradoxes during the late Paleozoic ice age: evaluating the equilibrium line altitude as a control on glaciation. Gondwana Research 22, p. 1-19.

Jaillard, E., Hérail G., Monfret T., Díaz-Martinez E., Baby P., Lavenu A., Dumont J. F., 2000. Tectonic evolution of the Andes of Ecuador, Peru, Bolivia and northernmost Chile. Sociedade Brasileira de Geologia 31st International Geological Congress, Rio de Janeiro, p. 481-559.

Kemp, R. A., 2001. Pedogenic modification of loess: significance for paleoclimate reconstruction. Earth Sciences Reviews 54, p. 145-156.

Kerans, C., 1993. Description and interpretation of karst-related breccia fabrics, Ellenburger Group, West Texas. In: Fritz, R. D., Wilson, J. L., and Yurewitz, D. A. (Eds.), Paleokarst-Related Hydrocarbon reservoirs. Tulsa, OK, Society of Sedimentary Geology Special Publication 91, p. 145-156.

Kohfeld, K. E., Graham, R. M., De Boer, A. M., Sime, L. C., Wolff, E. W., Le Quéré, C., & Bopp, L., 2013. Southern Hemisphere westerly wind changes during the Last Glacial Maximum: paleo-data synthesis. Quaternary Science Reviews 68, p. 76-95.

Kukla, G. J., and An, Z., 1989. Loess stratigraphy in central China. Palaeogeography, Palaeoclimatology, Palaeoecology 72, p. 203-225.

Lamy, F., Gersonde, R., Winckler, G., Esper, O., Jaeschke, A., Kuhn, G., Ullermann, J., Martinez-Garcia, F., Lambert, F., Kilian, R., 2014. Increased dust deposition in the Pacific Southern Ocean during glacial periods. Science 343, n 6169, p. 403-407.

Limarino, C. O., Césari, S. N., Net, L. I., Marenssi, S. A., Gutierrez, R. P., and Tripaldi, A., 2002. The Upper Carboniferous postglacial transgression in the Paganzo and Rio Blanco basins (northwestern Argentina): facies and stratigraphic significance. Journal of South American Earth Sciences 15, n 4, p. 445-460.

Limarino, C. O., and Spalleti, L. A., 2006. Paleogeography of the upper Paleozoic basins of South America: An overview. Journal of South America Earth Sciences 22, p. 134-155.

Limarino, C. O., Césari, S. N., Spalletti, L. A., Taboada, A. C., Isbell, J. L., Geuna, S., & Gulbranson, E. L., 2014. A paleoclimatic review of southern South America during the late Paleozoic: A record from icehouse to extreme greenhouse conditions. Gondwana Research 25, n 4, p. 1396-1421.

Lopez-Gamundi, O. R., and Breitkreuz, C., 1997. Carboniferous-to-Triassic evolution of the Panthalassan margin in southern South America. In: Dickins, J. M., Zuniy, Y., Honfu, Y., Lucas, S. G., and Acharyya, S. (Eds.), Late Paleozoic and Early Mesozoic Circum-Pacific Events and Their Global Correlation, Cambridge, UK, Cambridge University Press, vol. 10, p. 8-19.

Marshall, L. G., & Sempéré, T., 1991. The Eocene to Pleistocene vertebrates of Bolivia and their stratigraphic context: a review. Revista Técnica de Yacimientos Petrolíferos Fiscales Bolivianos 12 (3-4), p. 631-652.

Mamet, B. L., 1995. Late Paleozoic small foraminifers (endothyrids) from South America (Ecuador and Bolivia). Canadian Journal of Earth Sciences 33, p. 452-459.

Mamet, B. L., and Isaacson, P. E., 1997. Bashkirian (Early Pennsylvanian) small foraminifers from Bolivia, Prace Panstwowego Instytutu Geolgicznego CLVII, Proceeding of the XII International Congress on the Carboniferous and Permian, Krakow, p. 319-328.

McGee, D., Broecker, W. S., & Winckler, G., 2010. Gustiness: The driver of glacial dustiness? Quaternary Science Reviews 29, p. 2340-2350.

Melvin, J. L., 1991. Evaporites, Petroleum and Mineral Resources. Developments in Sedimentology, Amsterdam, Netherlands, Elsevier, vol. 50, p. 1-534.

Montañez, I. P., and Poulsen, C. J., 2013. The Late Paleozoic ice age: an evolving paradigm. Annual Review of Earth and Planetary Sciences 41, p. 629-656.

Mpodozis, C., and Kay, S. M. 1992. Late Paleozoic to Triassic evolution of Gondwana margin: evidence from Chilean Frontal Cordilleran batholiths (28˚ to 31˚S). Geological Society of America Bulletin 104, p. 999-1014.

Muhs, D. R., & Bettis, E. A., 2000. Geochemical variations in Peoria Loess of western Iowa indicate paleowinds of midcontinental North America during last glaciation. Quaternary Research 53, p. 49-61.

Muhs, D., Bettis, E., 2003. Quaternary loess-paleosol sequences as examples of climate-driven sedimentary extremes. In: Chan, M. A., and Archer, A. W. (Eds.), Extreme depositional environments: Mega end members in geologic time, Boulder, Colorado, Geological Society of America Special Paper 370, p. 53-74.

Muhs, D. R., and Budhan, J. R., 2006. Geochemical evidence for the origin of late Quaternary loess in central Alaska. Canadian Journal of Earth Sciences 43, p. 323-337.

Muhs, D.R., Cattle, S. R., Crouvi, O., Rosseau, D.D., Sun, J., Zárate, M. A., 2014. Loess records. In: Knipperts, P., and Stuut J. B. W, (Eds.), Mineral Dust: A Key Player in the Earth System, Dordrecht, Netherlands, Springer Science, p. 411-441.

Parrish, J. T., 1993. Climate of the supercontinent Pangea. The Journal of Geology 101, p. 215-233.

Pécsi, M., 1990. Loess in not just the accumulation of dust. Quaternary International 7/8, p. 1-21.

Platt, N. H., 1989. Lacustrine carbonate and pedogenesis: sedimentology and origin of palustrine deposits from the Early Createaceous Rupelo Formation, W Cameros Basin, N Spain. Sedimentology 36, p. 665-684.

Porter, S. C., and Zhisheng, A., 1995. Correlation between climate events in the North Atlantic and China during the last glaciation. Nature 375, p. 305–308.

Poulsen, C. J., Pollard, D., Montañez, I. P., and Rowley, D., 2007. Late Paleozoic tropical climate response to Gondwanan deglaciation. Geology 35, n 9, p. 771-774.

Peyser, C. E., & Poulsen, C. J., 2008. Controls on Permo-Carboniferous precipitation over tropical Pangaea: a GCM sensitivity study. Palaeogeography, Palaeoclimatology, Palaeoecology 268, p. 181-192.

Pye, K., 1995. The nature, origin and accumulation of loess. Quaternary Science Reviews 14, p. 653-667.

Rankey, E. C., Bachtel, S. L., Kaufman, J., 1999. Controls on Stratigraphic Architecture of icehouse mixed carbonate-siliciclastic systems: A case study from the holder formation (Pennsylvanian, Virgilian), Sacramento Mountains, New Mexico. In: Harris, P. M., Saller, A. H., and Simo, J. A. (Eds.), Advances in Carbonate Sequence Stratigraphy: Application to Reservoirs, Outcrops and Models, Tulsa, OK, SEPM Special Publication, n 63, p. 127-150.

Rakotosolofo, N. A., Tait, J. A., Carlotto, V., Cárdenas, J., 2006. Paleomagnetic results from the Early Permian Copacabana Group, southern Peru: Implication for Pangea paleogeography. Tectonophysics 413, p. 287-299.

Rea, D. K., and Bloomstine, M. K., 1986. Neogene history of the South Pacific tradewinds: evidence for hemispherical asymmetry of atmospheric circulation. Palaeogeography, Palaeoclimatology, Palaeoecology 55, p. 55–64.

Read, J. F., 1998. Phanerozoic carbonates ramps from greenhouse transitional and ice-house worlds: clues from field and modeling studies. In: Wright, V. P., Burchette, T. P. (Eds.), Carbonate Ramps, Geological Society Special Publications, London, UK, 149, p. 107-135.

Riding, R., 2000. Microbial carbonates: the geological record of calcified bacterial-algal mats and biofilms. Sedimentology 47 (Suppl. 1), p. 179-214.

Starck, D., and del Papa, C., 2006. The northwestern Argentina Tarija Basin: Stratigraphy, depositional systems, and controlling factors in a glaciated basin. Journal of South American Earth Sciences 22, n 3, p. 169-184.

Sageman, B. B., and Lyons, T. W., 2003. Geochemistry of fine-grained sediments and sedimentary rocks. In: Mackensie, F. T., Holland, H. D., Turekian, K. K. (Eds.), Treatise on Geochemistry, Elsevier, Amsterdam, Netherlands, 7, p. 115-158.

Sempere, T., 1995. Phanerozoic evolution of Bolivia and adjacent regions. In: A. J. Tankard, R. Suárez S., and H. J. Welsink, Petroleum Basins of South America, Tulsa, OK, American Association of Petroleum Geologists Memoir, 62, p. 207-320.

Sempere, T., Carlier, G., Soler, P., Fornari, M., Carlotto, V., Jacay, J., Arispe, O., Néraudeau, D., Cárdenas, J., Rosas, S., Jiménez, N., 2002. Late Permian – Middle Jurassic lithospheric thinning in Peru and Bolivia, and its bearing on the Andean-age tectonics. Tectonophysics 345, p. 153 -181.

Schaetzl, R. J., and Attig, J. W., 2013. The loess cover of northern Wisconsin. Quaternary Research 79, p. 199-214.

Schatz, A. K., Scholten, T., & Kühn, P., 2015. Paleoclimate and weathering of the Tokaj (Hungary) loess–paleosol sequence. Palaeogeography, Palaeoclimatology, Palaeoecology 426, p. 170-182.

Scheuvens, D., Schütz, L., Kandler, K., Ebert, M., & Weinbruch, S., 2013. Bulk composition of northern African dust and its source sediments—A compilation. Earth-Science Reviews 116, p. 170-194.

Schiappa, T. A., 2016. Gondwanan conodont biostratigraphy confirms climate change during the Late Carboniferous, Rocky Mountain section meeting, Boulder, Co, Geological Society of America Abstract with programs, vol. 48, n 6.

Smalley, I. J., 1966. The properties of glacial loess and the formation of loess deposits. Journal of Sedimentary Petrology 36, p. 669–676.

Smalley, I. J., 1997. Thick loess deposits reveal Quaternary climatic changes. Endeavour 21, p. 9-11.

Smith, D. B., 1971. Possible displacive halite in the Permian Upper Evaporite Group of Northeast Yorkshire. Sedimentology 17, p. 221-232.

Soreghan, G. S., 1994. The impact of glacioclimatic change on Pennsylvanian cyclostratigraphy. In: Embry, A.F., Beauchamp, B., and Glass, D.J. (eds.), Pangea: Global Environments and Resources, Canadian Society of Petroleum Geologists, Memoir 17, p. 523–543.

Soreghan, G. S., 1997. Walther's Law, climate change, and Paleozoic cyclostratigraphy in the Ancestral Rocky Mountains. Journal of Sedimentary 67, p. 1001-1004.

Soreghan, G. S., Elmore, R.D., Lewchuk, M.T., 2002, Sedimentologic–magnetic record of western Pangean climate in upper Paleozoic loessite (lower Cutler beds, Utah). Geological Society of America, Bulletin 114, p. 1019-1035.

Soreghan, G. S., Soreghan, M. J., Hamilton, M. A., 2008. Origin and significance of loess in late Paleozoic western Pangea: A record of tropical cold? Palaeogeography, Palaeoclimatology, Palaeoecology 268, p. 234-259.

Soreghan, G. S., & Soreghan, M. J., 2013. Tracing clastic delivery to the Permian Delaware Basin, USA: implications for paleogeography and circulation in westernmost equatorial Pangea. Journal of Sedimentary Research 83, n 9, p. 786-802.

Soreghan, G. S., Sweet, D. E., Heavens, N. G, 2014. Upland glaciation in tropical Pangaea: geological evidence and implications for late Paleozoic climate modeling. Journal of Geology 122, p. 137-163.

Soreghan, G.S, Young, J., Elwood Madden, M.E., Van Deventer, S. C., 2015. Silt production as a function of climate and lithology under simulated comminution. Quaternary International 399, p. 218-227.

Spassov, S., 2002. Loess Magnetism, Environment and Climate Change of the Chinese Loess Plateau, [PhD Dissertation], Zürich, Swiss Federal Institute of Technology, 143p.

Suarez Soruco, R., 2000. Cordillera Oriental, in Suarez Soruco, R., 2000, Compendio de Geología de Bolivia. Revista Tecnica de Yacimientos Petroleros Fiscales Bolivianos 18, n 1-2, p. 1-199.

Sur, S., Soreghan, G. S., Soreghan, M. J., Yang, W., Saller, A. H., 2010a. A record of glacial aridity and Milankovitch-scale fluctuations in atmospheric dust from the Pennsylvanian tropics. Journal of Sedimentary Research 80, p. 1046-1067.

Sur, S., Soreghan, M. J., Soreghan, G. S., Stagner, A. F., 2010b. Extracting the Silicate Mineral Fraction from Ancient Carbonate: Assessing the Geological Record of Dust. Journal of Sedimentary Research 80. P 763-769.

Taylor, S. R., McLennan, S. M., and McCulloch, M. T., 1983. Geochemistry of loess, continental crustal composition and crustal model ages. Geochimica et Cosmochimica Acta 47, p. 1897-1905.

Tait, J., Schätz, M., Bachtadse, V., Soffel, H., 2000. Paleomagnetism and Palaeozoic paleogeography of Gondwana and European terranes. Geological Society of London 179, p. 21-34.

Thompson, L. G., Mosley-Thompson, E., Davis, M. E., Lin, P, N., Henderson, K. A., Colde-Dai, J., Bolzna, J. F., Liu, K. B., 1995. Late glacial stage and Holocene tropical ice core records from Huascarán Peru. Science 269, p 46-50.

Totten, M. W., Hanan, M. A., Weaver, B. L., 2000. Beyond whole-rock geochemistry of shales: the importance of assessing mineralogic controls for revealing tectonic discriminants of multiple sediment sources for the Ouachita mountain flysch deposits. Geological Society of America Bulletin 112, p. 1012-1022.

Toomey, D. F., Winland, H. D., 1973. Rock and biotic facies associated with Middle Pennsylvanian (Desmoinesian) algal buildup, Nena Lucia Field, Nolan County, Texas. American Association of Petroleum Geologists Bulletin 57, p. 1053-1074.

Waksmundzka, M. I., 2013. Carboniferous coarsening-upward and non-gradational cyclothems in the Lublin Basin (SE Poland): palaeoclimatic implications. In: Gasiewitcz, A., and Slowakiewicz, M. (Eds.), Paleozoic Climate Cycles: The Evolutionary and Sedimentological Impact, London, UK, Geological Society, Special Publications, vol. 376, p. 141-175.

Wahlman, G. P., 2002. Upper Carboniferous–Lower Permian (Bashkirian–Kungarian) mounds and reefs. In: Kiessling, W., Flügel, E., Golonka, E. (Eds.), Phanerozoic reef patterns, Tulsa, OK, SEPM Special Publications 72, p. 271-338.

Wilson, J. L., 1975. Carbonate Facies in Geologic History, Berlin, Springer, 471 p.

Winchester, J. A., and Floyd, P. A., 1977. Geochemical discrimination of different magma series and their differentiation products using immobile elements. Chemical Geology 20, p. 325-343.

Wright, V., Platt, N. H., Wimbledon, W. A., 1988. Biogenic laminar calcretes: evidence of calcified root-mat horizons in paleosols. Sedimentology 35, p. 603-620.

Wright, V. P., 1992. Speculations on the controls on cyclic peritidal carbonates: ice-house versus greenhouse eustatic controls. Sedimentary Geology 76, p. 1-5.

Zarza, A. A., Wright, V. P., Calvo, J. P., Garcia del Cura, M. G., 1992. Soil-landscape and climatic relationships in the middle Miocene of the Madrid Basin. Sedimentology 39, p. 17-35.

Zappettini, E. O., Coira, B., Santos, J. O. S., Cisterna, C.E., Belousova, E., 2015. Combined U-Pb and Lu-Hf isotopes from the Las Lozas volcanics, Chaschuil Valley, NW Argentina: evidence of lower Pennsylvanian extensional volcanism in western Gondwana. Journal of South American Earth Sciences 59, p. 13-18.

Appendix I: Tables and Figures

Table 1: Facies Summary

Facies (code)	Lithology	Structures	Common Facies Associations	Allochems	Typical Thickness (cm)	Interpretation/ Association Facies	Dust %	Dust size mode range
Boundstone (8)	Light pink to grey	lamina red algae, clotted micrite	Crinoidal-bryozoan packstone and microkarst		20 - 40	Outer ramp	~ 4	~1 – 3
Bryozoan Wackestone (7)	buff grey to tan wackestone	bioturbation	Brachiopod-bryozoan packstone and micritic mudstones.	comminuted skeletal hash of bryozoa, crinoid; peloids	20 - 80	Low to moderate energy, proximal outer ramp	~1 - 3	~1 - 2
Crinoidal/bryozoan Packstone (6)	Grey to tan pink packstone		This facies is commonly subjacent to the bryozoan wackestone facies.	comminuted skeletal hash; common to abundant, crinoid, brachiopod, and bryozoan fragments	10 - 65	Open marine, low to moderate energy, proximal to outer ramp	~1 - 23	~1 – 15
Molluscan Packstone (5)	Tan orange to grey packstone			tubular forams, abundant gastropod and ostracod debris, stick bryozoa, calcispheres	10 - 30	Low energy, restricted inner ramp	~5 - 11	2 – 4
Molluscan mud-wackestone (4)	Tan orange to grey	bioturbation	Gastropod Packstone and microkarst	abundant thin pelecypods; calcite replaced ghosts	20 - 80	Low energy, restricted inner ramp subtidal	~3 - 43	~1 – 43
Dolomitic Mudstone (3)	Tan orange to grey dolomitic mudstone		microkarst	evaporitic psudomorphs	100 - 190	Highly restricted inner ramp	~3 - 7	~2 – 3
Microkarst (2)	red to orange tan microbreccias	mosaic and chaotic fractures - breccias	Dolomitic mudstone or gastropod packstone	angular clasts mudstone, detrital angular quartz, some clay coated (hematite)	10 - 40	prolonged subaerial exposure	~8 - 38	~4 – 95
Red Mudstone (1)	Red mudstone	circumgranular cracking	Crinoidal-bryozoan packstone microkarst	detrital angular quartz grains	2 - 12	Subaerial exposure	~7 - 64	~6 – 97
Green Claystone	Green Claystone		Random		<1-100	Volcanic Ash	-	-

Table 2: Geochemistry of representative facies Manuripi X-1 core (MAN) and quaternary loess samples from Taylor et al, 1983 (*)

Sample	La (ppm)	Th (ppm)	Sc (ppm)	Cr (ppm)	SiO_2 (%)	Al_2O_3 (%)	CaO (%)	K_2O (%)	Na_2O (%)	K_2O+Na_2O (%)	La/Sc	Th/Sc	La/Cr	Sc/Cr
MAN 872.7	15.3	3.7	3.0	40.0	20.0	4.0	39.5	1.1	0.1	1.2	18.3	6.7	0.4	0.1
MAN 873.9	5.6	1.7	1.0	40.0	13.3	1.8	45.6	0.5	0.0	0.5	6.6	2.7	0.1	0.0
MAN 875.7	7.8	4.8	3.0	20.0	17.0	5.5	40.1	1.3	0.1	1.4	10.8	7.8	0.4	0.2
MAN 876.0	14.6	7.7	3.0	80.0	26.1	6.7	32.7	1.8	0.1	1.9	17.6	10.7	0.2	0.0
MAN 876.8	3.5	34.2	8.0	10.0	51.2	22.6	1.8	4.9	0.2	5.0	11.5	42.2	0.4	0.8
MAN 880.6	4.0	0.4	<1	10.0	5.1	0.4	39.8	0.1	0.0	0.2	4.5	0.9	0.4	0.1
MAN 882.9	22.2	16.2	13.0	100.0	55.4	14.1	6.1	4.0	0.2	4.2	35.2	29.2	0.2	0.1
MAN 883.7	5.8	0.2	0.5	80.0	1.4	0.2	54.9	0.1	0.0	0.1	6.3	0.7	0.1	0.0
MAN 884.4	3.1	0.4	<1	50.0	2.9	0.3	52.7	0.1	0.0	0.1	3.6	0.9	0.1	0.0
MAN 885.4	3.7	0.3	<1	10.0	10.7	0.4	50.7	0.1	0.0	0.1	4.2	0.8	0.4	0.1
MAN 888.9	15.9	4.6	3.0	20.0	15.6	4.5	40.4	1.2	0.1	1.3	18.9	7.6	0.8	0.2
MAN 889.2	2.4	0.5	<1	60.0	3.5	0.5	52.0	0.1	0.0	0.2	2.9	1.0	0.0	0.0
MAN 891.8	22.9	3.2	1.0	20.0	27.8	2.0	37.8	0.8	0.1	0.9	23.9	4.2	1.1	0.1
MAN 895.1	15.9	1.6	3.0	30.0	8.2	2.5	47.3	0.9	0.1	0.9	18.9	4.6	0.5	0.1
MAN 895.4	6.9	0.4	1.0	10.0	2.8	0.3	55.4	0.1	0.0	0.1	7.9	1.4	0.7	0.1
MAN 962.8	21.0	6.9	7.0	30.0	31.3	8.6	25.5	2.7	0.2	2.9	28.0	13.9	0.7	0.2
**BP-1*	34.0	11.1	8.0	31.0	72.7	0.6	1.5	2.4	3.3	5.7	4.3	1.4	1.1	0.3
**BP-2*	32.0	10.3	8.4	32.0	74.0	0.6	1.5	2.3	3.1	5.4	3.8	1.2	1.0	0.3
**BP3*	41.0	9.8	8.5	32.0	72.5	0.7	1.3	2.3	3.1	5.4	4.8	1.1	1.3	0.3
**BP4*	35.6	10.2	8.0	30.0	74.0	0.6	1.3	2.4	3.4	5.9	4.5	1.3	1.2	0.3
**BP5*	35.2	9.5	7.6	30.0	72.5	0.5	1.6	2.5	3.6	6.0	4.6	1.3	1.2	0.3
**Kaiserstuhl 1+*	25.0	5.4	5.7	42.0	59.9	0.3	23.1	1.3	0.8	2.1	4.4	0.9	0.6	0.1
**Kaiserstuhl 2+*	25.0	5.8	6.0	42.0	59.1	0.3	22.9	1.3	0.9	2.2	4.2	1.0	0.6	0.1
**KANSAS A*	34.0	8.3	5.7	31.0	80.4	0.6	1.1	2.5	1.6	4.1	6.0	1.5	1.1	0.2
**KANSAS B*	31.0	7.0	5.4	33.0	80.8	0.6	1.1	2.6	1.6	4.2	5.7	1.3	0.9	0.2
**KANSAS C*	39.0	10.0	4.9	32.0	79.9	0.7	1.2	2.6	1.7	4.3	8.0	2.0	1.2	0.2
**IOWA*	33.1	12.8	-	-	79.5	0.7	0.9	2.2	1.5	3.6	-	-	-	-

Table 3: Correlation between element concentrations and principal components (PC)

	PC1	PC2	PC3	PC4	PC5	PC6
[1,]Ca	-0.2941	0.4696	-0.0453	0.0415	-0.1143	0.1616
[2,]Si	0.3987	0.0100	0.3721	0.1828	-0.0283	-0.6849
[3,]Mg	0.0264	-0.5520	-0.0990	-0.0801	0.0776	0.3488
[4,]Na	0.2324	-0.4133	-0.0261	-0.4257	0.3087	-0.1092
[5,]Fe	0.2606	-0.2146	-0.3770	0.0199	-0.8403	-0.0373
[6,]K	0.4562	0.2059	-0.1669	-0.0106	0.2050	0.1686
[7,]Al	0.4492	0.2079	-0.1394	0.0275	0.1570	0.3216
[8,]S	-0.0540	-0.2446	-0.3643	0.8198	0.2726	-0.0749
[9,]Ti	0.4042	0.3149	-0.2406	-0.0102	0.0449	0.0184
[10,]Mn	0.2359	-0.1150	0.6848	0.3222	-0.1890	0.4817
Port. Var.	37.26	28.59	11.06	9.11	6.41	4.51
Cumul. Var.	37.26	65.85	76.91	86.02	92.44	96.95

Table 4: Stratigraphic Location and Dust Analyses

Depth (sample)	Facies	Dust %	D (10) µm	D (50) µm	D (90) µm	Mode (µm)	% Below (5 µm) %	% Below (10 µm) %	% Below (20 µm) %	% in Range (5 - 20 µm) %	% in Range (20 - 200 µm) %	(5 - 20 µm)% / (20 - 200 µm) %
895.65	H-Boundstone	4%	0.9	2.6	9.9	2.5	76.3	90.1	94.5	18.2	5.5	3.3
897.35	H-Boundstone	4%	0.8	2.6	25.6	0.9	66.9	78.0	86.4	19.5	13.6	1.4
883.70	G-Bryozoa Wackestone	1%	0.8	2.4	10.1	1.0	73.4	89.9	98.6	25.3	1.4	18.5
884.35	G-Bryozoa Wackestone	3%	0.9	2.3	8.5	2.3	80.8	91.5	96.4	15.6	3.6	4.3
884.54	G-Bryozoa Wackestone		0.9	3.5	214.0	2.2	58.1	66.6	73.0	14.9	16.6	0.9
884.76	G-Bryozoa Wackestone	2%	0.8	1.7	7.4	1.0	85.9	92.3	97.7	11.7	2.3	5.0
875.45	F-Crinoidal/bryozoan Packstone	9%	1.1	3.7	9.6	4.6	37.8	64.2	84.5	46.6	15.5	3.0
881.02	F-Crinoidal/bryozoan Packstone	1%	0.8	2.4	9.3	2.3	76.3	91.3	99.5	23.2	0.5	47.6
881.84	F-Crinoidal/bryozoan Packstone	15%	1.2	8.5	47.7	12.7	37.4	54.2	72.4	34.9	27.6	1.3
886.62	F-Crinoidal/bryozoan Packstone	8%	2.3	9.7	39.5	9.0	26.4	51.0	74.4	48.0	25.6	1.9
891.98	F-Crinoidal/bryozoan Packstone	23%	2.3	21.0	249.0	15.0	20.5	33.8	48.9	28.4	38.9	0.7
892.40	F-Crinoidal/bryozoan Packstone	12%	1.7	8.7	315.0	5.2	34.7	53.4	67.0	32.3	19.6	1.7
892.73	F-Crinoidal/bryozoan Packstone	16%	1.3	24.4	505.0	2.8	33.8	42.6	48.4	14.6	27.6	0.5
893.30	F-Crinoidal/bryozoan Packstone		1.0	3.6	12.4	3.9	62.7	85.1	97.7	35.1	2.3	15.6
895.40	F-Crinoidal/bryozoan Packstone	2%	0.8	2.1	11.8	2.0	79.6	88.9	92.7	13.1	7.3	1.8
896.06	F-Crinoidal/bryozoan Packstone	1%	0.8	2.6	32.2	2.5	72.1	82.8	87.5	15.4	6.6	2.3
896.25	F-Crinoidal/bryozoan Packstone	2%	0.8	3.7	26.5	0.9	58.0	74.5	86.0	28.0	14.0	2.0
875.01	E-Gastropod Packstone	11%	1.5	5.0	20.3	4.4	49.8	74.3	89.7	40.0	10.3	3.9
890.12	E-Gastropod Packstone	3%	1.0	3.0	10.2	3.0	72.2	89.7	96.0	23.8	4.0	5.9
896.75	E-Gastropod Packstone		1.0	8.9	83.5	25.9	38.7	52.1	65.3	26.6	27.7	1.0

D10 = 10% of the population lies below this grain size
D50 = 50% of the population lies below this grain size
D90 = 90% of the population lies below this grain size
*All results are expressed in volume %

Table 5: Stratigraphic Location and Dust Analyses

Depth (sample)	Facies	Dust %	D (10) µm	D (50) µm	D (90) µm	Mode (µm)	% Below (5 µm) %	% Below (10 µm) %	% Below (20 µm) %	% in Range (5 - 20 µm) %	% in Range (20 - 200 µm) %	(5 - 20 µm)% / (20 - 200 µm) %
896.87	E-Gastropod Packstone		0.8	2.8	29.2	1.0	65.1	78.8	85.6	20.4	14.4	1.4
897.10	E-Gastropod Packstone	5%	0.9	2.3	16.2	2.3	77.6	86.4	92.1	14.5	7.9	1.8
870.80	D-Carbonate mud wackestone	5%	1.2	17.2	388.0	42.7	36.9	46.5	51.2	14.2	35.5	0.4
871.95	D-Carbonate mud wackestone	13%	2.2	12.3	46.1	25.2	26.2	44.5	64.4	38.2	35.6	1.1
872.65	D-Carbonate mud wackestone		1.7	5.4	31.7	4.0	46.7	67.4	80.8	34.0	19.2	1.8
873.31	D-Carbonate mud wackestone	17%	1.8	19.0	369.0	23.4	24.6	37.3	51.1	26.5	31.7	0.8
873.45	D-Carbonate mud wackestone	11%	0.9	3.9	96.7	2.3	54.9	62.7	68.8	13.9	27.2	0.5
873.72	D-Carbonate mud wackestone	5%	0.9	2.5	13.9	2.5	78.4	88.3	92.5	14.1	7.5	1.9
874.09	D-Carbonate mud wackestone	12%	0.9	2.8	18.7	2.5	68.9	80.5	91.0	22.1	9.0	2.5
874.10	D-Carbonate mud wackestone	8%	0.9	2.8	9.2	2.8	77.0	90.9	96.4	19.5	3.6	5.4
874.42	D-Carbonate mud wackestone	5%	0.8	2.0	22.9	0.9	73.5	80.7	88.0	14.5	12.0	1.2
874.62	D-Carbonate mud wackestone	5%	0.9	2.2	7.3	2.3	83.2	92.9	97.4	14.1	2.6	5.4
874.81	D-Carbonate mud wackestone	10%	1.3	5.0	15.5	6.1	49.8	78.0	94.2	44.4	5.8	7.7
875.23	D-Carbonate mud wackestone	10%	1.5	6.9	27.1	7.2	75.4	93.1	99.2	23.7	0.8	28.5
875.81	D-Carbonate mud wackestone	22%	2.6	19.7	106.0	17.2	36.6	49.3	58.8	22.2	41.2	0.5
875.96	D-Carbonate mud wackestone	12%	1.0	2.6	12.2	2.3	17.9	31.8	50.5	32.6	48.7	0.7
877.41	D-Carbonate mud wackestone	7%	1.3	5.8	27.5	5.6	14.9	23.4	35.3	20.4	56.4	0.4
877.58	D-Carbonate mud wackestone	7%	1.0	3.4	17.0	3.4	44.5	68.3	84.3	39.8	15.7	2.5
879.53	D-Carbonate mud wackestone	15%	0.8	2.1	5.5	2.3	82.3	90.6	93.8	11.5	6.2	1.8
879.79	D-Carbonate mud wackestone	17%	0.9	2.4	6.2	2.6	84.2	96.9	99.4	15.2	0.6	25.4

D10 = 10% of the population lies below this grain size
D50 = 50% of the population lies below this grain size
D90 = 90% of the population lies below this grain size
*All results are expressed in volume %

Table 6: Stratigraphic Location and Dust Analyses

Depth (sample)	Facies	Dust %	D (10) µm	D (50) µm	D (90) µm	Mode (µm)	% Below (5 µm) %	% Below (10 µm) %	% Below (20 µm) %	% in Range (5 - 20 µm) %	% in Range (20 - 200 µm) %	(5 - 20 µm)% / (20 - 200 µm) %
879.87	D-Carbonate mud wackestone	5%	1.5	9.0	64.2	6.5	35.2	52.7	67.7	32.5	32.3	1.0
880.37	D-Carbonate mud wackestone	5%	0.9	2.8	34.5	2.3	66.5	76.7	82.2	15.8	17.8	0.9
880.56	D-Carbonate mud wackestone	15%	1.4	6.2	16.5	9.7	42.3	70.2	95.0	52.8	5.0	10.6
880.79	D-Carbonate mud wackestone	6%	0.9	2.7	19.9	2.5	71.3	82.8	90.1	18.8	9.9	1.9
884.98	D-Carbonate mud wackestone	7%	0.9	2.7	6.6	3.1	80.7	96.9	99.2	18.5	0.8	22.8
885.18	D-Carbonate mud wackestone	11%	1.1	4.9	12.9	6.2	51.1	82.1	97.3	46.2	2.7	17.2
885.42	D-Carbonate mud wackestone	5%	1.0	4.0	12.4	4.6	60.0	85.3	96.2	36.2	3.8	9.7
885.62	D-Carbonate mud wackestone	43%	1.3	6.1	14.8	7.8	41.4	74.5	96.8	55.4	3.2	17.4
885.80	D-Carbonate mud wackestone	11%	1.0	3.8	10.3	4.6	62.4	89.2	98.8	36.4	1.2	31.3
886.00	D-Carbonate mud wackestone	10%	0.9	2.8	7.6	3.2	76.9	94.1	97.8	20.9	2.2	9.6
886.20	D-Carbonate mud wackestone	7%	0.7	2.2	12.6	0.8	78.4	87.9	94.9	16.5	5.1	3.3
886.42	D-Carbonate mud wackestone	10%	1.2	4.7	13.6	5.4	53.1	81.6	96.5	43.4	3.5	12.4
887.13	D-Carbonate mud wackestone	8%	5.1	24.3	72.2	31.5	9.7	22.1	42.5	32.8	57.2	0.6
887.62	D-Carbonate mud wackestone	10%	1.1	5.6	21.6	6.2	46.4	69.6	88.4	42.0	11.6	3.6
887.78	D-Carbonate mud wackestone	17%	2.1	9.9	48.9	6.8	29.5	50.4	69.4	40.0	28.0	1.4
889.00	D-Carbonate mud wackestone	3%	1.0	2.8	7.6	2.8	77.5	94.5	98.7	21.3	1.3	17.0
889.22	D-Carbonate mud wackestone	3%	0.8	1.9	21.1	0.9	76.1	83.5	89.4	13.3	10.6	1.3
889.42	D-Carbonate mud wackestone	4%	0.8	1.8	18.8	1.0	79.9	85.5	90.6	10.7	9.4	1.1
889.61	D-Carbonate mud wackestone	8%	1.0	2.9	8.3	3.1	75.0	93.0	98.4	23.5	1.6	15.1
889.69	D-Carbonate mud wackestone	8%	1.1	3.9	39.8	3.3	58.8	77.2	84.5	25.7	11.0	2.3

D10 = 10% of the population lies below this grain size
D50 = 50% of the population lies below this grain size
D90 = 90% of the population lies below this grain size
*All results are expressed in volume %

Table 7: Stratigraphic Location and Dust Analyses

Depth (sample)	Facies	Dust %	D (10) µm	D (50) µm	D (90) µm	Mode (µm)	% Below (5 µm) %	% Below (10 µm) %	% Below (20 µm) %	% in Range (5 - 20 µm) %	% in Range (20 - 200 µm) %	(5 - 20 µm)% / (20 - 200 µm) %
893.55	D-Carbonate mud wackestone	15%	1.2	6.7	28.2	8.2	41.2	62.5	82.3	41.1	17.5	2.3
877.83	C-Dolomitic Mudstone	4%	1.1	2.9	9.3	2.7	66.5	85.2	91.1	24.6	8.9	2.8
878.75	C-Dolomitic Mudstone	3%	0.9	2.5	22.0	2.3	75.3	90.8	95.1	19.8	4.9	4.0
879.12	C-Dolomitic Mudstone	4%	0.9	2.1	7.4	2.2	75.4	84.9	89.2	13.9	10.8	1.3
879.29	C-Dolomitic Mudstone	7%	0.8	2.2	9.1	2.3	84.5	92.1	96.0	11.6	4.0	2.9
888.86	B-Microbreccia	38%	4.0	18.0	85.0	17.8	14.0	30.7	53.6	39.6	46.1	0.9
888.90	B-Microbreccia	18%	3.0	37.6	120.0	70.0	14.7	23.0	34.8	20.1	63.2	0.3
891.75	B-Microbreccia	31%	2.9	39.8	254.0	94.6	15.8	25.4	37.2	21.4	48.0	0.4
895.10	B-Microbreccia	8%	1.4	4.9	21.2	4.2	50.9	74.0	89.0	38.1	11.0	3.5
871.00	A-Red Siltstone	7%	1.5	10.9	33.5	20.6	29.8	47.5	71.6	41.9	28.4	1.5
875.70	A-Red Siltstone	16%	1.2	10.5	64.2	46.7	64.3	91.2	99.1	34.8	0.9	39.9
876.77	A-Red Siltstone	64%	1.7	6.0	19.6	6.1	74.0	87.6	94.8	20.8	5.2	4.0
877.00	A-Red Siltstone	29%	3.0	40.1	173.0	85.3	42.5	70.9	90.4	47.9	9.6	5.0
882.03	A-Red Siltstone	15%	4.2	18.9	65.8	22.6	12.8	28.1	52.2	39.4	47.3	0.8
891.00	A-Red Siltstone	15%	6.8	65.0	210.0	96.6	7.7	13.7	22.5	14.8	66.4	0.2
891.37	A-Red Siltstone	28%	3.0	36.2	173.0	78.4	15.3	24.6	37.0	21.7	54.4	0.4
895.86	A-Red Siltstone	9%	1.3	5.4	15.6	7.0	46.6	75.7	94.8	48.2	5.2	9.3

D10 = 10% of the population lies below this grain size
D50 = 50% of the population lies below this grain size
D90 = 90% of the population lies below this grain size
*All results are expressed in volume %

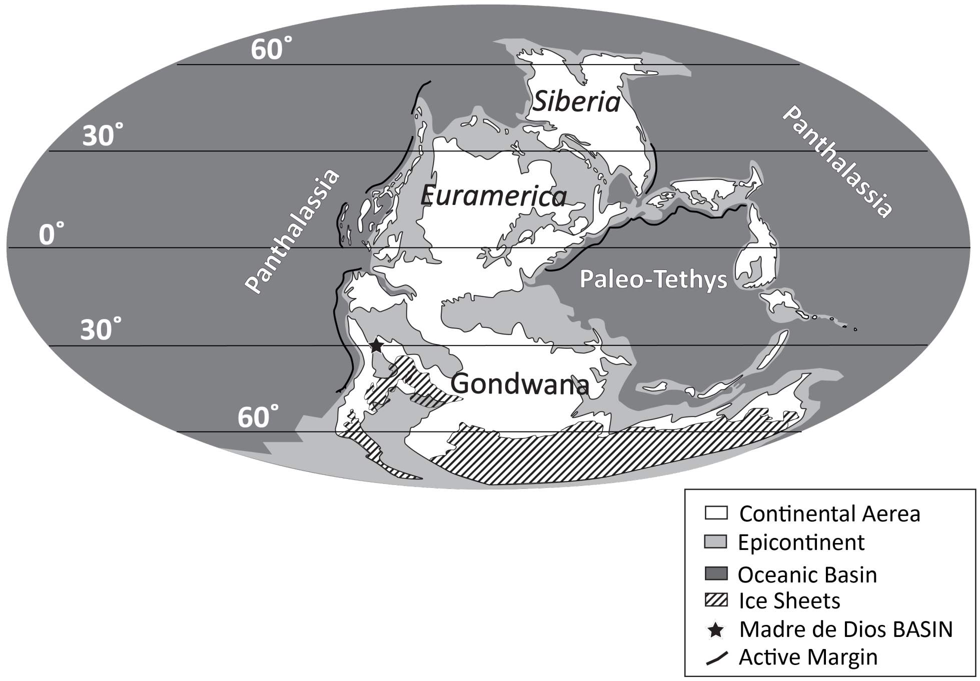
60°
30°
0°
30°
60°
Panthalassia
Siberia
Euramerica
Panthalassia
Paleo-Tethys
Gondwana
Continental Aerea
Epicontinent
Oceanic Basin
Ice Sheets
Madre de Dios BASIN
Active Margin

Figure 1

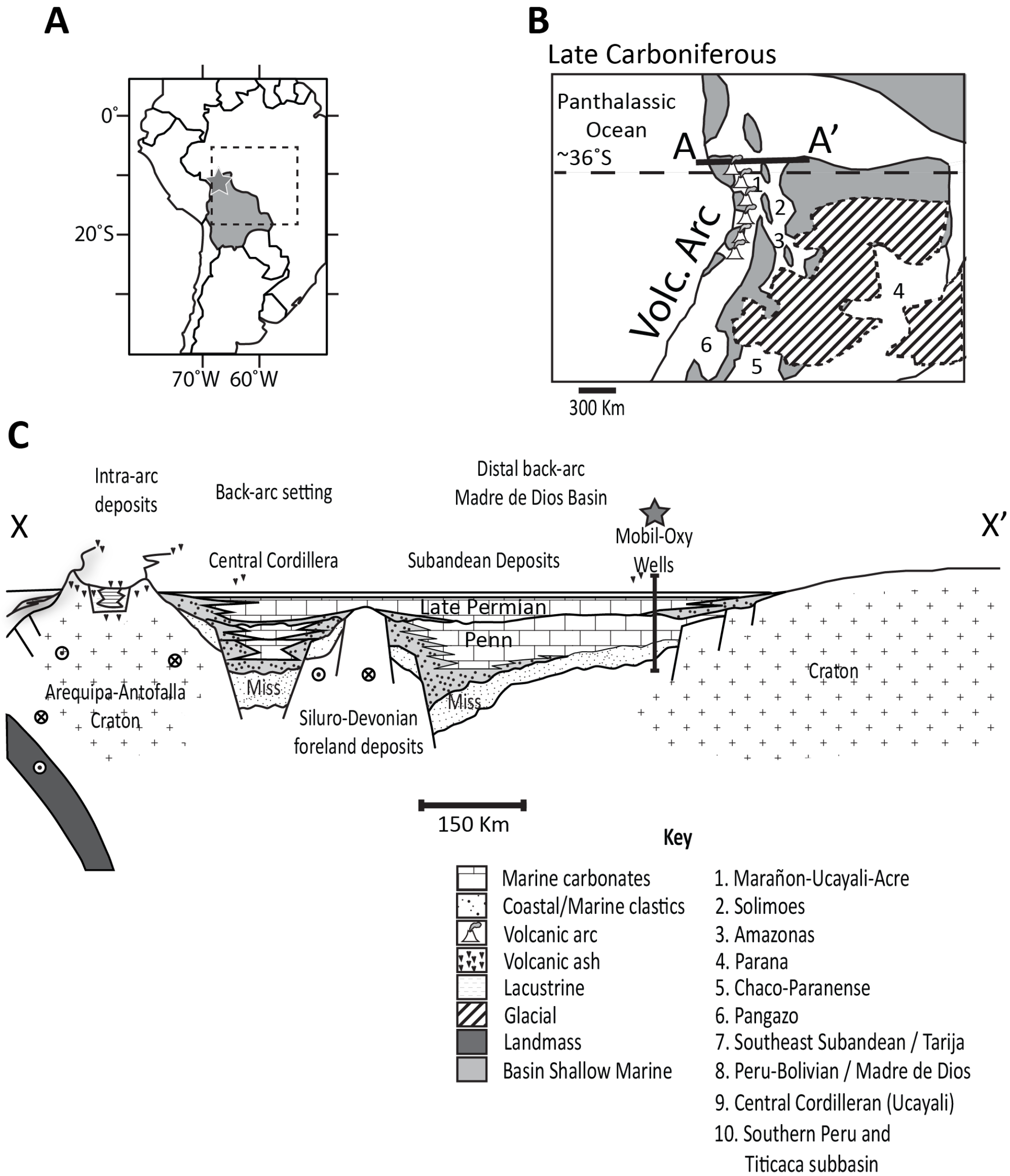
A
0˚
20˚S
70˚W 60˚W
B
Late Carboniferous
Panthalassic Ocean
~36˚S
A
A'
Volc. Arc
1
2
3
4
5
6
300 Km
C
Intra-arc deposits
Back-arc setting
Distal back-arc Madre de Dios Basin
X
X'
Mobil-Oxy Wells
Central Cordillera
Subandean Deposits
Late Permian
Penn
Miss
Miss
Craton
Arequipa-Antofalla Craton
Siluro-Devonian foreland deposits
150 Km
Key
Marine carbonates
Coastal/Marine clastics
Volcanic arc
Volcanic ash
Lacustrine
Glacial
Landmass
Basin Shallow Marine
1. Marañon-Ucayali-Acre
2. Solimoes
3. Amazonas
4. Parana
5. Chaco-Paranense
6. Pangazo
7. Southeast Subandean / Tarija
8. Peru-Bolivian / Madre de Dios
9. Central Cordilleran (Ucayali)
10. Southern Peru and Titicaca subbasin

Figure 2

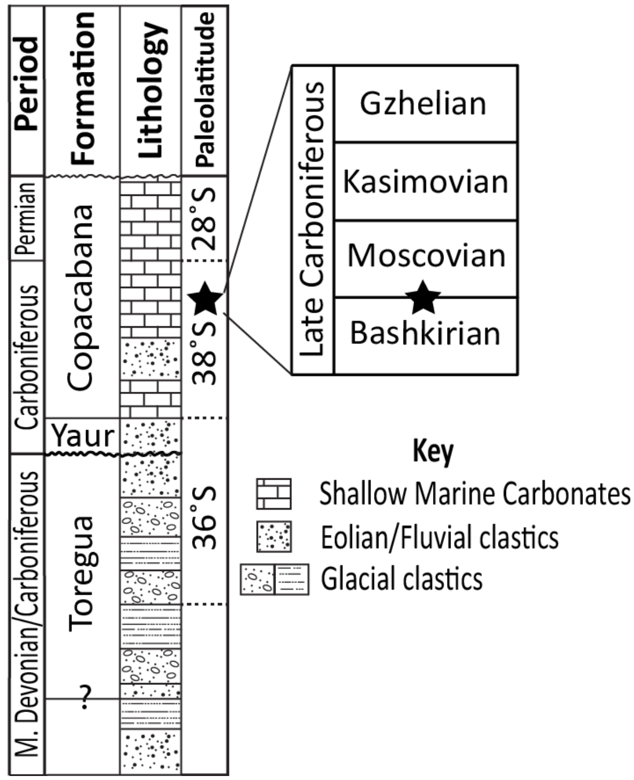

Period
Formation
Lithology
Paleolatitude
Permian
Carboniferous
M. Devonian/Carboniferous
Copacabana
Yaur
Toregua
?
28˚S
38˚S
36˚S
Late Carboniferous
Gzhelian
Kasimovian
Moscovian
Bashkirian
Key
Shallow Marine Carbonates
Eolian/Fluvial clastics
Glacial clastics

Figure 3

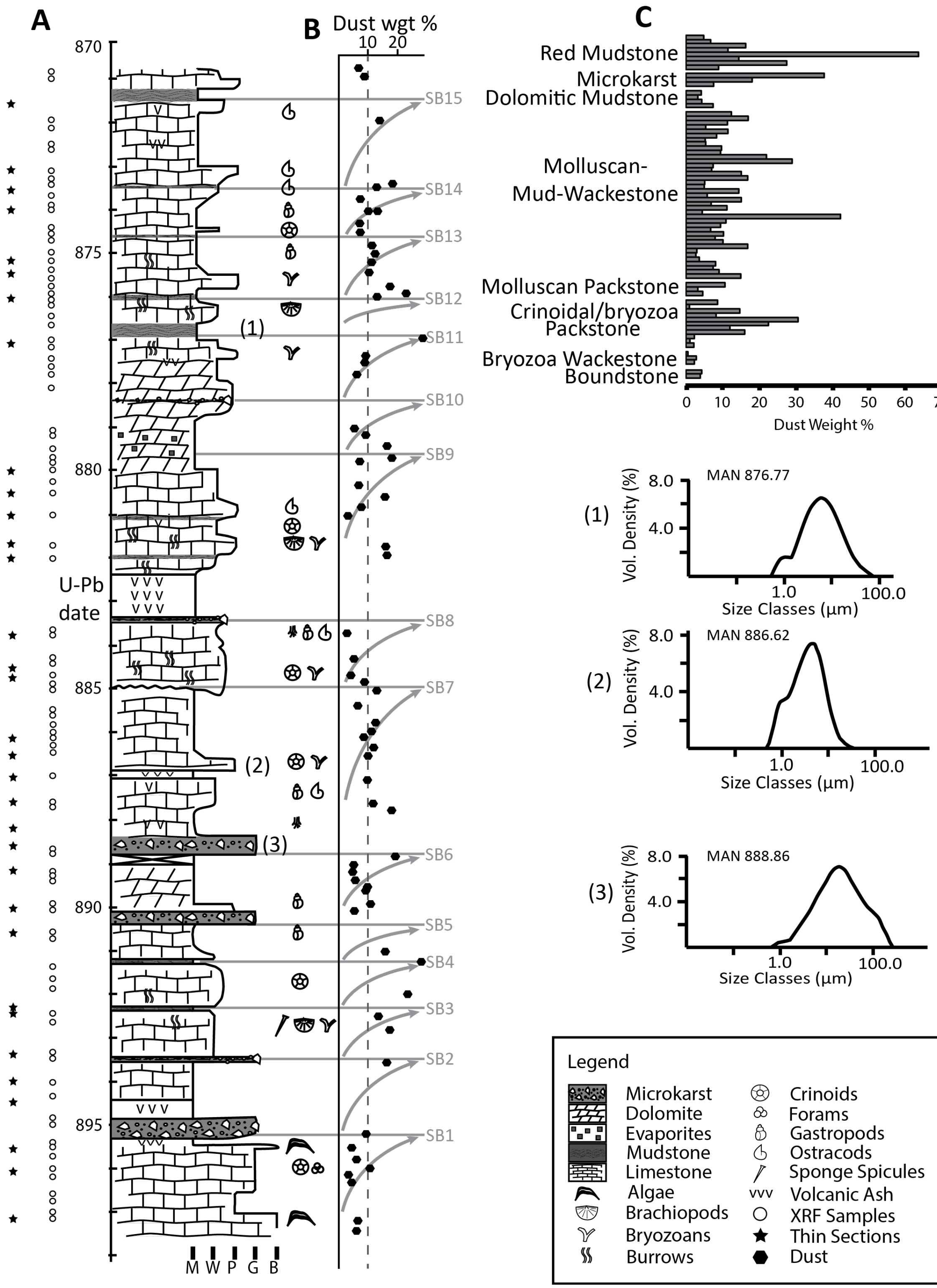
A
B
Dust wgt %
10
20
C
870
875
880
885
890
895
U-Pb
date
(1)
(2)
(3)
SB15
SB14
SB13
SB12
SB11
SB10
SB9
SB8
SB7
SB6
SB5
SB4
SB3
SB2
SB1
M W P G B
Red Mudstone
Microkarst
Dolomitic Mudstone
Molluscan-
Mud-Wackestone
Molluscan Packstone
Crinoidal/bryozoa
Packstone
Bryozoa Wackestone
Boundstone
0 10 20 30 40 50 60 70
Dust Weight %
MAN 876.77
Vol. Density (%)
8.0
4.0
1.0
100.0
Size Classes (µm)
MAN 886.62
MAN 888.86
Legend
Microkarst
Dolomite
Evaporites
Mudstone
Limestone
Algae
Brachiopods
Bryozoans
Burrows
Crinoids
Forams
Gastropods
Ostracods
Sponge Spicules
Volcanic Ash
XRF Samples
Thin Sections
Dust

Figure 4

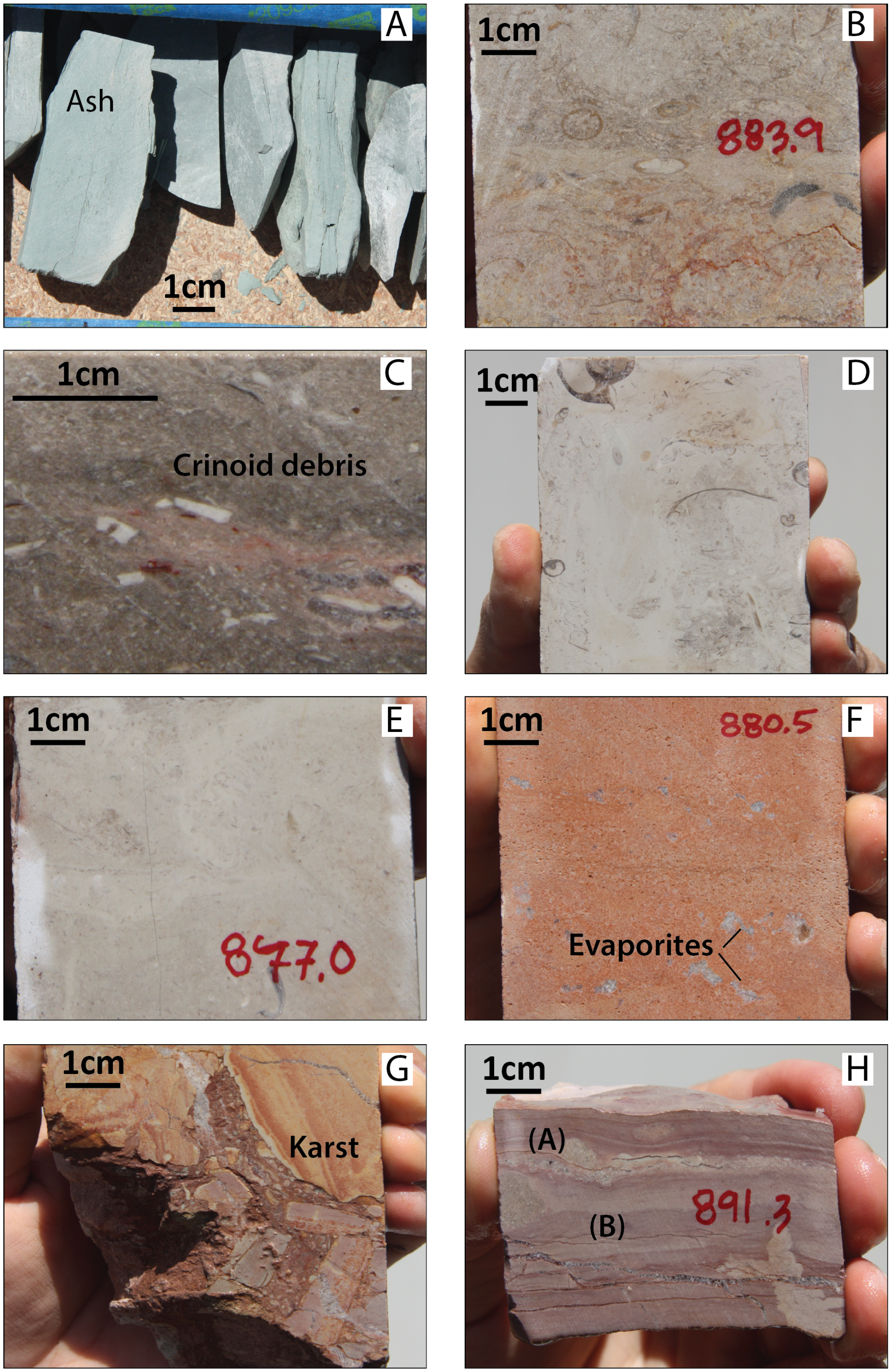
A
Ash
1cm
B
1cm
883.9
C
1cm
Crinoid debris
D
1cm
E
1cm
877.0
F
1cm
880.5
Evaporites
G
1cm
Karst
H
1cm
(A)
(B)
891.3

Figure 5

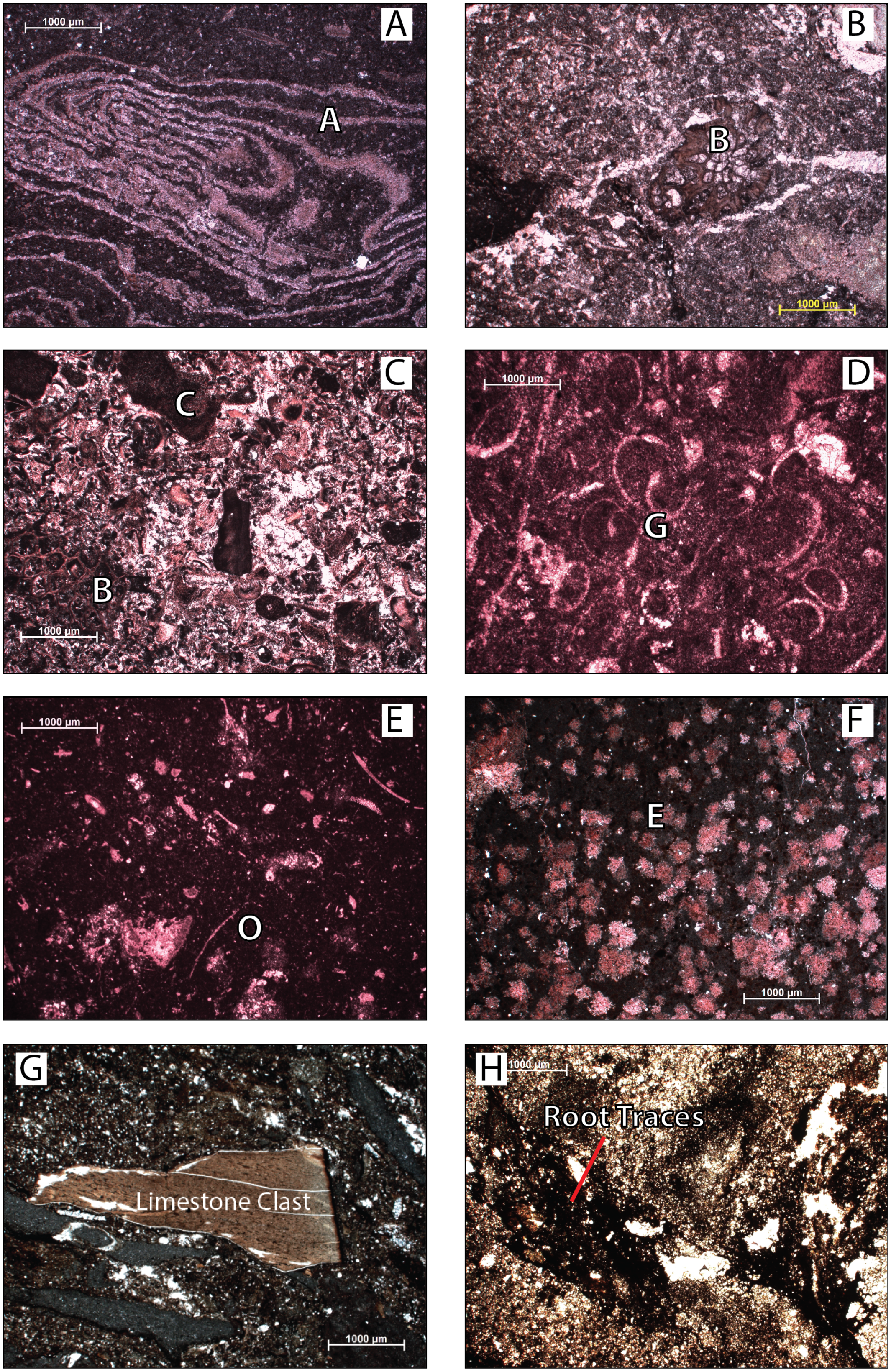
A
1000 µm
A
B
B
1000 µm
C
C
B
1000 µm
D
1000 µm
G
E
1000 µm
O
F
E
1000 µm
G
Limestone Clast
1000 µm
H
1000 µm
Root Traces

Figure 6

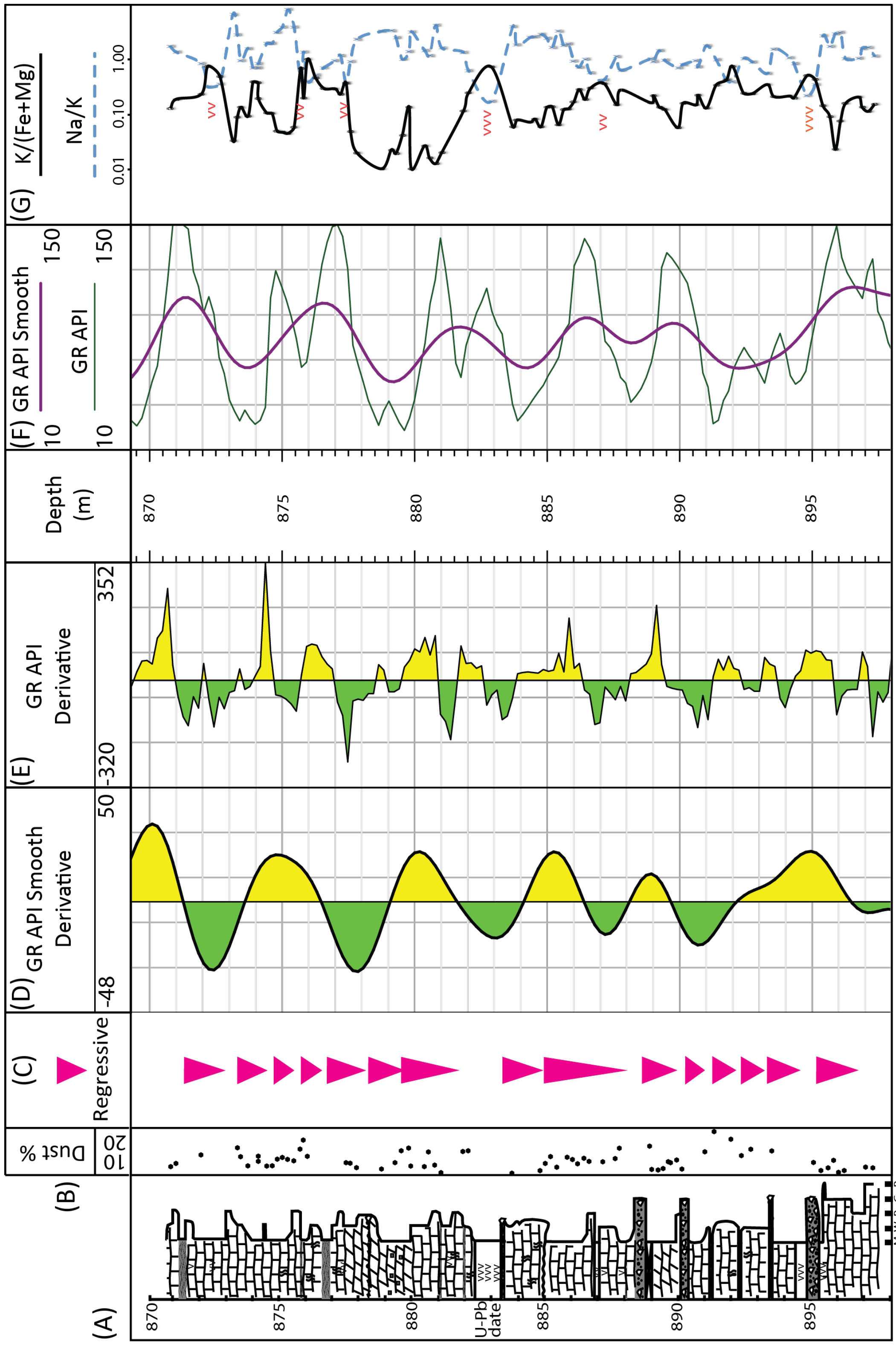
(A)
870
875
880
U-Pb date
885
890
895
M W P G B
(B)
Dust %
10 20
(C)
Regressive
(D) GR API Smooth Derivative
-48
50
(E) GR API Derivative
-320
352
Depth (m)
870
875
880
885
890
895
(F) GR API Smooth
10
150
GR API
10
150
(G) K/(Fe+Mg)
Na/K
0.01
0.10
1.00

Figure 7

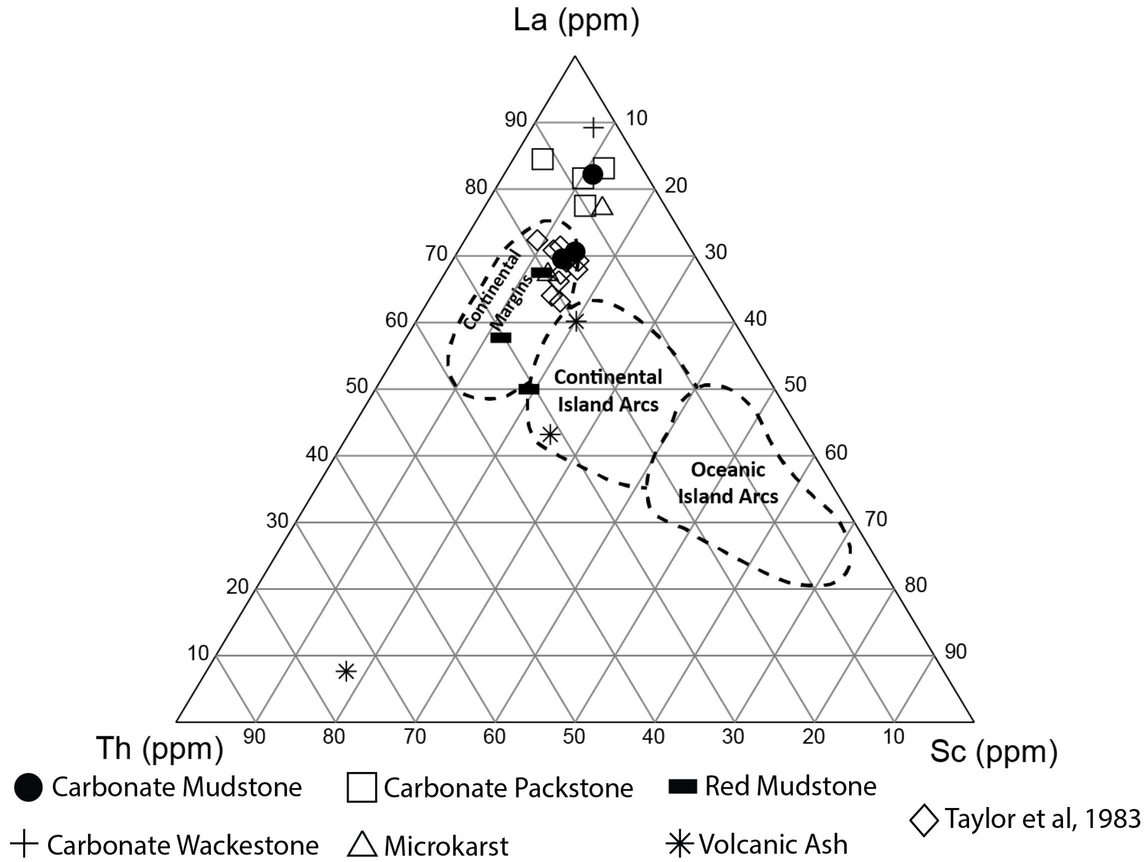
La (ppm)
Th (ppm)
Sc (ppm)
90
80
70
60
50
40
30
20
10
Continental Margins
Continental Island Arcs
Oceanic Island Arcs
Carbonate Mudstone
Carbonate Packstone
Red Mudstone
Taylor et al, 1983
Carbonate Wackestone
Microkarst
Volcanic Ash

Figure 8

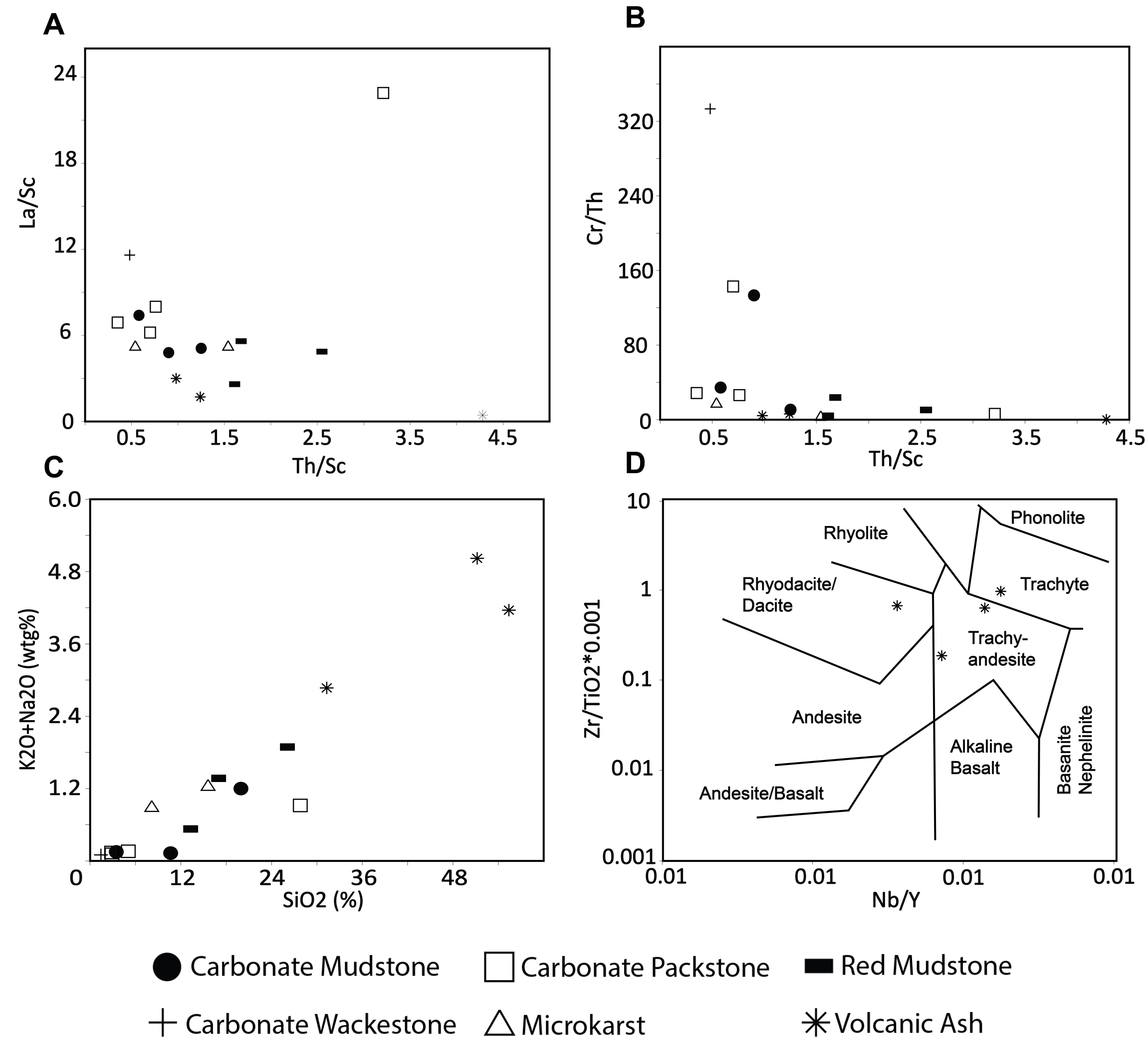

A
La/Sc
Th/Sc
B
Cr/Th
Th/Sc
C
K2O+Na2O (wtg%)
SiO2 (%)
D
Zr/TiO2*0.001
Nb/Y
Rhyolite
Phonolite
Rhyodacite/
Dacite
Trachyte
Trachy-
andesite
Andesite
Alkaline
Basalt
Andesite/Basalt
Basanite
Nephelinite
Carbonate Mudstone
Carbonate Packstone
Red Mudstone
Carbonate Wackestone
Microkarst
Volcanic Ash

Figure 9

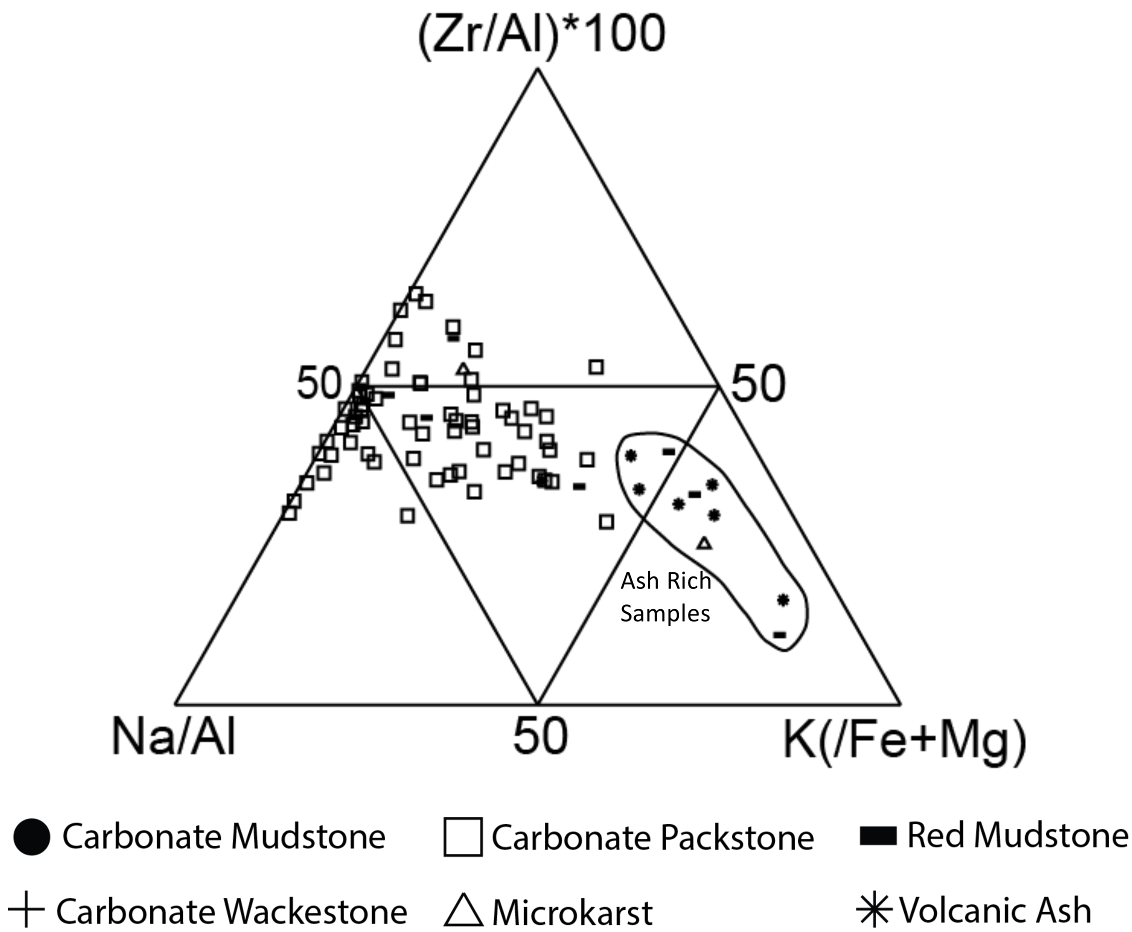
(Zr/Al)*100
50
50
Ash Rich
Samples
Na/Al
50
K(/Fe+Mg)
Carbonate Mudstone
Carbonate Packstone
Red Mudstone
Carbonate Wackestone
Microkarst
Volcanic Ash

Figure 10

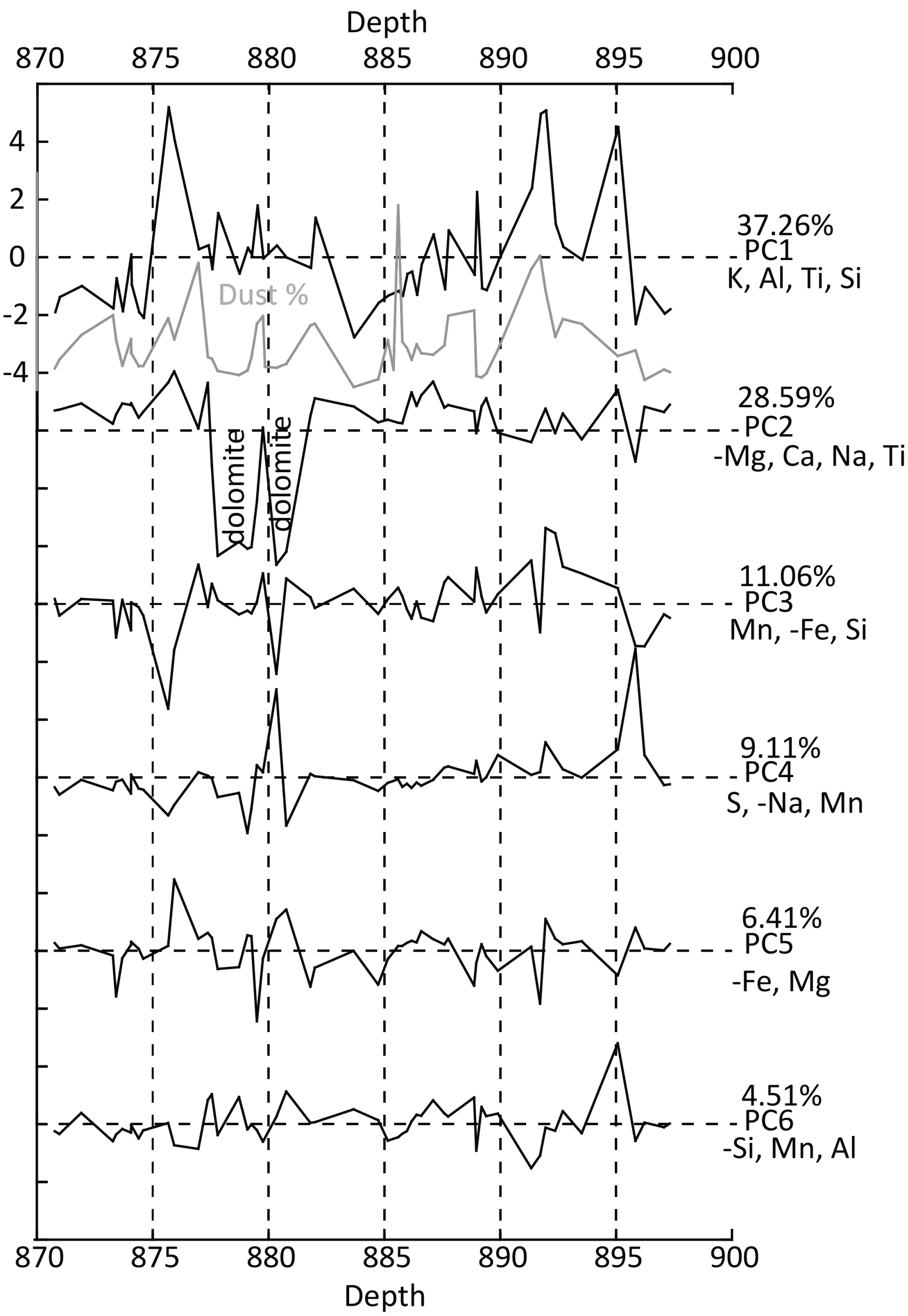
Depth
870
875
880
885
890
895
900
4
2
0
-2
-4
37.26%
PC1
K, Al, Ti, Si
Dust %
28.59%
PC2
-Mg, Ca, Na, Ti
dolomite
dolomite
11.06%
PC3
Mn, -Fe, Si
9.11%
PC4
S, -Na, Mn
6.41%
PC5
-Fe, Mg
4.51%
PC6
-Si, Mn, Al
870
875
880
885
890
895
900
Depth

Figure 11

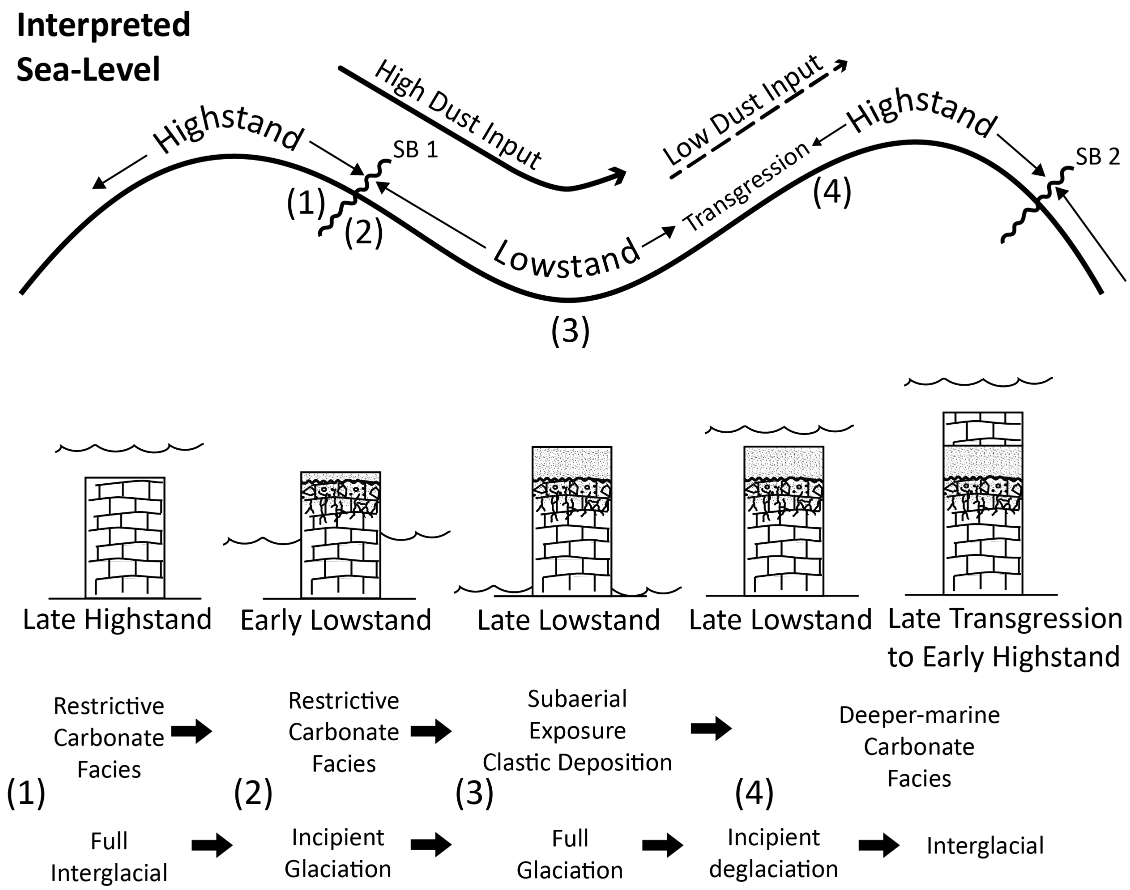
Interpreted
Sea-Level
Highstand
High Dust Input
Low Dust Input
Highstand
SB 1
SB 2
(1)
(2)
Lowstand
Transgression
(4)
(3)
Late Highstand
Early Lowstand
Late Lowstand
Late Lowstand
Late Transgression to Early Highstand
Restrictive Carbonate Facies
Restrictive Carbonate Facies
Subaerial Exposure Clastic Deposition
Deeper-marine Carbonate Facies
(1)
(2)
(3)
(4)
Full Interglacial
Incipient Glaciation
Full Glaciation
Incipient deglaciation
Interglacial

Figure 12

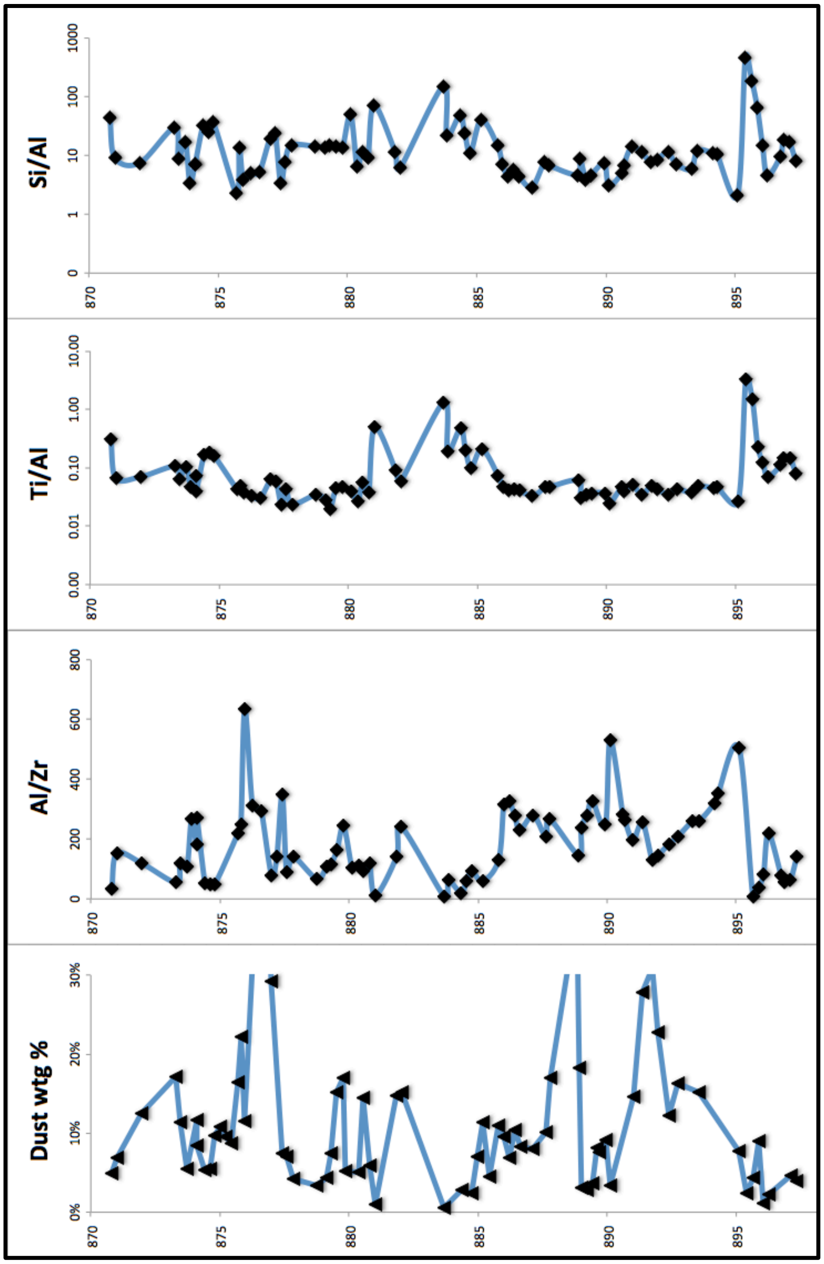
Si/Al
0
1
10
100
1000
Ti/Al
0.00
0.01
0.10
1.00
10.00
Al/Zr
0
200
400
600
800
Dust wtg %
0%
10%
20%
30%
870
875
880
885
890
895

Figure 13

Appendix II: Additional Figures

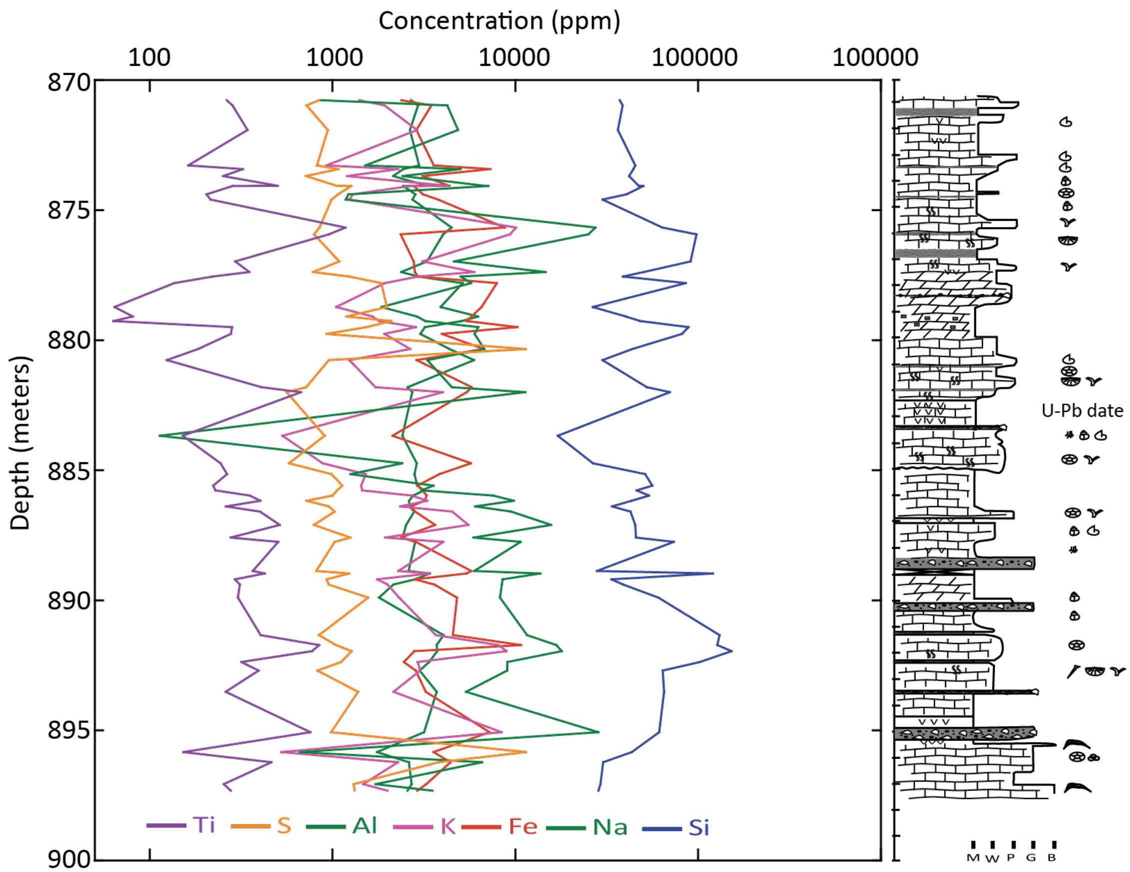

Concentration (ppm)
100
1000
10000
100000
100000
870
875
880
885
890
895
900
Depth (meters)
Ti
S
Al
K
Fe
Na
Si
U-Pb date
M W P G B

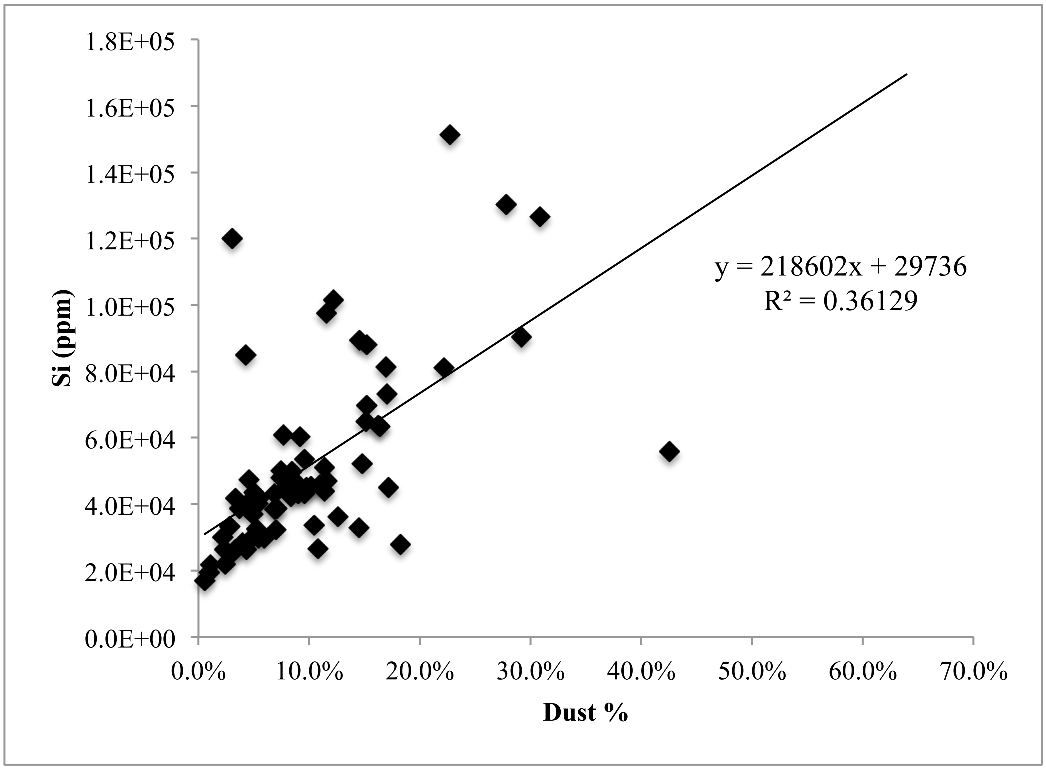

1.8E+05
1.6E+05
1.4E+05
1.2E+05
1.0E+05
8.0E+04
6.0E+04
4.0E+04
2.0E+04
0.0E+00
Si (ppm)
y = 218602x + 29736
R² = 0.36129
0.0%
10.0%
20.0%
30.0%
40.0%
50.0%
60.0%
70.0%
Dust %

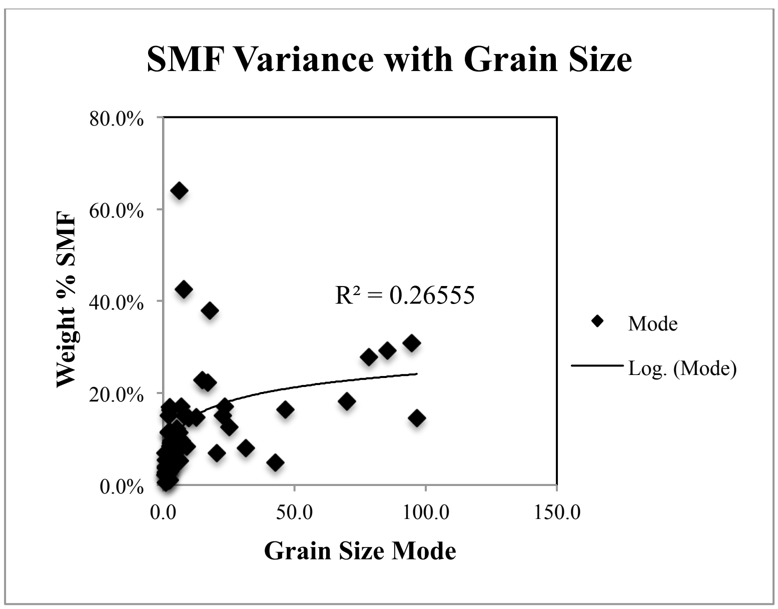

SMF Variance with Grain Size
80.0%
60.0%
40.0%
20.0%
0.0%
Weight % SMF
R² = 0.26555
Mode
Log. (Mode)
0.0
50.0
100.0
150.0
Grain Size Mode

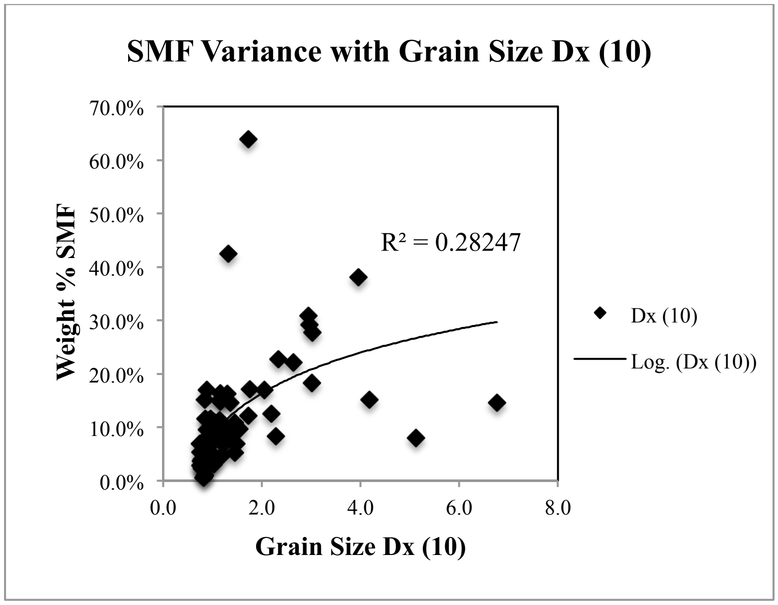
SMF Variance with Grain Size Dx (10)
70.0%
60.0%
50.0%
40.0%
30.0%
20.0%
10.0%
0.0%
Weight % SMF
R² = 0.28247
0.0
2.0
4.0
6.0
8.0
Grain Size Dx (10)
Dx (10)
Log. (Dx (10))

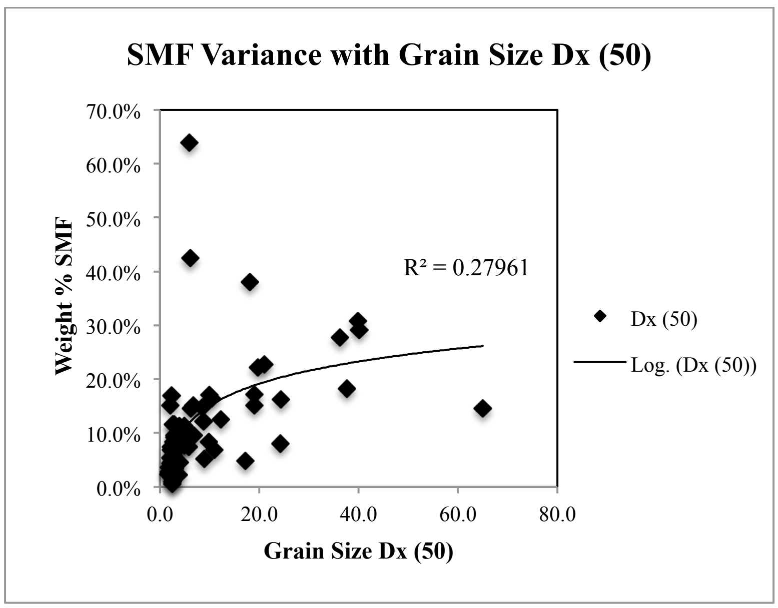
SMF Variance with Grain Size Dx (50)
70.0%
60.0%
50.0%
40.0%
30.0%
20.0%
10.0%
0.0%
Weight % SMF
R² = 0.27961
0.0
20.0
40.0
60.0
80.0
Grain Size Dx (50)
Dx (50)
Log. (Dx (50))

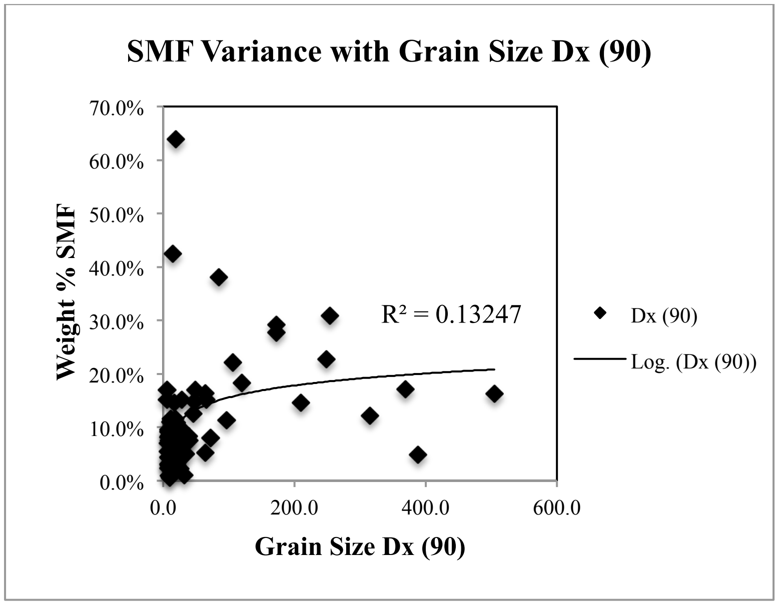
SMF Variance with Grain Size Dx (90)
Weight % SMF
70.0%
60.0%
50.0%
40.0%
30.0%
20.0%
10.0%
0.0%
0.0
200.0
400.0
600.0
Grain Size Dx (90)
R² = 0.13247
Dx (90)
Log. (Dx (90))

Appendix III: Field and Laboratory Supplements

Key to Symbols and Abbreviations Used in Field Logs

Abbreviations:

Bioclst: bioclast
Bra: brachiopod
Carb: carbonate
Cri: crinoid
For: Forams
Frag: fragment(s)
Gas: gastropod
Grn: green
Lam(s): laminations
Lgt: light
Mdst: mudstone
Org: orange (color)
Ost: ostracod
Packst: packstone
Wkst: wackstone

Symbols:

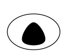 Chert

 Root Trace

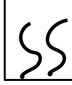 Mottling/burrowing

Date: 15 June 2015 Location: Univ. of Idaho, Moscow, Idaho Page: 1 of 7

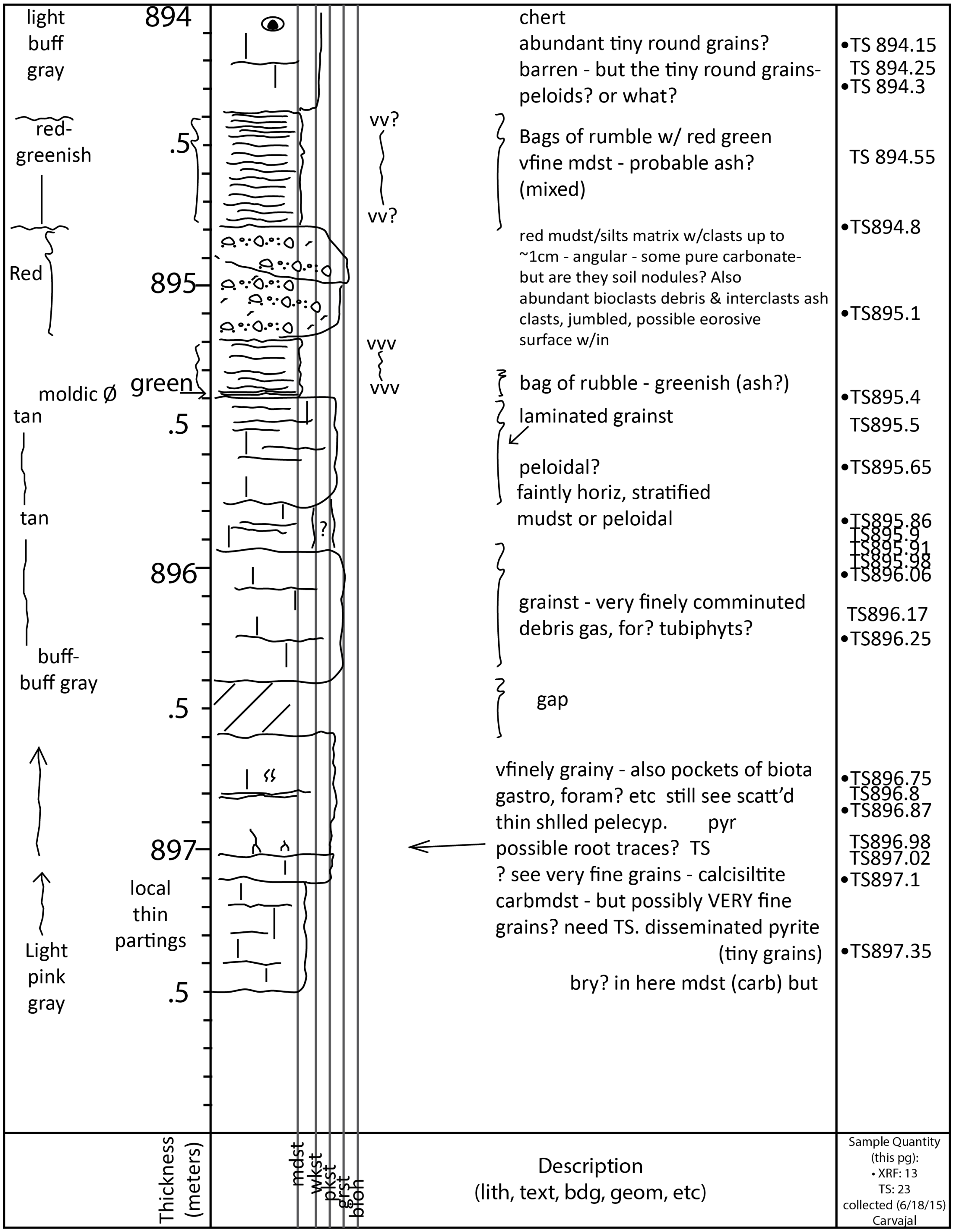

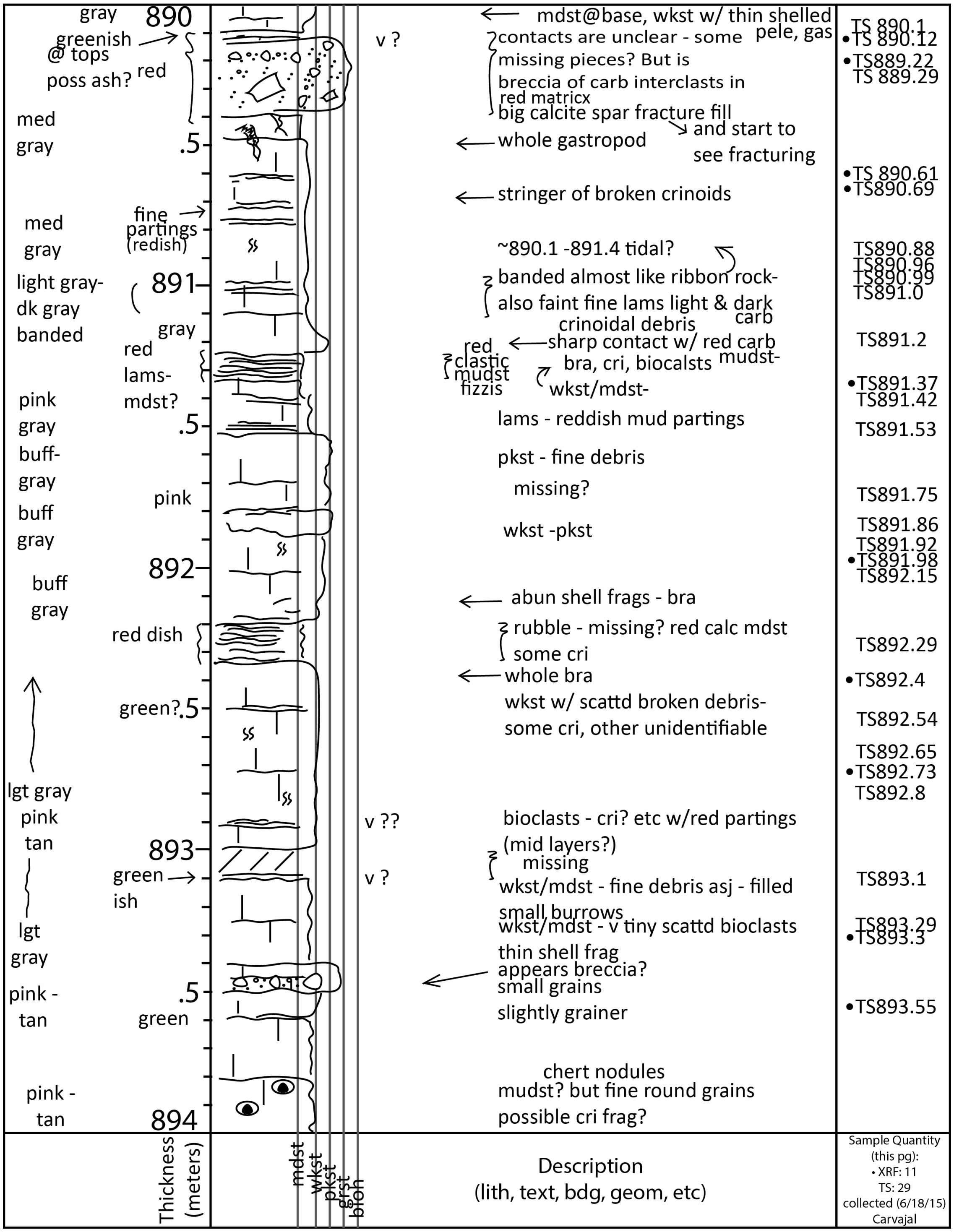
gray
890
greenish
@ tops
poss ash?
red
med
gray
.5
fine
partings
(redish)
med
gray
light gray-
dk gray
banded
891
gray
red
lams-
mdst?
pink
gray
buff-
gray
buff
gray
.5
pink
892
buff
gray
red dish
green?
.5
lgt gray
pink
tan
893
green
ish
lgt
gray
pink -
tan
.5
green
pink -
tan
894
v ?
v ??
v ?
mdst@base, wkst w/ thin shelled pele, gas
contacts are unclear - some missing pieces? But is breccia of carb interclasts in red matricx
big calcite spar fracture fill and start to see fracturing
whole gastropod
stringer of broken crinoids
~890.1 -891.4 tidal?
banded almost like ribbon rock- also faint fine lams light & dark carb
crinoidal debris
red clastic mudst fizzis
sharp contact w/ red carb mudst- bra, cri, biocalsts
wkst/mdst-
lams - reddish mud partings
pkst - fine debris
missing?
wkst -pkst
abun shell frags - bra
rubble - missing? red calc mdst some cri
whole bra
wkst w/ scattd broken debris- some cri, other unidentifiable
bioclasts - cri? etc w/red partings (mid layers?)
missing
wkst/mdst - fine debris asj - filled small burrows
wkst/mdst - v tiny scattd bioclasts
thin shell frag
appears breccia?
small grains
slightly grainer
chert nodules
mudst? but fine round grains
possible cri frag?
TS 890.1
•TS 890.12
•TS889.22
TS 889.29
•TS 890.61
•TS890.69
TS890.88
TS890.96
TS890.99
TS891.0
TS891.2
•TS891.37
TS891.42
TS891.53
TS891.75
TS891.86
TS891.92
•TS891.98
TS892.15
TS892.29
•TS892.4
TS892.54
TS892.65
•TS892.73
TS892.8
TS893.1
TS893.29
•TS893.3
•TS893.55
Thickness (meters)
mdst
wkst
pkst
grst
bioh
Description
(lith, text, bdg, geom, etc)
Sample Quantity (this pg):
• XRF: 11
TS: 29
collected (6/18/15)
Carvajal

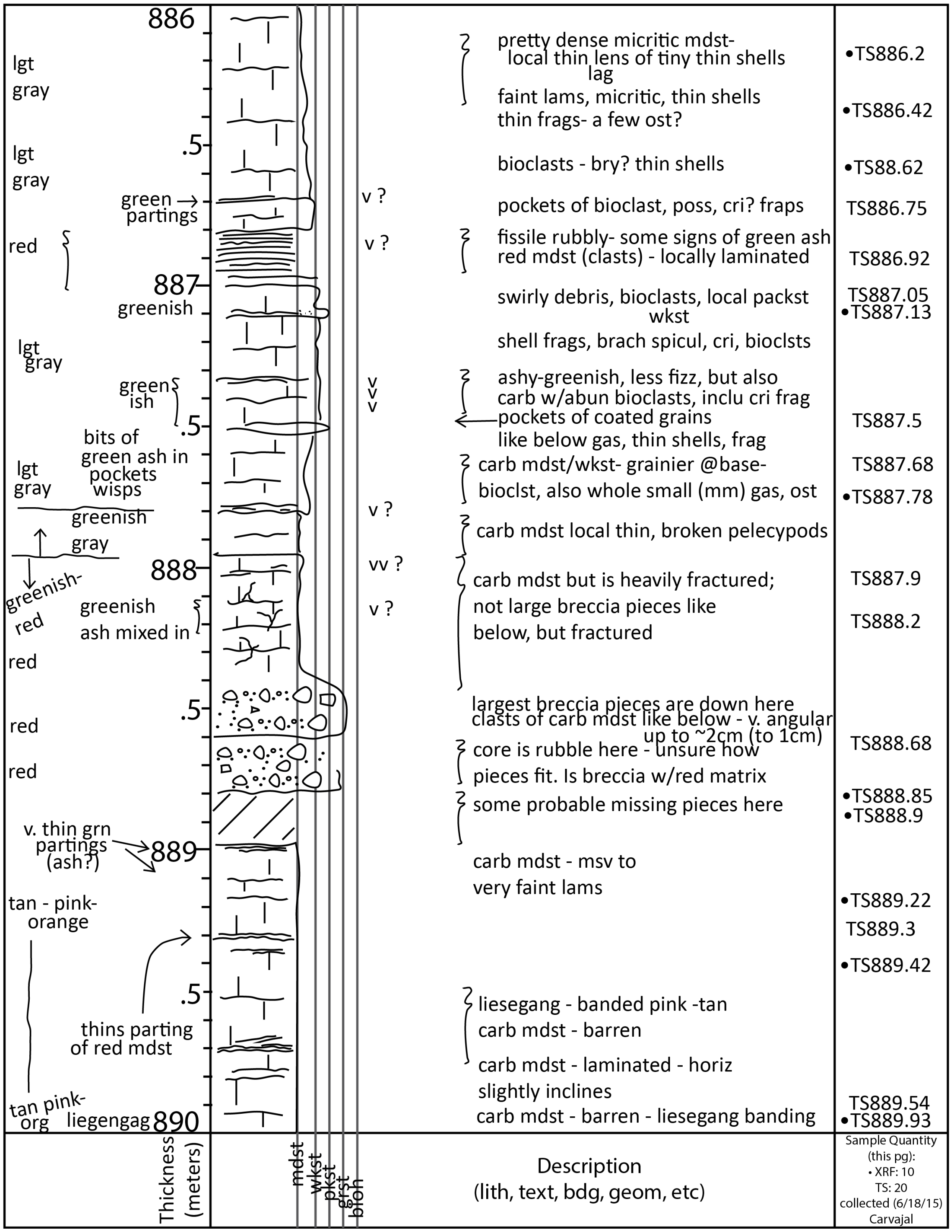
886
lgt gray
pretty dense micritic mdst- local thin lens of tiny thin shells lag
•TS886.2
faint lams, micritic, thin shells thin frags- a few ost?
•TS886.42
lgt gray
.5
bioclasts - bry? thin shells
•TS88.62
green partings
v ?
pockets of bioclast, poss, cri? fraps
TS886.75
red
v ?
fissile rubbly- some signs of green ash red mdst (clasts) - locally laminated
TS886.92
887
greenish
swirly debris, bioclasts, local packst wkst
TS887.05
•TS887.13
lgt gray
shell frags, brach spicul, cri, bioclsts
greenish
v v v
ashy-greenish, less fizz, but also carb w/abun bioclasts, inclu cri frag
pockets of coated grains
like below gas, thin shells, frag
TS887.5
.5
bits of green ash in pockets wisps
lgt gray
carb mdst/wkst- grainier @base- bioclst, also whole small (mm) gas, ost
TS887.68
•TS887.78
greenish gray
v ?
carb mdst local thin, broken pelecypods
888
greenish-red
vv ?
carb mdst but is heavily fractured; not large breccia pieces like below, but fractured
TS887.9
greenish ash mixed in
v ?
TS888.2
red
.5
red
largest breccia pieces are down here clasts of carb mdst like below - v. angular up to ~2cm (to 1cm)
red
core is rubble here - unsure how pieces fit. Is breccia w/red matrix
TS888.68
some probable missing pieces here
•TS888.85
•TS888.9
v. thin grn partings (ash?)
889
carb mdst - msv to very faint lams
tan - pink- orange
•TS889.22
TS889.3
•TS889.42
.5
liesegang - banded pink -tan carb mdst - barren
thins parting of red mdst
carb mdst - laminated - horiz slightly inclines
TS889.54
tan pink- org
liegengag
890
carb mdst - barren - liesegang banding
•TS889.93
Thickness (meters)
mdst wkst pkst grst bloh
Description (lith, text, bdg, geom, etc)
Sample Quantity (this pg): • XRF: 10 TS: 20 collected (6/18/15) Carvajal

Date: 15 June 2015 Location: Univ. of Idaho, Moscow, Idaho Page: 4 of 7

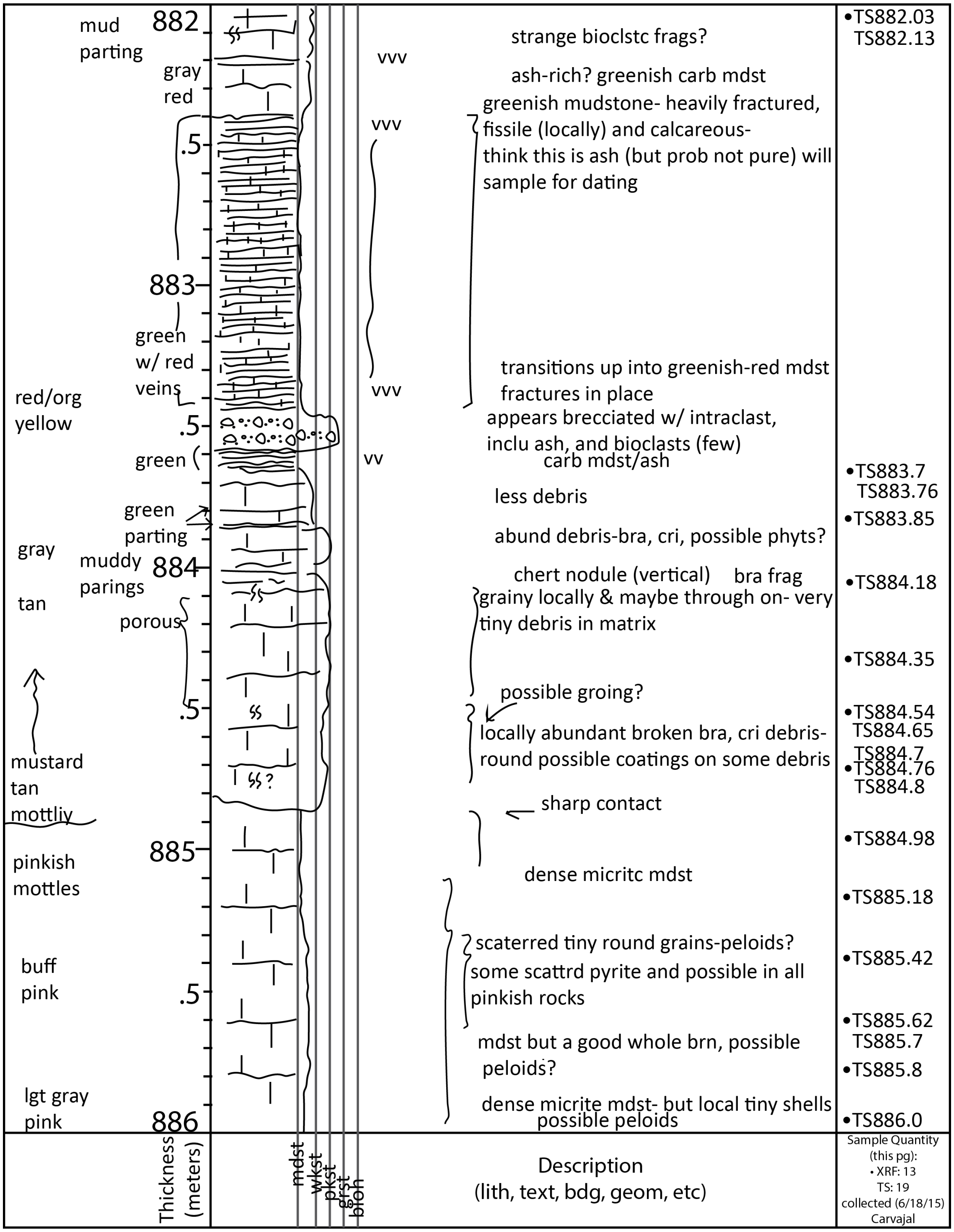

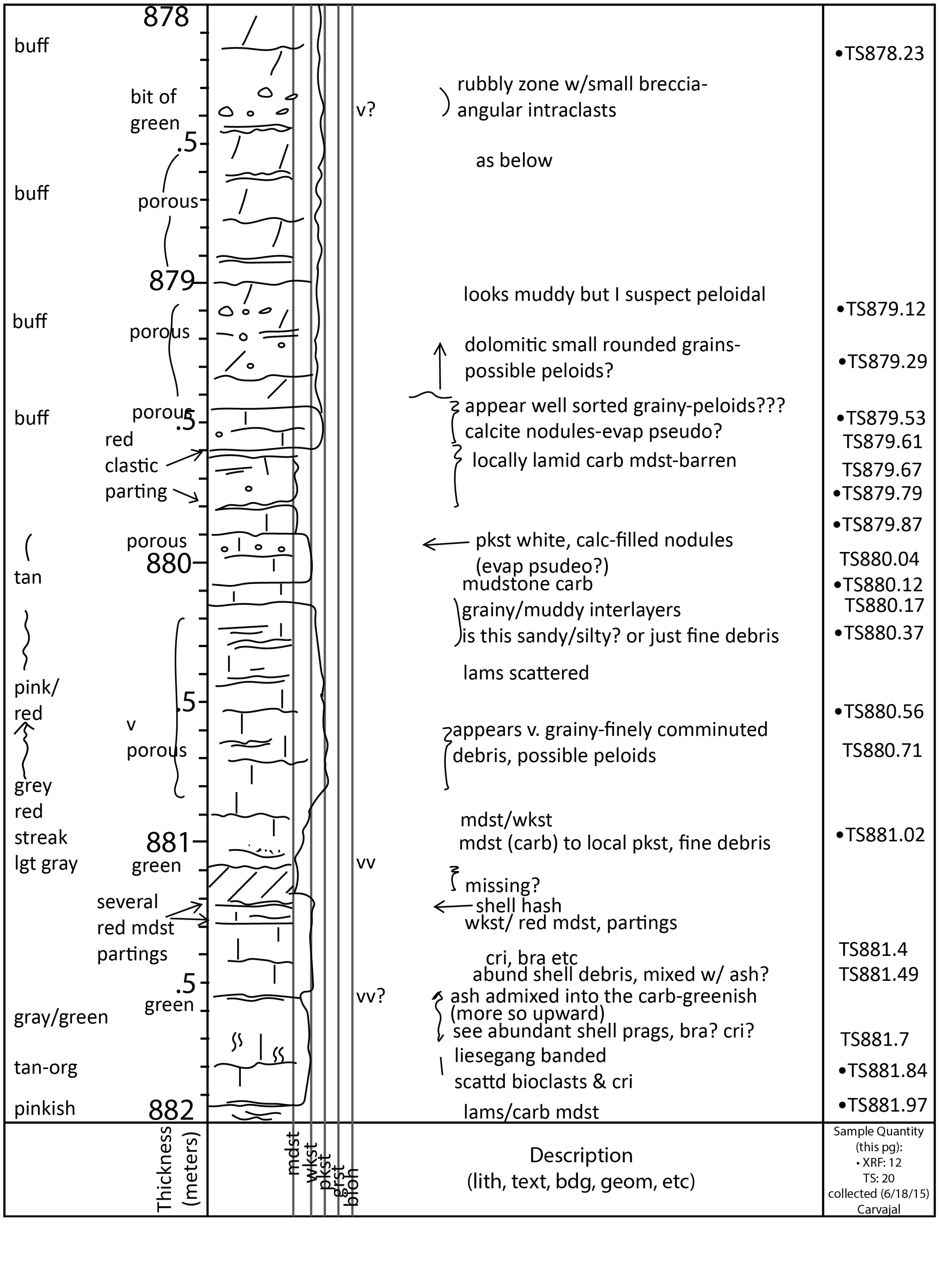
878
buff
•TS878.23
bit of green
v?
rubbly zone w/small breccia-angular intraclasts
.5
as below
buff
porous
879
looks muddy but I suspect peloidal
buff
porous
•TS879.12
dolomitic small rounded grains-possible peloids?
•TS879.29
buff
porous
.5
appear well sorted grainy-peloids???
calcite nodules-evap pseudo?
•TS879.53
red clastic parting
TS879.61
locally lamid carb mdst-barren
TS879.67
•TS879.79
•TS879.87
porous
pkst white, calc-filled nodules (evap psudeo?)
880
tan
TS880.04
mudstone carb
•TS880.12
grainy/muddy interlayers
TS880.17
is this sandy/silty? or just fine debris
•TS880.37
lams scattered
pink/red
.5
•TS880.56
v porous
appears v. grainy-finely comminuted debris, possible peloids
TS880.71
grey
red
streak
lgt gray
mdst/wkst
881
mdst (carb) to local pkst, fine debris
•TS881.02
green
vv
missing?
several red mdst partings
shell hash
wkst/ red mdst, partings
cri, bra etc
TS881.4
abund shell debris, mixed w/ ash?
TS881.49
.5
green
vv?
ash admixed into the carb-greenish (more so upward)
gray/green
see abundant shell prags, bra? cri?
TS881.7
liesegang banded
tan-org
scattd bioclasts & cri
•TS881.84
pinkish
882
lams/carb mdst
•TS881.97
Thickness (meters)
mdst
wkst
pkst
grst
bloh
Description
(lith, text, bdg, geom, etc)
Sample Quantity (this pg):
• XRF: 12
TS: 20
collected (6/18/15)
Carvajal

Date: 15 June 2015 Location: Univ. of Idaho, Moscow, Idaho Page: 6 of 7

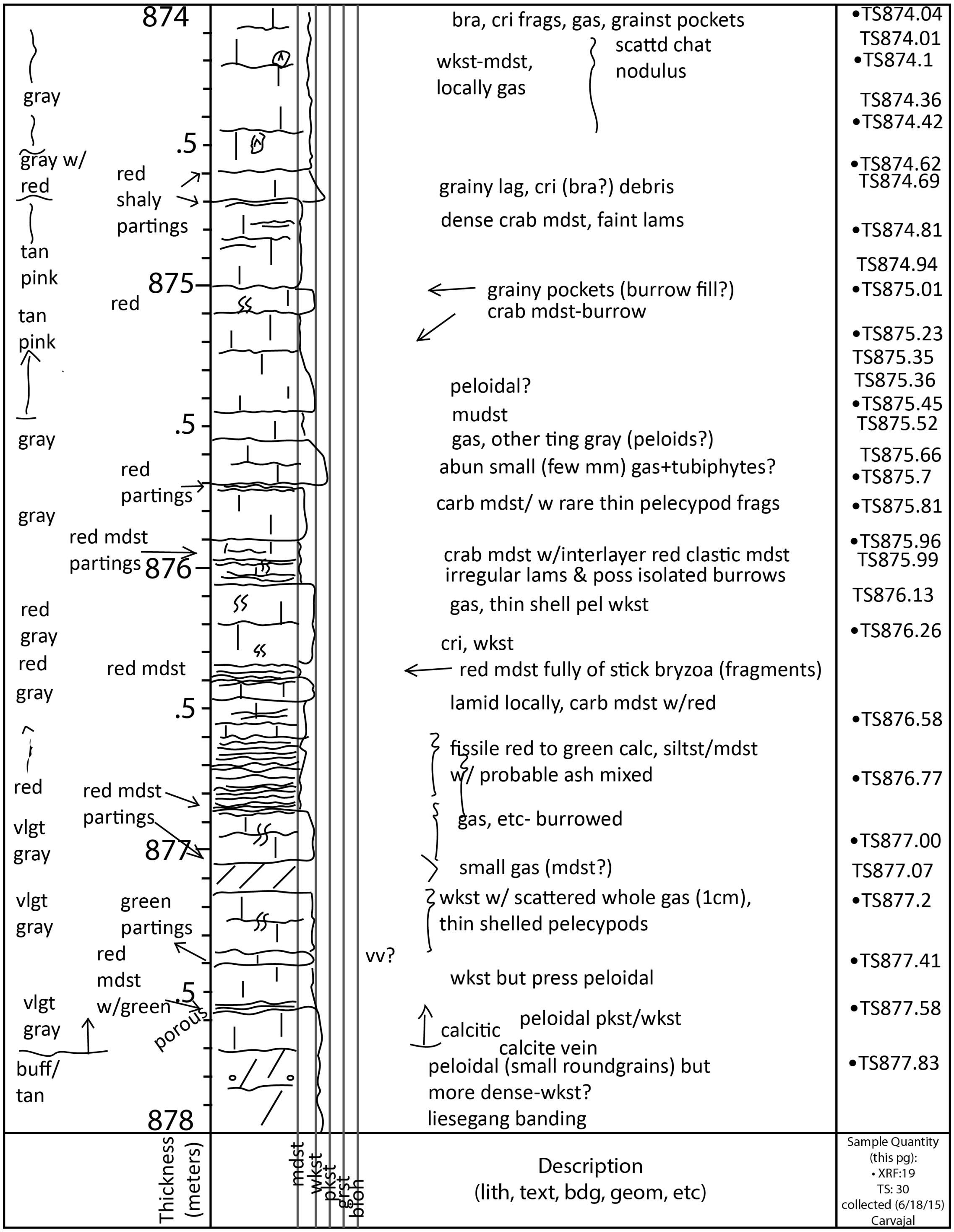

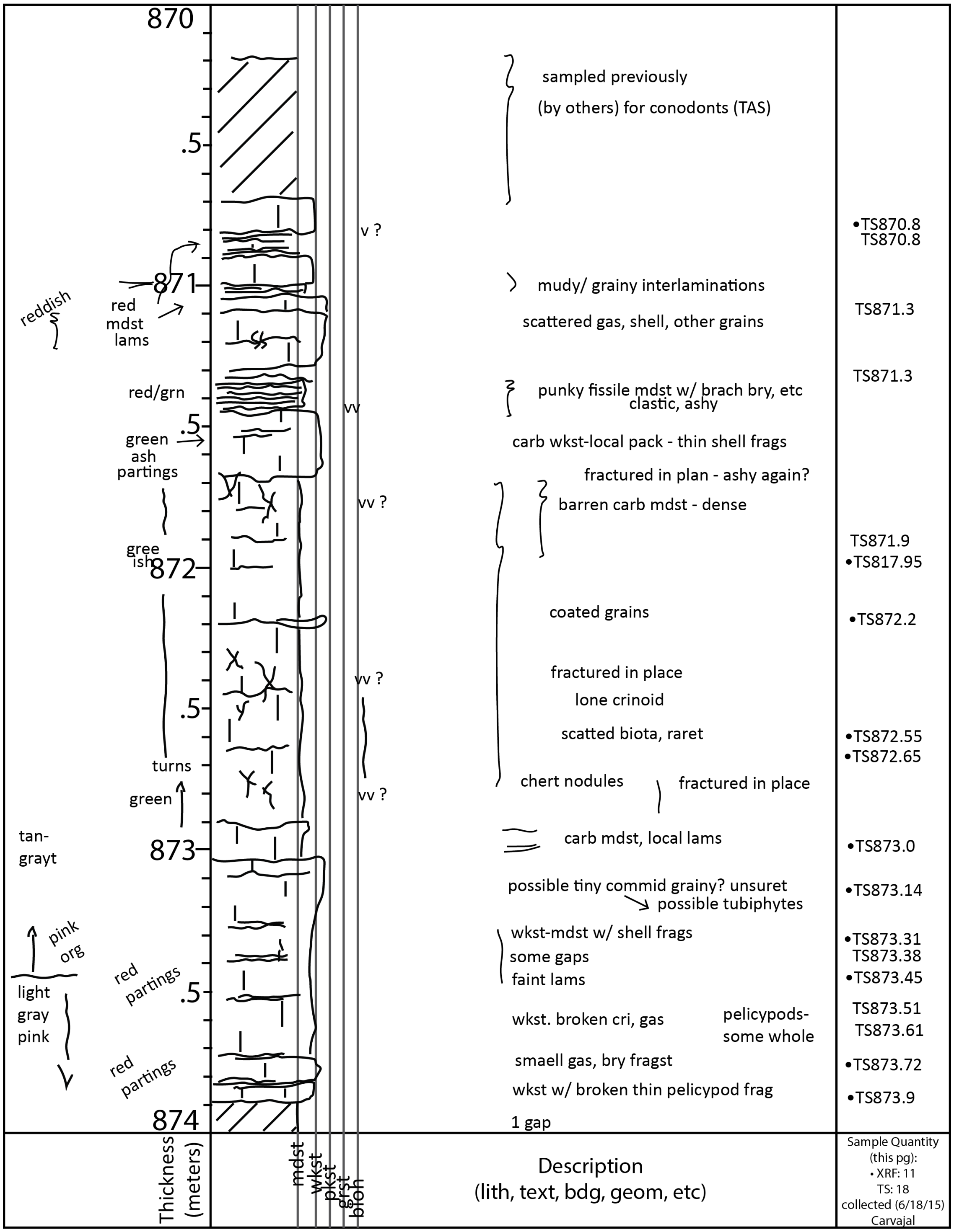
870
.5
871
.5
872
.5
873
.5
874
sampled previously
(by others) for conodonts (TAS)
v ?
•TS870.8
TS870.8
reddish
red
mdst
lams
mudy/ grainy interlaminations
scattered gas, shell, other grains
TS871.3
TS871.3
red/grn
punky fissile mdst w/ brach bry, etc
clastic, ashy
vv
green
ash
partings
carb wkst-local pack - thin shell frags
fractured in plan - ashy again?
vv ?
barren carb mdst - dense
gree
ish
TS871.9
•TS817.95
coated grains
•TS872.2
vv ?
fractured in place
lone crinoid
scatted biota, raret
•TS872.55
•TS872.65
turns
green
chert nodules
fractured in place
vv ?
tan-
grayt
carb mdst, local lams
•TS873.0
possible tiny commid grainy? unsuret
possible tubiphytes
•TS873.14
pink
org
wkst-mdst w/ shell frags
some gaps
faint lams
•TS873.31
TS873.38
•TS873.45
red
partings
light
gray
pink
wkst. broken cri, gas
pelicypods-
some whole
TS873.51
TS873.61
red
partings
smaell gas, bry fragst
•TS873.72
wkst w/ broken thin pelicypod frag
•TS873.9
1 gap
Thickness
(meters)
mdst
wkst
pkst
grst
bloh
Description
(lith, text, bdg, geom, etc)
Sample Quantity
(this pg):
• XRF: 11
TS: 18
collected (6/18/15)
Carvajal

Malvern Mastersizer 3000 LP Particle Size Analyzer

MAN 870.8

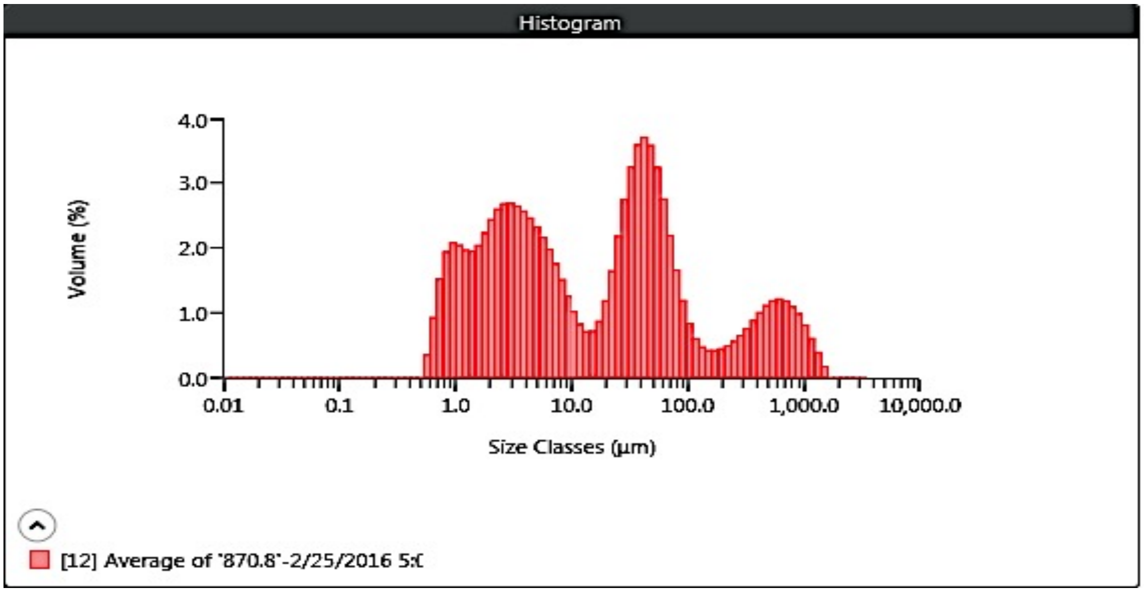

Result

Concentration	0.0024 %	**Span**	22.415
Uniformity	5.917	**Result Units**	Volume
Specific Surface Area	596.8 m^2/kg	**Dv (10)**	1.21 μm
D [3,2]	3.87 μm	**Dv (50)**	17.2 μm
D [4,3]	106 μm	**Dv (90)**	388 μm
Volume Below (5) μm	36.95 %	**Mode**	42.7 μm
Volume Below (10) μm	46.50 %		
Volume Below (20) μm	**51.19 %**	**Volume In Range (500,1000) μm**	6.10 %
Volume In Range (5,20) μm	**14.24 %**	**Volume Above (1000) μm**	1.84 %
Volume In Range (20,200) μm	**35.48 %**		
Volume In Range (200,500) μm	5.40 %	**Volume In Range (1,2.5) μm**	15.89 %
Volume In Range (2.5,5) μm	14.05 %	**Volume In Range (5,10) μm**	9.56 %
D [3,3]	15.8 μm	**Kurtosis [3]**	9.992
Skew [3]	3.131		

Malvern Mastersizer 3000 LP Particle Size Analyzer

Replicate MAN 870.8

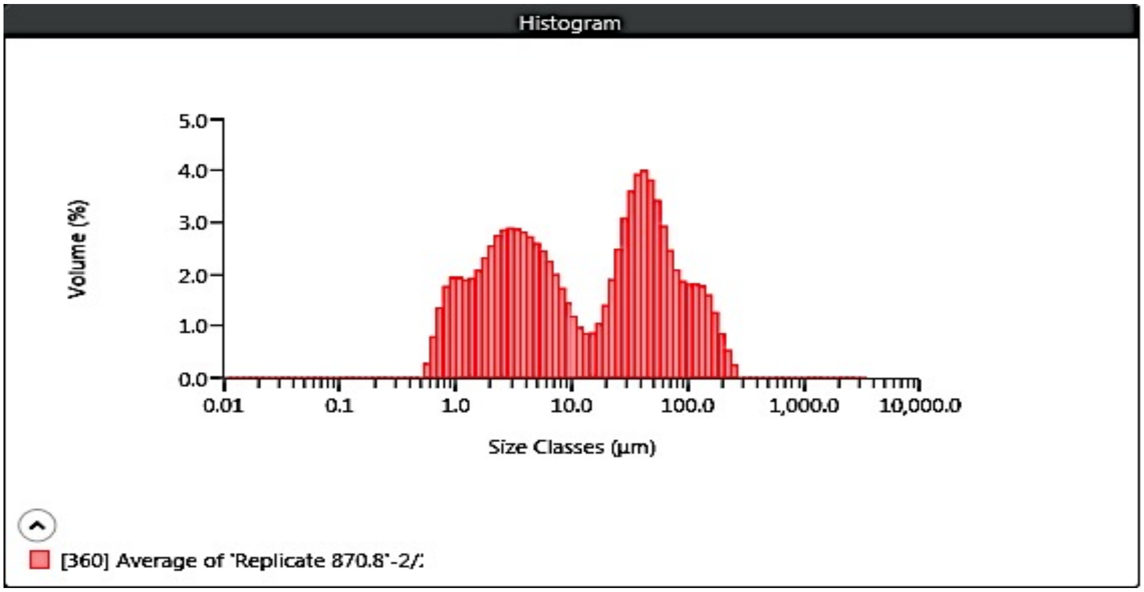

Result

Concentration	0.0024 %	Span	7.875
Uniformity	2.517	Result Units	Volume
Specific Surface Area	588.2 m²/kg	Dv (10)	1.29 µm
D [3,2]	3.92 µm	Dv (50)	12.2 µm
D [4,3]	34.2 µm	Dv (90)	97.1 µm
Volume Below (5) µm	37.52 %	Mode	41.7 µm
Volume Below (10) µm	48.32 %		
Volume Below (20) µm	53.86 %	Volume In Range (500,1000) µm	0.00 %
Volume In Range (5,20) µm	16.34 %	Volume Above (1000) µm	0.00 %
Volume In Range (20,200) µm	45.01 %		
Volume In Range (200,500) µm	1.13 %	Volume In Range (1,2.5) µm	16.00 %
Volume In Range (2.5,5) µm	15.27 %	Volume In Range (5,10) µm	10.81 %
D [3,3]	11.9 µm	Kurtosis [3]	4.086
Skew [3]	1.988		

Malvern Mastersizer 3000 LP Particle Size Analyzer

MAN 871

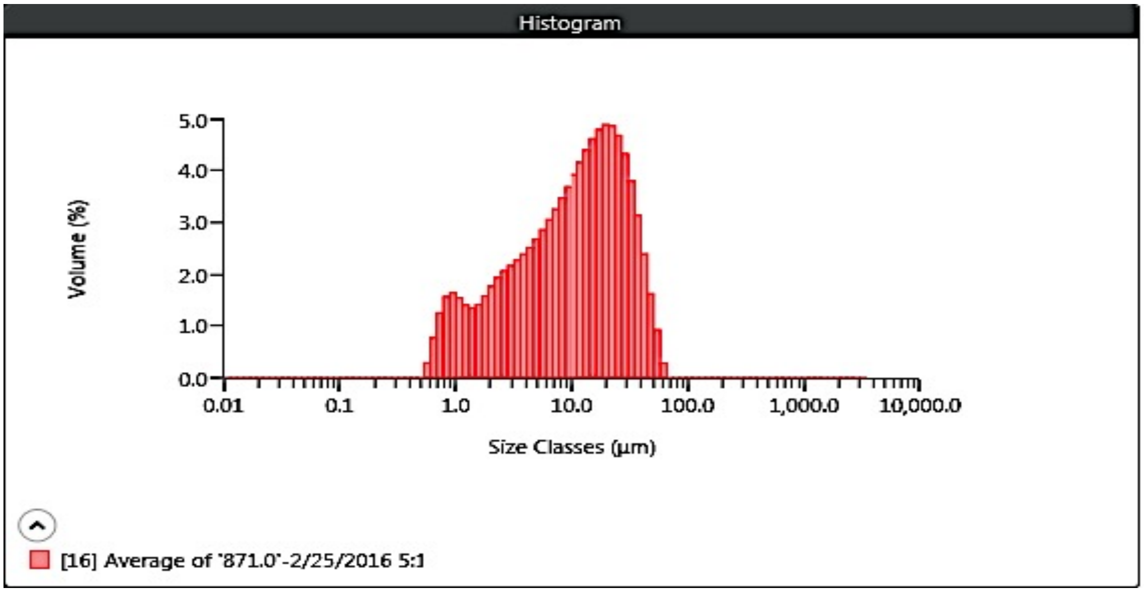

Result

Concentration	0.0050 %	**Span**	2.948
Uniformity	0.921	**Result Units**	Volume
Specific Surface Area	538.7 m^2/kg	**Dv (10)**	1.48 µm
D [3,2]	4.28 µm	**Dv (50)**	10.9 µm
D [4,3]	14.5 µm	**Dv (90)**	33.5 µm
Volume Below (5) µm	29.77 %	**Mode**	20.6 µm
Volume Below (10) µm	47.48 %		
Volume Below (20) µm	**71.65 %**	**Volume In Range (500,1000) µm**	0.00 %
Volume In Range (5,20) µm	**41.88 %**	**Volume Above (1000) µm**	0.00 %
Volume In Range (20,200) µm	**28.35 %**		
Volume In Range (200,500) µm	0.00 %	**Volume In Range (1,2.5) µm**	11.39 %
Volume In Range (2.5,5) µm	12.73 %	**Volume In Range (5,10) µm**	17.71 %
D [3,3]	8.73 µm	**Kurtosis [3]**	0.751
Skew [3]	1.118		

Malvern Mastersizer 3000 LP Particle Size Analyzer

MAN 871.95

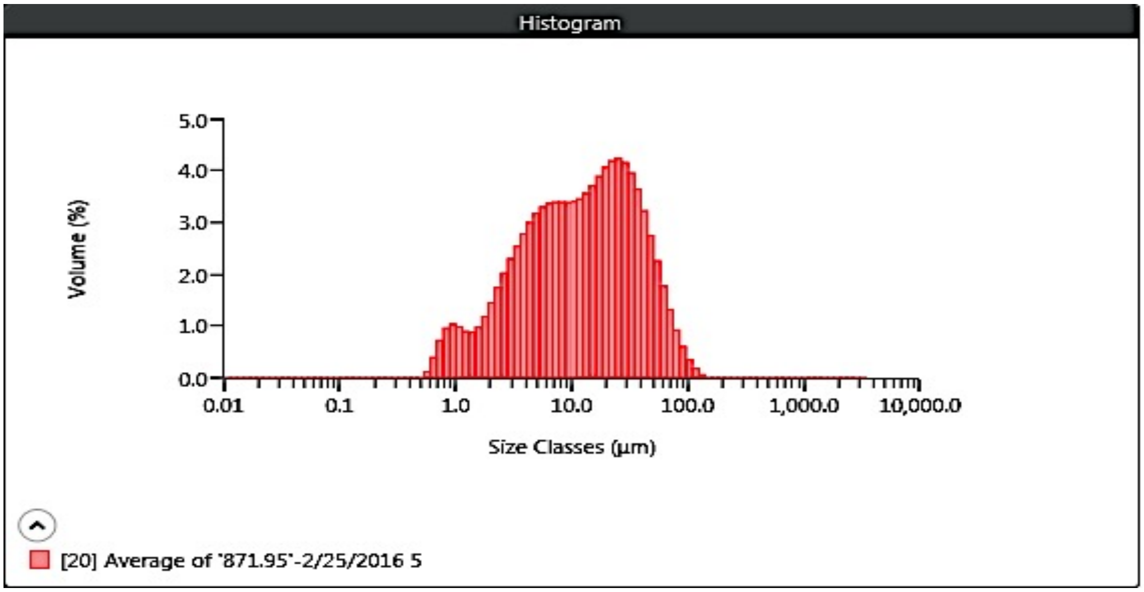

Result

Concentration	0.0033 %	**Span**	3.579
Uniformity	1.140	**Result Units**	Volume
Specific Surface Area	428.5 m^2/kg	**Dv (10)**	2.19 µm
D [3,2]	5.38 µm	**Dv (50)**	12.3 µm
D [4,3]	19.3 µm	**Dv (90)**	46.1 µm
Volume Below (5) µm	26.20 %	**Mode**	25.2 µm
Volume Below (10) µm	44.50 %		
Volume Below (20) µm	**64.42 %**	**Volume In Range (500,1000) µm**	0.00 %
Volume In Range (5,20) µm	**38.22 %**	**Volume Above (1000) µm**	0.00 %
Volume In Range (20,200) µm	**35.58 %**		
Volume In Range (200,500) µm	0.00 %	**Volume In Range (1,2.5) µm**	8.55 %
Volume In Range (2.5,5) µm	14.35 %	**Volume In Range (5,10) µm**	18.30 %
D [3,3]	11.0 µm	**Kurtosis [3]**	3.797
Skew [3]	1.775		

Malvern Mastersizer 3000 LP Particle Size Analyzer

MAN 872.2

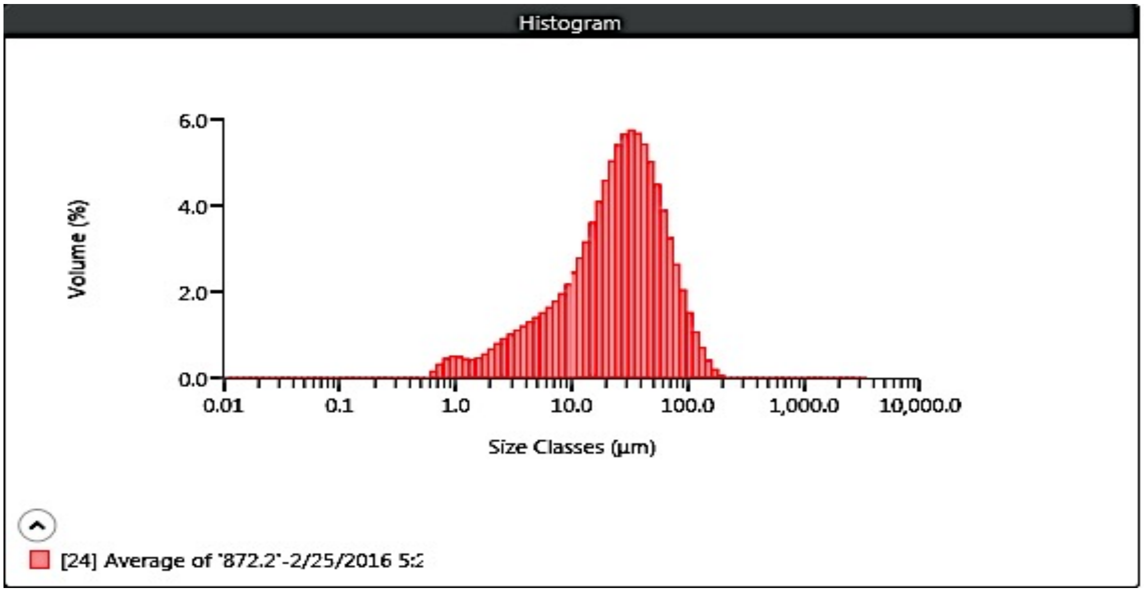

Result

Concentration	0.0040 %	**Span**	2.604
Uniformity	0.808	**Result Units**	Volume
Specific Surface Area	235.5 m^2/kg	**Dv (10)**	4.27 µm
D [3,2]	9.80 µm	**Dv (50)**	26.0 µm
D [4,3]	33.3 µm	**Dv (90)**	71.9 µm
Volume Below (5) µm	11.67 %	**Mode**	33.4 µm
Volume Below (10) µm	21.40 %		
Volume Below (20) µm	**39.70 %**	**Volume In Range (500,1000) µm**	0.00 %
Volume In Range (5,20) µm	**28.03 %**	**Volume Above (1000) µm**	0.00 %
Volume In Range (20,200) µm	**60.28 %**		
Volume In Range (200,500) µm	0.02 %	**Volume In Range (1,2.5) µm**	4.00 %
Volume In Range (2.5,5) µm	6.22 %	**Volume In Range (5,10) µm**	9.73 %
D [3,3]	21.2 µm	**Kurtosis [3]**	3.204
Skew [3]	1.577		

Malvern Mastersizer 3000 LP Particle Size Analyzer

MAN 872.65

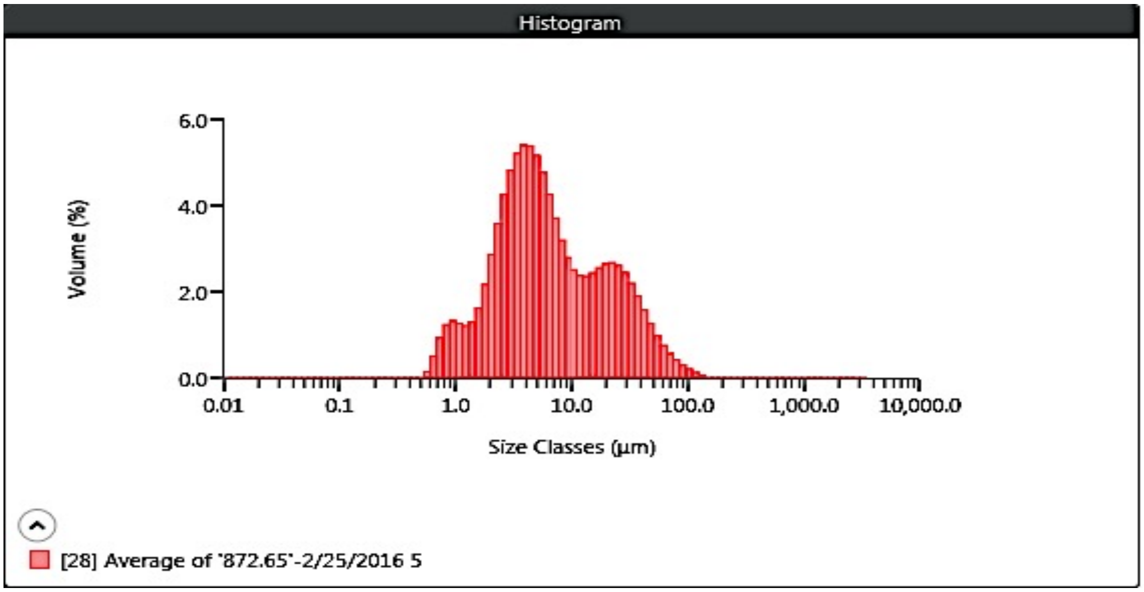

Result

Concentration	0.0045 %	**Span**	5.511
Uniformity	1.679	**Result Units**	Volume
Specific Surface Area	614.7 m^2/kg	**Dv (10)**	1.70 µm
D [3,2]	3.75 µm	**Dv (50)**	5.44 µm
D [4,3]	12.1 µm	**Dv (90)**	31.7 µm
Volume Below (5) µm	46.74 %	**Mode**	3.99 µm
Volume Below (10) µm	67.43 %		
Volume Below (20) µm	**80.78 %**	**Volume In Range (500,1000) µm**	0.00 %
Volume In Range (5,20) µm	**34.03 %**	**Volume Above (1000) µm**	0.00 %
Volume In Range (20,200) µm	**19.22 %**		
Volume In Range (200,500) µm	0.00 %	**Volume In Range (1,2.5) µm**	14.96 %
Volume In Range (2.5,5) µm	27.56 %	**Volume In Range (5,10) µm**	20.69 %
D [3,3]	6.43 µm	**Kurtosis [3]**	10.330
Skew [3]	2.803		

Malvern Mastersizer 3000 LP Particle Size Analyzer

MAN 873.31

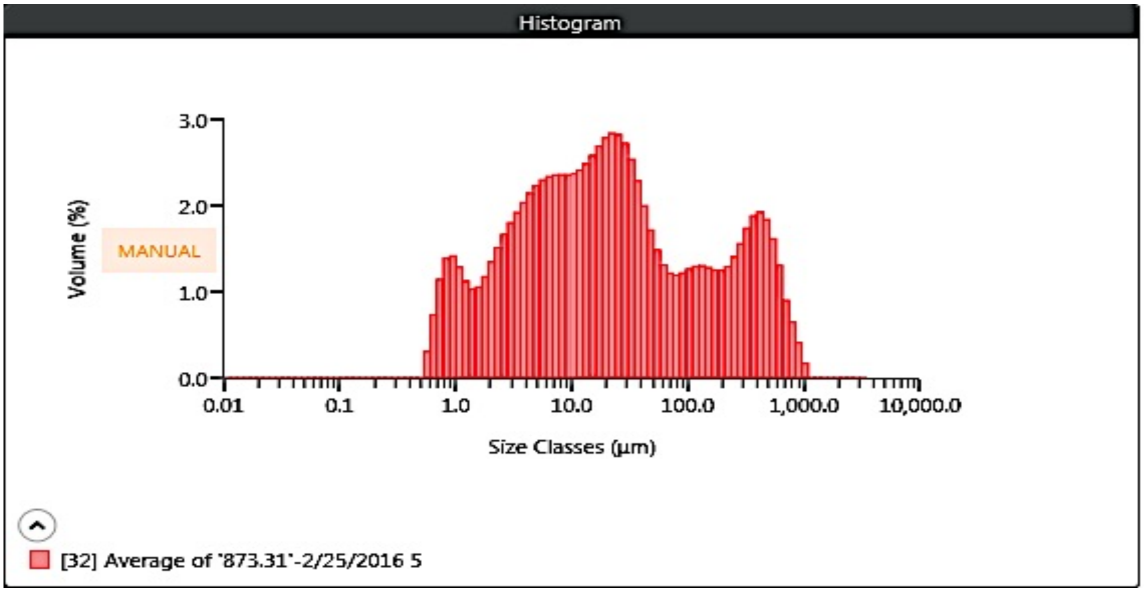

Result

Concentration	0.0026 %	**Span**	19.278
Uniformity	4.916	**Result Units**	Volume
Specific Surface Area	435.9 m^2/kg	**Dv (10)**	1.75 µm
D [3,2]	5.29 µm	**Dv (50)**	19.0 µm
D [4,3]	100 µm	**Dv (90)**	369 µm
Volume Below (5) µm	24.59 %	**Mode**	23.4 µm
Volume Below (10) µm	37.29 %		
Volume Below (20) µm	51.08 %	**Volume In Range (500,1000) µm**	5.35 %
Volume In Range (5,20) µm	26.49 %	**Volume Above (1000) µm**	0.14 %
Volume In Range (20,200) µm	31.70 %		
Volume In Range (200,500) µm	11.72 %	**Volume In Range (1,2.5) µm**	8.83 %
Volume In Range (2.5,5) µm	10.69 %	**Volume In Range (5,10) µm**	12.70 %
D [3,3]	21.4 µm	**Kurtosis [3]**	5.565
Skew [3]	2.386		

Malvern Mastersizer 3000 LP Particle Size Analyzer

Replicate MAN 873.31

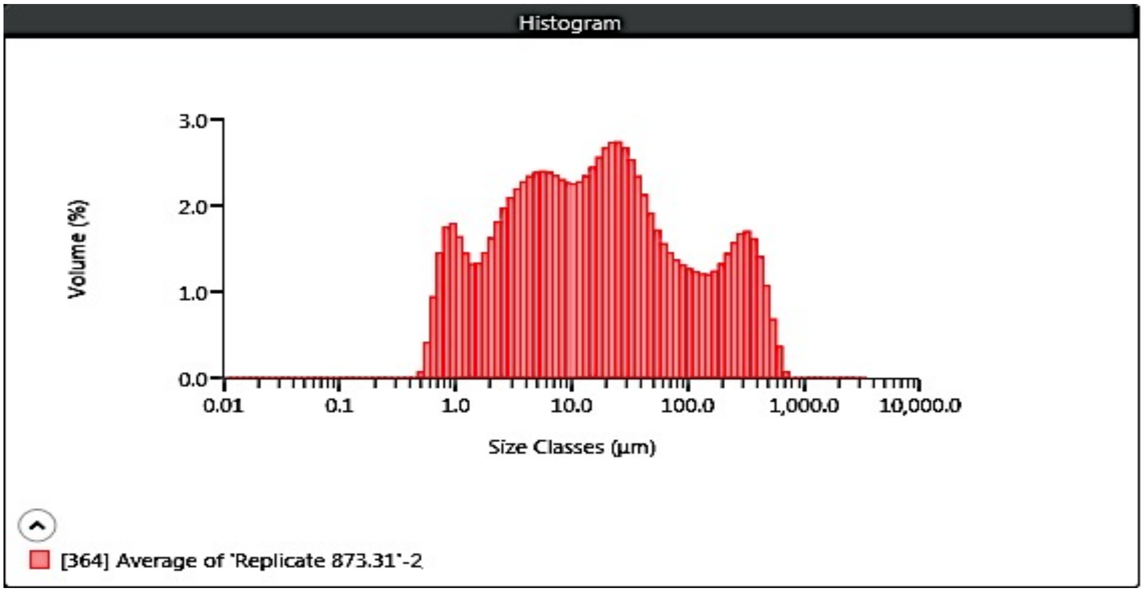

Result

Concentration	0.0016 %	**Span**	15.725
Uniformity	4.036	**Result Units**	Volume
Specific Surface Area	522.3 m^2/kg	**Dv (10)**	1.34 µm
D [3,2]	4.42 µm	**Dv (50)**	15.3 µm
D [4,3]	67.1 µm	**Dv (90)**	243 µm
Volume Below (5) µm	29.52 %	**Mode**	24.3 µm
Volume Below (10) µm	42.23 %		
Volume Below (20) µm	55.31 %	**Volume In Range (500,1000) µm**	1.37 %
Volume In Range (5,20) µm	25.79 %	**Volume Above (1000) µm**	0.00000000002 %
Volume In Range (20,200) µm	32.55 %		
Volume In Range (200,500) µm	10.78 %	**Volume In Range (1,2.5) µm**	10.98 %
Volume In Range (2.5,5) µm	12.01 %	**Volume In Range (5,10) µm**	12.71 %
D [3,3]	16.0 µm	**Kurtosis [3]**	5.706
Skew [3]	2.447		

Malvern Mastersizer 3000 LP Particle Size Analyzer

Replicate MAN 873.45

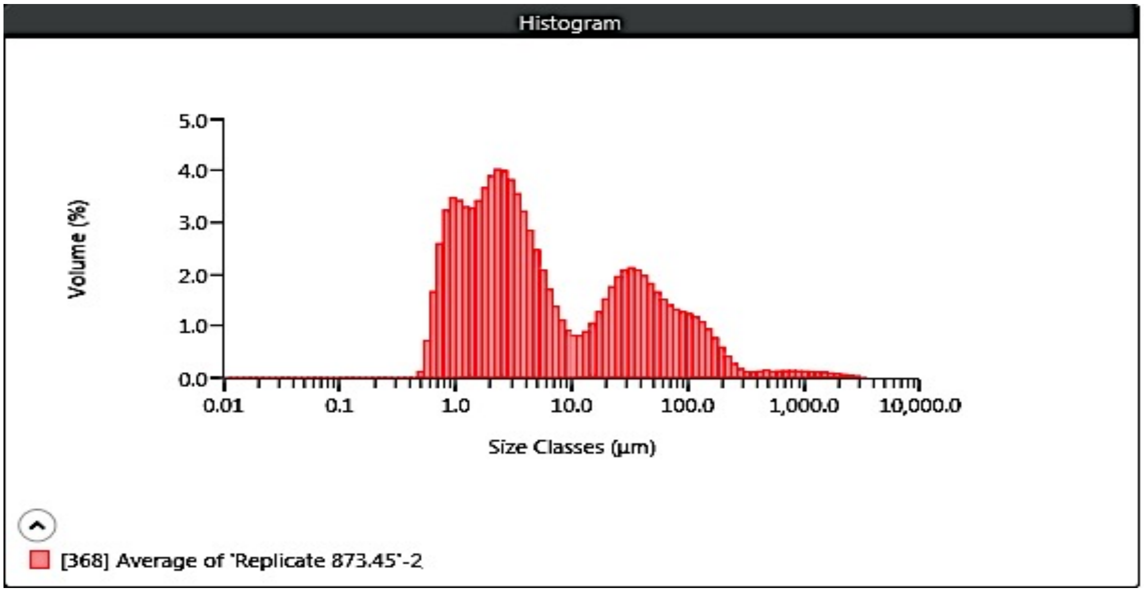

Result

Concentration	0.0022 %	**Span**	22.221
Uniformity	10.654	**Result Units**	Volume
Specific Surface Area	923.8 m²/kg	**Dv (10)**	0.926 µm
D [3,2]	2.50 µm	**Dv (50)**	3.79 µm
D [4,3]	42.1 µm	**Dv (90)**	85.0 µm
Volume Below (5) µm	56.15 %	**Mode**	2.37 µm
Volume Below (10) µm	64.21 %		
Volume Below (20) µm	69.80 %	**Volume In Range (500,1000) µm**	0.71 %
Volume In Range (5,20) µm	13.65 %	**Volume Above (1000) µm**	0.76 %
Volume In Range (20,200) µm	27.17 %		
Volume In Range (200,500) µm	1.57 %	**Volume In Range (1,2.5) µm**	25.87 %
Volume In Range (2.5,5) µm	18.18 %	**Volume In Range (5,10) µm**	8.06 %
D [3,3]	6.62 µm	**Kurtosis [3]**	114.695
Skew [3]	9.699		

Malvern Mastersizer 3000 LP Particle Size Analyzer

MAN 873.72

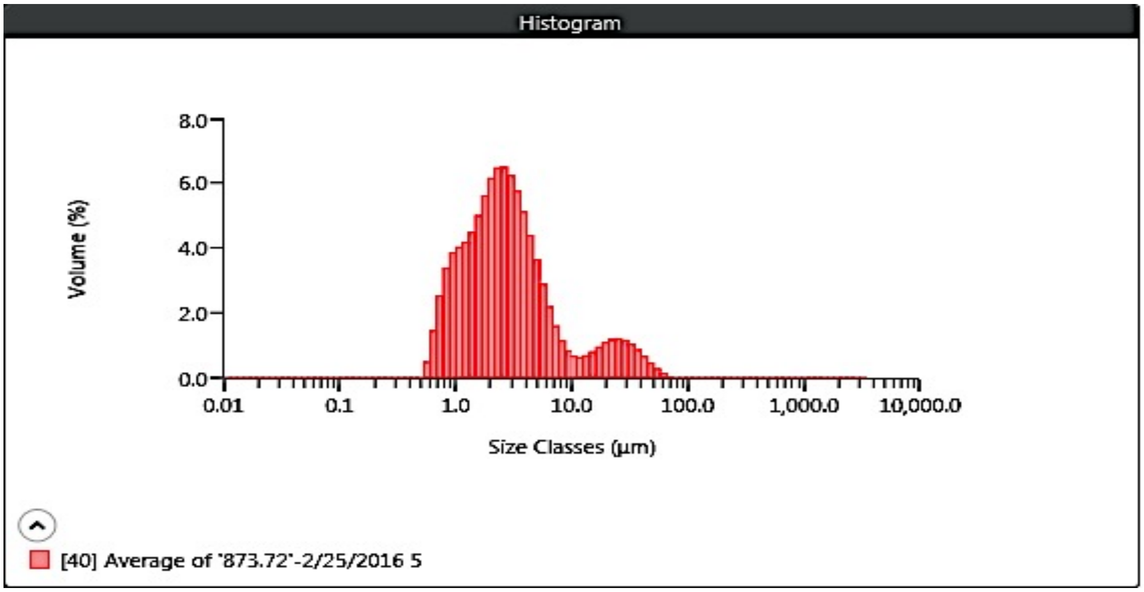

Result

Concentration	0.0022 %	**Span**	5.135
Uniformity	1.566	**Result Units**	Volume
Specific Surface Area	1141 m^2/kg	**Dv (10)**	0.936 µm
D [3,2]	2.02 µm	**Dv (50)**	2.53 µm
D [4,3]	5.46 µm	**Dv (90)**	13.9 µm
Volume Below (5) µm	78.45 %	**Mode**	2.45 µm
Volume Below (10) µm	88.32 %		
Volume Below (20) µm	**92.54 %**	**Volume In Range (500,1000) µm**	0.00 %
Volume In Range (5,20) µm	**14.09 %**	**Volume Above (1000) µm**	0.00 %
Volume In Range (20,200) µm	**7.46 %**		
Volume In Range (200,500) µm	0.00 %	**Volume In Range (1,2.5) µm**	37.46 %
Volume In Range (2.5,5) µm	28.98 %	**Volume In Range (5,10) µm**	9.87 %
D [3,3]	2.92 µm	**Kurtosis [3]**	12.092
Skew [3]	3.329		

Malvern Mastersizer 3000 LP Particle Size Analyzer

MAN 874.09

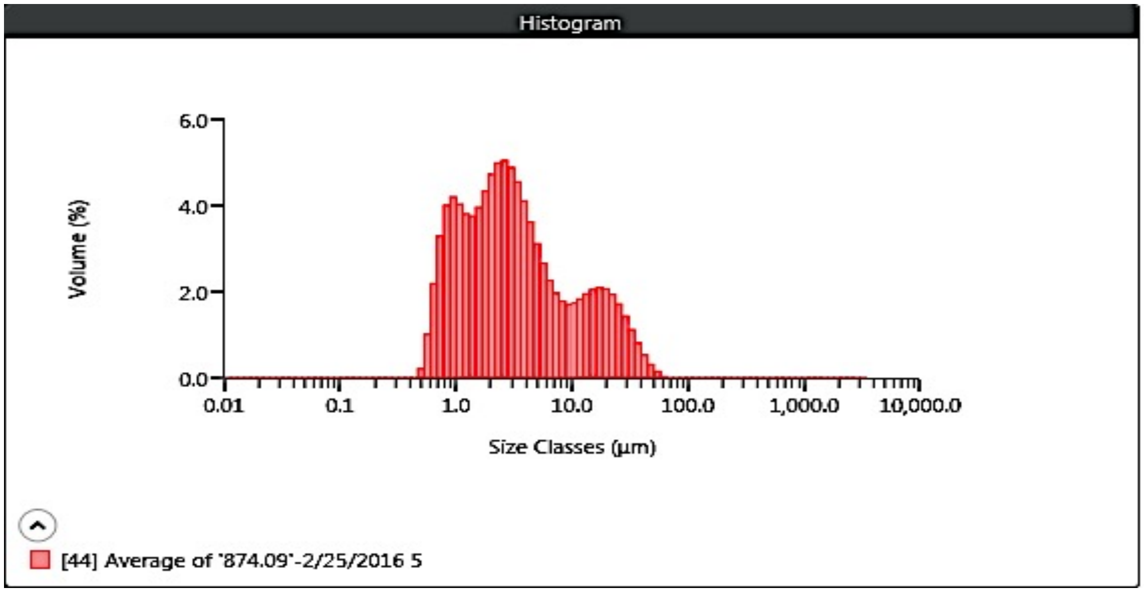

Result

Concentration	0.0023 %	**Span**	6.442
Uniformity	1.778	**Result Units**	Volume
Specific Surface Area	1136 m^2/kg	**Dv (10)**	0.852 μm
D [3,2]	2.03 μm	**Dv (50)**	2.78 μm
D [4,3]	6.42 μm	**Dv (90)**	18.7 μm
Volume Below (5) μm	68.94 %	**Mode**	2.50 μm
Volume Below (10) μm	80.49 %		
Volume Below (20) μm	**91.04 %**	**Volume In Range (500,1000) μm**	0.00 %
Volume In Range (5,20) μm	**22.10 %**	**Volume Above (1000) μm**	0.00000000000001 %
Volume In Range (20,200) μm	**8.96 %**		
Volume In Range (200,500) μm	0.00 %	**Volume In Range (1,2.5) μm**	30.63 %
Volume In Range (2.5,5) μm	23.10 %	**Volume In Range (5,10) μm**	11.55 %
D [3,3]	3.31 μm	**Kurtosis [3]**	6.321
Skew [3]	2.415		

Malvern Mastersizer 3000 LP Particle Size Analyzer

MAN 874.10

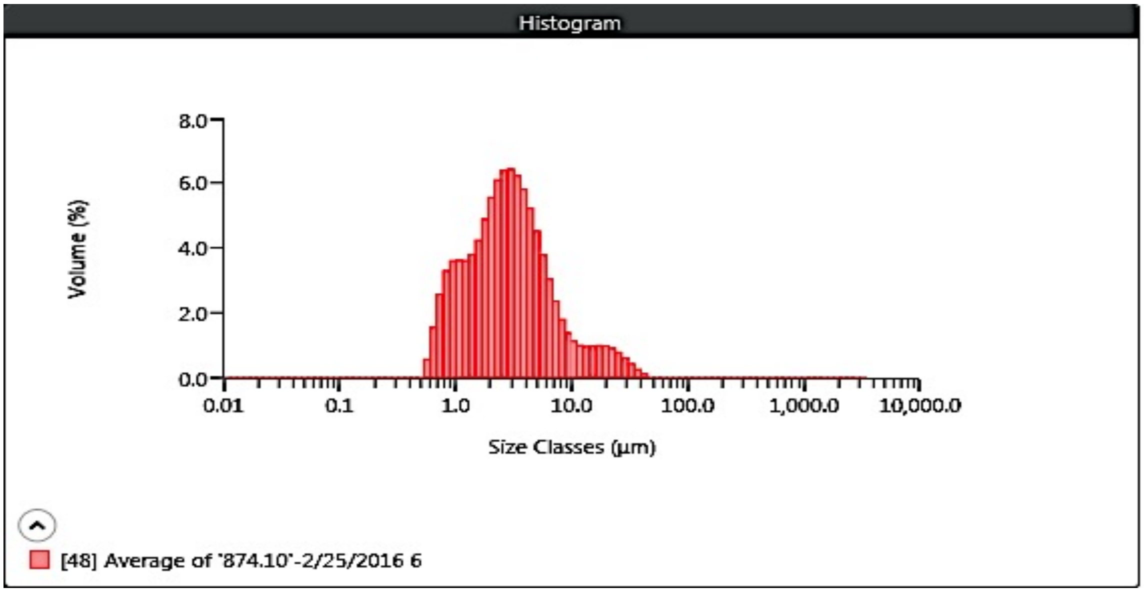

Result

Concentration	0.0041 %	Span	2.990
Uniformity	1.053	Result Units	Volume
Specific Surface Area	1107 m^2/kg	Dv (10)	0.935 µm
D [3,2]	2.08 µm	Dv (50)	2.75 µm
D [4,3]	4.48 µm	Dv (90)	9.16 µm
Volume Below (5) µm	76.96 %	Mode	2.80 µm
Volume Below (10) µm	90.93 %		
Volume Below (20) µm	96.42 %	Volume In Range (500,1000) µm	0.00 %
Volume In Range (5,20) µm	19.46 %	Volume Above (1000) µm	0.00 %
Volume In Range (20,200) µm	3.58 %		
Volume In Range (200,500) µm	0.00 %	Volume In Range (1,2.5) µm	33.32 %
Volume In Range (2.5,5) µm	31.75 %	Volume In Range (5,10) µm	13.98 %
D [3,3]	2.89 µm	Kurtosis [3]	12.339
Skew [3]	3.253		

<u>**Malvern Mastersizer 3000 LP Particle Size Analyzer**</u>

MAN 874.42

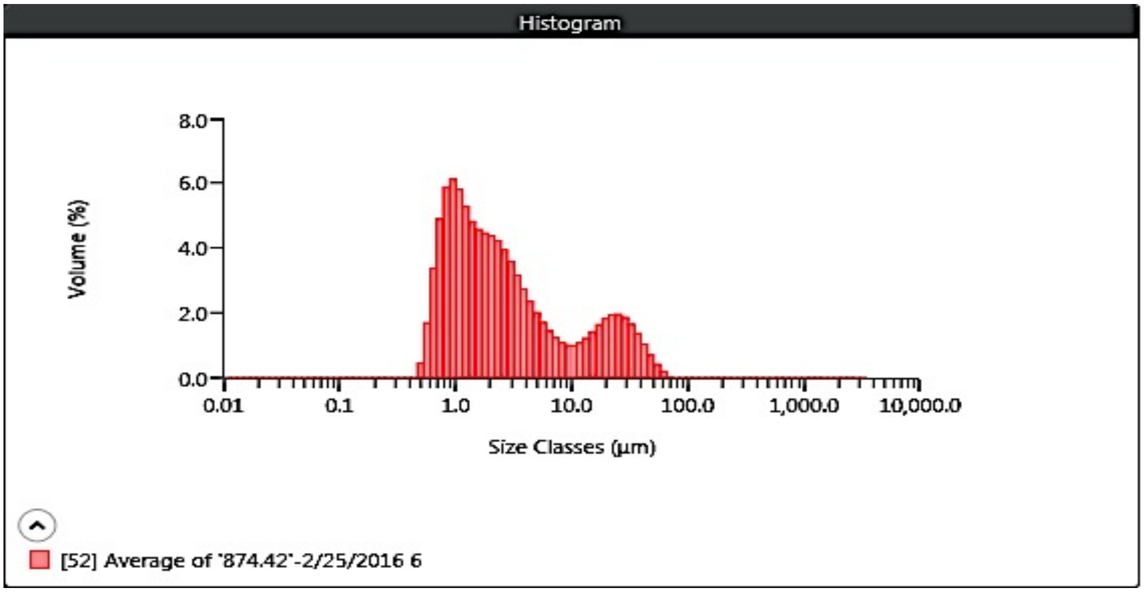

Result

Concentration	0.0020 %	**Span**	11.042
Uniformity	2.807	**Result Units**	Volume
Specific Surface Area	1394 m^2/kg	**Dv (10)**	0.758 µm
D [3,2]	1.66 µm	**Dv (50)**	2.01 µm
D [4,3]	6.77 µm	**Dv (90)**	22.9 µm
Volume Below (5) µm	73.49 %	**Mode**	0.922 µm
Volume Below (10) µm	80.72 %		
Volume Below (20) µm	**87.97 %**	**Volume In Range (500,1000) µm**	0.00 %
Volume In Range (5,20) µm	**14.47 %**	**Volume Above (1000) µm**	0.00 %
Volume In Range (20,200) µm	**12.03 %**		
Volume In Range (200,500) µm	0.00 %	**Volume In Range (1,2.5) µm**	34.32 %
Volume In Range (2.5,5) µm	16.20 %	**Volume In Range (5,10) µm**	7.23 %
D [3,3]	2.80 µm	**Kurtosis [3]**	5.827
Skew [3]	2.427		

Malvern Mastersizer 3000 LP Particle Size Analyzer

MAN 874.62

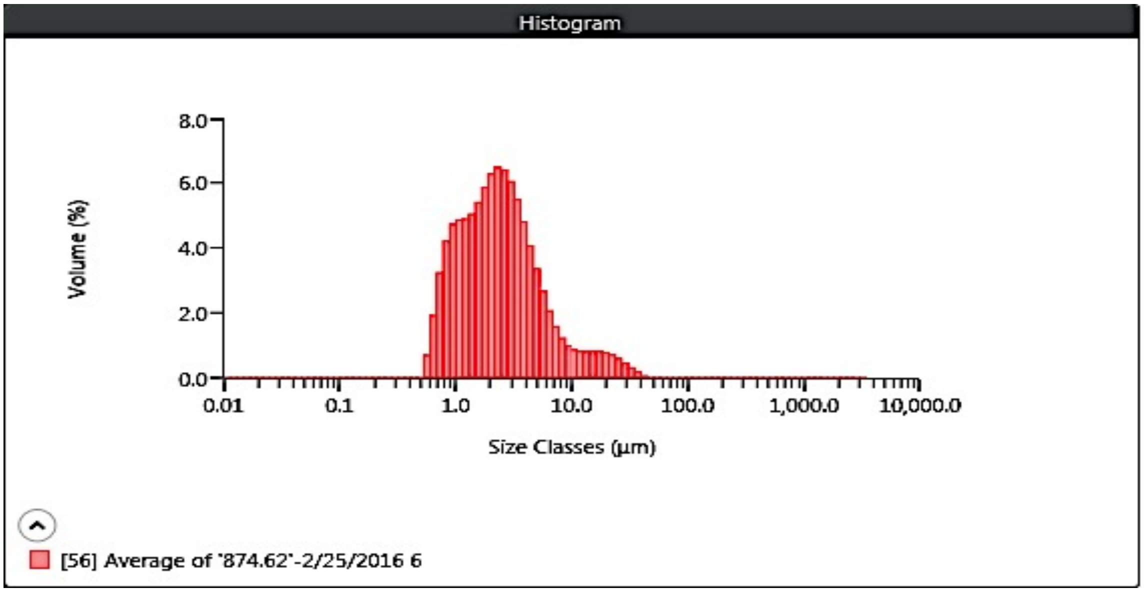

Result

Concentration	0.0030 %	**Span**	2.856
Uniformity	1.075	**Result Units**	Volume
Specific Surface Area	1277 m^2/kg	**Dv (10)**	0.869 µm
D [3,2]	1.81 µm	**Dv (50)**	2.24 µm
D [4,3]	3.75 µm	**Dv (90)**	7.27 µm
Volume Below (5) µm	83.23 %	**Mode**	2.33 µm
Volume Below (10) µm	92.93 %		
Volume Below (20) µm	**97.36 %**	**Volume In Range (500,1000) µm**	0.00 %
Volume In Range (5,20) µm	**14.13 %**	**Volume Above (1000) µm**	0.00000000000001 %
Volume In Range (20,200) µm	**2.64 %**		
Volume In Range (200,500) µm	0.00 %	**Volume In Range (1,2.5) µm**	40.34 %
Volume In Range (2.5,5) µm	27.64 %	**Volume In Range (5,10) µm**	9.70 %
D [3,3]	2.42 µm	**Kurtosis [3]**	15.792
Skew [3]	3.655		

Malvern Mastersizer 3000 LP Particle Size Analyzer

MAN 874.81

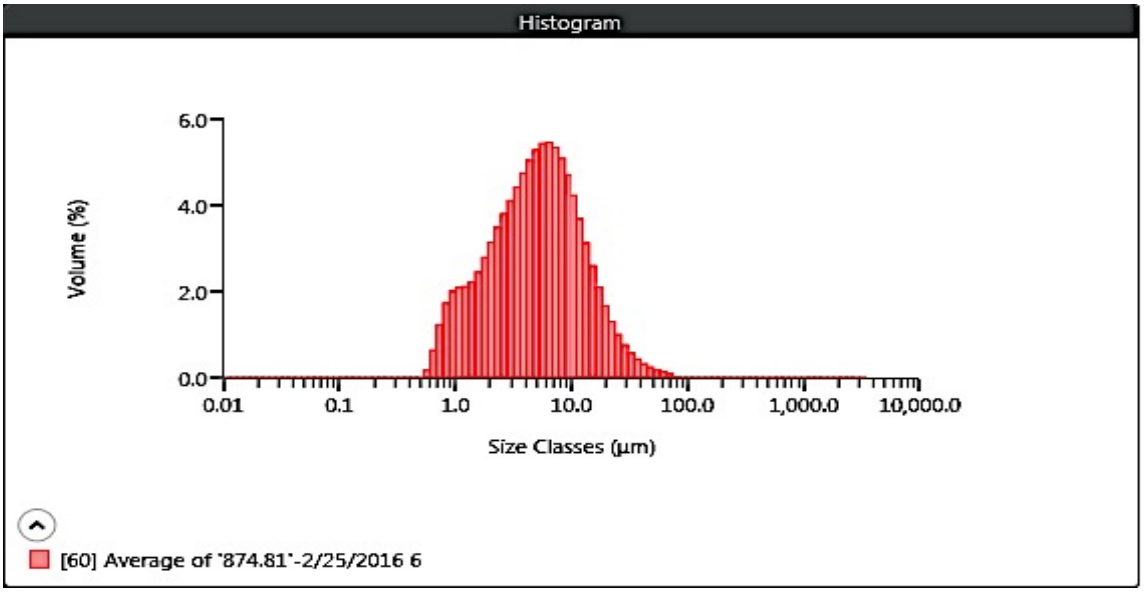

Result

Concentration	0.0045 %	**Span**	2.825
Uniformity	0.936	**Result Units**	Volume
Specific Surface Area	734.9 m^2/kg	**Dv (10)**	1.28 µm
D [3,2]	3.14 µm	**Dv (50)**	5.02 µm
D [4,3]	7.30 µm	**Dv (90)**	15.5 µm
Volume Below (5) µm	49.81 %	**Mode**	6.05 µm
Volume Below (10) µm	78.02 %		
Volume Below (20) µm	**94.21 %**	**Volume In Range (500,1000) µm**	0.00 %
Volume In Range (5,20) µm	**44.40 %**	**Volume Above (1000) µm**	0.00000000000001 %
Volume In Range (20,200) µm	**5.79 %**		
Volume In Range (200,500) µm	0.00 %	**Volume In Range (1,2.5) µm**	19.08 %
Volume In Range (2.5,5) µm	24.82 %	**Volume In Range (5,10) µm**	28.21 %
D [3,3]	4.79 µm	**Kurtosis [3]**	15.266
Skew [3]	3.164		

Malvern Mastersizer 3000 LP Particle Size Analyzer

MAN 875.01

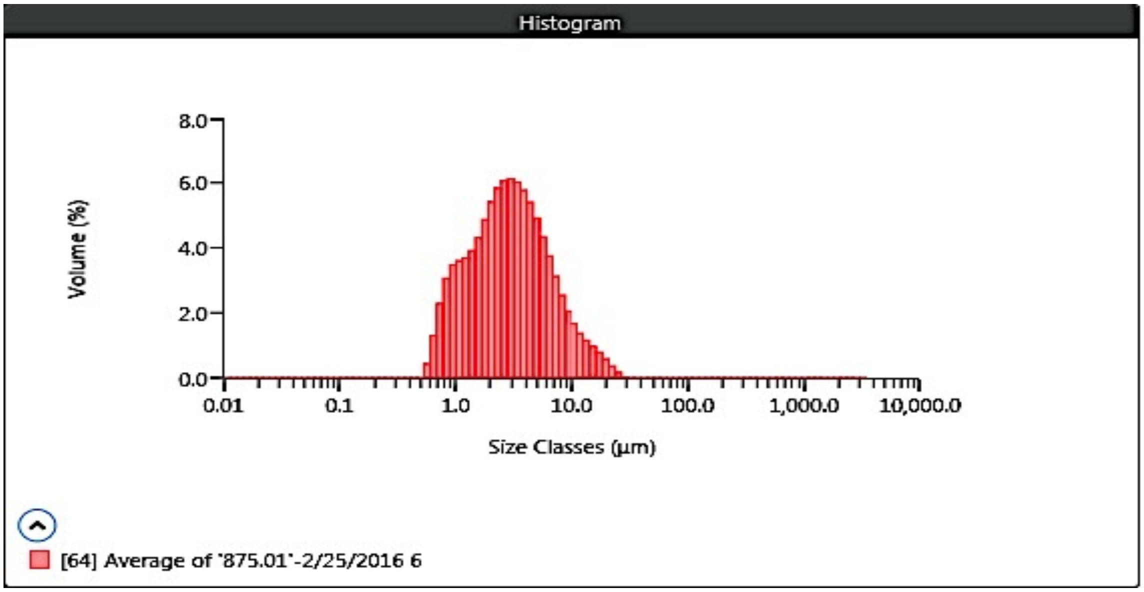

Result

Concentration	0.0040 %	**Span**	2.594
Uniformity	0.833	**Result Units**	Volume
Specific Surface Area	1081 m^2/kg	**Dv (10)**	0.970 μm
D [3,2]	2.14 μm	**Dv (50)**	2.83 μm
D [4,3]	3.99 μm	**Dv (90)**	8.32 μm
Volume Below (5) μm	75.43 %	**Mode**	2.87 μm
Volume Below (10) μm	93.08 %		
Volume Below (20) μm	**99.17 %**	**Volume In Range (500,1000) μm**	0.00 %
Volume In Range (5,20) μm	**23.74 %**	**Volume Above (1000) μm**	0.00000000000003 %
Volume In Range (20,200) μm	**0.83 %**		
Volume In Range (200,500) μm	0.00 %	**Volume In Range (1,2.5) μm**	33.12 %
Volume In Range (2.5,5) μm	31.46 %	**Volume In Range (5,10) μm**	17.65 %
D [3,3]	2.87 μm	**Kurtosis [3]**	7.266
Skew [3]	2.393		

Malvern Mastersizer 3000 LP Particle Size Analyzer

Replicate MAN 875.01

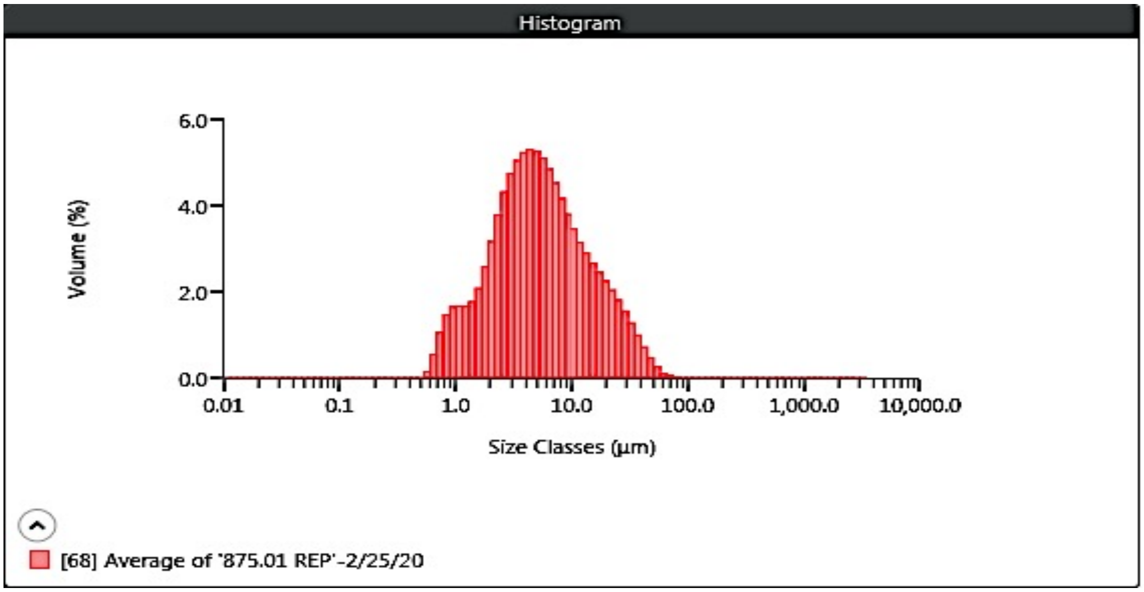

Result

Concentration	0.0023 %	**Span**	3.750
Uniformity	1.133	**Result Units**	Volume
Specific Surface Area	685.6 m^2/kg	**Dv (10)**	1.46 μm
D [3,2]	3.37 μm	**Dv (50)**	5.03 μm
D [4,3]	8.41 μm	**Dv (90)**	20.3 μm
Volume Below (5) μm	49.77 %	**Mode**	4.36 μm
Volume Below (10) μm	74.30 %		
Volume Below (20) μm	**89.72 %**	**Volume In Range (500,1000) μm**	0.00 %
Volume In Range (5,20) μm	**39.96 %**	**Volume Above (1000) μm**	0.00 %
Volume In Range (20,200) μm	**10.28 %**		
Volume In Range (200,500) μm	0.00 %	**Volume In Range (1,2.5) μm**	17.64 %
Volume In Range (2.5,5) μm	27.16 %	**Volume In Range (5,10) μm**	24.53 %
D [3,3]	5.25 μm	**Kurtosis [3]**	7.517
Skew [3]	2.435		

Malvern Mastersizer 3000 LP Particle Size Analyzer

MAN 875.70

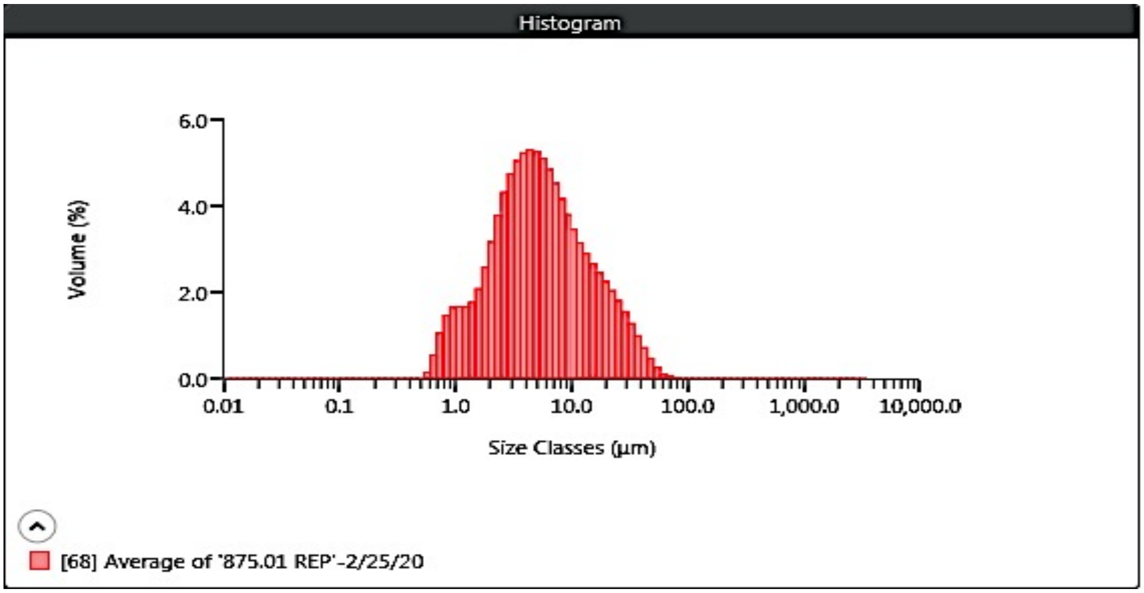

Result

Concentration	0.0023 %	Span	3.750
Uniformity	1.133	Result Units	Volume
Specific Surface Area	685.6 m²/kg	Dv (10)	1.46 µm
D [3,2]	3.37 µm	Dv (50)	5.03 µm
D [4,3]	8.41 µm	Dv (90)	20.3 µm
Volume Below (5) µm	49.77 %	Mode	4.36 µm
Volume Below (10) µm	74.30 %		
Volume Below (20) µm	89.72 %	Volume In Range (500,1000) µm	0.00 %
Volume In Range (5,20) µm	39.96 %	Volume Above (1000) µm	0.00 %
Volume In Range (20,200) µm	10.28 %		
Volume In Range (200,500) µm	0.00 %	Volume In Range (1,2.5) µm	17.64 %
Volume In Range (2.5,5) µm	27.16 %	Volume In Range (5,10) µm	24.53 %
D [3,3]	5.25 µm	Kurtosis [3]	7.517
Skew [3]	2.435		

Malvern Mastersizer 3000 LP Particle Size Analyzer

Replicate MAN 875.70

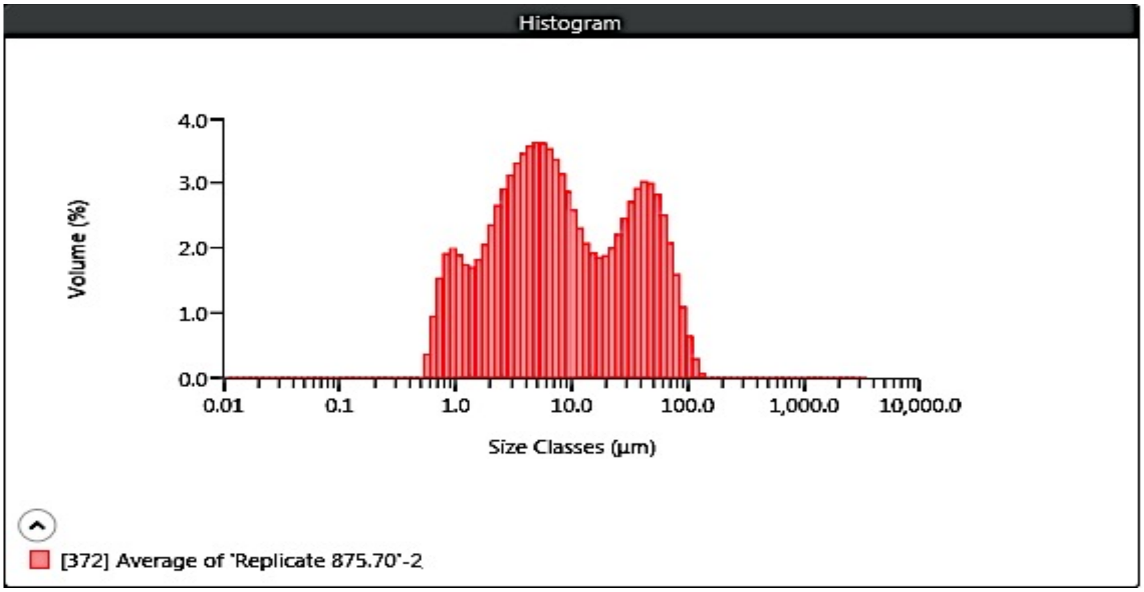

Result

Concentration	0.0021 %	**Span**	7.442
Uniformity	2.160	**Result Units**	Volume
Specific Surface Area	639.7 m²/kg	**Dv (10)**	1.24 μm
D [3,2]	3.61 μm	**Dv (50)**	7.16 μm
D [4,3]	18.6 μm	**Dv (90)**	54.5 μm
Volume Below (5) μm	39.98 %	**Mode**	5.10 μm
Volume Below (10) μm	58.04 %		
Volume Below (20) μm	**69.56 %**	**Volume In Range (500,1000) μm**	0.00 %
Volume In Range (5,20) μm	**29.58 %**	**Volume Above (1000) μm**	0.00000000000001 %
Volume In Range (20,200) μm	**30.44 %**		
Volume In Range (200,500) μm	0.00 %	**Volume In Range (1,2.5) μm**	14.87 %
Volume In Range (2.5,5) μm	18.20 %	**Volume In Range (5,10) μm**	18.06 %
D [3,3]	8.12 μm	**Kurtosis [3]**	2.616
Skew [3]	1.732		

Malvern Mastersizer 3000 LP Particle Size Analyzer

MAN 875.81

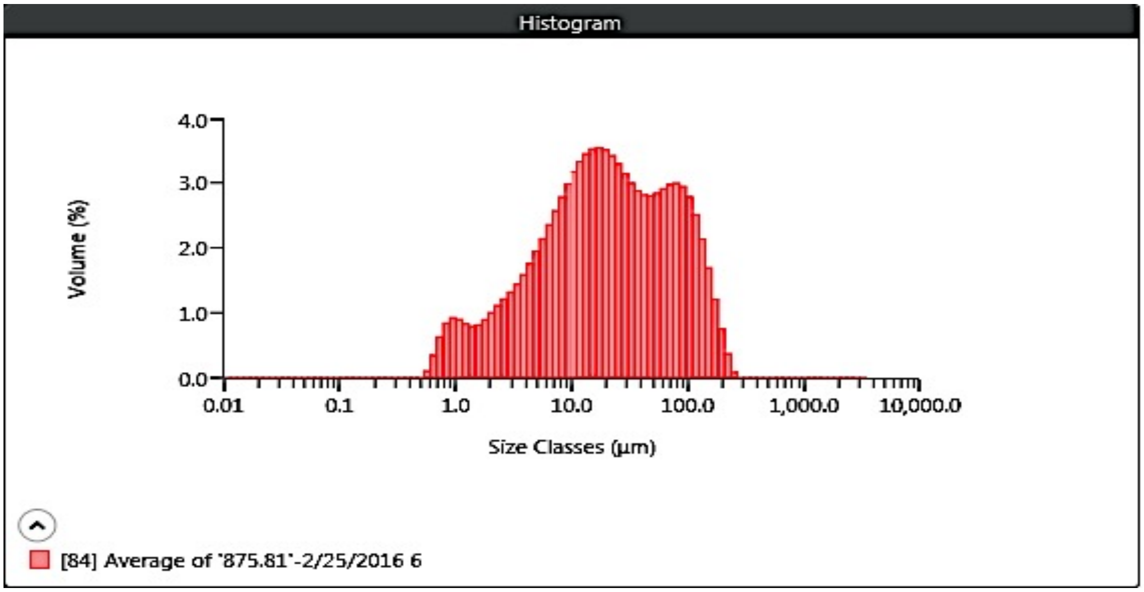

Result

Concentration	0.0037 %	**Span**	5.241
Uniformity	1.548	**Result Units**	Volume
Specific Surface Area	337.5 m^2/kg	**Dv (10)**	2.63 μm
D [3,2]	6.84 μm	**Dv (50)**	19.7 μm
D [4,3]	38.6 μm	**Dv (90)**	106 μm
Volume Below (5) μm	17.88 %	**Mode**	17.2 μm
Volume Below (10) μm	31.81 %		
Volume Below (20) μm	**50.49 %**	**Volume In Range (500,1000) μm**	0.00 %
Volume In Range (5,20) μm	**32.60 %**	**Volume Above (1000) μm**	0.00000000000001 %
Volume In Range (20,200) μm	**48.74 %**		
Volume In Range (200,500) μm	0.78 %	**Volume In Range (1,2.5) μm**	6.60 %
Volume In Range (2.5,5) μm	8.36 %	**Volume In Range (5,10) μm**	13.92 %
D [3,3]	18.3 μm	**Kurtosis [3]**	2.692
Skew [3]	1.711		

Malvern Mastersizer 3000 LP Particle Size Analyzer

MAN 875.96

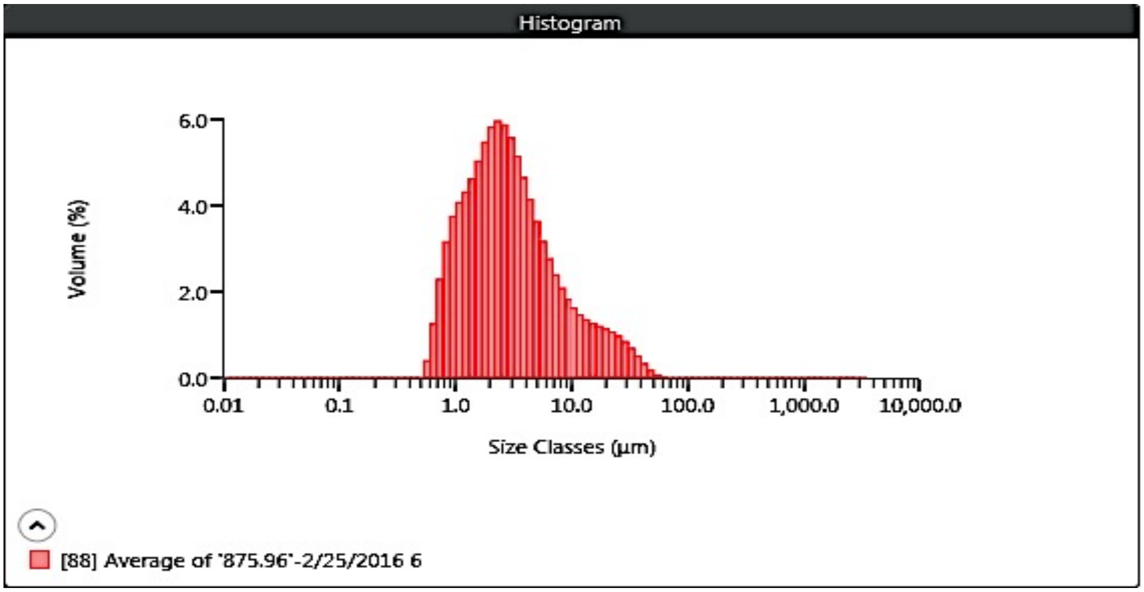

Result

Concentration	0.0052 %	**Span**	4.284
Uniformity	1.362	**Result Units**	Volume
Specific Surface Area	1101 m^2/kg	**Dv (10)**	0.962 µm
D [3,2]	2.10 µm	**Dv (50)**	2.63 µm
D [4,3]	5.12 µm	**Dv (90)**	12.2 µm
Volume Below (5) µm	74.02 %	**Mode**	2.30 µm
Volume Below (10) µm	87.56 %		
Volume Below (20) µm	**94.84 %**	**Volume In Range (500,1000) µm**	0.00 %
Volume In Range (5,20) µm	**20.82 %**	**Volume Above (1000) µm**	0.00000000000001 %
Volume In Range (20,200) µm	**5.16 %**		
Volume In Range (200,500) µm	0.00 %	**Volume In Range (1,2.5) µm**	36.48 %
Volume In Range (2.5,5) µm	26.39 %	**Volume In Range (5,10) µm**	13.54 %
D [3,3]	3.02 µm	**Kurtosis [3]**	12.223
Skew [3]	3.202		

Malvern Mastersizer 3000 LP Particle Size Analyzer

MAN 876.77

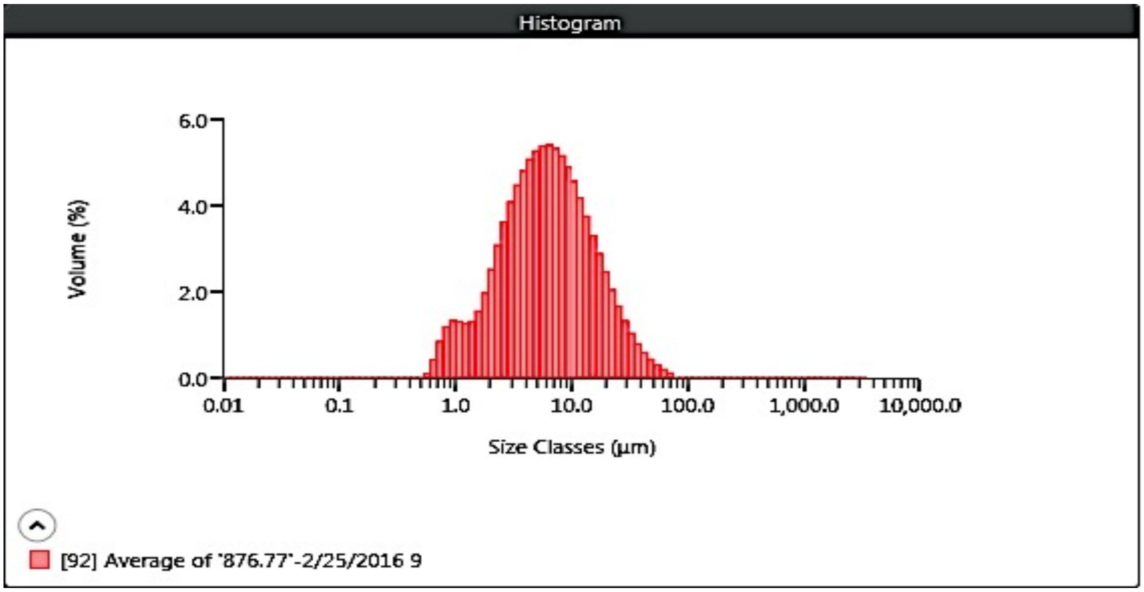

Result

Concentration	0.0029 %	**Span**	2.987
Uniformity	0.954	**Result Units**	Volume
Specific Surface Area	602.5 m^2/kg	**Dv (10)**	1.73 μm
D [3,2]	3.83 μm	**Dv (50)**	5.97 μm
D [4,3]	8.90 μm	**Dv (90)**	19.6 μm
Volume Below (5) μm	42.52 %	**Mode**	6.07 μm
Volume Below (10) μm	70.90 %		
Volume Below (20) μm	**90.41 %**	**Volume In Range (500,1000) μm**	0.00 %
Volume In Range (5,20) μm	**47.89 %**	**Volume Above (1000) μm**	0.00 %
Volume In Range (20,200) μm	**9.59 %**		
Volume In Range (200,500) μm	0.00 %	**Volume In Range (1,2.5) μm**	13.79 %
Volume In Range (2.5,5) μm	24.77 %	**Volume In Range (5,10) μm**	28.37 %
D [3,3]	5.89 μm	**Kurtosis [3]**	8.890
Skew [3]	2.553		

Malvern Mastersizer 3000 LP Particle Size Analyzer

MAN 877

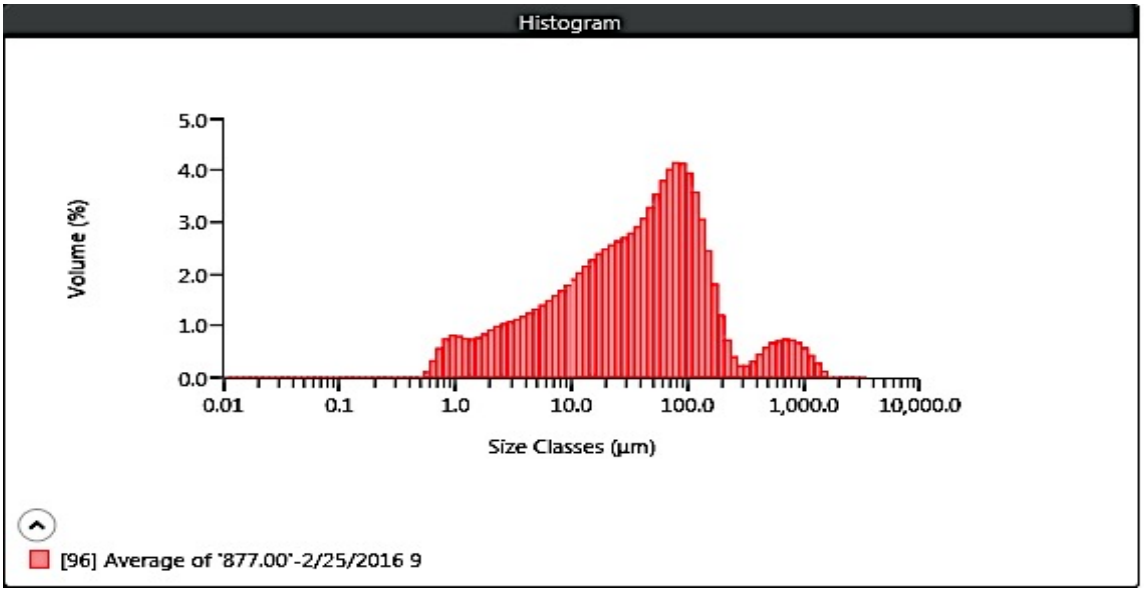

Result

Concentration	0.0055 %	Span	4.243
Uniformity	2.091	Result Units	Volume
Specific Surface Area	278.7 m^2/kg	Dv (10)	2.96 µm
D [3,2]	8.28 µm	Dv (50)	40.1 µm
D [4,3]	97.8 µm	Dv (90)	173 µm
Volume Below (5) µm	14.88 %	Mode	85.3 µm
Volume Below (10) µm	23.41 %		
Volume Below (20) µm	35.25 %	Volume In Range (500,1000) µm	3.74 %
Volume In Range (5,20) µm	20.37 %	Volume Above (1000) µm	1.29 %
Volume In Range (20,200) µm	56.45 %		
Volume In Range (200,500) µm	3.28 %	Volume In Range (1,2.5) µm	5.99 %
Volume In Range (2.5,5) µm	6.27 %	Volume In Range (5,10) µm	8.53 %
D [3,3]	31.6 µm	Kurtosis [3]	17.860
Skew [3]	4.025		

Malvern Mastersizer 3000 LP Particle Size Analyzer

MAN 877.41

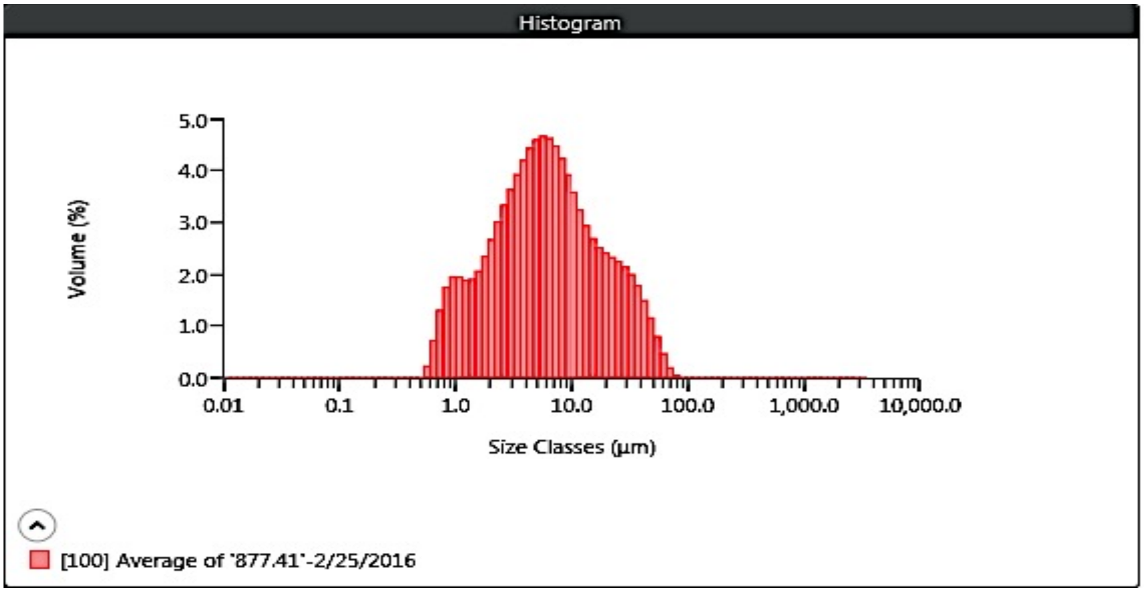

Result

Concentration	0.0035 %	**Span**	4.501
Uniformity	1.306	**Result Units**	Volume
Specific Surface Area	678.5 m^2/kg	**Dv (10)**	1.30 μm
D [3,2]	3.40 μm	**Dv (50)**	5.81 μm
D [4,3]	10.5 μm	**Dv (90)**	27.5 μm
Volume Below (5) μm	44.50 %	**Mode**	5.64 μm
Volume Below (10) μm	68.34 %		
Volume Below (20) μm	84.27 %	**Volume In Range (500,1000) μm**	0.00 %
Volume In Range (5,20) μm	39.78 %	**Volume Above (1000) μm**	0.00 %
Volume In Range (20,200) μm	15.73 %		
Volume In Range (200,500) μm	0.00 %	**Volume In Range (1,2.5) μm**	16.52 %
Volume In Range (2.5,5) μm	21.89 %	**Volume In Range (5,10) μm**	23.84 %
D [3,3]	5.93 μm	**Kurtosis [3]**	4.867
Skew [3]	2.132		

<u>**Malvern Mastersizer 3000 LP Particle Size Analyzer**</u>

MAN 876.77

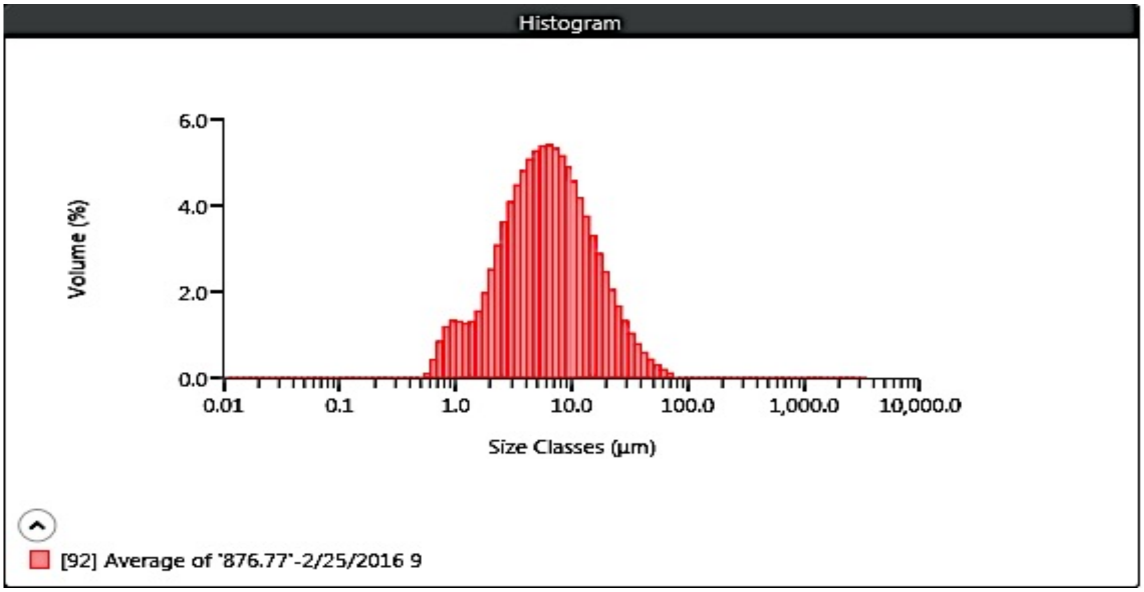

Result

Concentration	0.0029 %	**Span**	2.987
Uniformity	0.954	**Result Units**	Volume
Specific Surface Area	602.5 m^2/kg	**Dv (10)**	1.73 µm
D [3,2]	3.83 µm	**Dv (50)**	5.97 µm
D [4,3]	8.90 µm	**Dv (90)**	19.6 µm
Volume Below (5) µm	42.52 %	**Mode**	6.07 µm
Volume Below (10) µm	70.90 %		
Volume Below (20) µm	**90.41 %**	**Volume In Range (500,1000) µm**	0.00 %
Volume In Range (5,20) µm	**47.89 %**	**Volume Above (1000) µm**	0.00 %
Volume In Range (20,200) µm	**9.59 %**		
Volume In Range (200,500) µm	0.00 %	**Volume In Range (1,2.5) µm**	13.79 %
Volume In Range (2.5,5) µm	24.77 %	**Volume In Range (5,10) µm**	28.37 %
D [3,3]	5.89 µm	**Kurtosis [3]**	8.890
Skew [3]	2.553		

Malvern Mastersizer 3000 LP Particle Size Analyzer

MAN 877.00

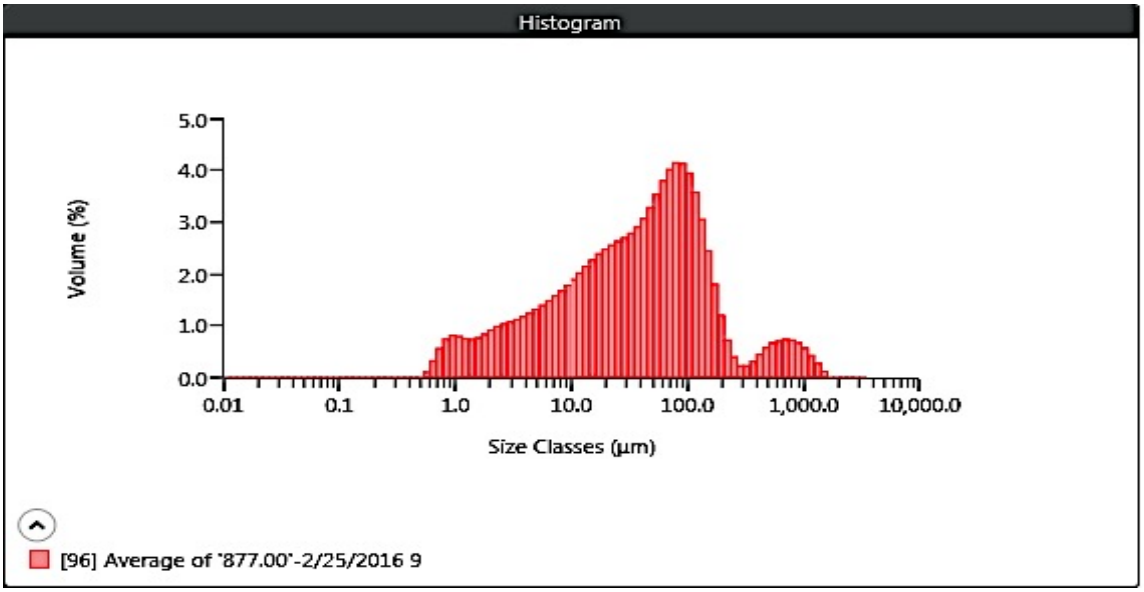

Result

Concentration	0.0055 %	Span	4.243
Uniformity	2.091	Result Units	Volume
Specific Surface Area	278.7 m^2/kg	Dv (10)	2.96 µm
D [3,2]	8.28 µm	Dv (50)	40.1 µm
D [4,3]	97.8 µm	Dv (90)	173 µm
Volume Below (5) µm	14.88 %	Mode	85.3 µm
Volume Below (10) µm	23.41 %		
Volume Below (20) µm	35.25 %	Volume In Range (500,1000) µm	3.74 %
Volume In Range (5,20) µm	20.37 %	Volume Above (1000) µm	1.29 %
Volume In Range (20,200) µm	56.45 %		
Volume In Range (200,500) µm	3.28 %	Volume In Range (1,2.5) µm	5.99 %
Volume In Range (2.5,5) µm	6.27 %	Volume In Range (5,10) µm	8.53 %
D [3,3]	31.6 µm	Kurtosis [3]	17.860
Skew [3]	4.025		

Malvern Mastersizer 3000 LP Particle Size Analyzer

MAN 877.41

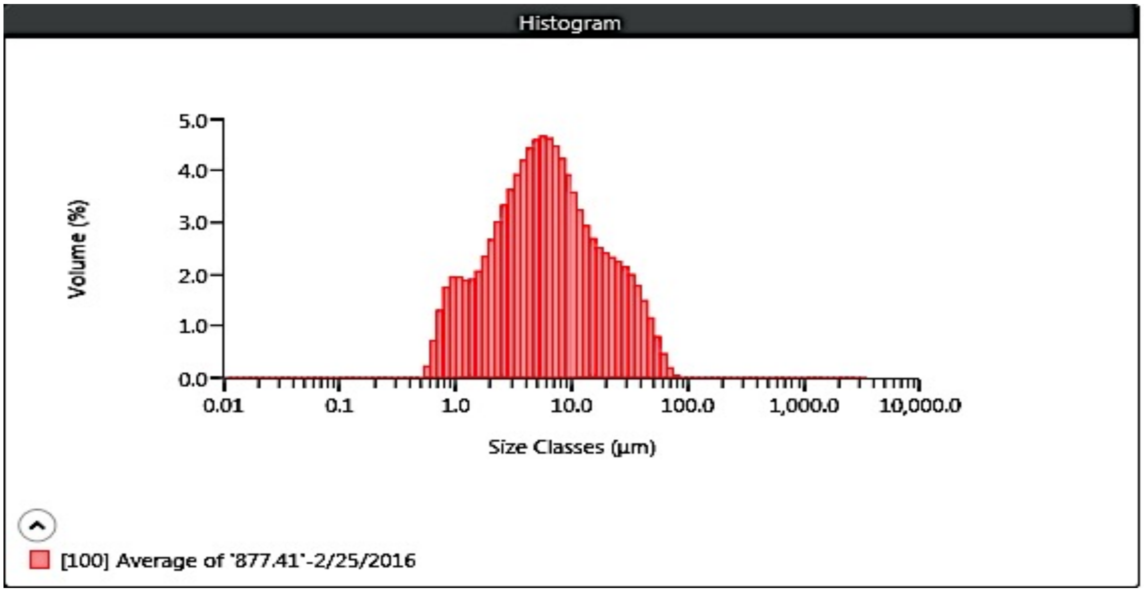

Result

Concentration	0.0035 %	**Span**	4.501
Uniformity	1.306	**Result Units**	Volume
Specific Surface Area	678.5 m^2/kg	**Dv (10)**	1.30 µm
D [3,2]	3.40 µm	**Dv (50)**	5.81 µm
D [4,3]	10.5 µm	**Dv (90)**	27.5 µm
Volume Below (5) µm	44.50 %	**Mode**	5.64 µm
Volume Below (10) µm	68.34 %		
Volume Below (20) µm	84.27 %	**Volume In Range (500,1000) µm**	0.00 %
Volume In Range (5,20) µm	39.78 %	**Volume Above (1000) µm**	0.00 %
Volume In Range (20,200) µm	15.73 %		
Volume In Range (200,500) µm	0.00 %	**Volume In Range (1,2.5) µm**	16.52 %
Volume In Range (2.5,5) µm	21.89 %	**Volume In Range (5,10) µm**	23.84 %
D [3,3]	5.93 µm	**Kurtosis [3]**	4.867
Skew [3]	2.132		

<u>**Malvern Mastersizer 3000 LP Particle Size Analyzer**</u>

MAN 877.58

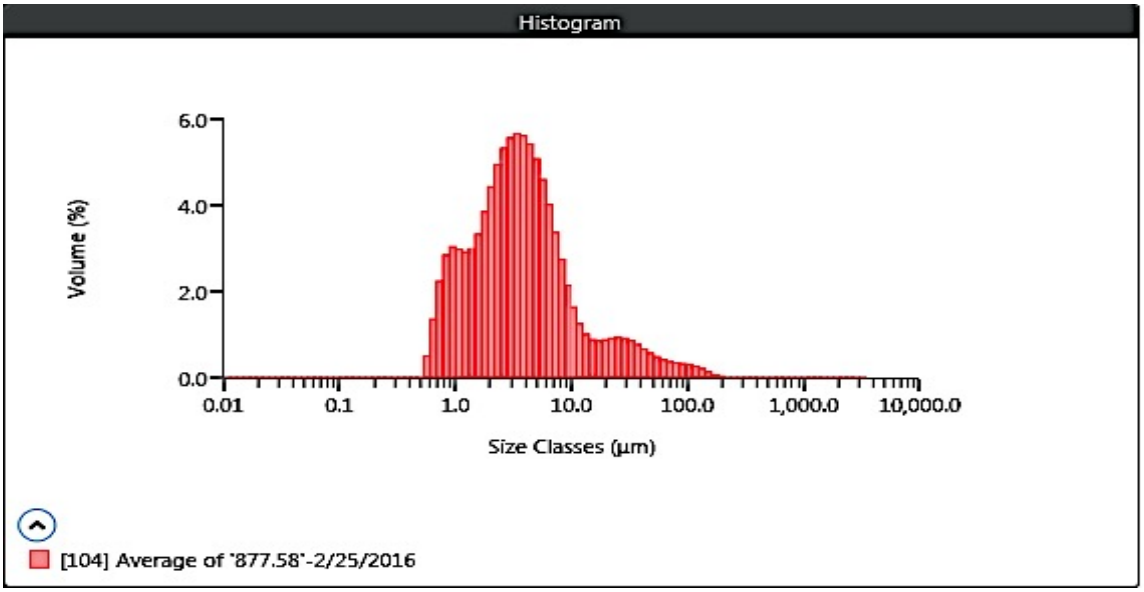

Result

Concentration	0.0040 %	**Span**	4.709
Uniformity	1.881	**Result Units**	Volume
Specific Surface Area	963.3 m^2/kg	**Dv (10)**	0.992 μm
D [3,2]	2.40 μm	**Dv (50)**	3.39 μm
D [4,3]	8.24 μm	**Dv (90)**	17.0 μm
Volume Below (5) μm	66.52 %	**Mode**	3.41 μm
Volume Below (10) μm	85.20 %		
Volume Below (20) μm	**91.10 %**	**Volume In Range (500,1000) μm**	0.00 %
Volume In Range (5,20) μm	**24.58 %**	**Volume Above (1000) μm**	0.00 %
Volume In Range (20,200) μm	**8.88 %**		
Volume In Range (200,500) μm	0.01 %	**Volume In Range (1,2.5) μm**	26.61 %
Volume In Range (2.5,5) μm	29.73 %	**Volume In Range (5,10) μm**	18.68 %
D [3,3]	3.78 μm	**Kurtosis [3]**	32.590
Skew [3]	5.140		

Malvern Mastersizer 3000 LP Particle Size Analyzer

MAN 877.83

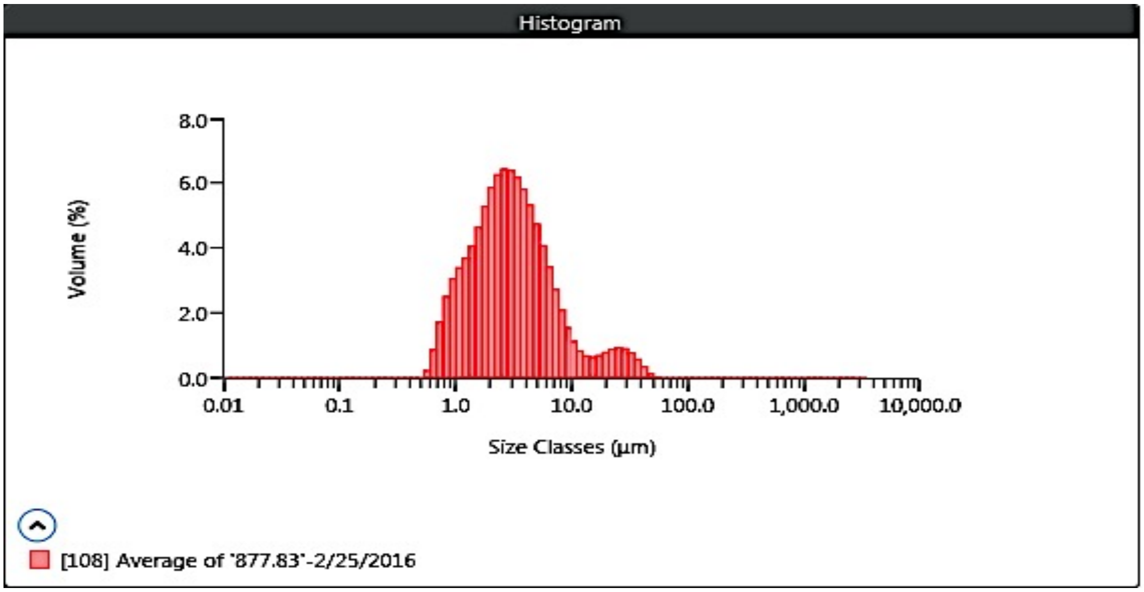

Result

Concentration	0.0034 %	**Span**	2.894
Uniformity	1.127	**Result Units**	Volume
Specific Surface Area	1027 m^2/kg	**Dv (10)**	1.05 µm
D [3,2]	2.25 µm	**Dv (50)**	2.85 µm
D [4,3]	4.91 µm	**Dv (90)**	9.30 µm
Volume Below (5) µm	75.30 %	**Mode**	2.68 µm
Volume Below (10) µm	90.83 %		
Volume Below (20) µm	**95.09 %**	**Volume In Range (500,1000) µm**	0.00 %
Volume In Range (5,20) µm	**19.79 %**	**Volume Above (1000) µm**	0.00000000000001 %
Volume In Range (20,200) µm	**4.91 %**		
Volume In Range (200,500) µm	0.00 %	**Volume In Range (1,2.5) µm**	34.75 %
Volume In Range (2.5,5) µm	31.92 %	**Volume In Range (5,10) µm**	15.53 %
D [3,3]	3.09 µm	**Kurtosis [3]**	13.402
Skew [3]	3.464		

Malvern Mastersizer 3000 LP Particle Size Analyzer

MAN 878.75

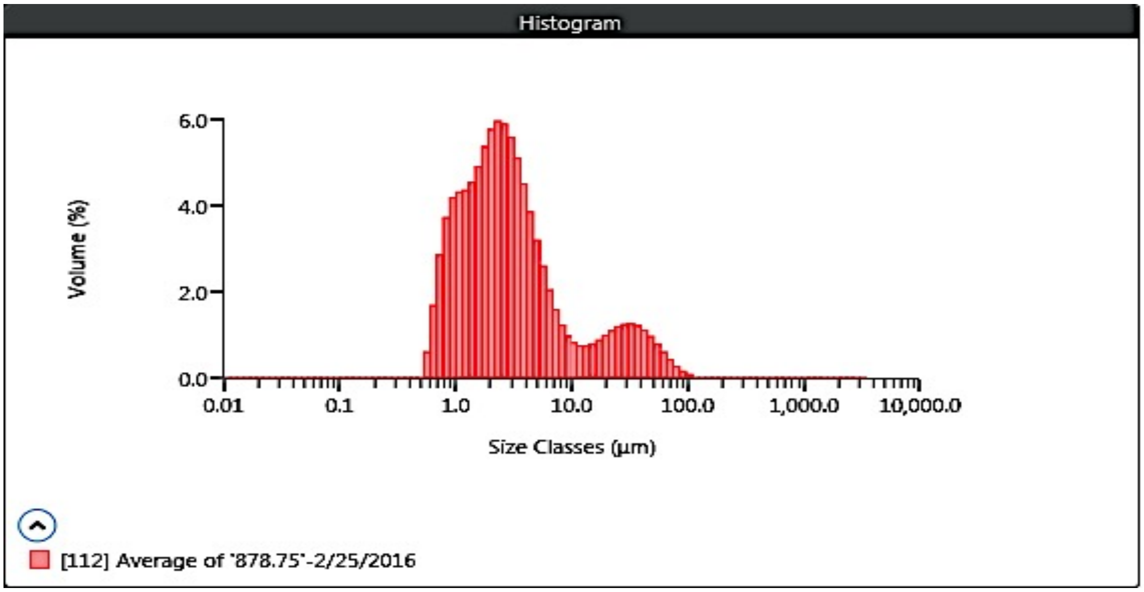

Result

Concentration	0.0039 %	**Span**	8.380
Uniformity	2.296	**Result Units**	Volume
Specific Surface Area	1151 m^2/kg	**Dv (10)**	0.903 µm
D [3,2]	2.01 µm	**Dv (50)**	2.51 µm
D [4,3]	7.23 µm	**Dv (90)**	22.0 µm
Volume Below (5) µm	75.38 %	**Mode**	2.34 µm
Volume Below (10) µm	84.87 %		
Volume Below (20) µm	**89.25 %**	**Volume In Range (500,1000) µm**	0.00 %
Volume In Range (5,20) µm	**13.87 %**	**Volume Above (1000) µm**	0.00 %
Volume In Range (20,200) µm	**10.75 %**		
Volume In Range (200,500) µm	0.00 %	**Volume In Range (1,2.5) µm**	36.39 %
Volume In Range (2.5,5) µm	25.64 %	**Volume In Range (5,10) µm**	9.49 %
D [3,3]	3.15 µm	**Kurtosis [3]**	12.467
Skew [3]	3.336		

Malvern Mastersizer 3000 LP Particle Size Analyzer

MAN 879.12

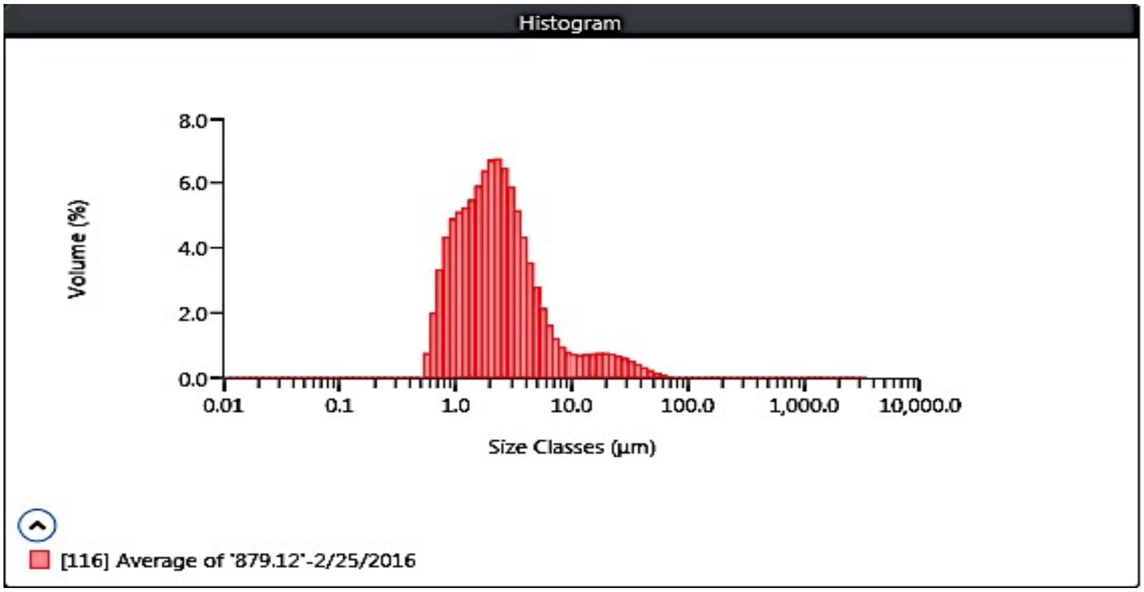

Result

Concentration	0.0041 %	**Span**	3.080
Uniformity	1.308	**Result Units**	Volume
Specific Surface Area	1313 m^2/kg	**Dv (10)**	0.861 μm
D [3,2]	1.76 μm	**Dv (50)**	2.12 μm
D [4,3]	4.06 μm	**Dv (90)**	7.38 μm
Volume Below (5) μm	84.48 %	**Mode**	2.16 μm
Volume Below (10) μm	92.13 %		
Volume Below (20) μm	**96.04 %**	**Volume In Range (500,1000) μm**	0.00 %
Volume In Range (5,20) μm	**11.56 %**	**Volume Above (1000) μm**	0.00 %
Volume In Range (20,200) μm	**3.96 %**		
Volume In Range (200,500) μm	0.00 %	**Volume In Range (1,2.5) μm**	43.01 %
Volume In Range (2.5,5) μm	25.74 %	**Volume In Range (5,10) μm**	7.65 %
D [3,3]	2.38 μm	**Kurtosis [3]**	22.914
Skew [3]	4.362		

Malvern Mastersizer 3000 LP Particle Size Analyzer

MAN 879.29

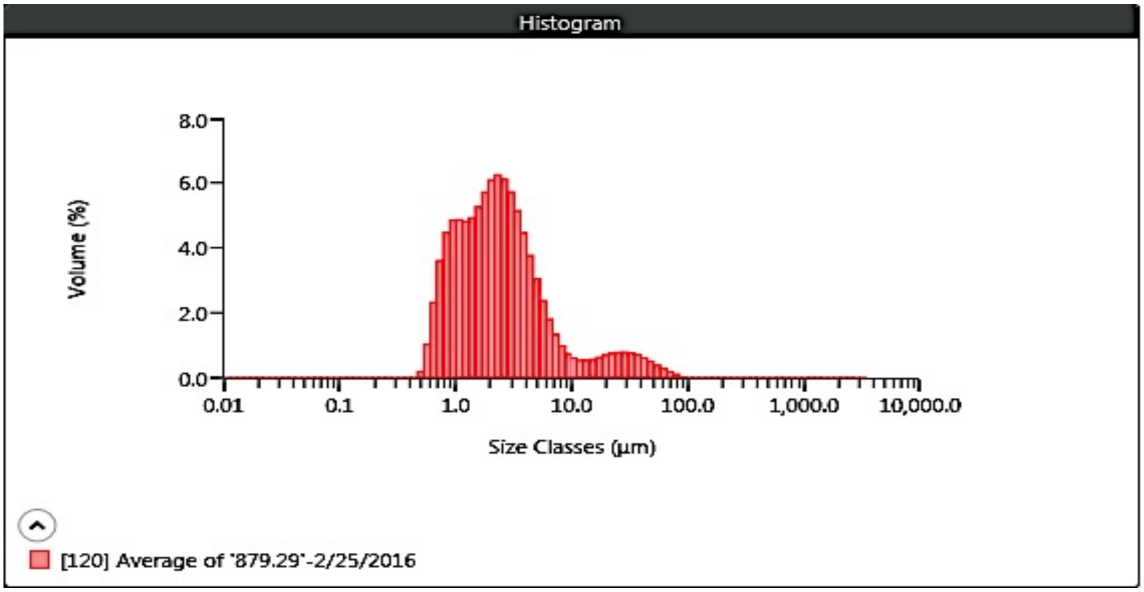

Result

Concentration	0.0049 %	**Span**	3.748
Uniformity	1.704	**Result Units**	Volume
Specific Surface Area	1309 m^2/kg	**Dv (10)**	0.831 µm
D [3,2]	1.76 µm	**Dv (50)**	2.20 µm
D [4,3]	5.04 µm	**Dv (90)**	9.06 µm
Volume Below (5) µm	82.25 %	**Mode**	2.28 µm
Volume Below (10) µm	90.56 %		
Volume Below (20) µm	**93.76 %**	**Volume In Range (500,1000) µm**	0.00 %
Volume In Range (5,20) µm	**11.51 %**	**Volume Above (1000) µm**	0.00000000000001 %
Volume In Range (20,200) µm	**6.24 %**		
Volume In Range (200,500) µm	0.00 %	**Volume In Range (1,2.5) µm**	39.40 %
Volume In Range (2.5,5) µm	25.91 %	**Volume In Range (5,10) µm**	8.31 %
D [3,3]	2.53 µm	**Kurtosis [3]**	20.239
Skew [3]	4.198		

Malvern Mastersizer 3000 LP Particle Size Analyzer

MAN 879.53.00

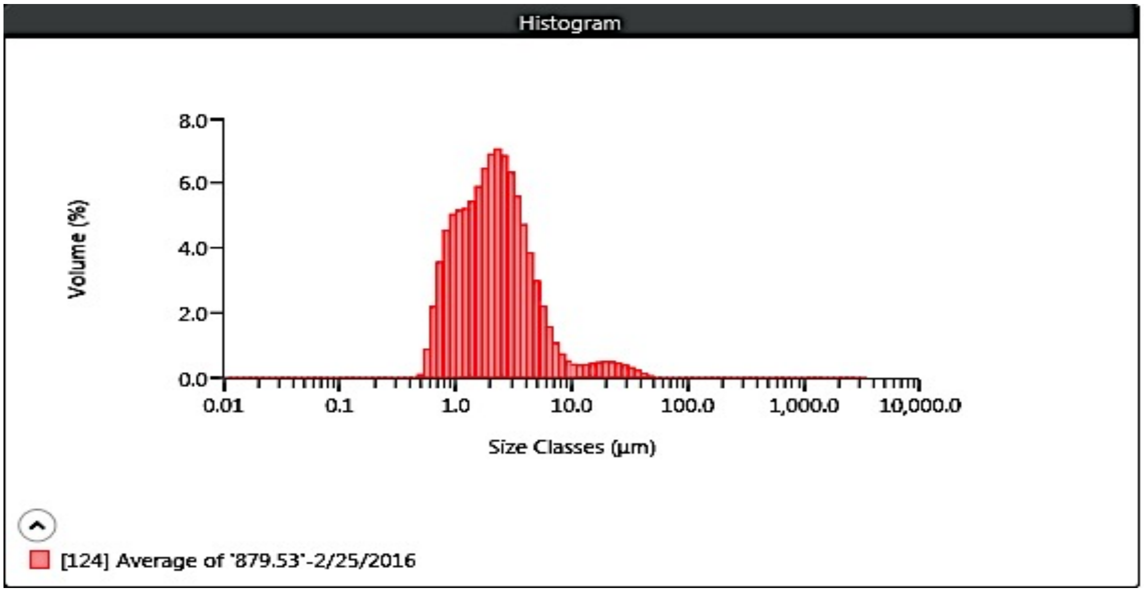

Result

Concentration	0.0032 %	**Span**	2.230
Uniformity	0.979	**Result Units**	Volume
Specific Surface Area	1365 m^2/kg	**Dv (10)**	0.840 µm
D [3,2]	1.69 µm	**Dv (50)**	2.07 µm
D [4,3]	3.29 µm	**Dv (90)**	5.45 µm
Volume Below (5) µm	88.26 %	**Mode**	2.25 µm
Volume Below (10) µm	95.36 %		
Volume Below (20) µm	**97.70 %**	**Volume In Range (500,1000) µm**	0.00 %
Volume In Range (5,20) µm	**9.44 %**	**Volume Above (1000) µm**	0.00000000000001 %
Volume In Range (20,200) µm	**2.30 %**		
Volume In Range (200,500) µm	0.00 %	**Volume In Range (1,2.5) µm**	43.69 %
Volume In Range (2.5,5) µm	27.79 %	**Volume In Range (5,10) µm**	7.10 %
D [3,3]	2.18 µm	**Kurtosis [3]**	27.762
Skew [3]	4.821		

Malvern Mastersizer 3000 LP Particle Size Analyzer

Replicate MAN 879.53

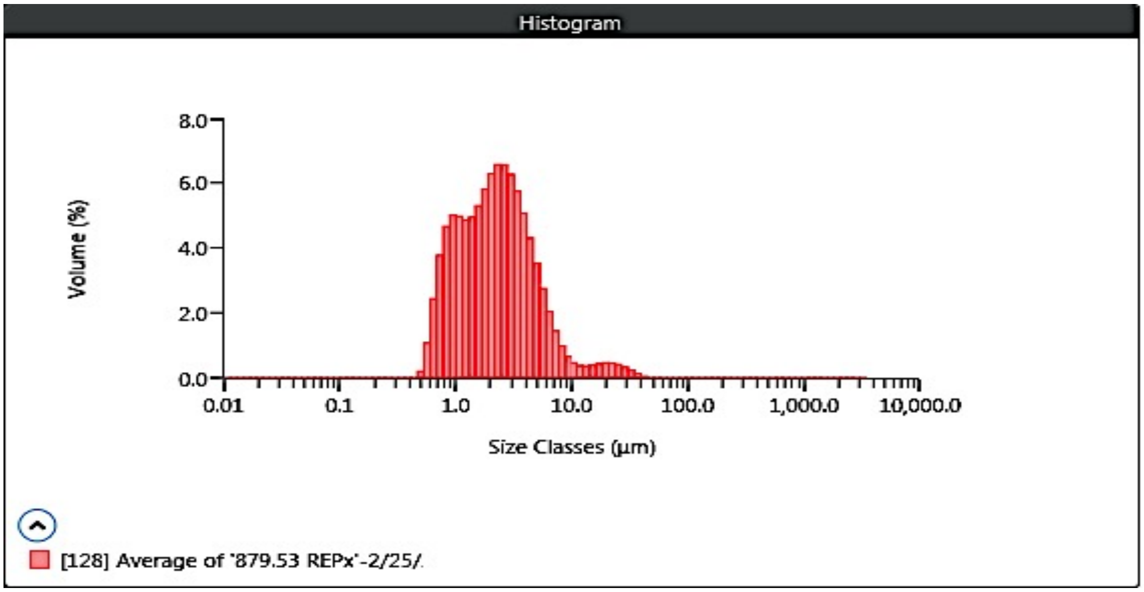

Result

Concentration	0.0039 %	**Span**	2.285
Uniformity	0.919	**Result Units**	Volume
Specific Surface Area	1360 m^2/kg	**Dv (10)**	0.821 µm
D [3,2]	1.70 µm	**Dv (50)**	2.14 µm
D [4,3]	3.24 µm	**Dv (90)**	5.72 µm
Volume Below (5) µm	86.84 %	**Mode**	2.41 µm
Volume Below (10) µm	95.92 %		
Volume Below (20) µm	98.15 %	**Volume In Range (500,1000) µm**	0.00 %
Volume In Range (5,20) µm	11.32 %	**Volume Above (1000) µm**	0.00 %
Volume In Range (20,200) µm	1.85 %		
Volume In Range (200,500) µm	0.00 %	**Volume In Range (1,2.5) µm**	40.31 %
Volume In Range (2.5,5) µm	28.90 %	**Volume In Range (5,10) µm**	9.08 %
D [3,3]	2.21 µm	**Kurtosis [3]**	25.973
Skew [3]	4.581		

Malvern Mastersizer 3000 LP Particle Size Analyzer

MAN 879.00

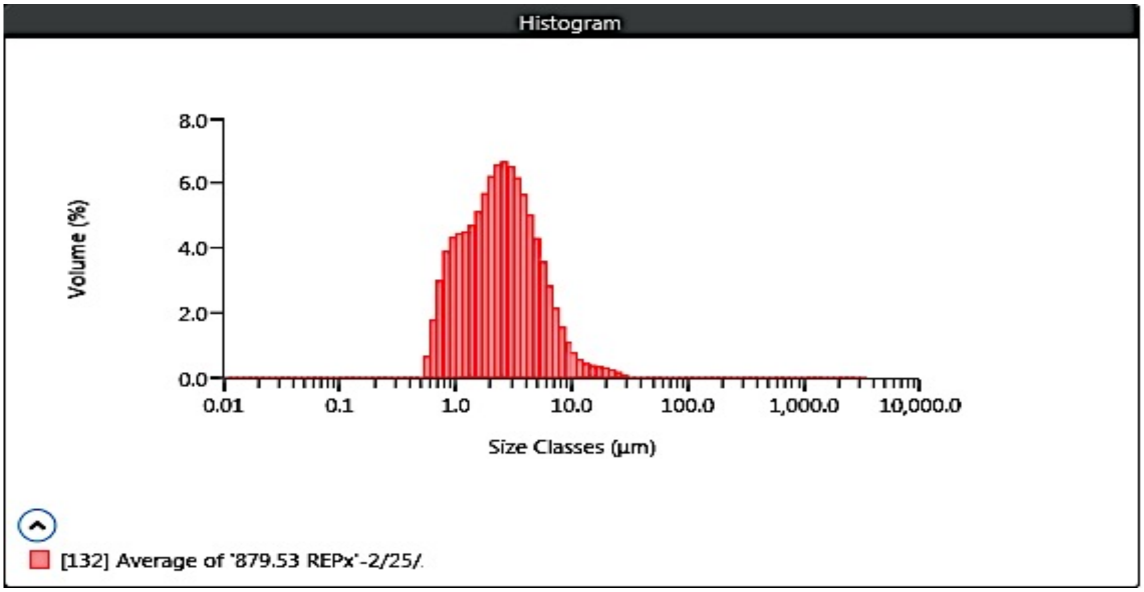

Result

Concentration	0.0049 %	**Span**	2.220
Uniformity	0.756	**Result Units**	Volume
Specific Surface Area	1242 m^2/kg	**Dv (10)**	0.889 μm
D [3,2]	1.86 μm	**Dv (50)**	2.37 μm
D [4,3]	3.20 μm	**Dv (90)**	6.15 μm
Volume Below (5) μm	84.19 %	**Mode**	2.55 μm
Volume Below (10) μm	96.85 %		
Volume Below (20) μm	**99.40 %**	**Volume In Range (500,1000) μm**	0.00 %
Volume In Range (5,20) μm	**15.21 %**	**Volume Above (1000) μm**	0.00 %
Volume In Range (20,200) μm	**0.60 %**		
Volume In Range (200,500) μm	0.00 %	**Volume In Range (1,2.5) μm**	38.77 %
Volume In Range (2.5,5) μm	31.41 %	**Volume In Range (5,10) μm**	12.66 %
D [3,3]	2.39 μm	**Kurtosis [3]**	16.832
Skew [3]	3.379		

Malvern Mastersizer 3000 LP Particle Size Analyzer

MAN 879.87

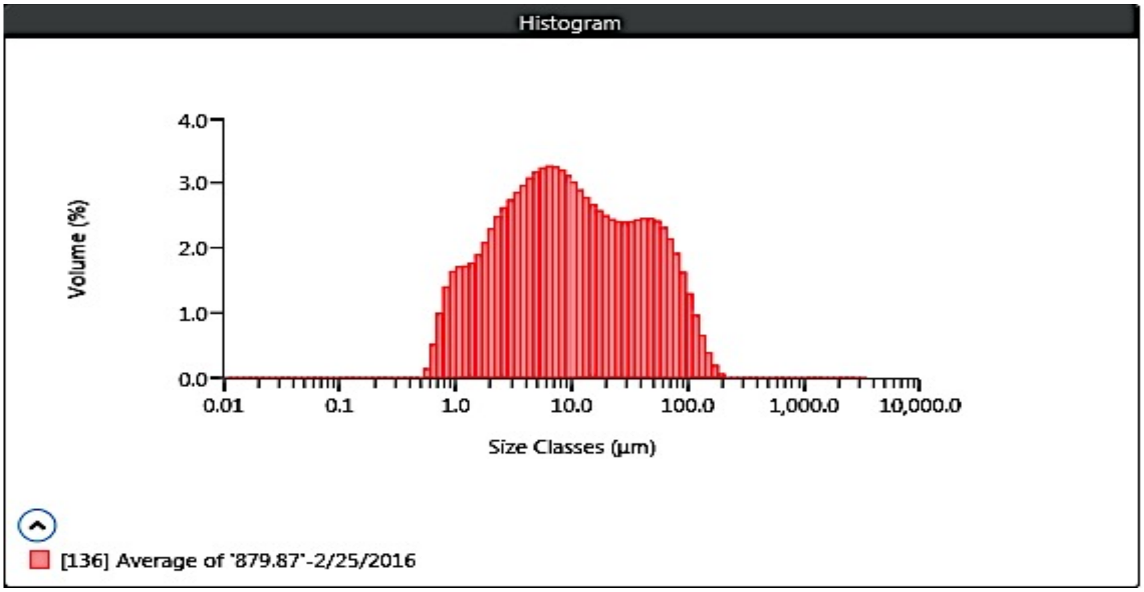

Result

Concentration	0.0031 %	**Span**	7.003
Uniformity	2.059	**Result Units**	Volume
Specific Surface Area	556.5 m^2/kg	**Dv (10)**	1.46 μm
D [3,2]	4.15 μm	**Dv (50)**	8.96 μm
D [4,3]	22.2 μm	**Dv (90)**	64.2 μm
Volume Below (5) μm	35.19 %	**Mode**	6.45 μm
Volume Below (10) μm	52.69 %		
Volume Below (20) μm	67.72 %	**Volume In Range (500,1000) μm**	0.00 %
Volume In Range (5,20) μm	32.53 %	**Volume Above (1000) μm**	0.00 %
Volume In Range (20,200) μm	32.25 %		
Volume In Range (200,500) μm	0.03 %	**Volume In Range (1,2.5) μm**	14.54 %
Volume In Range (2.5,5) μm	15.84 %	**Volume In Range (5,10) μm**	17.49 %
D [3,3]	9.50 μm	**Kurtosis [3]**	4.962
Skew [3]	2.142		

Malvern Mastersizer 3000 LP Particle Size Analyzer

MAN 880.37

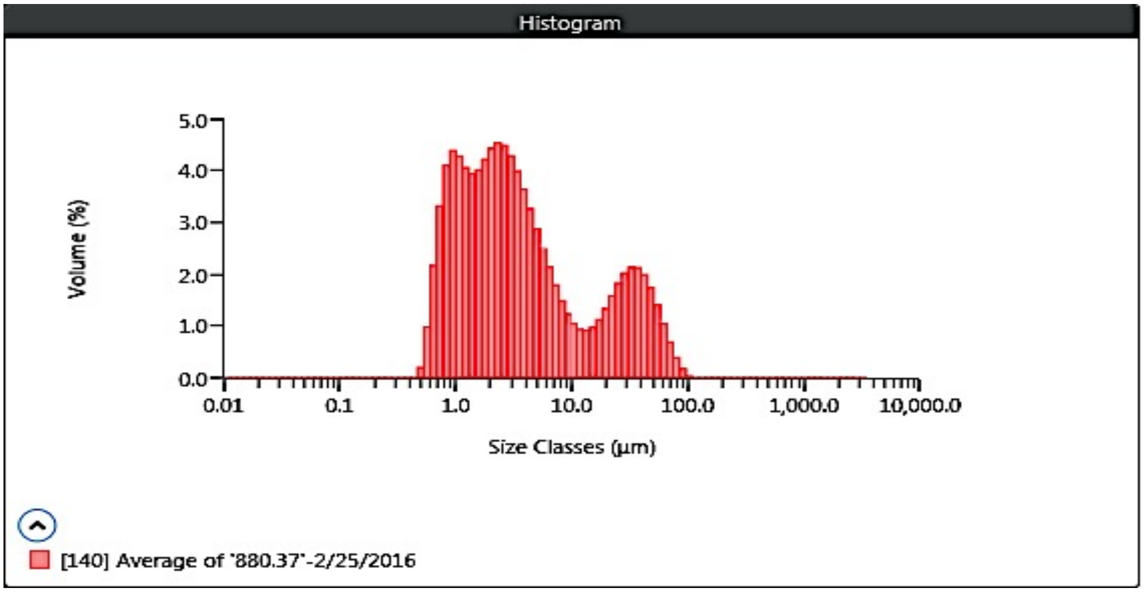

Result

Concentration	0.0040 %	**Span**	11.960
Uniformity	3.050	**Result Units**	Volume
Specific Surface Area	1121 m^2/kg	**Dv (10)**	0.851 µm
D [3,2]	2.06 µm	**Dv (50)**	2.81 µm
D [4,3]	10.0 µm	**Dv (90)**	34.5 µm
Volume Below (5) µm	66.47 %	**Mode**	2.32 µm
Volume Below (10) µm	76.65 %		
Volume Below (20) µm	82.24 %	**Volume In Range (500,1000) µm**	0.00 %
Volume In Range (5,20) µm	15.78 %	**Volume Above (1000) µm**	0.00 %
Volume In Range (20,200) µm	17.76 %		
Volume In Range (200,500) µm	0.00 %	**Volume In Range (1,2.5) µm**	30.38 %
Volume In Range (2.5,5) µm	20.57 %	**Volume In Range (5,10) µm**	10.19 %
D [3,3]	3.83 µm	**Kurtosis [3]**	5.186
Skew [3]	2.309		

Malvern Mastersizer 3000 LP Particle Size Analyzer

Replicate MAN 880.37

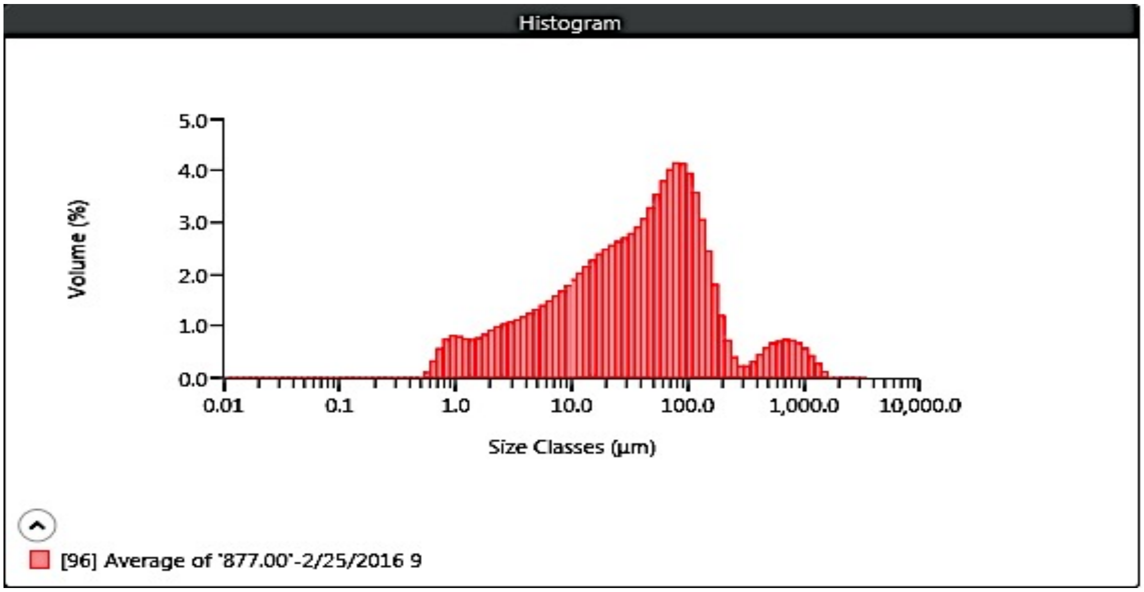

Result

Concentration	0.0055 %	Span	4.243
Uniformity	2.091	Result Units	Volume
Specific Surface Area	278.7 m^2/kg	Dv (10)	2.96 μm
D [3,2]	8.28 μm	Dv (50)	40.1 μm
D [4,3]	97.8 μm	Dv (90)	173 μm
Volume Below (5) μm	14.88 %	Mode	85.3 μm
Volume Below (10) μm	23.41 %		
Volume Below (20) μm	35.25 %	Volume In Range (500,1000) μm	3.74 %
Volume In Range (5,20) μm	20.37 %	Volume Above (1000) μm	1.29 %
Volume In Range (20,200) μm	56.45 %		
Volume In Range (200,500) μm	3.28 %	Volume In Range (1,2.5) μm	5.99 %
Volume In Range (2.5,5) μm	6.27 %	Volume In Range (5,10) μm	8.53 %
D [3,3]	31.6 μm	Kurtosis [3]	17.860
Skew [3]	4.025		

Malvern Mastersizer 3000 LP Particle Size Analyzer

MAN 877.00

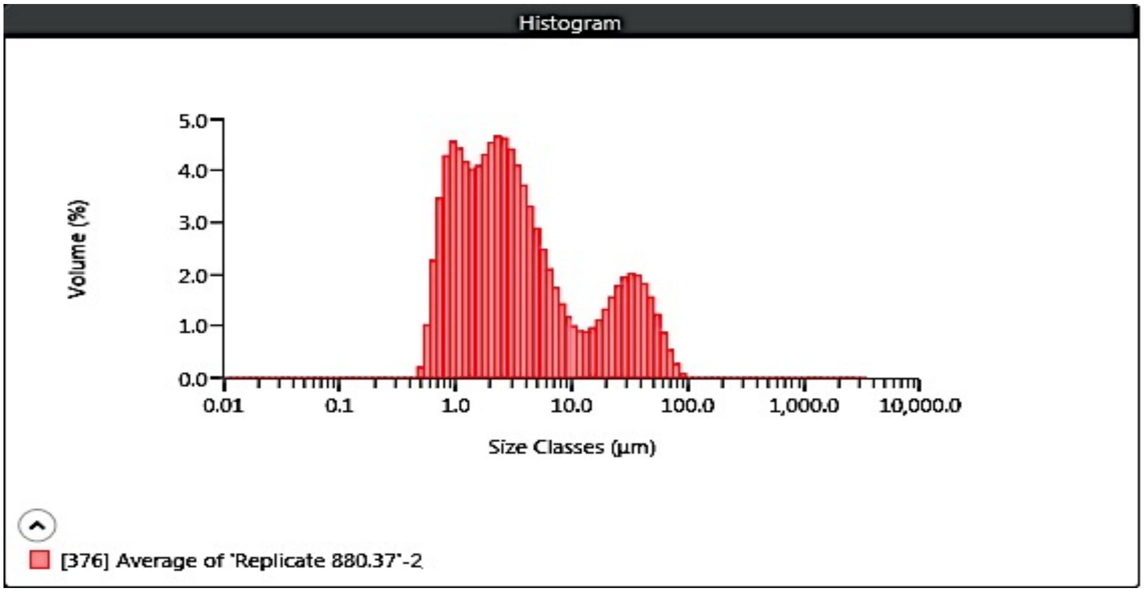

Result

Concentration	0.0026 %	**Span**	11.502
Uniformity	2.891	**Result Units**	Volume
Specific Surface Area	1154 m²/kg	**Dv (10)**	0.840 µm
D [3,2]	2.00 µm	**Dv (50)**	2.69 µm
D [4,3]	9.20 µm	**Dv (90)**	31.8 µm
Volume Below (5) µm	68.36 %	**Mode**	2.34 µm
Volume Below (10) µm	78.31 %		
Volume Below (20) µm	**83.78 %**	**Volume In Range (500,1000) µm**	0.00 %
Volume In Range (5,20) µm	**15.42 %**	**Volume Above (1000) µm**	0.00000000000001 %
Volume In Range (20,200) µm	**16.22 %**		
Volume In Range (200,500) µm	0.00 %	**Volume In Range (1,2.5) µm**	31.15 %
Volume In Range (2.5,5) µm	21.03 %	**Volume In Range (5,10) µm**	9.95 %
D [3,3]	3.61 µm	**Kurtosis [3]**	5.462
Skew [3]	2.376		

Malvern Mastersizer 3000 LP Particle Size Analyzer

MAN 880.56

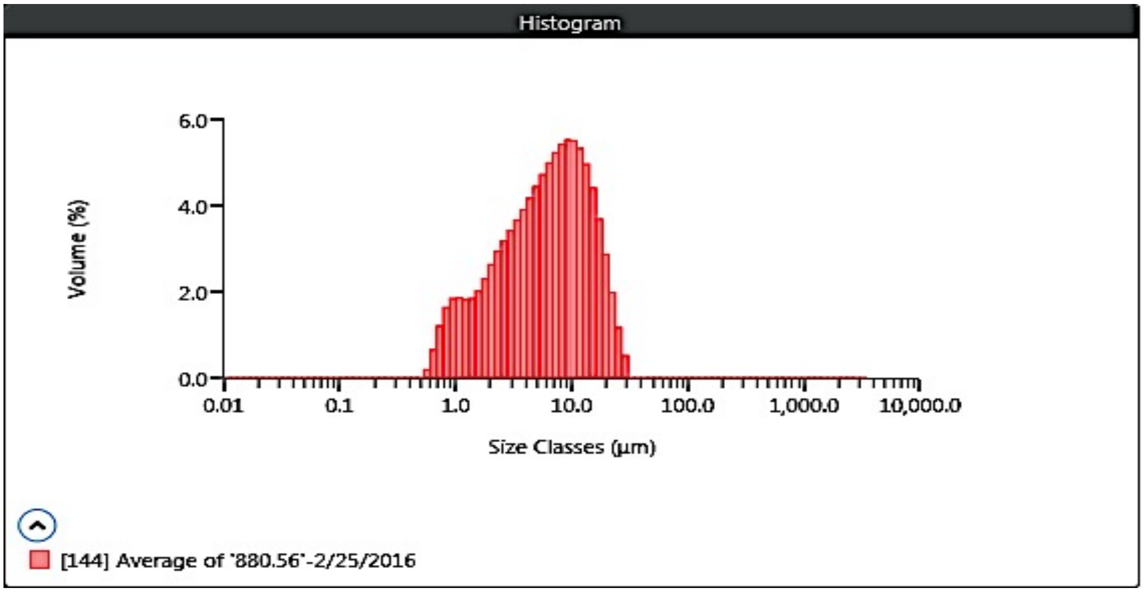

Result

Concentration	0.0049 %	**Span**	2.465
Uniformity	0.765	**Result Units**	Volume
Specific Surface Area	669.2 m^2/kg	**Dv (10)**	1.36 μm
D [3,2]	3.45 μm	**Dv (50)**	6.16 μm
D [4,3]	7.74 μm	**Dv (90)**	16.5 μm
Volume Below (5) μm	42.26 %	**Mode**	9.66 μm
Volume Below (10) μm	70.19 %		
Volume Below (20) μm	**95.03 %**	**Volume In Range (500,1000) μm**	0.00 %
Volume In Range (5,20) μm	**52.77 %**	**Volume Above (1000) μm**	0.00000000000001 %
Volume In Range (20,200) μm	**4.97 %**		
Volume In Range (200,500) μm	0.00 %	**Volume In Range (1,2.5) μm**	16.00 %
Volume In Range (2.5,5) μm	20.61 %	**Volume In Range (5,10) μm**	27.93 %
D [3,3]	5.41 μm	**Kurtosis [3]**	0.660
Skew [3]	1.062		

Malvern Mastersizer 3000 LP Particle Size Analyzer

MAN 880.79

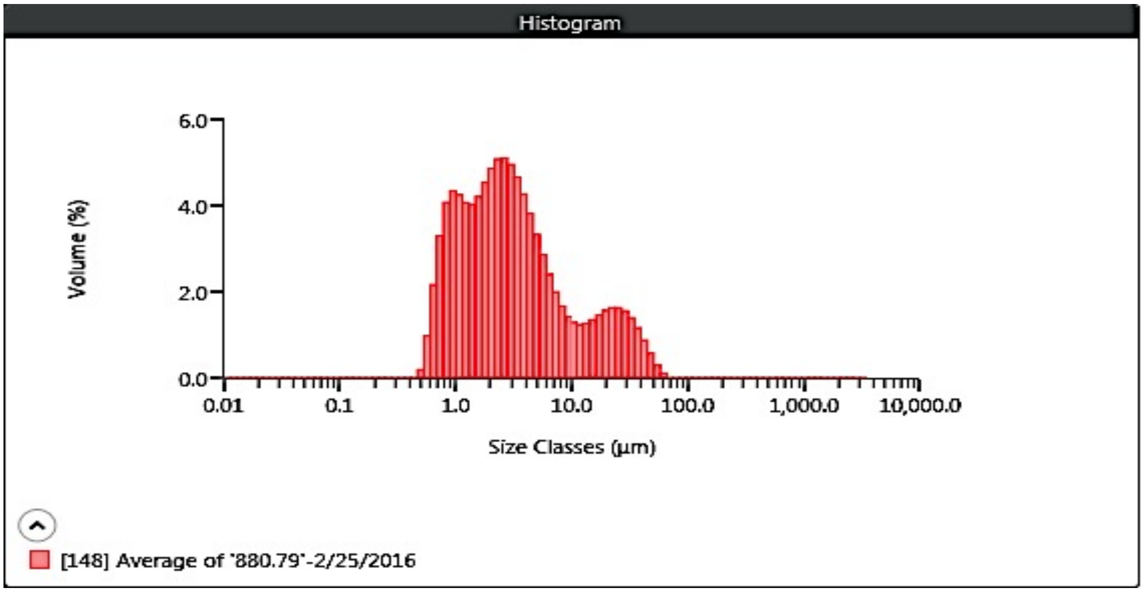

Result

Concentration	0.0040 %	**Span**	7.138
Uniformity	1.902	**Result Units**	Volume
Specific Surface Area	1162 m^2/kg	**Dv (10)**	0.853 µm
D [3,2]	1.99 µm	**Dv (50)**	2.66 µm
D [4,3]	6.51 µm	**Dv (90)**	19.9 µm
Volume Below (5) µm	71.27 %	**Mode**	2.47 µm
Volume Below (10) µm	82.80 %		
Volume Below (20) µm	**90.08 %**	**Volume In Range (500,1000) µm**	0.00 %
Volume In Range (5,20) µm	**18.81 %**	**Volume Above (1000) µm**	0.00 %
Volume In Range (20,200) µm	**9.92 %**		
Volume In Range (200,500) µm	0.00 %	**Volume In Range (1,2.5) µm**	32.06 %
Volume In Range (2.5,5) µm	23.82 %	**Volume In Range (5,10) µm**	11.53 %
D [3,3]	3.20 µm	**Kurtosis [3]**	7.061
Skew [3]	2.621		

<u>Malvern Mastersizer 3000 LP Particle Size Analyzer</u>

MAN 881.02

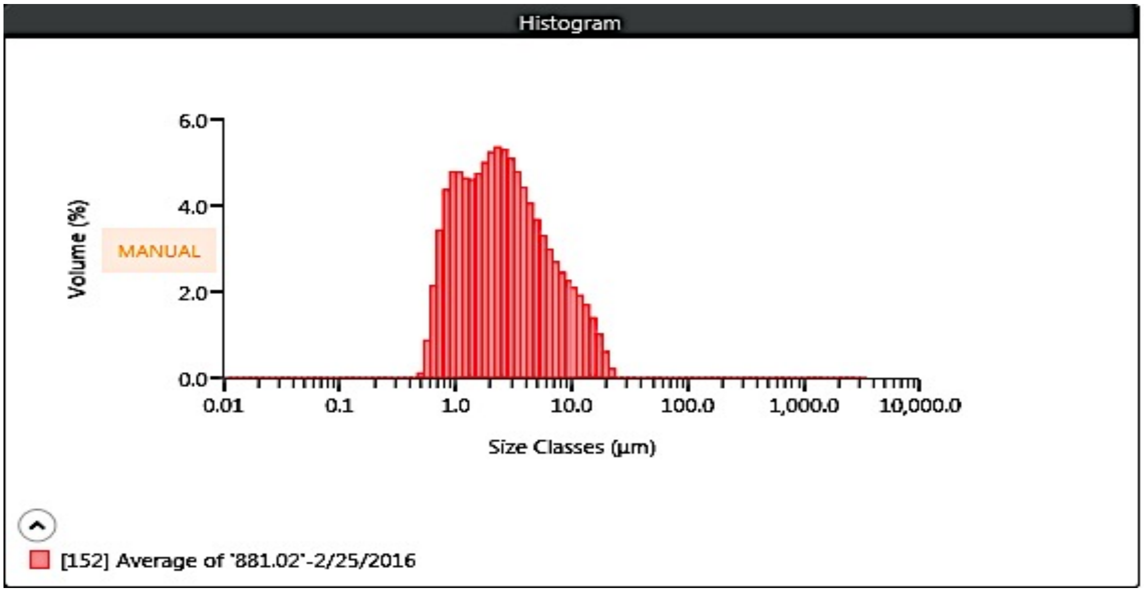

Result

Concentration	0.0009 %	**Span**	3.482
Uniformity	1.033	**Result Units**	Volume
Specific Surface Area	1243 m^2/kg	**Dv (10)**	0.849 µm
D [3,2]	1.86 µm	**Dv (50)**	2.42 µm
D [4,3]	3.85 µm	**Dv (90)**	9.26 µm
Volume Below (5) µm	76.28 %	**Mode**	2.32 µm
Volume Below (10) µm	91.33 %		
Volume Below (20) µm	**99.51 %**	**Volume In Range (500,1000) µm**	0.00 %
Volume In Range (5,20) µm	**23.24 %**	**Volume Above (1000) µm**	0.00 %
Volume In Range (20,200) µm	**0.49 %**		
Volume In Range (200,500) µm	0.00 %	**Volume In Range (1,2.5) µm**	35.36 %
Volume In Range (2.5,5) µm	24.85 %	**Volume In Range (5,10) µm**	15.06 %
D [3,3]	2.59 µm	**Kurtosis [3]**	4.148
Skew [3]	2.013		

Malvern Mastersizer 3000 LP Particle Size Analyzer

MAN 881.84

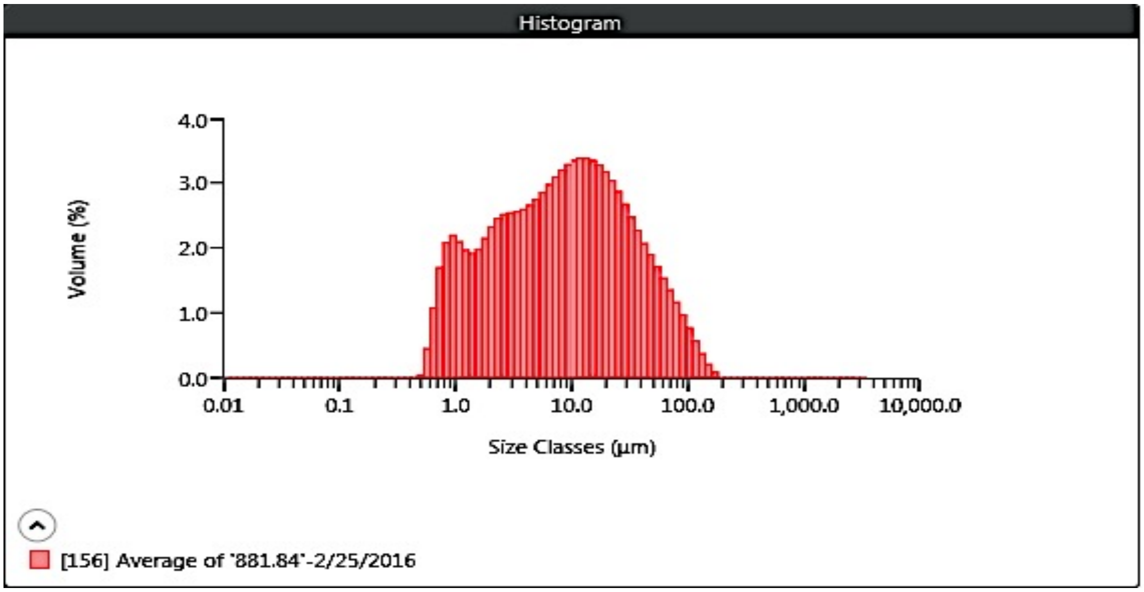

Result

Concentration	0.0046 %	**Span**	5.472
Uniformity	1.709	**Result Units**	Volume
Specific Surface Area	658.6 m²/kg	**Dv (10)**	1.15 µm
D [3,2]	3.50 µm	**Dv (50)**	8.50 µm
D [4,3]	17.9 µm	**Dv (90)**	47.7 µm
Volume Below (5) µm	37.42 %	**Mode**	12.7 µm
Volume Below (10) µm	54.19 %		
Volume Below (20) µm	72.37 %	**Volume In Range (500,1000) µm**	0.00 %
Volume In Range (5,20) µm	34.95 %	**Volume Above (1000) µm**	0.00 %
Volume In Range (20,200) µm	27.63 %		
Volume In Range (200,500) µm	0.0007 %	**Volume In Range (1,2.5) µm**	15.46 %
Volume In Range (2.5,5) µm	14.21 %	**Volume In Range (5,10) µm**	16.77 %
D [3,3]	7.96 µm	**Kurtosis [3]**	7.746
Skew [3]	2.545		

Malvern Mastersizer 3000 LP Particle Size Analyzer

MAN 882.03 REP

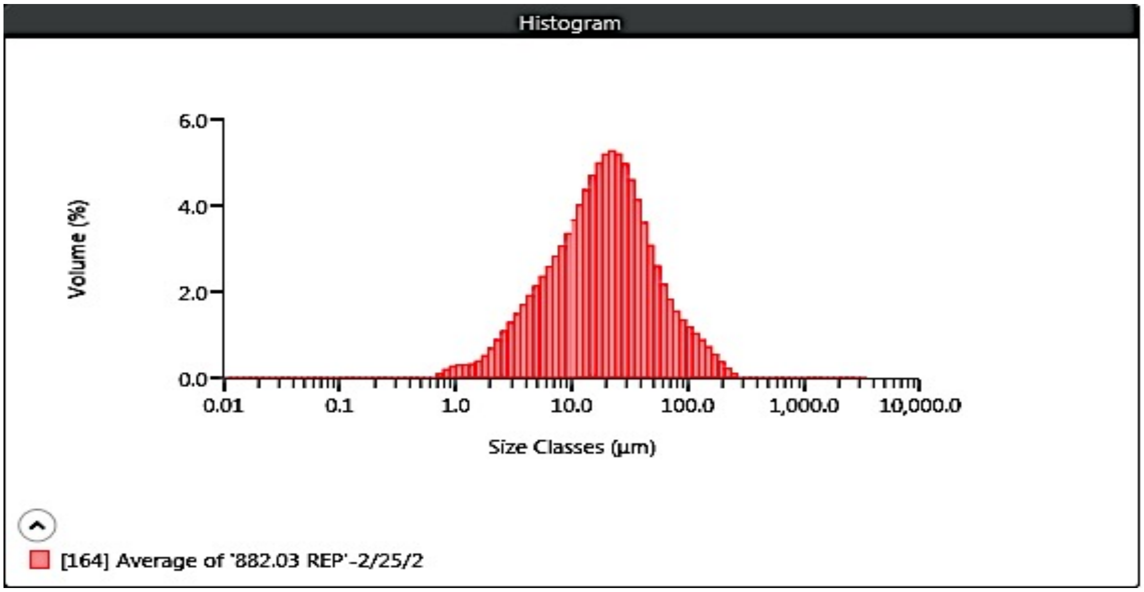

Result

Concentration	0.0032 %	**Span**	3.256
Uniformity	1.062	**Result Units**	Volume
Specific Surface Area	238.2 m²/kg	**Dv (10)**	4.18 µm
D [3,2]	9.69 µm	**Dv (50)**	18.9 µm
D [4,3]	29.4 µm	**Dv (90)**	65.8 µm
Volume Below (5) µm	12.82 %	**Mode**	22.6 µm
Volume Below (10) µm	28.07 %		
Volume Below (20) µm	52.24 %	**Volume In Range (500,1000) µm**	0.00 %
Volume In Range (5,20) µm	39.42 %	**Volume Above (1000) µm**	0.00000000000003 %
Volume In Range (20,200) µm	47.29 %		
Volume In Range (200,500) µm	0.47 %	**Volume In Range (1,2.5) µm**	3.63 %
Volume In Range (2.5,5) µm	8.62 %	**Volume In Range (5,10) µm**	15.25 %
D [3,3]	17.6 µm	**Kurtosis [3]**	9.341
Skew [3]	2.712		

Malvern Mastersizer 3000 LP Particle Size Analyzer

Replicate MAN 882.03 REP

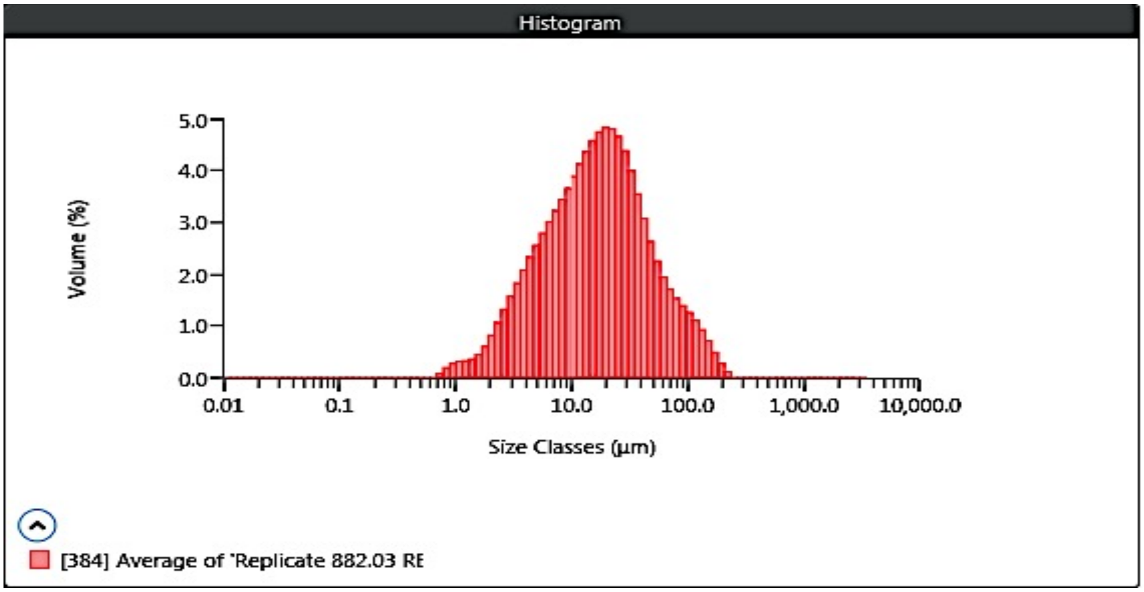

Result

Concentration	0.0030 %	**Span**	3.669
Uniformity	1.164	**Result Units**	Volume
Specific Surface Area	263.1 m^2/kg	**Dv (10)**	3.72 µm
D [3,2]	8.77 µm	**Dv (50)**	16.7 µm
D [4,3]	27.5 µm	**Dv (90)**	64.9 µm
Volume Below (5) µm	15.40 %	**Mode**	20.6 µm
Volume Below (10) µm	32.87 %		
Volume Below (20) µm	**56.83 %**	**Volume In Range (500,1000) µm**	0.00 %
Volume In Range (5,20) µm	**41.44 %**	**Volume Above (1000) µm**	0.00000000000001 %
Volume In Range (20,200) µm	**42.93 %**		
Volume In Range (200,500) µm	0.24 %	**Volume In Range (1,2.5) µm**	4.26 %
Volume In Range (2.5,5) µm	10.55 %	**Volume In Range (5,10) µm**	17.47 %
D [3,3]	15.9 µm	**Kurtosis [3]**	7.693
Skew [3]	2.538		

Malvern Mastersizer 3000 LP Particle Size Analyzer

MAN 883.70

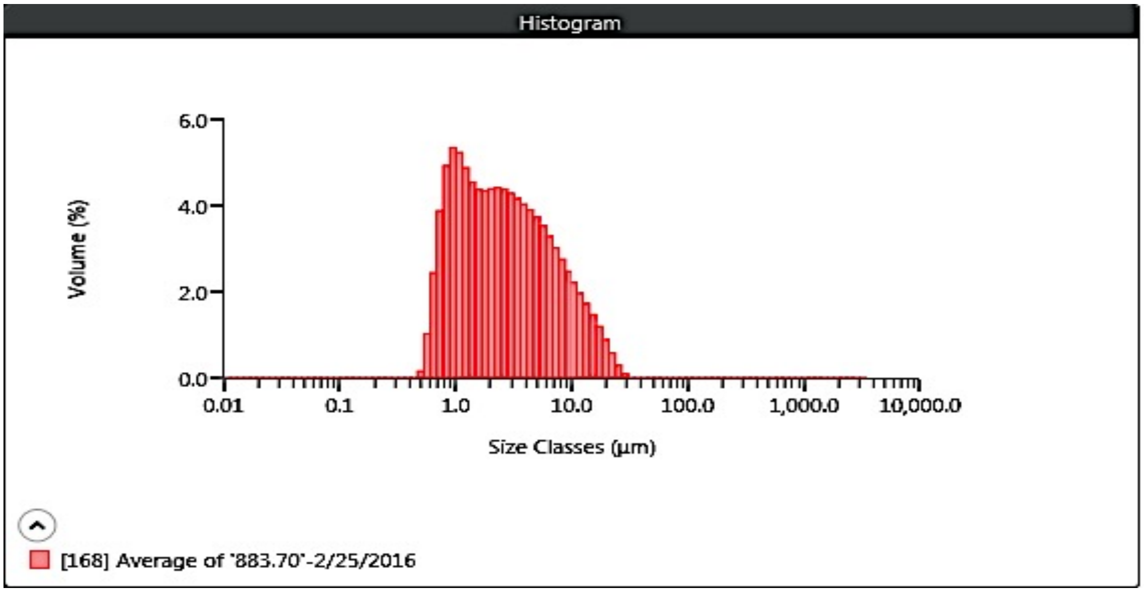

Result

Concentration	0.0012 %	**Span**	3.827
Uniformity	1.177	**Result Units**	Volume
Specific Surface Area	1272 m^2/kg	**Dv (10)**	0.819 µm
D [3,2]	1.81 µm	**Dv (50)**	2.42 µm
D [4,3]	4.14 µm	**Dv (90)**	10.1 µm
Volume Below (5) µm	73.36 %	**Mode**	0.965 µm
Volume Below (10) µm	89.86 %		
Volume Below (20) µm	98.63 %	**Volume In Range (500,1000) µm**	0.00 %
Volume In Range (5,20) µm	25.27 %	**Volume Above (1000) µm**	0.00 %
Volume In Range (20,200) µm	1.37 %		
Volume In Range (200,500) µm	0.00 %	**Volume In Range (1,2.5) µm**	32.94 %
Volume In Range (2.5,5) µm	22.24 %	**Volume In Range (5,10) µm**	16.51 %
D [3,3]	2.64 µm	**Kurtosis [3]**	5.123
Skew [3]	2.143		

Malvern Mastersizer 3000 LP Particle Size Analyzer

MAN 884.35

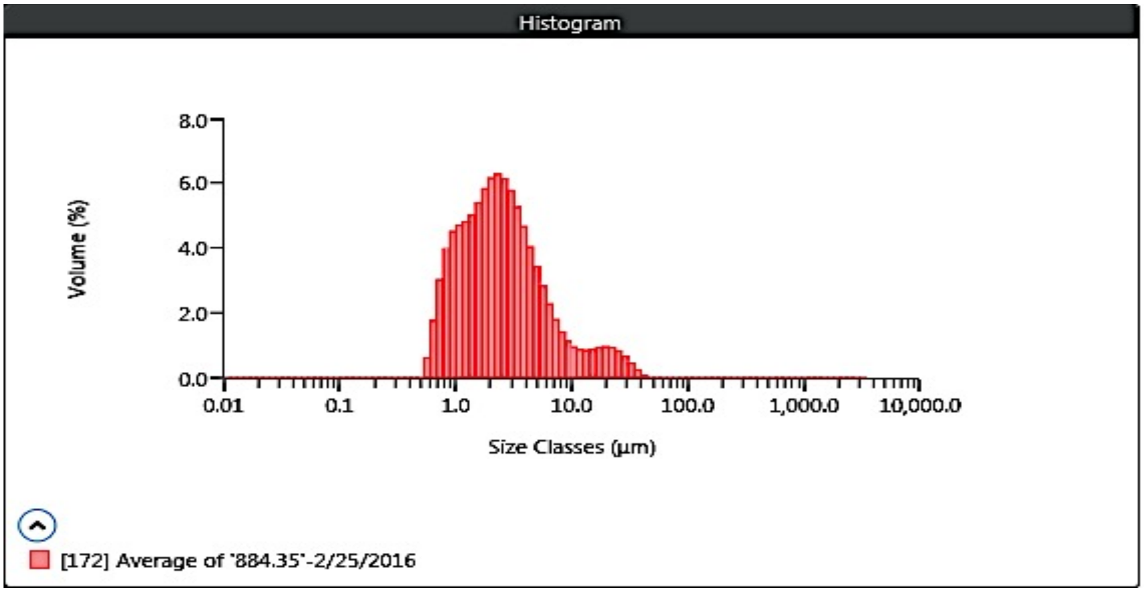

Result

Concentration	0.0023 %	**Span**	3.308
Uniformity	1.192	**Result Units**	Volume
Specific Surface Area	1238 m^2/kg	**Dv (10)**	0.886 µm
D [3,2]	1.86 µm	**Dv (50)**	2.31 µm
D [4,3]	4.12 µm	**Dv (90)**	8.51 µm
Volume Below (5) µm	80.80 %	**Mode**	2.26 µm
Volume Below (10) µm	91.45 %		
Volume Below (20) µm	**96.36 %**	**Volume In Range (500,1000) µm**	0.00 %
Volume In Range (5,20) µm	**15.56 %**	**Volume Above (1000) µm**	0.00000000000001 %
Volume In Range (20,200) µm	**3.64 %**		
Volume In Range (200,500) µm	0.00 %	**Volume In Range (1,2.5) µm**	39.64 %
Volume In Range (2.5,5) µm	26.83 %	**Volume In Range (5,10) µm**	10.66 %
D [3,3]	2.56 µm	**Kurtosis [3]**	12.422
Skew [3]	3.329		

Malvern Mastersizer 3000 LP Particle Size Analyzer

MAN 884.54

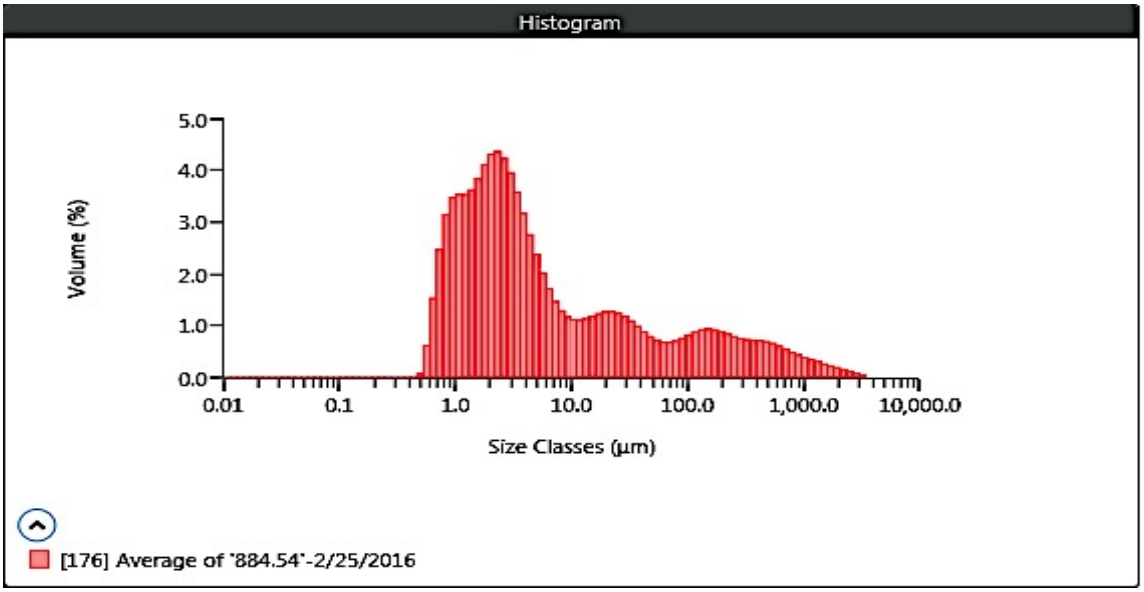

Result

Concentration	0.0032 %	**Span**	61.134
Uniformity	24.352	**Result Units**	Volume
Specific Surface Area	937.8 m^2/kg	**Dv (10)**	0.943 µm
D [3,2]	2.46 µm	**Dv (50)**	3.48 µm
D [4,3]	86.5 µm	**Dv (90)**	214 µm
Volume Below (5) µm	58.12 %	**Mode**	2.21 µm
Volume Below (10) µm	66.65 %		
Volume Below (20) µm	72.98 %	**Volume In Range (500,1000) µm**	2.98 %
Volume In Range (5,20) µm	14.86 %	**Volume Above (1000) µm**	2.04 %
Volume In Range (20,200) µm	16.56 %		
Volume In Range (200,500) µm	5.44 %	**Volume In Range (1,2.5) µm**	28.20 %
Volume In Range (2.5,5) µm	18.31 %	**Volume In Range (5,10) µm**	8.53 %
D [3,3]	7.34 µm	**Kurtosis [3]**	39.109
Skew [3]	5.594		

Malvern Mastersizer 3000 LP Particle Size Analyzer

MAN 884.76

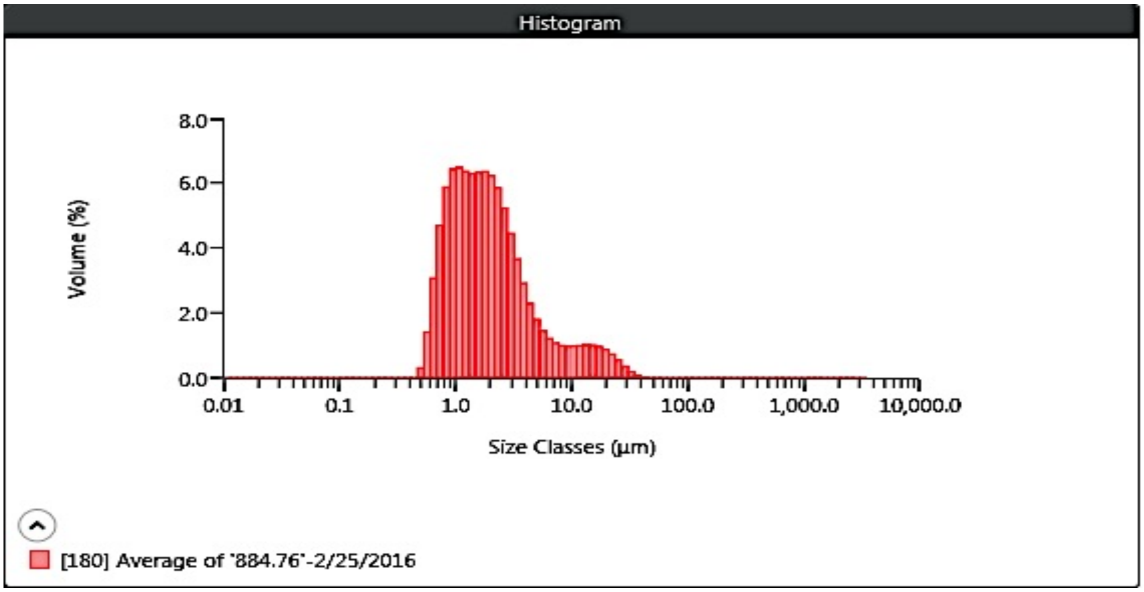

Result

Concentration	0.0009 %	**Span**	3.826
Uniformity	1.297	**Result Units**	Volume
Specific Surface Area	1525 m^2/kg	**Dv (10)**	0.775 μm
D [3,2]	1.51 μm	**Dv (50)**	1.73 μm
D [4,3]	3.34 μm	**Dv (90)**	7.41 μm
Volume Below (5) μm	85.94 %	**Mode**	1.03 μm
Volume Below (10) μm	92.33 %		
Volume Below (20) μm	97.66 %	**Volume In Range (500,1000) μm**	0.00 %
Volume In Range (5,20) μm	11.73 %	**Volume Above (1000) μm**	0.00 %
Volume In Range (20,200) μm	2.34 %		
Volume In Range (200,500) μm	0.00 %	**Volume In Range (1,2.5) μm**	45.00 %
Volume In Range (2.5,5) μm	18.54 %	**Volume In Range (5,10) μm**	6.40 %
D [3,3]	2.03 μm	**Kurtosis [3]**	13.665
Skew [3]	3.454		

Malvern Mastersizer 3000 LP Particle Size Analyzer

MAN 884.98

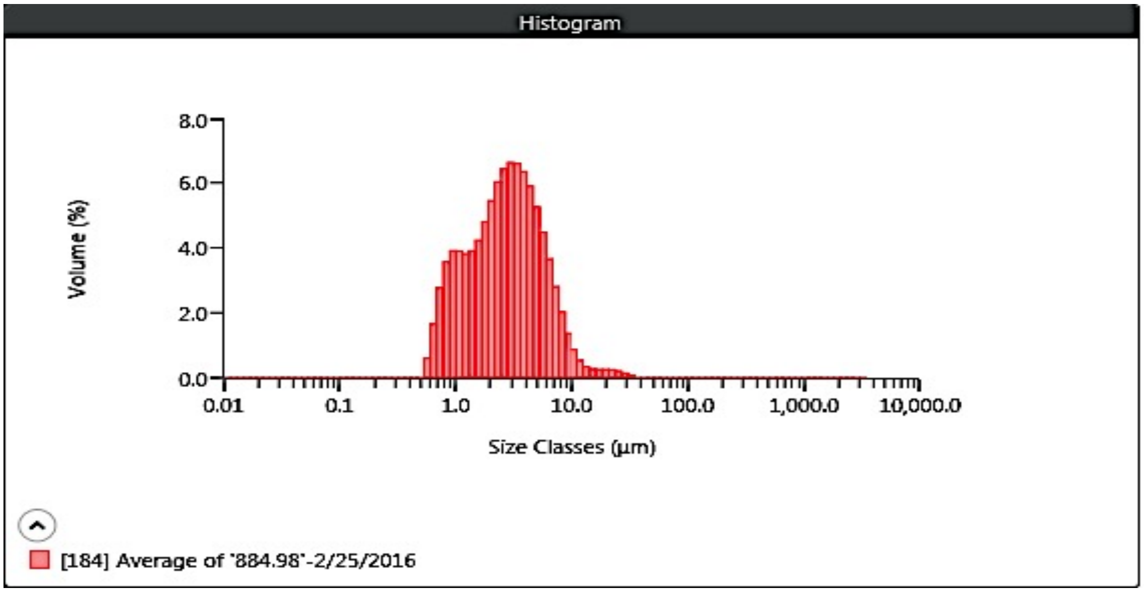

Result

Concentration	0.0037 %	**Span**	2.125
Uniformity	0.725	**Result Units**	Volume
Specific Surface Area	1160 m^2/kg	**Dv (10)**	0.911 µm
D [3,2]	1.99 µm	**Dv (50)**	2.68 µm
D [4,3]	3.48 µm	**Dv (90)**	6.60 µm
Volume Below (5) µm	80.66 %	**Mode**	3.07 µm
Volume Below (10) µm	96.86 %		
Volume Below (20) µm	99.19 %	**Volume In Range (500,1000) µm**	0.00 %
Volume In Range (5,20) µm	18.53 %	**Volume Above (1000) µm**	0.00 %
Volume In Range (20,200) µm	0.81 %		
Volume In Range (200,500) µm	0.00 %	**Volume In Range (1,2.5) µm**	33.70 %
Volume In Range (2.5,5) µm	34.11 %	**Volume In Range (5,10) µm**	16.20 %
D [3,3]	2.60 µm	**Kurtosis [3]**	20.721
Skew [3]	3.635		

Malvern Mastersizer 3000 LP Particle Size Analyzer

MAN 885.18

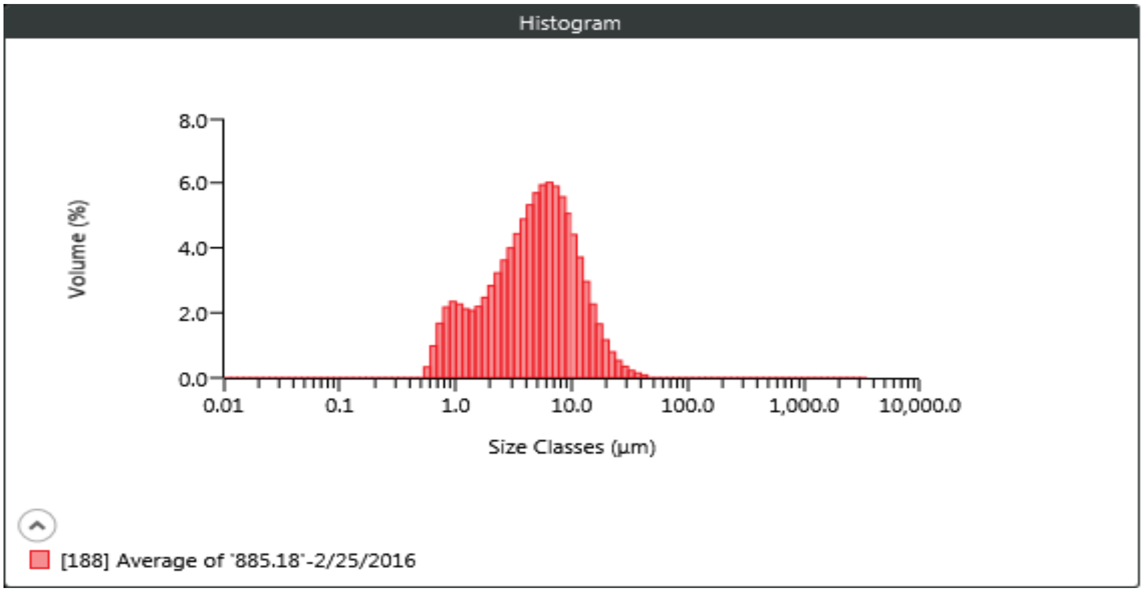

Result

Concentration	0.0041 %	**Span**	2.400
Uniformity	0.764	**Result Units**	Volume
Specific Surface Area	786.9 m^2/kg	**Dv (10)**	1.14 µm
D [3,2]	2.93 µm	**Dv (50)**	4.88 µm
D [4,3]	6.25 µm	**Dv (90)**	12.9 µm
Volume Below (5) µm	51.10 %	**Mode**	6.22 µm
Volume Below (10) µm	82.10 %		
Volume Below (20) µm	97.31 %	**Volume In Range (500,1000) µm**	0.00 %
Volume In Range (5,20) µm	46.22 %	**Volume Above (1000) µm**	0.00 %
Volume In Range (20,200) µm	2.69 %		
Volume In Range (200,500) µm	0.00 %	**Volume In Range (1,2.5) µm**	17.97 %
Volume In Range (2.5,5) µm	25.43 %	**Volume In Range (5,10) µm**	31.00 %
D [3,3]	4.40 µm	**Kurtosis [3]**	6.392
Skew [3]	2.025		

Malvern Mastersizer 3000 LP Particle Size Analyzer

MAN 885.42

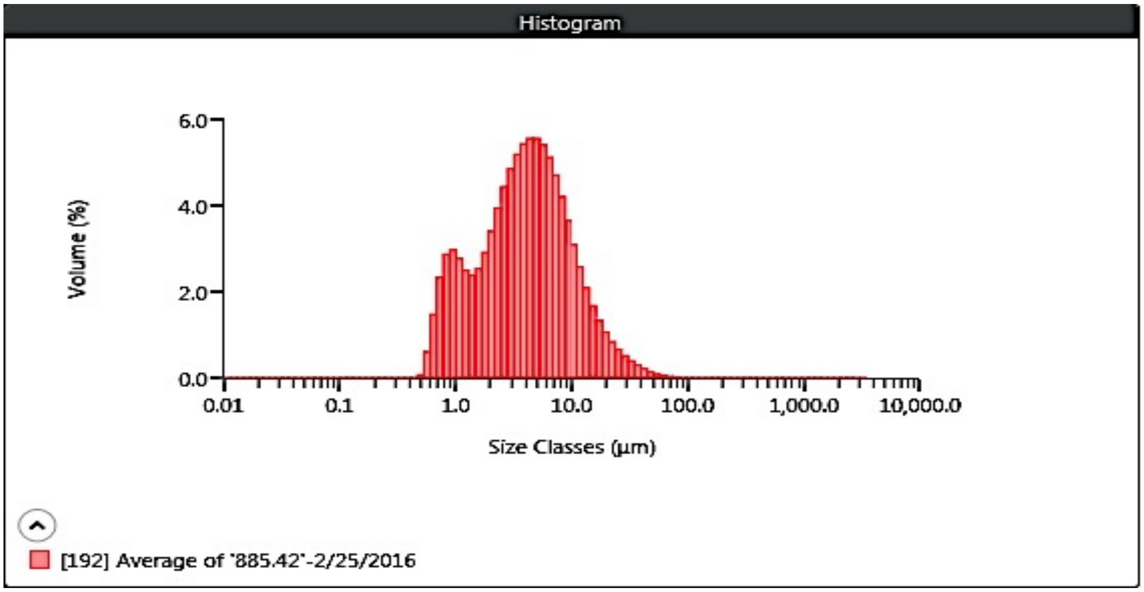

Result

Concentration	0.0025 %	**Span**	2.865
Uniformity	0.959	**Result Units**	Volume
Specific Surface Area	919.0 m^2/kg	**Dv (10)**	0.978 µm
D [3,2]	2.51 µm	**Dv (50)**	3.97 µm
D [4,3]	5.87 µm	**Dv (90)**	12.4 µm
Volume Below (5) µm	60.03 %	**Mode**	4.57 µm
Volume Below (10) µm	85.27 %		
Volume Below (20) µm	96.25 %	**Volume In Range (500,1000) µm**	0.00 %
Volume In Range (5,20) µm	36.22 %	**Volume Above (1000) µm**	0.00000000000001 %
Volume In Range (20,200) µm	3.75 %		
Volume In Range (200,500) µm	0.00 %	**Volume In Range (1,2.5) µm**	21.35 %
Volume In Range (2.5,5) µm	28.17 %	**Volume In Range (5,10) µm**	25.24 %
D [3,3]	3.81 µm	**Kurtosis [3]**	20.613
Skew [3]	3.596		

Malvern Mastersizer 3000 LP Particle Size Analyzer

MAN 885.62

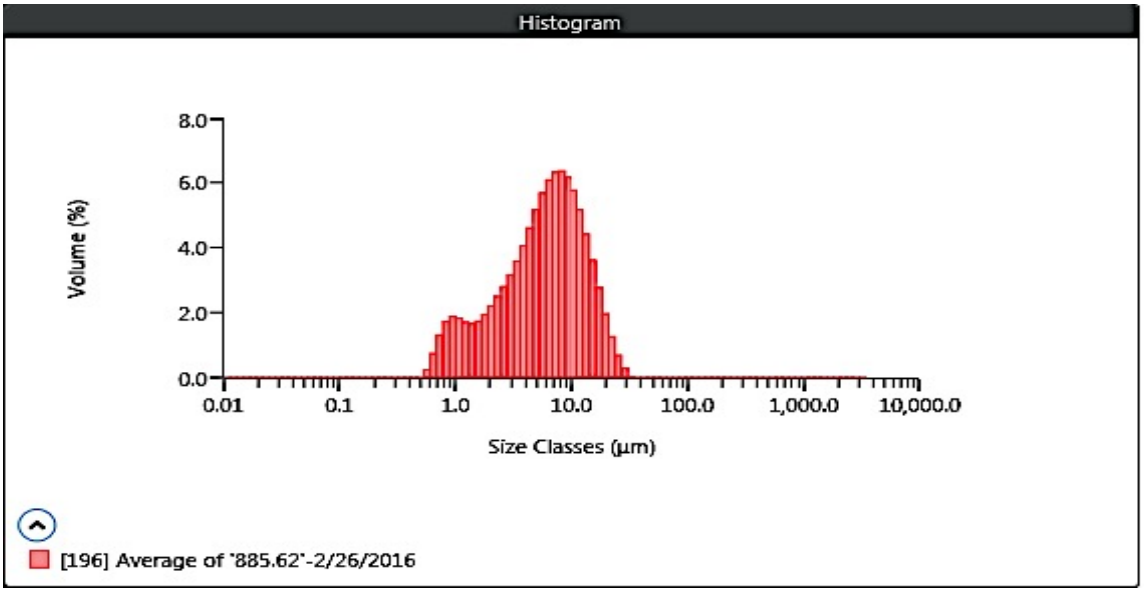

Result

Concentration	0.0049 %	**Span**	2.218
Uniformity	0.682	**Result Units**	Volume
Specific Surface Area	672.5 m^2/kg	**Dv (10)**	1.33 µm
D [3,2]	3.43 µm	**Dv (50)**	6.07 µm
D [4,3]	7.25 µm	**Dv (90)**	14.8 µm
Volume Below (5) µm	41.41 %	**Mode**	7.80 µm
Volume Below (10) µm	74.54 %		
Volume Below (20) µm	96.82 %	**Volume In Range (500,1000) µm**	0.00 %
Volume In Range (5,20) µm	55.41 %	**Volume Above (1000) µm**	0.00000000000001 %
Volume In Range (20,200) µm	3.18 %		
Volume In Range (200,500) µm	0.00 %	**Volume In Range (1,2.5) µm**	14.19 %
Volume In Range (2.5,5) µm	21.16 %	**Volume In Range (5,10) µm**	33.14 %
D [3,3]	5.26 µm	**Kurtosis [3]**	1.325
Skew [3]	1.155		

Malvern Mastersizer 3000 LP Particle Size Analyzer

MAN 885.80

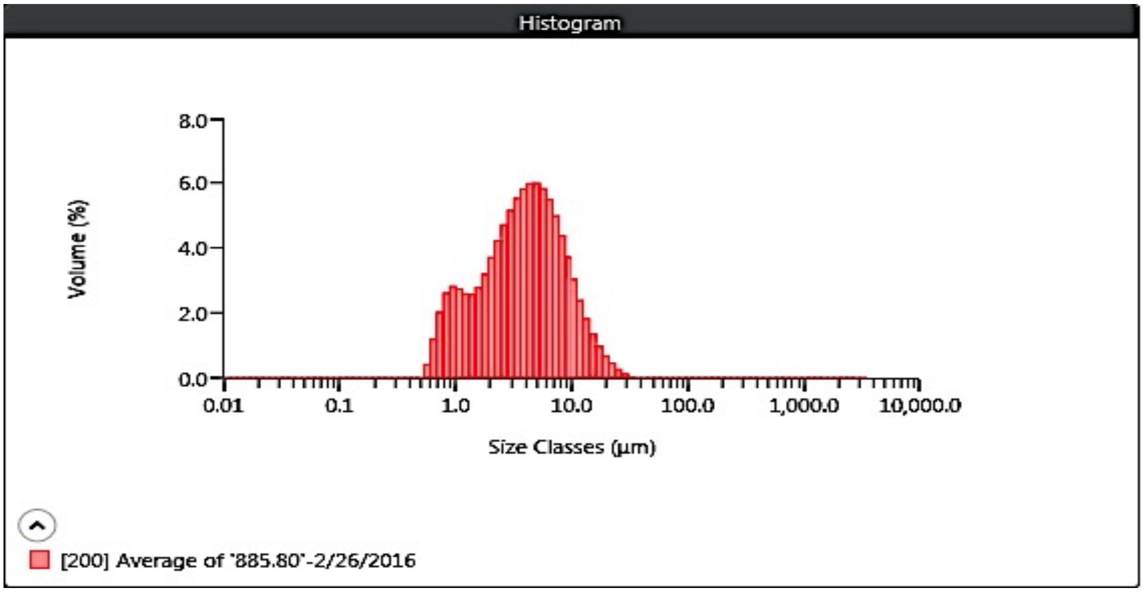

Result

Concentration	0.0037 %	**Span**	2.422
Uniformity	0.762	**Result Units**	Volume
Specific Surface Area	912.3 m²/kg	**Dv (10)**	1.03 µm
D [3,2]	2.53 µm	**Dv (50)**	3.84 µm
D [4,3]	4.99 µm	**Dv (90)**	10.3 µm
Volume Below (5) µm	62.41 %	**Mode**	4.62 µm
Volume Below (10) µm	89.22 %		
Volume Below (20) µm	98.84 %	**Volume In Range (500,1000) µm**	0.00 %
Volume In Range (5,20) µm	36.42 %	**Volume Above (1000) µm**	0.00 %
Volume In Range (20,200) µm	1.16 %		
Volume In Range (200,500) µm	0.00 %	**Volume In Range (1,2.5) µm**	22.86 %
Volume In Range (2.5,5) µm	30.30 %	**Volume In Range (5,10) µm**	26.81 %
D [3,3]	3.60 µm	**Kurtosis [3]**	4.962
Skew [3]	1.895		

Malvern Mastersizer 3000 LP Particle Size Analyzer

MAN 886.00

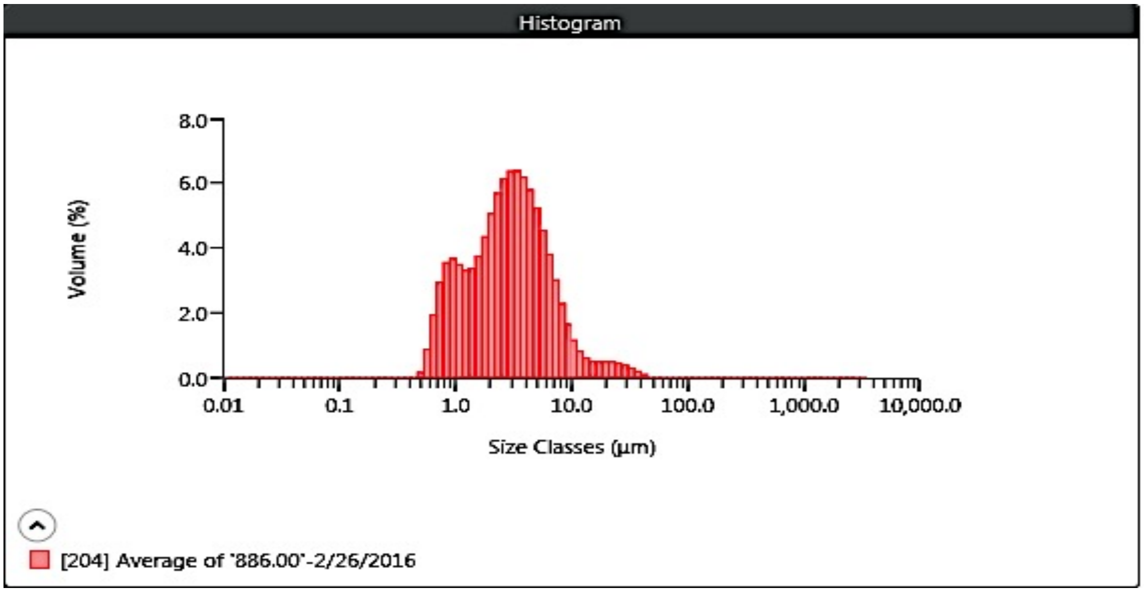

Result

Concentration	0.0047 %	**Span**	2.379
Uniformity	0.877	**Result Units**	Volume
Specific Surface Area	1135 m^2/kg	**Dv (10)**	0.888 μm
D [3,2]	2.03 μm	**Dv (50)**	2.84 μm
D [4,3]	4.08 μm	**Dv (90)**	7.63 μm
Volume Below (5) μm	76.92 %	**Mode**	3.15 μm
Volume Below (10) μm	94.09 %		
Volume Below (20) μm	**97.82 %**	**Volume In Range (500,1000) μm**	0.00 %
Volume In Range (5,20) μm	**20.89 %**	**Volume Above (1000) μm**	0.00000000000001 %
Volume In Range (20,200) μm	**2.18 %**		
Volume In Range (200,500) μm	0.00 %	**Volume In Range (1,2.5) μm**	30.42 %
Volume In Range (2.5,5) μm	33.08 %	**Volume In Range (5,10) μm**	17.16 %
D [3,3]	2.79 μm	**Kurtosis [3]**	19.907
Skew [3]	3.898		

<u>Malvern Mastersizer 3000 LP Particle Size Analyzer</u>

MAN 886.20

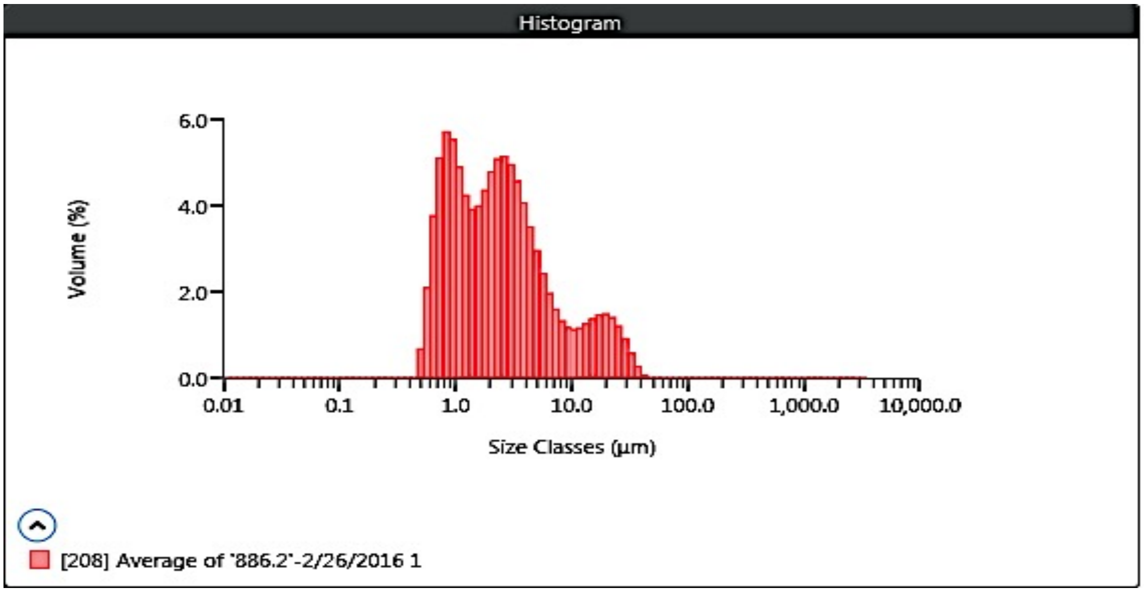

Result

Concentration	0.0018 %	**Span**	5.459
Uniformity	1.542	**Result Units**	Volume
Specific Surface Area	1416 m^2/kg	**Dv (10)**	0.737 µm
D [3,2]	1.63 µm	**Dv (50)**	2.18 µm
D [4,3]	4.53 µm	**Dv (90)**	12.6 µm
Volume Below (5) µm	78.42 %	**Mode**	0.847 µm
Volume Below (10) µm	87.92 %		
Volume Below (20) µm	**94.93 %**	**Volume In Range (500,1000) µm**	0.00 %
Volume In Range (5,20) µm	**16.50 %**	**Volume Above (1000) µm**	0.00 %
Volume In Range (20,200) µm	**5.07 %**		
Volume In Range (200,500) µm	0.00 %	**Volume In Range (1,2.5) µm**	32.22 %
Volume In Range (2.5,5) µm	22.95 %	**Volume In Range (5,10) µm**	9.50 %
D [3,3]	2.46 µm	**Kurtosis [3]**	7.518
Skew [3]	2.703		

Malvern Mastersizer 3000 LP Particle Size Analyzer

MAN 886.42

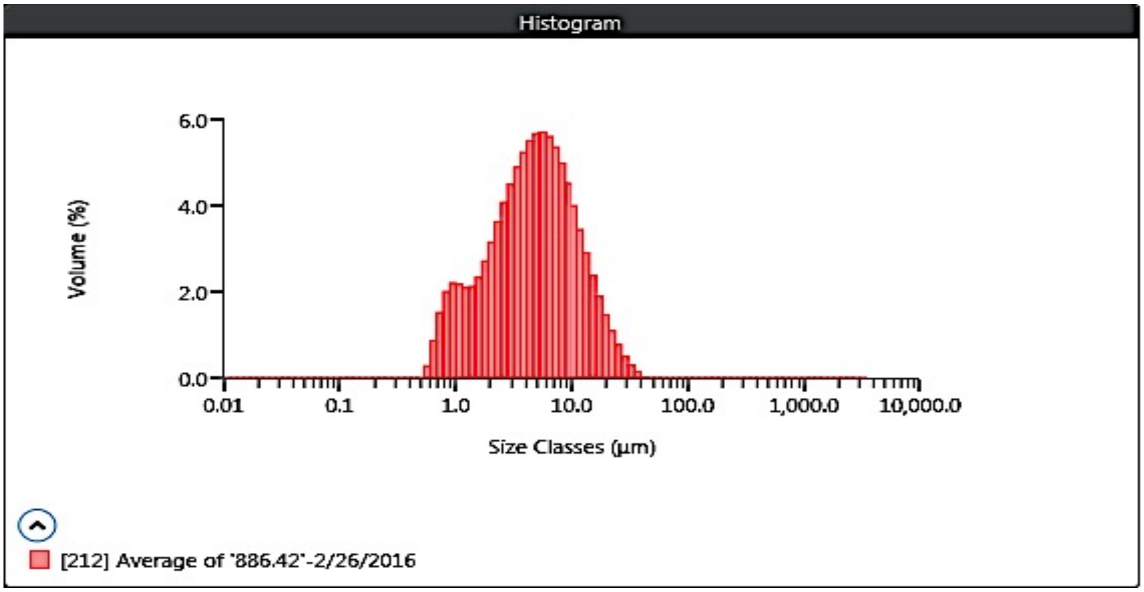

Result

Concentration	0.0053 %	**Span**	2.652
Uniformity	0.827	**Result Units**	Volume
Specific Surface Area	780.5 m^2/kg	**Dv (10)**	1.20 μm
D [3,2]	2.96 μm	**Dv (50)**	4.66 μm
D [4,3]	6.31 μm	**Dv (90)**	13.6 μm
Volume Below (5) μm	53.13 %	**Mode**	5.37 μm
Volume Below (10) μm	81.56 %		
Volume Below (20) μm	**96.51 %**	**Volume In Range (500,1000) μm**	0.00 %
Volume In Range (5,20) μm	**43.39 %**	**Volume Above (1000) μm**	0.00000000000001 %
Volume In Range (20,200) μm	**3.49 %**		
Volume In Range (200,500) μm	0.00 %	**Volume In Range (1,2.5) μm**	19.06 %
Volume In Range (2.5,5) μm	27.07 %	**Volume In Range (5,10) μm**	28.44 %
D [3,3]	4.39 μm	**Kurtosis [3]**	4.906
Skew [3]	1.937		

Malvern Mastersizer 3000 LP Particle Size Analyzer

MAN 886.62

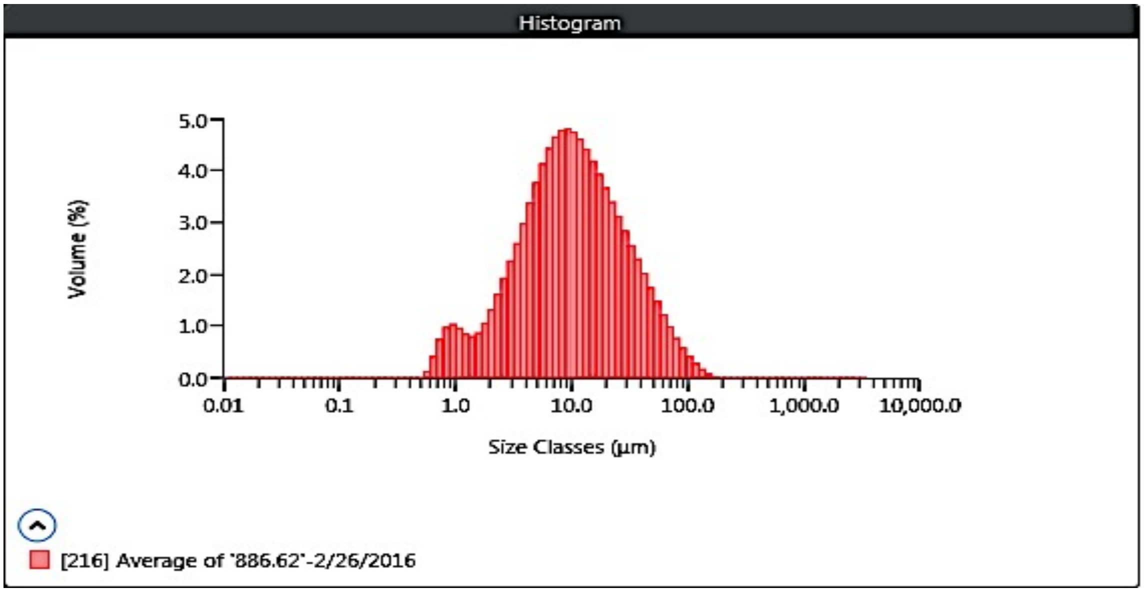

Result

Concentration	0.0035 %	**Span**	3.818
Uniformity	1.201	**Result Units**	Volume
Specific Surface Area	444.6 m^2/kg	**Dv (10)**	2.29 µm
D [3,2]	5.19 µm	**Dv (50)**	9.74 µm
D [4,3]	16.6 µm	**Dv (90)**	39.5 µm
Volume Below (5) µm	26.42 %	**Mode**	9.04 µm
Volume Below (10) µm	50.99 %		
Volume Below (20) µm	74.38 %	**Volume In Range (500,1000) µm**	0.00 %
Volume In Range (5,20) µm	47.96 %	**Volume Above (1000) µm**	0.00 %
Volume In Range (20,200) µm	25.62 %		
Volume In Range (200,500) µm	0.0002 %	**Volume In Range (1,2.5) µm**	7.83 %
Volume In Range (2.5,5) µm	15.24 %	**Volume In Range (5,10) µm**	24.57 %
D [3,3]	9.56 µm	**Kurtosis [3]**	9.658
Skew [3]	2.697		

Malvern Mastersizer 3000 LP Particle Size Analyzer

MAN 887.13

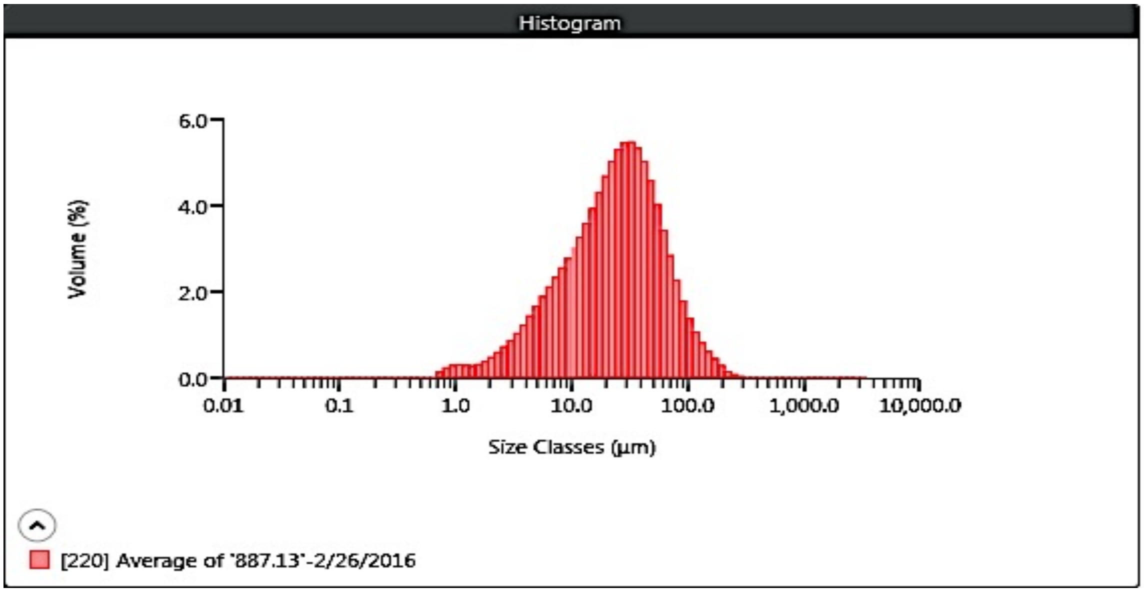

Result

Concentration	0.0033 %	**Span**	2.761
Uniformity	0.894	**Result Units**	Volume
Specific Surface Area	204.4 m^2/kg	**Dv (10)**	5.13 μm
D [3,2]	11.3 μm	**Dv (50)**	24.3 μm
D [4,3]	33.5 μm	**Dv (90)**	72.2 μm
Volume Below (5) μm	9.66 %	**Mode**	31.5 μm
Volume Below (10) μm	22.14 %		
Volume Below (20) μm	**42.46 %**	**Volume In Range (500,1000) μm**	0.00 %
Volume In Range (5,20) μm	**32.80 %**	**Volume Above (1000) μm**	0.00000000000003 %
Volume In Range (20,200) μm	**57.17 %**		
Volume In Range (200,500) μm	0.37 %	**Volume In Range (1,2.5) μm**	2.78 %
Volume In Range (2.5,5) μm	6.20 %	**Volume In Range (5,10) μm**	12.48 %
D [3,3]	21.3 μm	**Kurtosis [3]**	8.120
Skew [3]	2.343		

Malvern Mastersizer 3000 LP Particle Size Analyzer

MAN 887.62

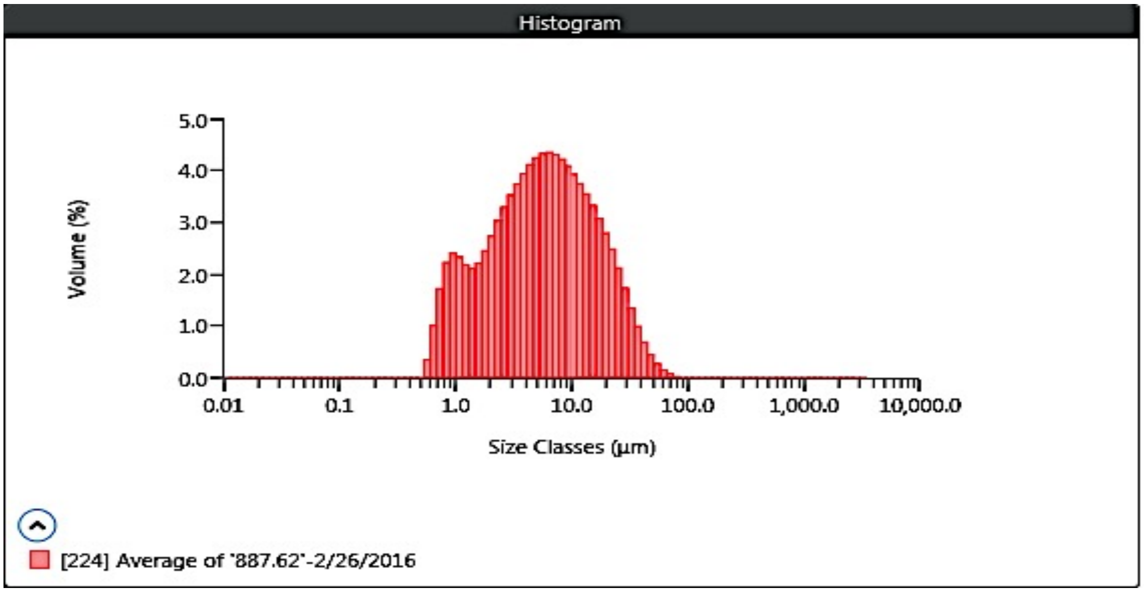

Result

Concentration	0.0027 %	**Span**	3.681
Uniformity	1.141	**Result Units**	Volume
Specific Surface Area	748.2 m^2/kg	**Dv (10)**	1.12 μm
D [3,2]	3.08 μm	**Dv (50)**	5.56 μm
D [4,3]	8.98 μm	**Dv (90)**	21.6 μm
Volume Below (5) μm	46.40 %	**Mode**	6.18 μm
Volume Below (10) μm	69.57 %		
Volume Below (20) μm	**88.36 %**	**Volume In Range (500,1000) μm**	0.00 %
Volume In Range (5,20) μm	**41.96 %**	**Volume Above (1000) μm**	0.00000000000001 %
Volume In Range (20,200) μm	**11.64 %**		
Volume In Range (200,500) μm	0.00 %	**Volume In Range (1,2.5) μm**	17.75 %
Volume In Range (2.5,5) μm	20.76 %	**Volume In Range (5,10) μm**	23.17 %
D [3,3]	5.33 μm	**Kurtosis [3]**	6.580
Skew [3]	2.220		

Malvern Mastersizer 3000 LP Particle Size Analyzer

MAN 887.78

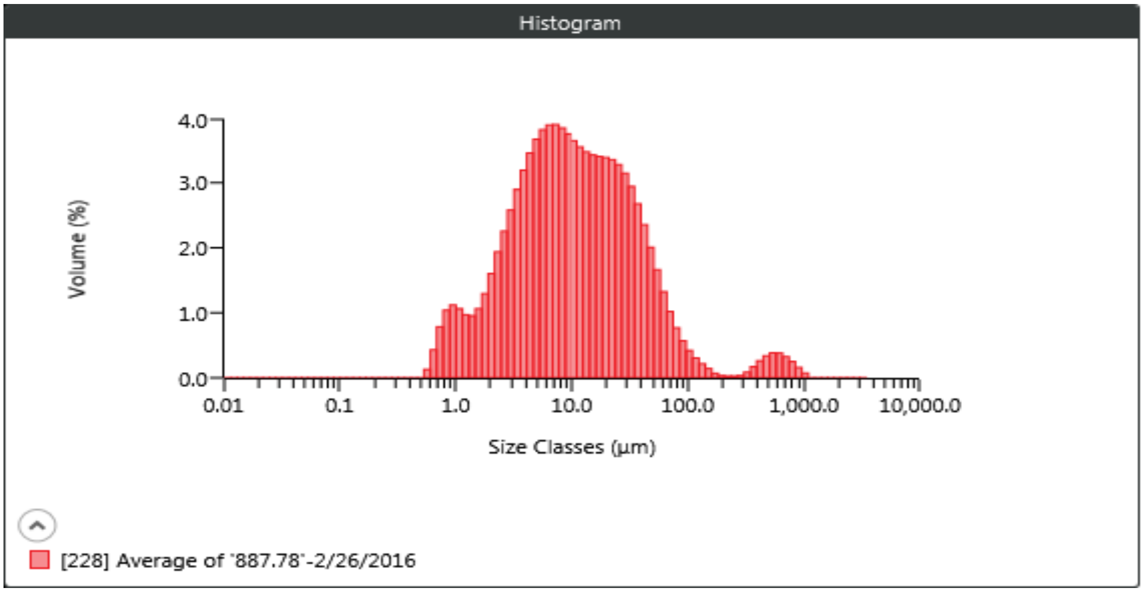

Result

Concentration	0.0040 %	**Span**	4.746
Uniformity	2.787	**Result Units**	Volume
Specific Surface Area	465.2 m²/kg	**Dv (10)**	2.05 µm
D [3,2]	4.96 µm	**Dv (50)**	9.87 µm
D [4,3]	32.1 µm	**Dv (90)**	48.9 µm
Volume Below (5) µm	29.46 %	**Mode**	6.78 µm
Volume Below (10) µm	50.36 %		
Volume Below (20) µm	**69.43 %**	**Volume In Range (500,1000) µm**	1.60 %
Volume In Range (5,20) µm	**39.97 %**	**Volume Above (1000) µm**	0.06 %
Volume In Range (20,200) µm	**28.03 %**		
Volume In Range (200,500) µm	0.88 %	**Volume In Range (1,2.5) µm**	9.41 %
Volume In Range (2.5,5) µm	16.45 %	**Volume In Range (5,10) µm**	20.90 %
D [3,3]	10.5 µm	**Kurtosis [3]**	45.351
Skew [3]	6.477		

Malvern Mastersizer 3000 LP Particle Size Analyzer

MAN 888.86

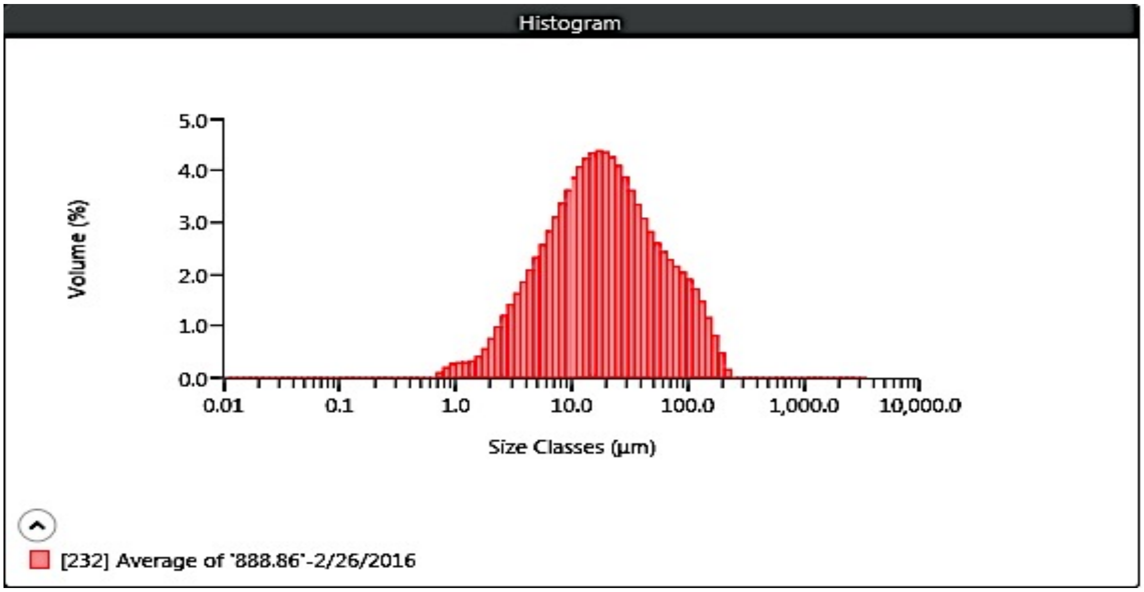

Result

Concentration	0.0034 %	Span	4.500
Uniformity	1.323	Result Units	Volume
Specific Surface Area	246.8 m^2/kg	Dv (10)	3.96 μm
D [3,2]	9.35 μm	Dv (50)	18.0 μm
D [4,3]	32.5 μm	Dv (90)	85.0 μm
Volume Below (5) μm	13.95 %	Mode	17.8 μm
Volume Below (10) μm	30.69 %		
Volume Below (20) μm	53.58 %	Volume In Range (500,1000) μm	0.00 %
Volume In Range (5,20) μm	39.63 %	Volume Above (1000) μm	0.00 %
Volume In Range (20,200) μm	46.05 %		
Volume In Range (200,500) μm	0.36 %	Volume In Range (1,2.5) μm	3.91 %
Volume In Range (2.5,5) μm	9.45 %	Volume In Range (5,10) μm	16.74 %
D [3,3]	17.9 μm	Kurtosis [3]	4.597
Skew [3]	2.100		

Malvern Mastersizer 3000 LP Particle Size Analyzer

MAN 888.90

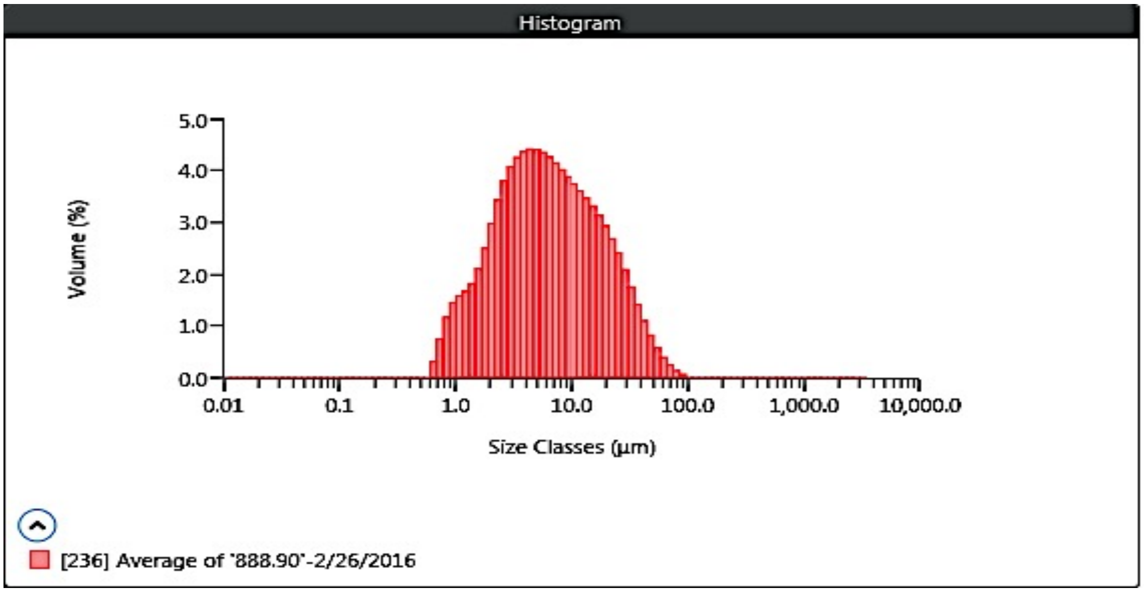

Result

Concentration	0.0073 %	Span	3.988
Uniformity	1.240	Result Units	Volume
Specific Surface Area	616.0 m^2/kg	Dv (10)	1.57 μm
D [3,2]	3.75 μm	Dv (50)	5.99 μm
D [4,3]	10.4 μm	Dv (90)	25.4 μm
Volume Below (5) μm	43.84 %	Mode	4.52 μm
Volume Below (10) μm	66.39 %		
Volume Below (20) μm	84.92 %	Volume In Range (500,1000) μm	0.00 %
Volume In Range (5,20) μm	41.09 %	Volume Above (1000) μm	0.00 %
Volume In Range (20,200) μm	15.08 %		
Volume In Range (200,500) μm	0.00 %	Volume In Range (1,2.5) μm	16.99 %
Volume In Range (2.5,5) μm	23.04 %	Volume In Range (5,10) μm	22.56 %
D [3,3]	6.19 μm	Kurtosis [3]	7.435
Skew [3]	2.395		

Malvern Mastersizer 3000 LP Particle Size Analyzer

MAN 888.90

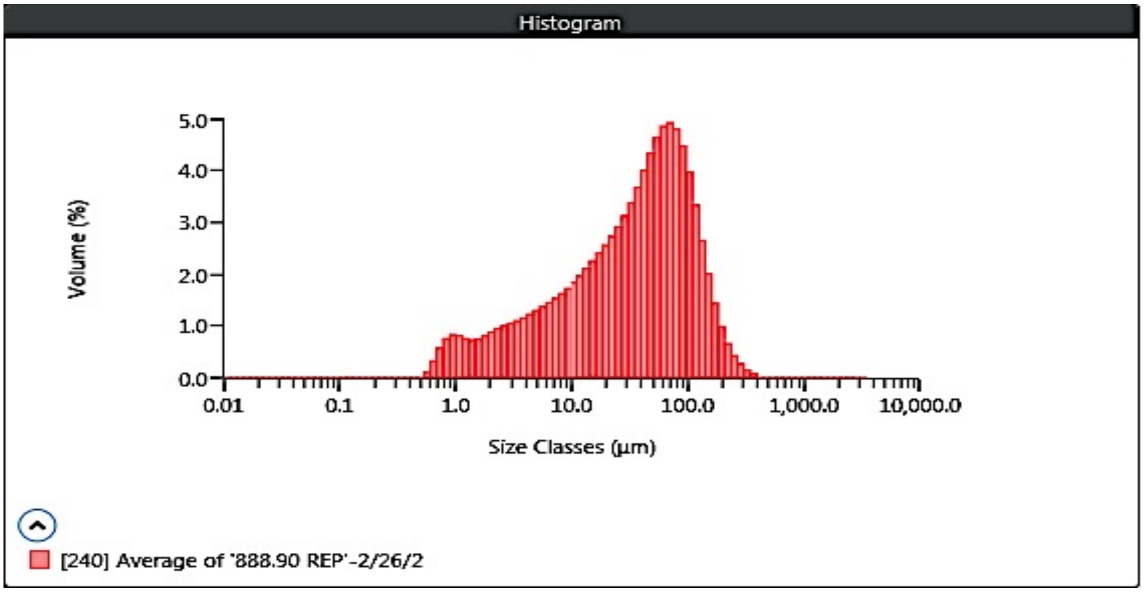

Result

Concentration	0.0044 %	Span	3.120
Uniformity	1.013	Result Units	Volume
Specific Surface Area	280.3 m²/kg	Dv (10)	3.01 µm
D [3,2]	8.23 µm	Dv (50)	37.6 µm
D [4,3]	52.2 µm	Dv (90)	120 µm
Volume Below (5) µm	14.68 %	Mode	70.0 µm
Volume Below (10) µm	23.01 %		
Volume Below (20) µm	34.77 %	Volume In Range (500,1000) µm	0.00 %
Volume In Range (5,20) µm	20.09 %	Volume Above (1000) µm	0.00000000000001 %
Volume In Range (20,200) µm	63.22 %		
Volume In Range (200,500) µm	2.01 %	Volume In Range (1,2.5) µm	5.87 %
Volume In Range (2.5,5) µm	6.16 %	Volume In Range (5,10) µm	8.33 %
D [3,3]	26.6 µm	Kurtosis [3]	4.177
Skew [3]	1.716		

<u>**Malvern Mastersizer 3000 LP Particle Size Analyzer**</u>

MAN 889.00

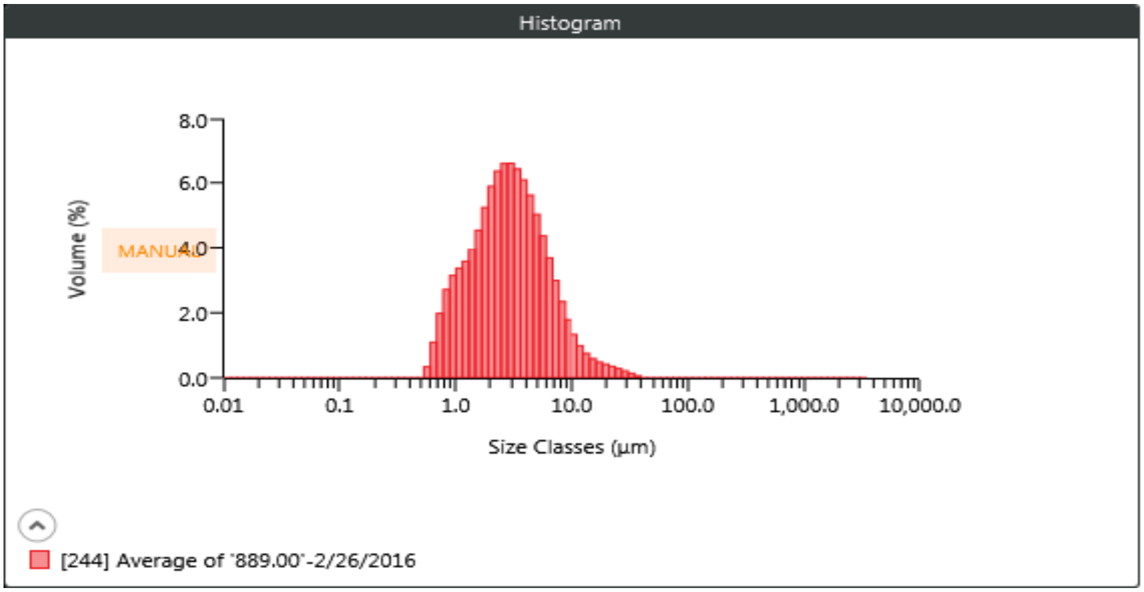

Result

Concentration	0.0051 %	**Span**	2.342
Uniformity	0.799	**Result Units**	Volume
Specific Surface Area	1065 m^2/kg	**Dv (10)**	1.02 µm
D [3,2]	2.17 µm	**Dv (50)**	2.80 µm
D [4,3]	3.90 µm	**Dv (90)**	7.57 µm
Volume Below (5) µm	77.50 %	**Mode**	2.77 µm
Volume Below (10) µm	94.52 %		
Volume Below (20) µm	**98.75 %**	**Volume In Range (500,1000) µm**	0.00 %
Volume In Range (5,20) µm	**21.25 %**	**Volume Above (1000) µm**	0.00 %
Volume In Range (20,200) µm	**1.25 %**		
Volume In Range (200,500) µm	0.00 %	**Volume In Range (1,2.5) µm**	34.59 %
Volume In Range (2.5,5) µm	33.34 %	**Volume In Range (5,10) µm**	17.02 %
D [3,3]	2.84 µm	**Kurtosis [3]**	17.081
Skew [3]	3.451		

Malvern Mastersizer 3000 LP Particle Size Analyzer

MAN 889.22

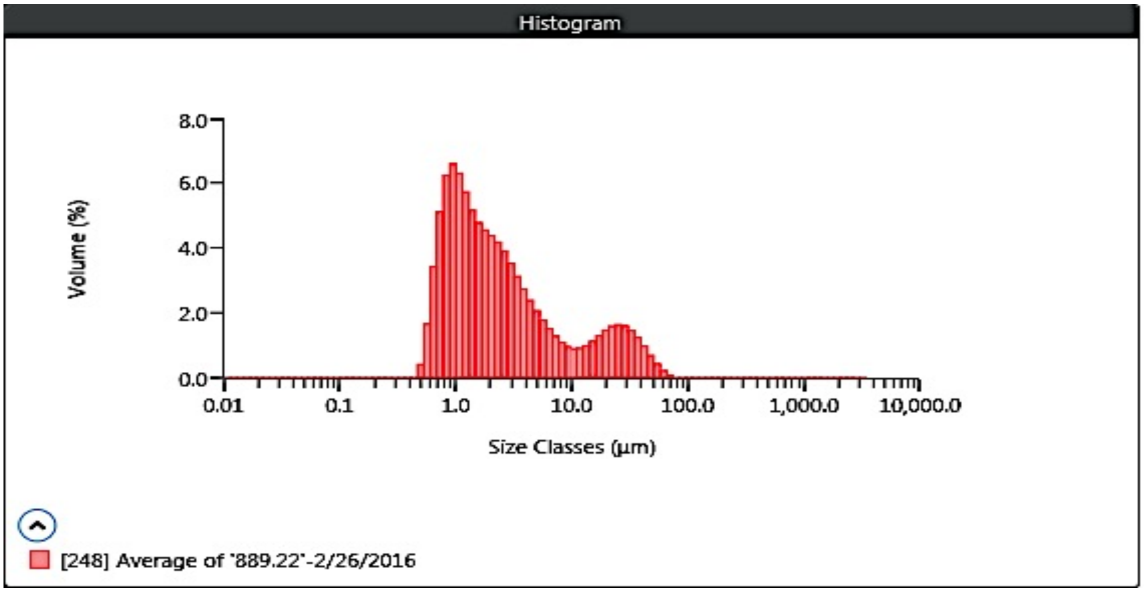

Result

Concentration	0.0011 %	**Span**	10.931
Uniformity	2.767	**Result Units**	Volume
Specific Surface Area	1448 m^2/kg	**Dv (10)**	0.755 µm
D [3,2]	1.59 µm	**Dv (50)**	1.86 µm
D [4,3]	6.23 µm	**Dv (90)**	21.1 µm
Volume Below (5) µm	76.05 %	**Mode**	0.935 µm
Volume Below (10) µm	83.46 %		
Volume Below (20) µm	**89.39 %**	**Volume In Range (500,1000) µm**	0.00 %
Volume In Range (5,20) µm	**13.34 %**	**Volume Above (1000) µm**	0.00000000000001 %
Volume In Range (20,200) µm	**10.61 %**		
Volume In Range (200,500) µm	0.00 %	**Volume In Range (1,2.5) µm**	35.86 %
Volume In Range (2.5,5) µm	16.15 %	**Volume In Range (5,10) µm**	7.41 %
D [3,3]	2.59 µm	**Kurtosis [3]**	7.546
Skew [3]	2.714		

<u>**Malvern Mastersizer 3000 LP Particle Size Analyzer**</u>

MAN 889.42

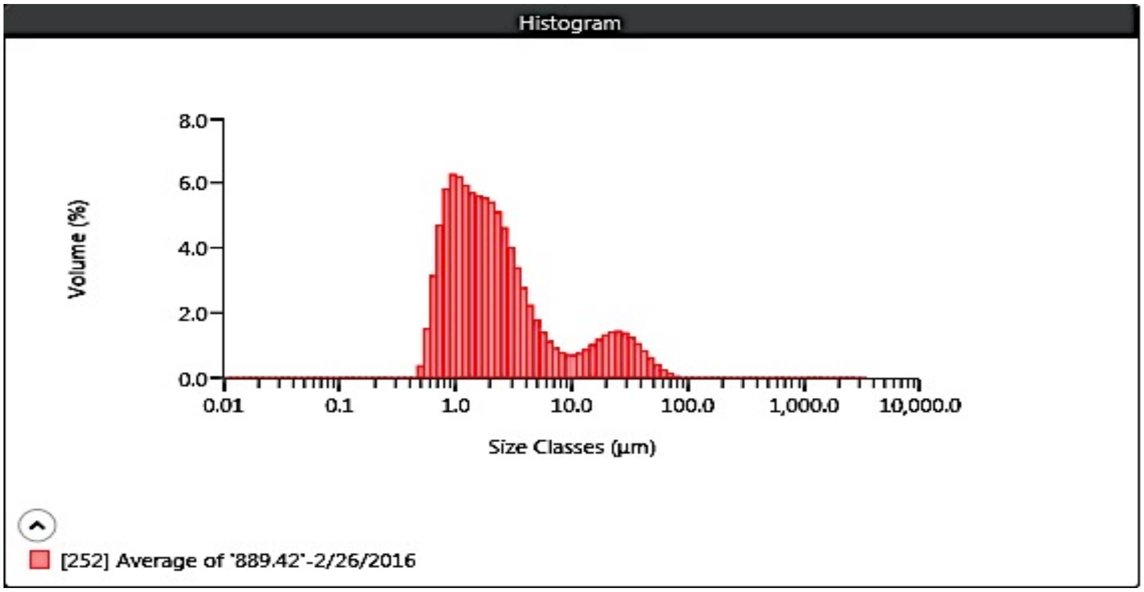

Result

Concentration	0.0037 %	**Span**	9.865
Uniformity	2.531	**Result Units**	Volume
Specific Surface Area	1454 m^2/kg	**Dv (10)**	0.771 μm
D [3,2]	1.59 μm	**Dv (50)**	1.83 μm
D [4,3]	5.74 μm	**Dv (90)**	18.8 μm
Volume Below (5) μm	79.93 %	**Mode**	0.975 μm
Volume Below (10) μm	85.48 %		
Volume Below (20) μm	**90.62 %**	**Volume In Range (500,1000) μm**	0.00 %
Volume In Range (5,20) μm	**10.69 %**	**Volume Above (1000) μm**	0.00 %
Volume In Range (20,200) μm	**9.38 %**		
Volume In Range (200,500) μm	0.00 %	**Volume In Range (1,2.5) μm**	40.42 %
Volume In Range (2.5,5) μm	17.13 %	**Volume In Range (5,10) μm**	5.55 %
D [3,3]	2.45 μm	**Kurtosis [3]**	10.623
Skew [3]	3.111		

Malvern Mastersizer 3000 LP Particle Size Analyzer

MAN 889.61

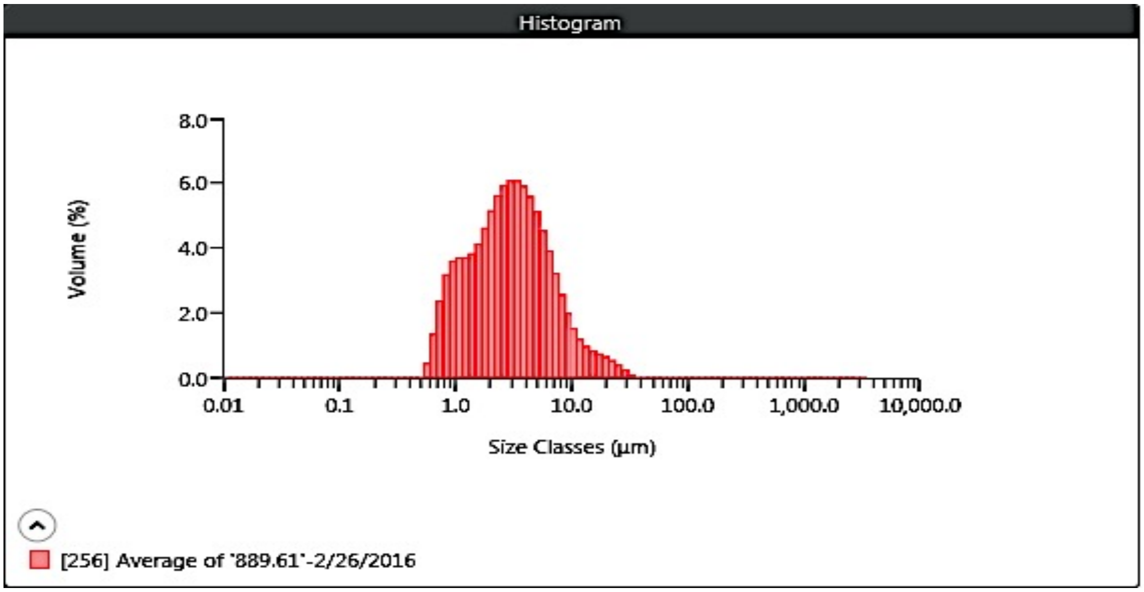

Result

Concentration	0.0035 %	**Span**	2.545
Uniformity	0.857	**Result Units**	Volume
Specific Surface Area	1080 m^2/kg	**Dv (10)**	0.959 µm
D [3,2]	2.14 µm	**Dv (50)**	2.89 µm
D [4,3]	4.11 µm	**Dv (90)**	8.30 µm
Volume Below (5) µm	74.99 %	**Mode**	3.10 µm
Volume Below (10) µm	93.04 %		
Volume Below (20) µm	98.45 %	**Volume In Range (500,1000) µm**	0.00 %
Volume In Range (5,20) µm	23.46 %	**Volume Above (1000) µm**	0.00 %
Volume In Range (20,200) µm	1.55 %		
Volume In Range (200,500) µm	0.00 %	**Volume In Range (1,2.5) µm**	32.05 %
Volume In Range (2.5,5) µm	31.75 %	**Volume In Range (5,10) µm**	18.05 %
D [3,3]	2.90 µm	**Kurtosis [3]**	10.931
Skew [3]	2.881		

Malvern Mastersizer 3000 LP Particle Size Analyzer

MAN 889.69

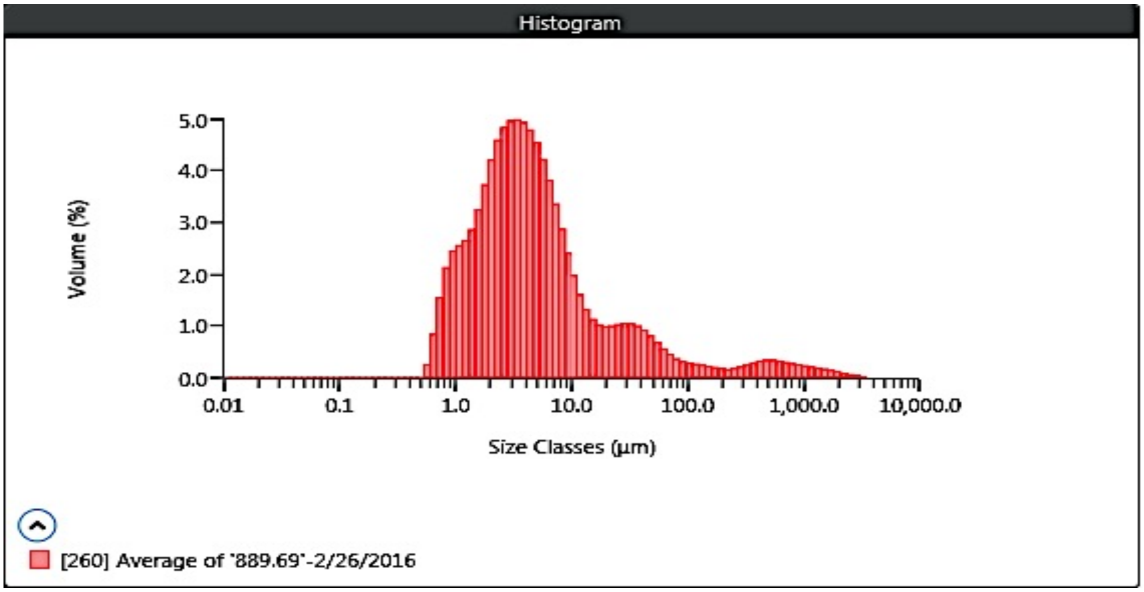

Result

Concentration	0.0039 %	Span	9.804
Uniformity	11.194	Result Units	Volume
Specific Surface Area	831.5 m^2/kg	Dv (10)	1.14 µm
D [3,2]	2.78 µm	Dv (50)	3.94 µm
D [4,3]	46.2 µm	Dv (90)	39.8 µm
Volume Below (5) µm	58.78 %	Mode	3.26 µm
Volume Below (10) µm	77.16 %		
Volume Below (20) µm	84.51 %	Volume In Range (500,1000) µm	1.59 %
Volume In Range (5,20) µm	25.73 %	Volume Above (1000) µm	1.21 %
Volume In Range (20,200) µm	10.96 %		
Volume In Range (200,500) µm	1.72 %	Volume In Range (1,2.5) µm	24.95 %
Volume In Range (2.5,5) µm	26.44 %	Volume In Range (5,10) µm	18.38 %
D [3,3]	5.46 µm	Kurtosis [3]	71.937
Skew [3]	7.680		

Malvern Mastersizer 3000 LP Particle Size Analyzer

MAN 889.93

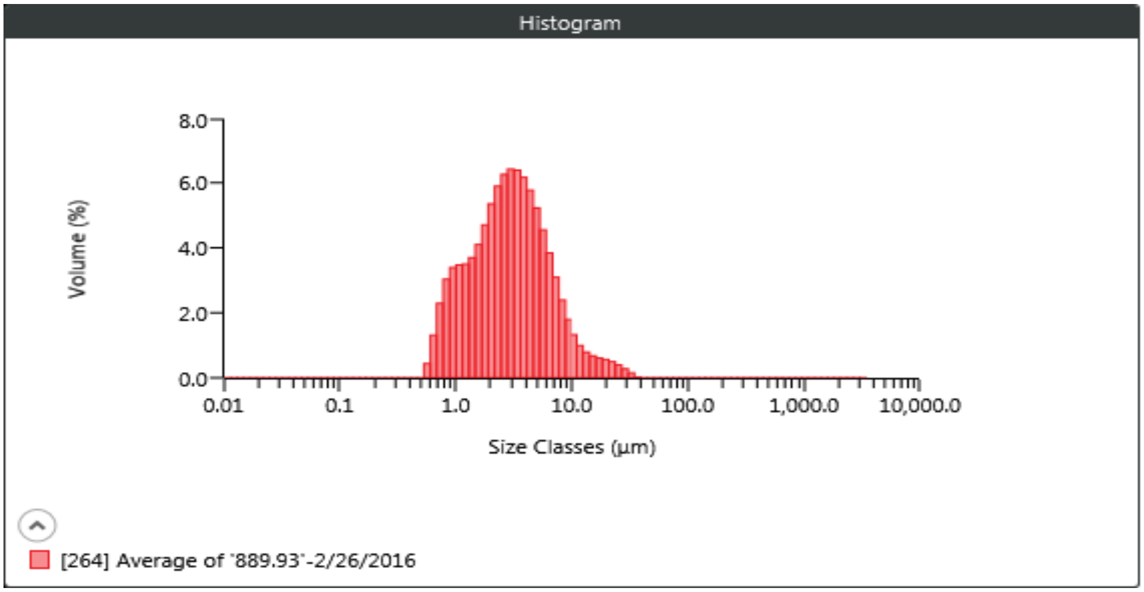

Result

Concentration	0.0028 %	**Span**	2.392
Uniformity	0.826	**Result Units**	Volume
Specific Surface Area	1074 m^2/kg	**Dv (10)**	0.972 µm
D [3,2]	2.15 µm	**Dv (50)**	2.88 µm
D [4,3]	4.04 µm	**Dv (90)**	7.85 µm
Volume Below (5) µm	76.25 %	**Mode**	3.06 µm
Volume Below (10) µm	93.83 %		
Volume Below (20) µm	98.39 %	**Volume In Range (500,1000) µm**	0.00 %
Volume In Range (5,20) µm	22.14 %	**Volume Above (1000) µm**	0.00 %
Volume In Range (20,200) µm	1.61 %		
Volume In Range (200,500) µm	0.00 %	**Volume In Range (1,2.5) µm**	32.25 %
Volume In Range (2.5,5) µm	33.24 %	**Volume In Range (5,10) µm**	17.58 %
D [3,3]	2.88 µm	**Kurtosis [3]**	13.916
Skew [3]	3.220		

Malvern Mastersizer 3000 LP Particle Size Analyzer

MAN 890.12

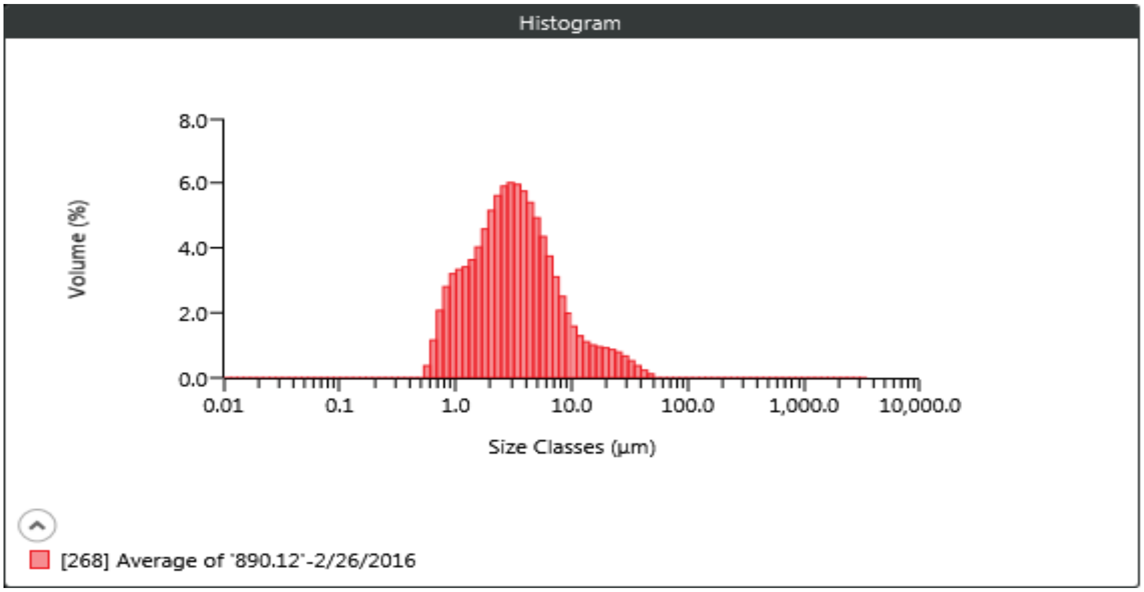

Result

Concentration	0.0038 %	**Span**	3.057
Uniformity	1.066	**Result Units**	Volume
Specific Surface Area	1022 m^2/kg	**Dv (10)**	1.00 µm
D [3,2]	2.26 µm	**Dv (50)**	3.02 µm
D [4,3]	4.95 µm	**Dv (90)**	10.2 µm
Volume Below (5) µm	72.17 %	**Mode**	2.99 µm
Volume Below (10) µm	89.70 %		
Volume Below (20) µm	**95.98 %**	**Volume In Range (500,1000) µm**	0.00 %
Volume In Range (5,20) µm	**23.81 %**	**Volume Above (1000) µm**	0.00 %
Volume In Range (20,200) µm	**4.02 %**		
Volume In Range (200,500) µm	0.00 %	**Volume In Range (1,2.5) µm**	31.18 %
Volume In Range (2.5,5) µm	31.10 %	**Volume In Range (5,10) µm**	17.52 %
D [3,3]	3.18 µm	**Kurtosis [3]**	13.278
Skew [3]	3.312		

Malvern Mastersizer 3000 LP Particle Size Analyzer

MAN 891.00

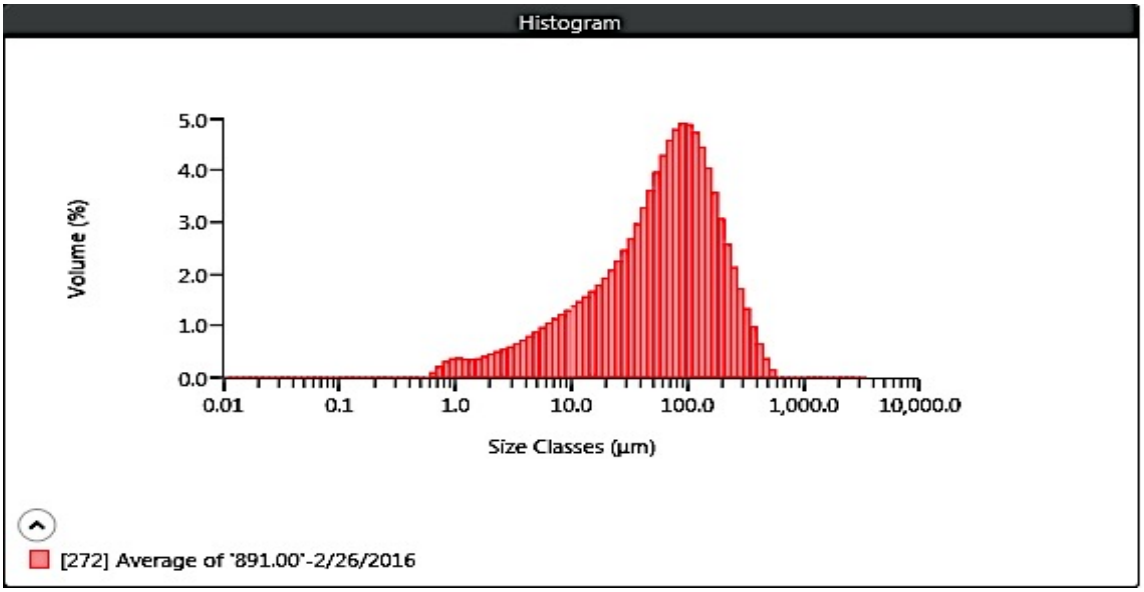

Result

Concentration	0.0045 %	**Span**	3.130
Uniformity	0.985	**Result Units**	Volume
Specific Surface Area	155.9 m^2/kg	**Dv (10)**	6.76 µm
D [3,2]	14.8 µm	**Dv (50)**	65.0 µm
D [4,3]	90.6 µm	**Dv (90)**	210 µm
Volume Below (5) µm	7.66 %	**Mode**	96.6 µm
Volume Below (10) µm	13.74 %		
Volume Below (20) µm	22.46 %	**Volume In Range (500,1000) µm**	0.24 %
Volume In Range (5,20) µm	14.80 %	**Volume Above (1000) µm**	0.00000000005 %
Volume In Range (20,200) µm	66.35 %		
Volume In Range (200,500) µm	10.95 %	**Volume In Range (1,2.5) µm**	2.90 %
Volume In Range (2.5,5) µm	3.75 %	**Volume In Range (5,10) µm**	6.08 %
D [3,3]	48.5 µm	**Kurtosis [3]**	3.389
Skew [3]	1.690		

Malvern Mastersizer 3000 LP Particle Size Analyzer

MAN 891.37

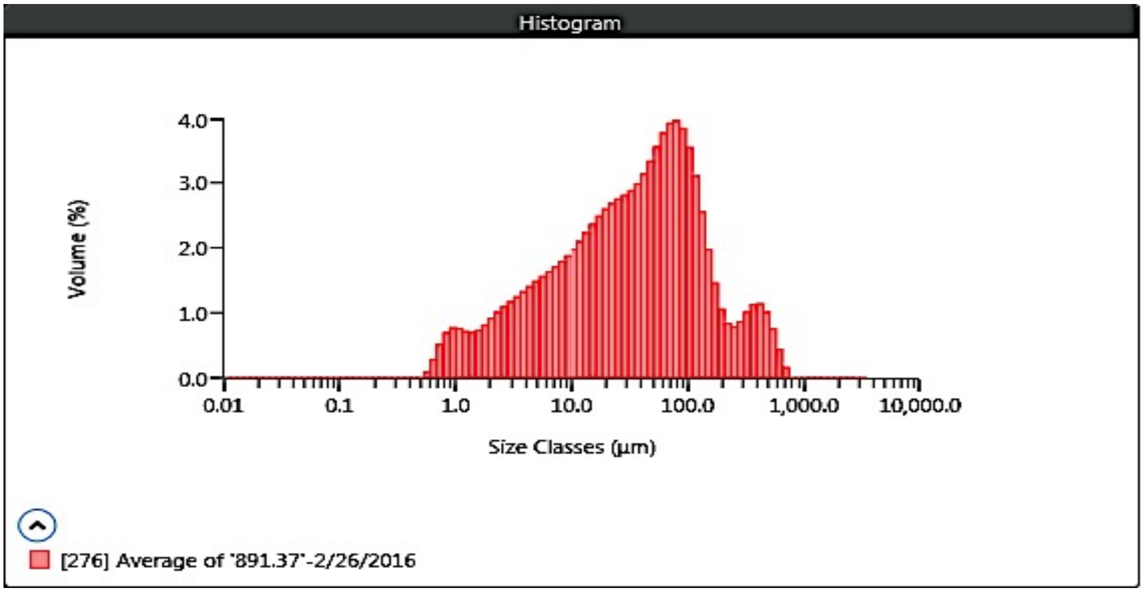

Result

Concentration	0.0028 %	Span	4.694
Uniformity	1.705	Result Units	Volume
Specific Surface Area	278.2 m^2/kg	Dv (10)	3.03 µm
D [3,2]	8.30 µm	Dv (50)	36.2 µm
D [4,3]	74.7 µm	Dv (90)	173 µm
Volume Below (5) µm	15.28 %	Mode	78.4 µm
Volume Below (10) µm	24.55 %		
Volume Below (20) µm	37.00 %	Volume In Range (500,1000) µm	1.60 %
Volume In Range (5,20) µm	21.73 %	Volume Above (1000) µm	0.0000000001 %
Volume In Range (20,200) µm	54.42 %		
Volume In Range (200,500) µm	6.98 %	Volume In Range (1,2.5) µm	5.87 %
Volume In Range (2.5,5) µm	6.99 %	Volume In Range (5,10) µm	9.28 %
D [3,3]	29.0 µm	Kurtosis [3]	8.695
Skew [3]	2.812		

Malvern Mastersizer 3000 LP Particle Size Analyzer

MAN 891.75

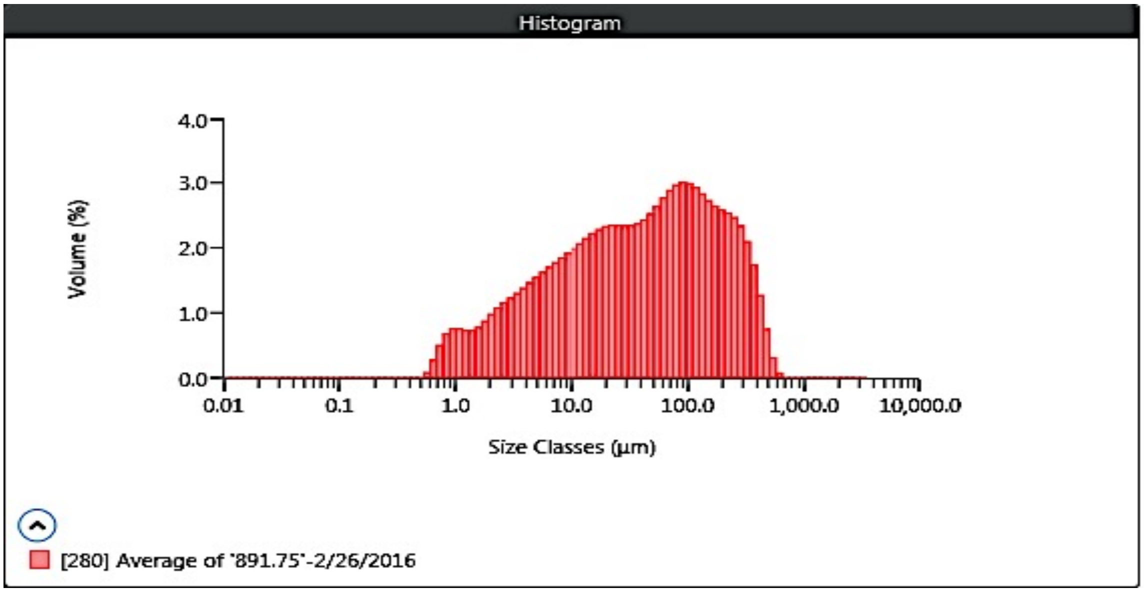

Result

Concentration	0.0051 %	**Span**	6.301
Uniformity	1.872	**Result Units**	Volume
Specific Surface Area	278.7 m^2/kg	**Dv (10)**	2.94 µm
D [3,2]	8.28 µm	**Dv (50)**	39.8 µm
D [4,3]	87.5 µm	**Dv (90)**	254 µm
Volume Below (5) µm	15.80 %	**Mode**	94.6 µm
Volume Below (10) µm	25.40 %		
Volume Below (20) µm	37.23 %	**Volume In Range (500,1000) µm**	0.57 %
Volume In Range (5,20) µm	21.43 %	**Volume Above (1000) µm**	0.00000000003 %
Volume In Range (20,200) µm	48.01 %		
Volume In Range (200,500) µm	14.19 %	**Volume In Range (1,2.5) µm**	6.16 %
Volume In Range (2.5,5) µm	7.30 %	**Volume In Range (5,10) µm**	9.60 %
D [3,3]	32.4 µm	**Kurtosis [3]**	2.766
Skew [3]	1.748		

Malvern Mastersizer 3000 LP Particle Size Analyzer

MAN 891.98

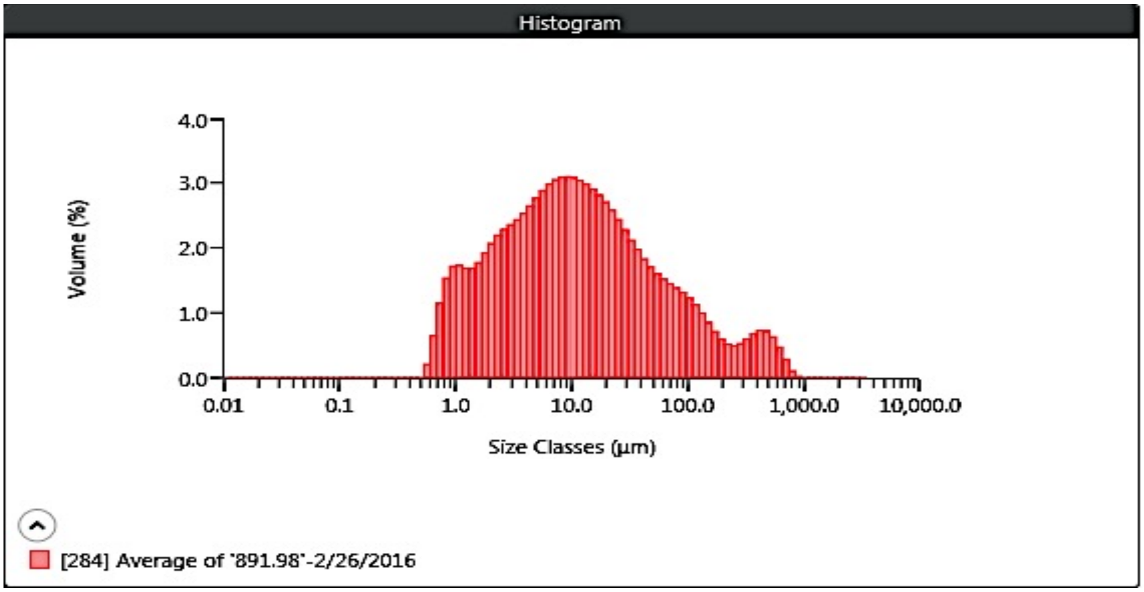

Result

Concentration	0.0046 %	Span	10.709
Uniformity	4.135	Result Units	Volume
Specific Surface Area	545.9 m^2/kg	Dv (10)	1.41 µm
D [3,2]	4.23 µm	Dv (50)	10.4 µm
D [4,3]	47.1 µm	Dv (90)	113 µm
Volume Below (5) µm	32.65 %	Mode	9.06 µm
Volume Below (10) µm	49.09 %		
Volume Below (20) µm	65.13 %	Volume In Range (500,1000) µm	1.70 %
Volume In Range (5,20) µm	32.48 %	Volume Above (1000) µm	0.0004 %
Volume In Range (20,200) µm	28.82 %		
Volume In Range (200,500) µm	4.35 %	Volume In Range (1,2.5) µm	13.58 %
Volume In Range (2.5,5) µm	13.67 %	Volume In Range (5,10) µm	16.44 %
D [3,3]	11.7 µm	Kurtosis [3]	17.065
Skew [3]	3.938		

Malvern Mastersizer 3000 LP Particle Size Analyzer

MAN 891.98 REP

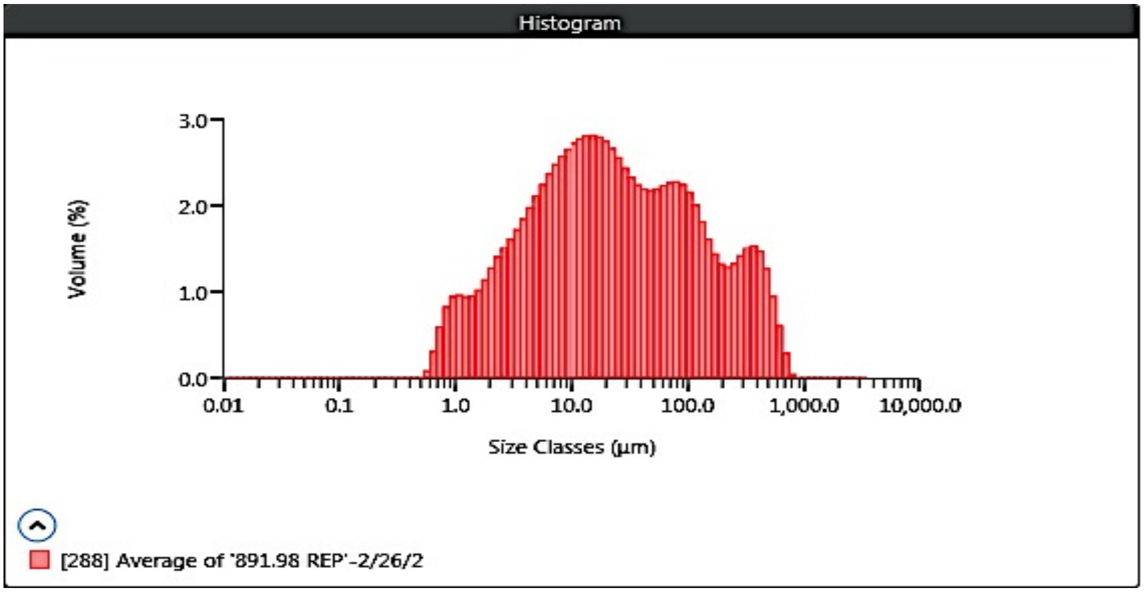

Result

Concentration	0.0031 %	**Span**	11.711
Uniformity	3.294	**Result Units**	Volume
Specific Surface Area	349.3 m^2/kg	**Dv (10)**	2.34 µm
D [3,2]	6.61 µm	**Dv (50)**	21.0 µm
D [4,3]	77.0 µm	**Dv (90)**	249 µm
Volume Below (5) µm	20.51 %	**Mode**	15.0 µm
Volume Below (10) µm	33.82 %		
Volume Below (20) µm	48.93 %	**Volume In Range (500,1000) µm**	2.18 %
Volume In Range (5,20) µm	28.41 %	**Volume Above (1000) µm**	0.00000000003 %
Volume In Range (20,200) µm	38.87 %		
Volume In Range (200,500) µm	10.03 %	**Volume In Range (1,2.5) µm**	7.97 %
Volume In Range (2.5,5) µm	9.74 %	**Volume In Range (5,10) µm**	13.30 %
D [3,3]	22.5 µm	**Kurtosis [3]**	6.232
Skew [3]	2.496		

Malvern Mastersizer 3000 LP Particle Size Analyzer

MAN 892.40

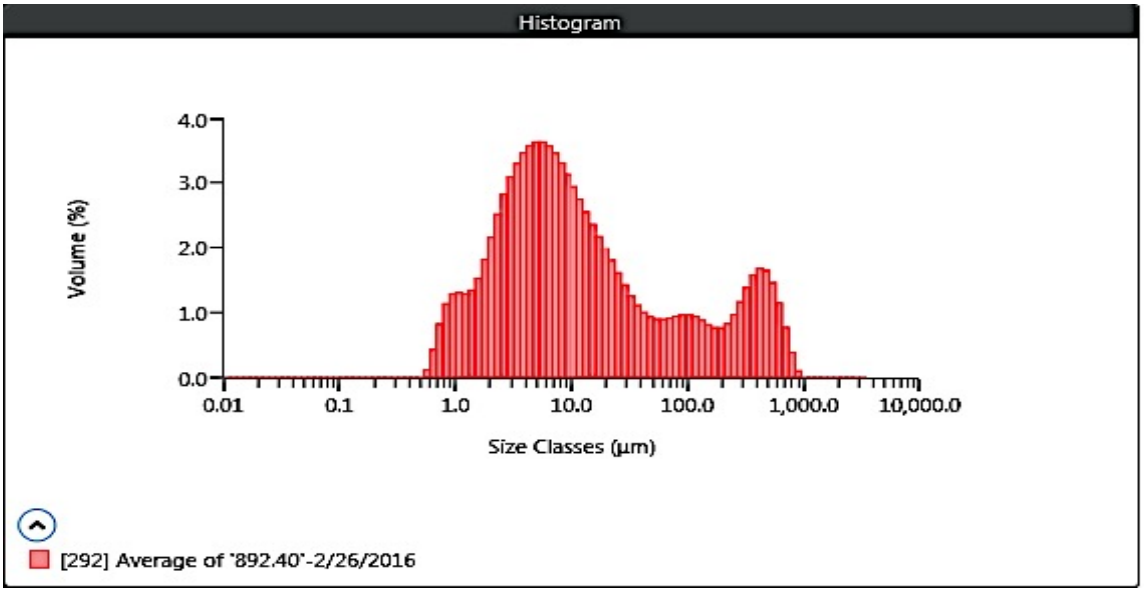

Result

Concentration	0.0027 %	**Span**	35.898
Uniformity	8.310	**Result Units**	Volume
Specific Surface Area	508.0 m²/kg	**Dv (10)**	1.73 µm
D [3,2]	4.54 µm	**Dv (50)**	8.72 µm
D [4,3]	76.4 µm	**Dv (90)**	315 µm
Volume Below (5) µm	34.67 %	**Mode**	5.18 µm
Volume Below (10) µm	53.35 %		
Volume Below (20) µm	**66.97 %**	**Volume In Range (500,1000) µm**	4.28 %
Volume In Range (5,20) µm	**32.30 %**	**Volume Above (1000) µm**	0.0004 %
Volume In Range (20,200) µm	**19.55 %**		
Volume In Range (200,500) µm	9.20 %	**Volume In Range (1,2.5) µm**	12.64 %
Volume In Range (2.5,5) µm	18.12 %	**Volume In Range (5,10) µm**	18.68 %
D [3,3]	13.5 µm	**Kurtosis [3]**	6.233
Skew [3]	2.593		

Malvern Mastersizer 3000 LP Particle Size Analyzer

MAN 892.73

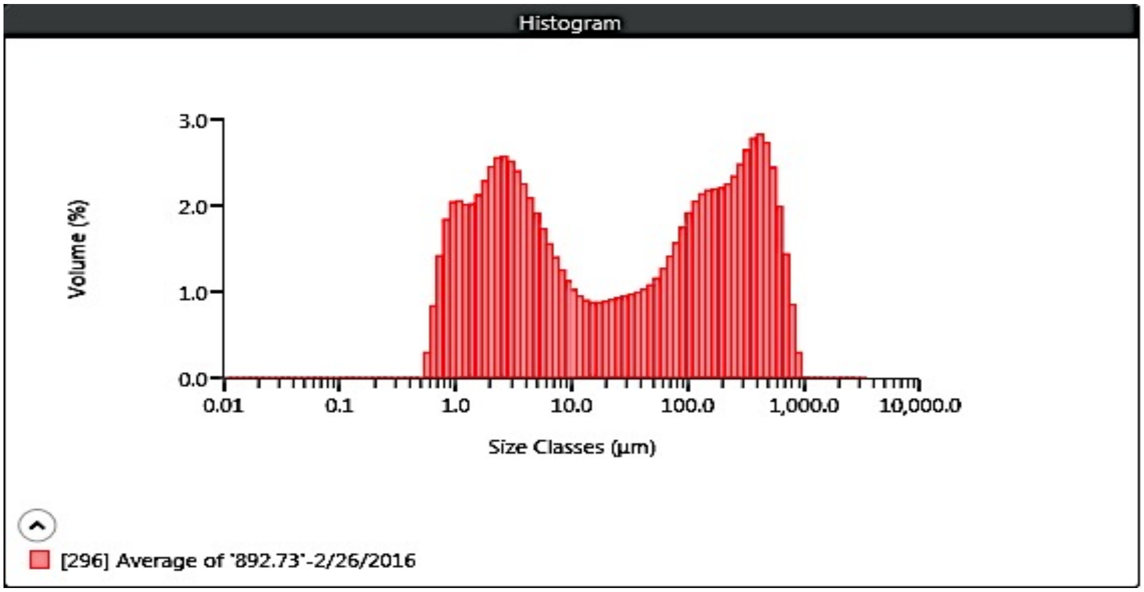

Result

Concentration	0.0028 %	**Span**	16.548
Uniformity	4.878	**Result Units**	Volume
Specific Surface Area	561.7 m^2/kg	**Dv (10)**	1.24 µm
D [3,2]	4.11 µm	**Dv (50)**	27.0 µm
D [4,3]	137 µm	**Dv (90)**	449 µm
Volume Below (5) µm	35.10 %	**Mode**	416 µm
Volume Below (10) µm	42.88 %		
Volume Below (20) µm	47.85 %	**Volume In Range (500,1000) µm**	7.68 %
Volume In Range (5,20) µm	12.76 %	**Volume Above (1000) µm**	0.005 %
Volume In Range (20,200) µm	26.14 %		
Volume In Range (200,500) µm	18.33 %	**Volume In Range (1,2.5) µm**	16.02 %
Volume In Range (2.5,5) µm	12.50 %	**Volume In Range (5,10) µm**	7.79 %
D [3,3]	24.4 µm	**Kurtosis [3]**	1.871
Skew [3]	1.610		

<u>**Malvern Mastersizer 3000 LP Particle Size Analyzer**</u>

Replicate MAN 892.73

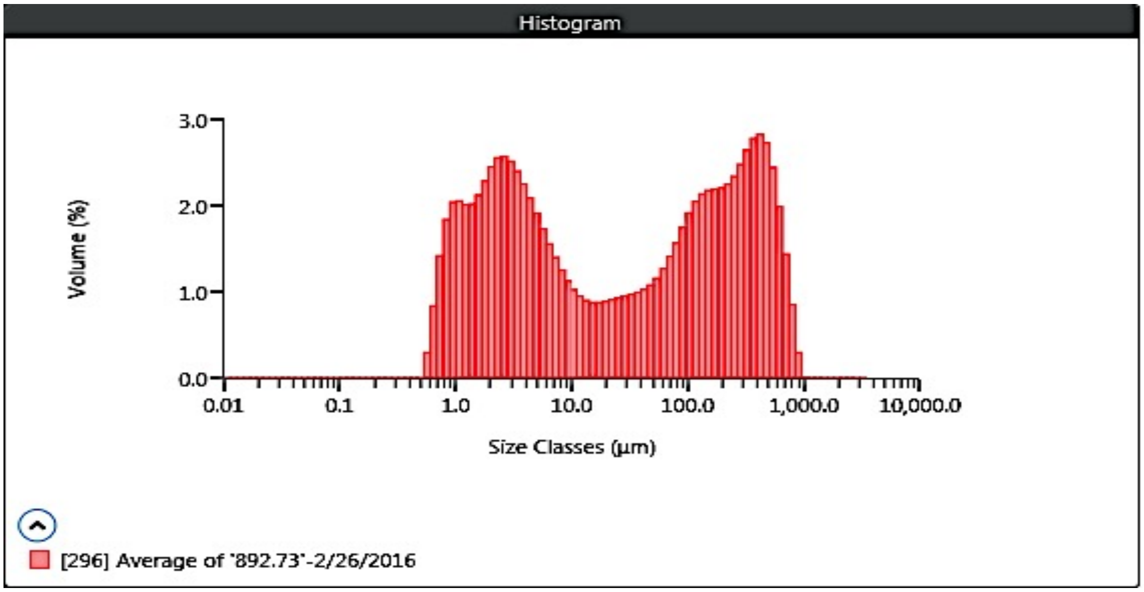

Result

Concentration	0.0028 %	**Span**	16.548
Uniformity	4.878	**Result Units**	Volume
Specific Surface Area	561.7 m^2/kg	**Dv (10)**	1.24 μm
D [3,2]	4.11 μm	**Dv (50)**	27.0 μm
D [4,3]	137 μm	**Dv (90)**	449 μm
Volume Below (5) μm	35.10 %	**Mode**	416 μm
Volume Below (10) μm	42.88 %		
Volume Below (20) μm	47.85 %	**Volume In Range (500,1000) μm**	7.68 %
Volume In Range (5,20) μm	12.76 %	**Volume Above (1000) μm**	0.005 %
Volume In Range (20,200) μm	26.14 %		
Volume In Range (200,500) μm	18.33 %	**Volume In Range (1,2.5) μm**	16.02 %
Volume In Range (2.5,5) μm	12.50 %	**Volume In Range (5,10) μm**	7.79 %
D [3,3]	24.4 μm	**Kurtosis [3]**	1.871
Skew [3]	1.610		

Malvern Mastersizer 3000 LP Particle Size Analyzer

MAN 893.30

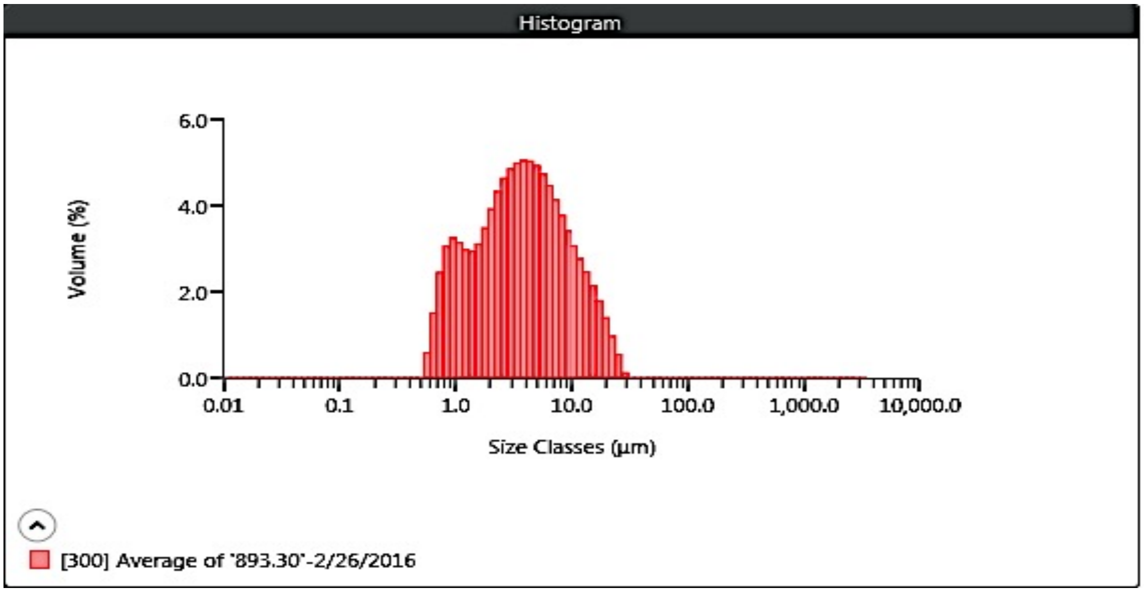

Result

Concentration	0.0028 %	**Span**	3.150
Uniformity	0.950	**Result Units**	Volume
Specific Surface Area	970.3 m²/kg	**Dv (10)**	0.958 µm
D [3,2]	2.38 µm	**Dv (50)**	3.62 µm
D [4,3]	5.31 µm	**Dv (90)**	12.4 µm
Volume Below (5) µm	62.69 %	**Mode**	3.92 µm
Volume Below (10) µm	85.15 %		
Volume Below (20) µm	97.75 %	**Volume In Range (500,1000) µm**	0.00 %
Volume In Range (5,20) µm	35.06 %	**Volume Above (1000) µm**	0.00000000000001 %
Volume In Range (20,200) µm	2.25 %		
Volume In Range (200,500) µm	0.00 %	**Volume In Range (1,2.5) µm**	24.83 %
Volume In Range (2.5,5) µm	26.77 %	**Volume In Range (5,10) µm**	22.46 %
D [3,3]	3.55 µm	**Kurtosis [3]**	3.056
Skew [3]	1.733		

Malvern Mastersizer 3000 LP Particle Size Analyzer

MAN 893.55

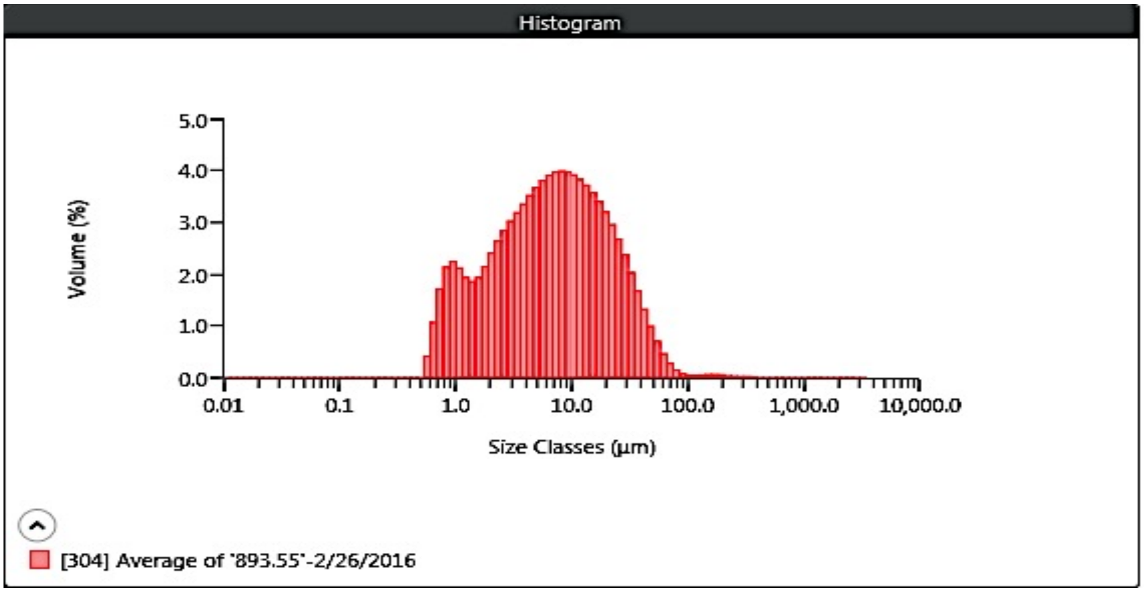

Result

Concentration	0.0031 %	**Span**	4.035
Uniformity	1.350	**Result Units**	Volume
Specific Surface Area	694.6 m^2/kg	**Dv (10)**	1.15 μm
D [3,2]	3.32 μm	**Dv (50)**	6.70 μm
D [4,3]	12.0 μm	**Dv (90)**	28.2 μm
Volume Below (5) μm	41.16 %	**Mode**	8.16 μm
Volume Below (10) μm	62.49 %		
Volume Below (20) μm	82.31 %	**Volume In Range (500,1000) μm**	0.00 %
Volume In Range (5,20) μm	41.15 %	**Volume Above (1000) μm**	0.00 %
Volume In Range (20,200) μm	17.53 %		
Volume In Range (200,500) μm	0.17 %	**Volume In Range (1,2.5) μm**	15.61 %
Volume In Range (2.5,5) μm	17.81 %	**Volume In Range (5,10) μm**	21.33 %
D [3,3]	6.33 μm	**Kurtosis [3]**	102.391
Skew [3]	7.637		

Malvern Mastersizer 3000 LP Particle Size Analyzer

MAN 894.80

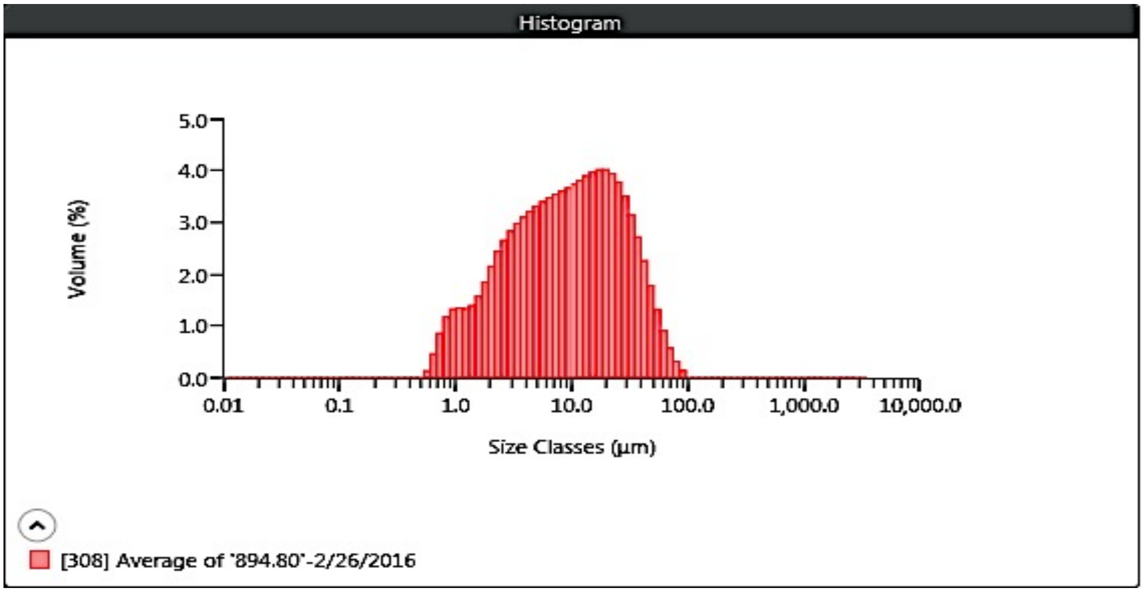

Result

Concentration	0.0083 %	**Span**	3.662
Uniformity	1.149	**Result Units**	Volume
Specific Surface Area	524.6 m²/kg	**Dv (10)**	1.70 μm
D [3,2]	4.40 μm	**Dv (50)**	9.20 μm
D [4,3]	14.6 μm	**Dv (90)**	35.4 μm
Volume Below (5) μm	33.17 %	**Mode**	18.6 μm
Volume Below (10) μm	52.41 %		
Volume Below (20) μm	73.68 %	**Volume In Range (500,1000) μm**	0.00 %
Volume In Range (5,20) μm	40.51 %	**Volume Above (1000) μm**	0.00000000000001 %
Volume In Range (20,200) μm	26.32 %		
Volume In Range (200,500) μm	0.00 %	**Volume In Range (1,2.5) μm**	12.66 %
Volume In Range (2.5,5) μm	16.46 %	**Volume In Range (5,10) μm**	19.24 %
D [3,3]	8.41 μm	**Kurtosis [3]**	3.317
Skew [3]	1.723		

<u>Malvern Mastersizer 3000 LP Particle Size Analyzer</u>

MAN 895.10

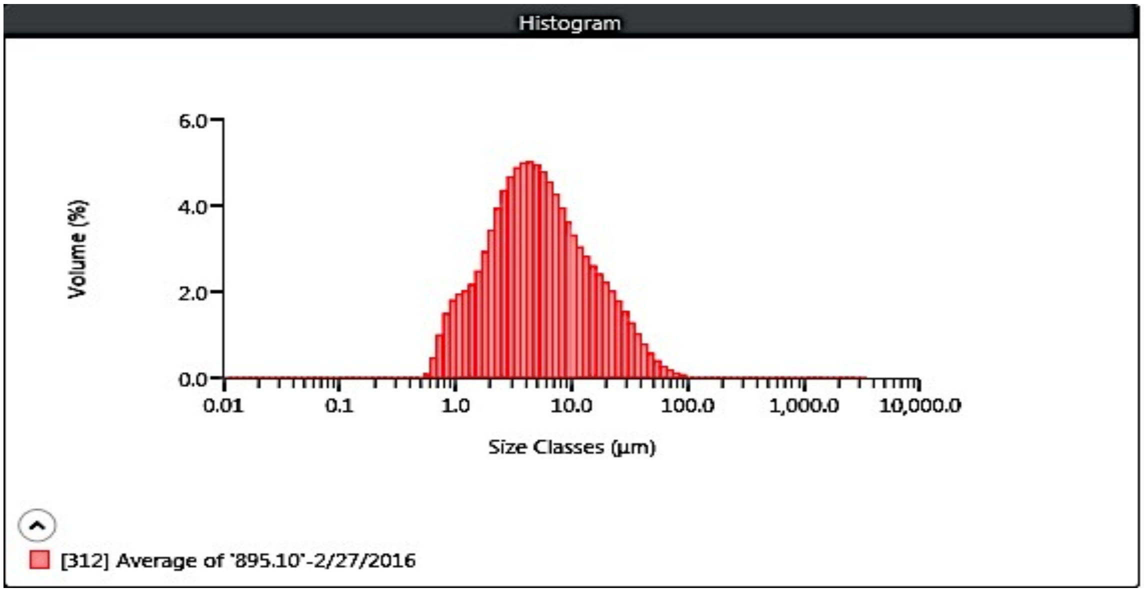

Result

Concentration	0.0046 %	**Span**	4.051
Uniformity	1.255	**Result Units**	Volume
Specific Surface Area	705.7 m^2/kg	**Dv (10)**	1.38 μm
D [3,2]	3.27 μm	**Dv (50)**	4.88 μm
D [4,3]	8.72 μm	**Dv (90)**	21.2 μm
Volume Below (5) μm	50.93 %	**Mode**	4.16 μm
Volume Below (10) μm	74.04 %		
Volume Below (20) μm	89.03 %	**Volume In Range (500,1000) μm**	0.00 %
Volume In Range (5,20) μm	38.10 %	**Volume Above (1000) μm**	0.00000000000001 %
Volume In Range (20,200) μm	10.97 %		
Volume In Range (200,500) μm	0.00 %	**Volume In Range (1,2.5) μm**	19.79 %
Volume In Range (2.5,5) μm	26.18 %	**Volume In Range (5,10) μm**	23.11 %
D [3,3]	5.18 μm	**Kurtosis [3]**	11.342
Skew [3]	2.896		

Malvern Mastersizer 3000 LP Particle Size Analyzer

MAN 895.40

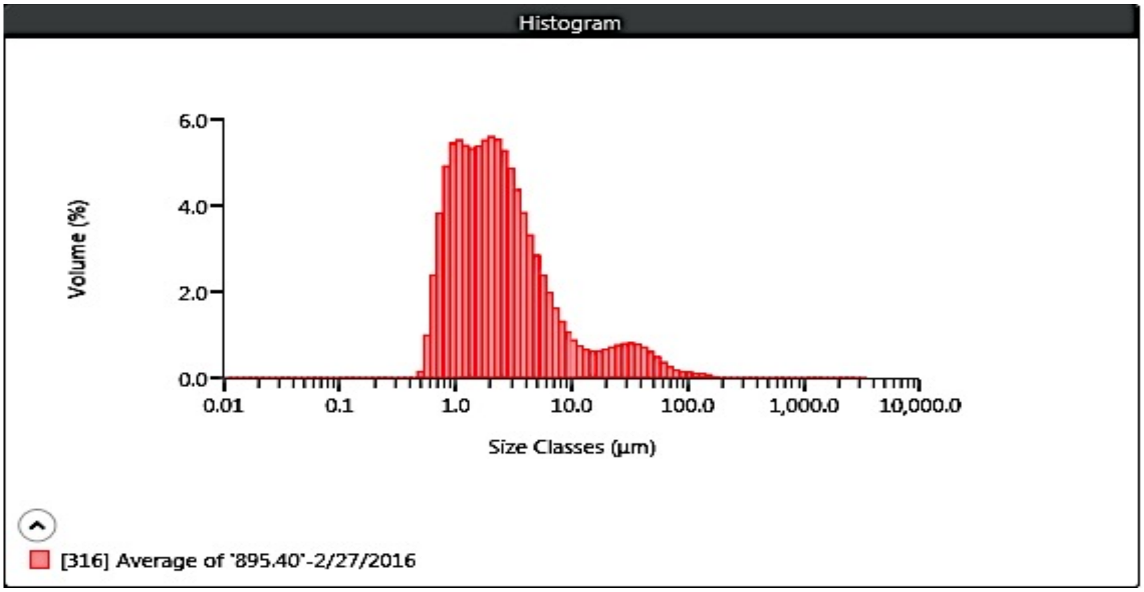

Result

Concentration	0.0037 %	**Span**	5.193
Uniformity	2.266	**Result Units**	Volume
Specific Surface Area	1330 m^2/kg	**Dv (10)**	0.822 μm
D [3,2]	1.74 μm	**Dv (50)**	2.11 μm
D [4,3]	6.01 μm	**Dv (90)**	11.8 μm
Volume Below (5) μm	79.62 %	**Mode**	2.02 μm
Volume Below (10) μm	88.94 %		
Volume Below (20) μm	92.71 %	**Volume In Range (500,1000) μm**	0.00 %
Volume In Range (5,20) μm	13.09 %	**Volume Above (1000) μm**	0.00000000000001 %
Volume In Range (20,200) μm	7.29 %		
Volume In Range (200,500) μm	0.0002 %	**Volume In Range (1,2.5) μm**	39.20 %
Volume In Range (2.5,5) μm	22.29 %	**Volume In Range (5,10) μm**	9.32 %
D [3,3]	2.59 μm	**Kurtosis [3]**	39.809
Skew [3]	5.480		

Malvern Mastersizer 3000 LP Particle Size Analyzer

MAN 895.65

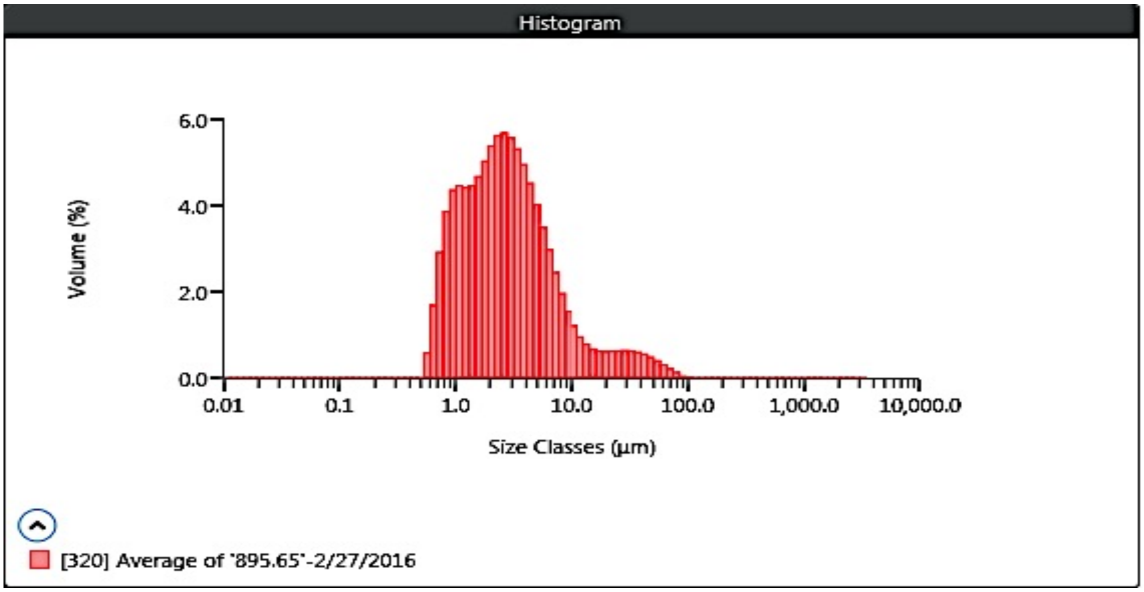

Result

Concentration	0.0019 %	Span	3.508
Uniformity	1.524	Result Units	Volume
Specific Surface Area	1169 m^2/kg	Dv (10)	0.897 μm
D [3,2]	1.97 μm	Dv (50)	2.56 μm
D [4,3]	5.36 μm	Dv (90)	9.88 μm
Volume Below (5) μm	76.30 %	Mode	2.53 μm
Volume Below (10) μm	90.11 %		
Volume Below (20) μm	94.52 %	Volume In Range (500,1000) μm	0.00 %
Volume In Range (5,20) μm	18.21 %	Volume Above (1000) μm	0.00 %
Volume In Range (20,200) μm	5.48 %		
Volume In Range (200,500) μm	0.00 %	Volume In Range (1,2.5) μm	35.19 %
Volume In Range (2.5,5) μm	27.38 %	Volume In Range (5,10) μm	13.81 %
D [3,3]	2.86 μm	Kurtosis [3]	24.497
Skew [3]	4.515		

Malvern Mastersizer 3000 LP Particle Size Analyzer

MAN 895.86

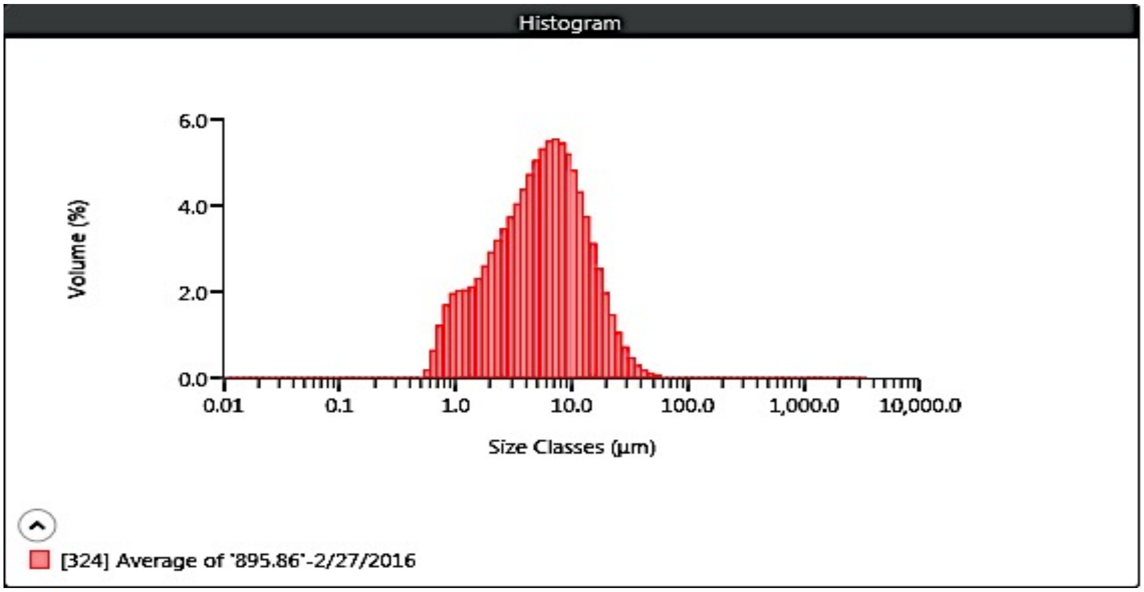

Result

Concentration	0.0069 %	**Span**	2.637
Uniformity	0.838	**Result Units**	Volume
Specific Surface Area	710.2 m^2/kg	**Dv (10)**	1.30 µm
D [3,2]	3.25 µm	**Dv (50)**	5.44 µm
D [4,3]	7.32 µm	**Dv (90)**	15.6 µm
Volume Below (5) µm	46.59 %	**Mode**	7.02 µm
Volume Below (10) µm	75.73 %		
Volume Below (20) µm	**94.79 %**	**Volume In Range (500,1000) µm**	0.00 %
Volume In Range (5,20) µm	**48.20 %**	**Volume Above (1000) µm**	0.00 %
Volume In Range (20,200) µm	**5.21 %**		
Volume In Range (200,500) µm	0.00 %	**Volume In Range (1,2.5) µm**	17.86 %
Volume In Range (2.5,5) µm	22.92 %	**Volume In Range (5,10) µm**	29.14 %
D [3,3]	4.99 µm	**Kurtosis [3]**	6.724
Skew [3]	2.104		

Malvern Mastersizer 3000 LP Particle Size Analyzer

MAN 896.06

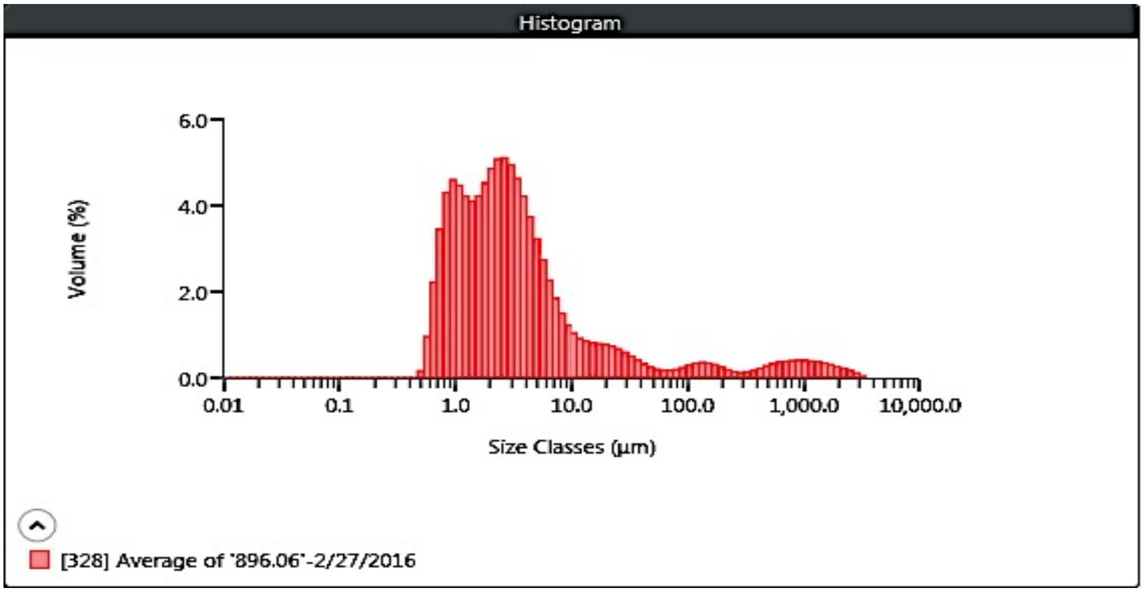

Result

Concentration	0.0017 %	**Span**	12.074
Uniformity	26.153	**Result Units**	Volume
Specific Surface Area	1177 m^2/kg	**Dv (10)**	0.844 µm
D [3,2]	1.96 µm	**Dv (50)**	2.59 µm
D [4,3]	69.3 µm	**Dv (90)**	32.2 µm
Volume Below (5) µm	72.11 %	**Mode**	2.47 µm
Volume Below (10) µm	82.81 %		
Volume Below (20) µm	**87.52 %**	**Volume In Range (500,1000) µm**	2.03 %
Volume In Range (5,20) µm	**15.41 %**	**Volume Above (1000) µm**	2.55 %
Volume In Range (20,200) µm	**6.62 %**		
Volume In Range (200,500) µm	1.29 %	**Volume In Range (1,2.5) µm**	32.47 %
Volume In Range (2.5,5) µm	23.60 %	**Volume In Range (5,10) µm**	10.70 %
D [3,3]	4.01 µm	**Kurtosis [3]**	39.246
Skew [3]	5.892		

Malvern Mastersizer 3000 LP Particle Size Analyzer

MAN 896.25

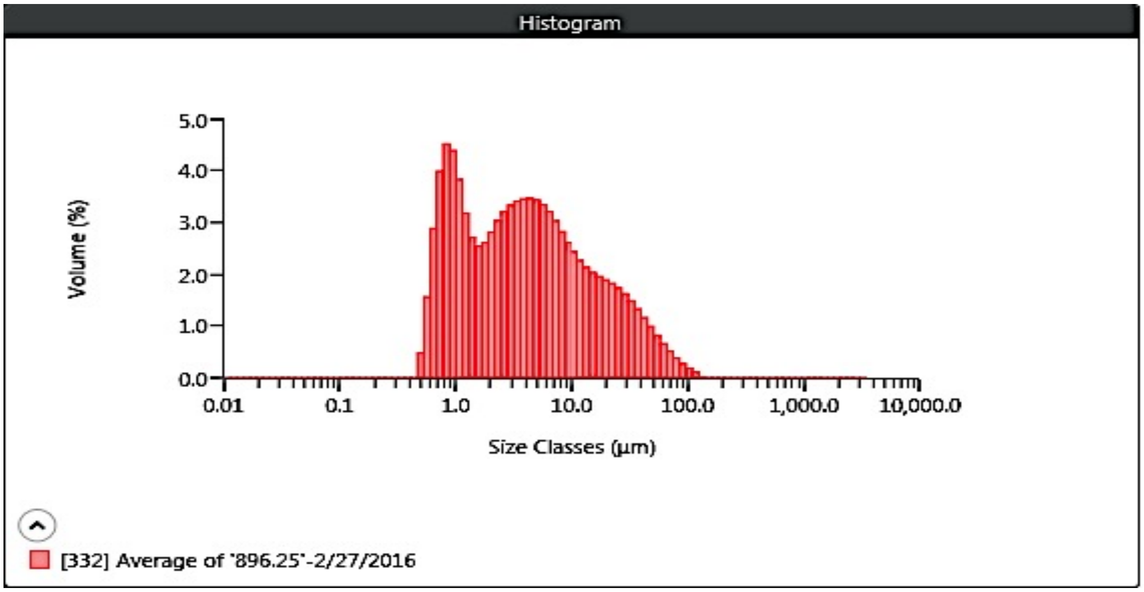

Result

Concentration	0.0025 %	Span	6.900
Uniformity	2.140	Result Units	Volume
Specific Surface Area	1101 m^2/kg	Dv (10)	0.790 µm
D [3,2]	2.10 µm	Dv (50)	3.73 µm
D [4,3]	9.59 µm	Dv (90)	26.5 µm
Volume Below (5) µm	57.99 %	Mode	0.851 µm
Volume Below (10) µm	74.46 %		
Volume Below (20) µm	86.02 %	Volume In Range (500,1000) µm	0.00 %
Volume In Range (5,20) µm	28.03 %	Volume Above (1000) µm	0.00 %
Volume In Range (20,200) µm	13.98 %		
Volume In Range (200,500) µm	0.00 %	Volume In Range (1,2.5) µm	21.35 %
Volume In Range (2.5,5) µm	18.48 %	Volume In Range (5,10) µm	16.47 %
D [3,3]	4.07 µm	Kurtosis [3]	12.636
Skew [3]	3.167		

Malvern Mastersizer 3000 LP Particle Size Analyzer

MAN 896.75

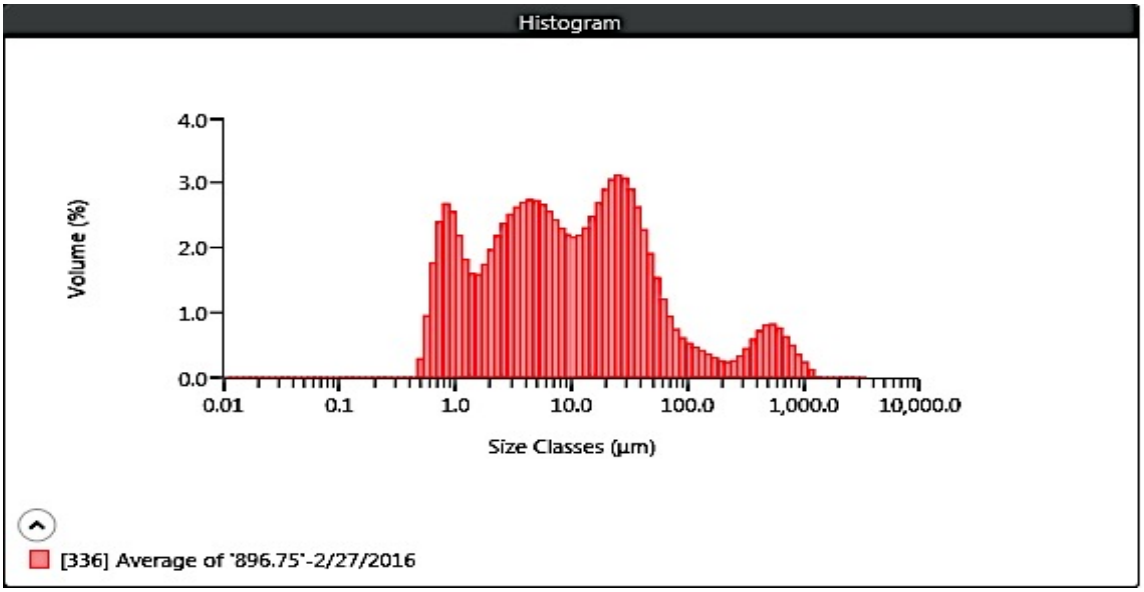

Result

Concentration	0.0021 %	**Span**	9.308
Uniformity	5.850	**Result Units**	Volume
Specific Surface Area	721.8 m^2/kg	**Dv (10)**	0.957 μm
D [3,2]	3.20 μm	**Dv (50)**	8.86 μm
D [4,3]	55.0 μm	**Dv (90)**	83.5 μm
Volume Below (5) μm	38.73 %	**Mode**	25.9 μm
Volume Below (10) μm	52.09 %		
Volume Below (20) μm	65.35 %	**Volume In Range (500,1000) μm**	3.31 %
Volume In Range (5,20) μm	26.62 %	**Volume Above (1000) μm**	0.33 %
Volume In Range (20,200) μm	27.70 %		
Volume In Range (200,500) μm	3.31 %	**Volume In Range (1,2.5) μm**	13.57 %
Volume In Range (2.5,5) μm	14.30 %	**Volume In Range (5,10) μm**	13.36 %
D [3,3]	9.81 μm	**Kurtosis [3]**	19.034
Skew [3]	4.217		

<u>**Malvern Mastersizer 3000 LP Particle Size Analyzer**</u>

Replicate MAN 896.75

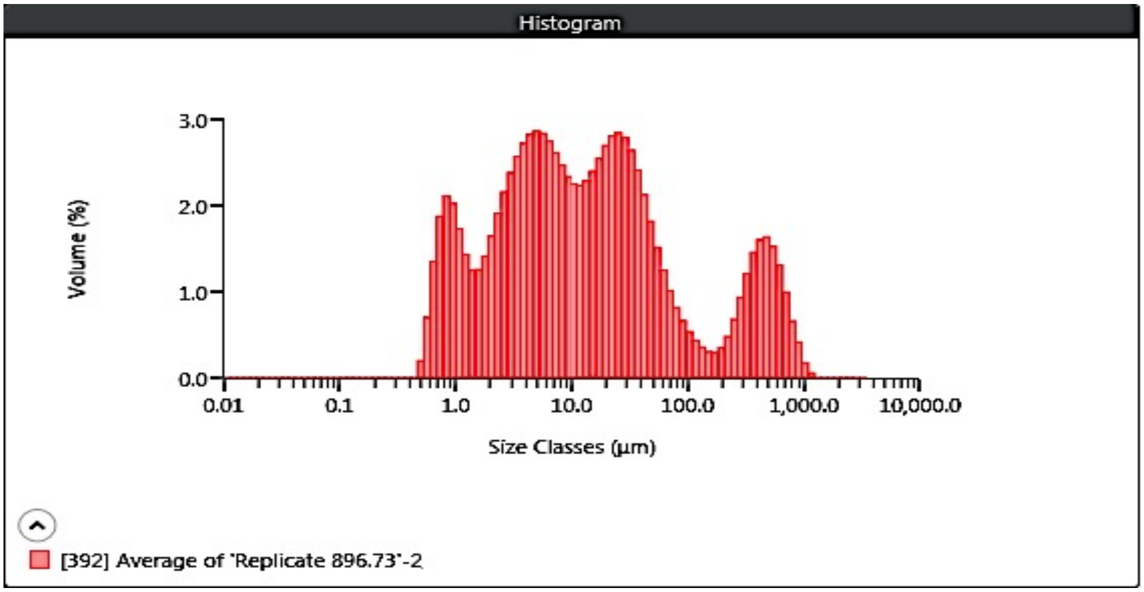

Result

Concentration	0.0025 %	**Span**	30.244
Uniformity	6.800	**Result Units**	Volume
Specific Surface Area	603.3 m^2/kg	**Dv (10)**	1.12 µm
D [3,2]	3.83 µm	**Dv (50)**	11.4 µm
D [4,3]	81.5 µm	**Dv (90)**	346 µm
Volume Below (5) µm	33.53 %	**Mode**	4.94 µm
Volume Below (10) µm	47.71 %		
Volume Below (20) µm	**60.65 %**	**Volume In Range (500,1000) µm**	5.33 %
Volume In Range (5,20) µm	**27.12 %**	**Volume Above (1000) µm**	0.20 %
Volume In Range (20,200) µm	**26.07 %**		
Volume In Range (200,500) µm	7.75 %	**Volume In Range (1,2.5) µm**	11.05 %
Volume In Range (2.5,5) µm	14.08 %	**Volume In Range (5,10) µm**	14.18 %
D [3,3]	13.6 µm	**Kurtosis [3]**	7.796
Skew [3]	2.824		

<u>Malvern Mastersizer 3000 LP Particle Size Analyzer</u>

MAN 896.87

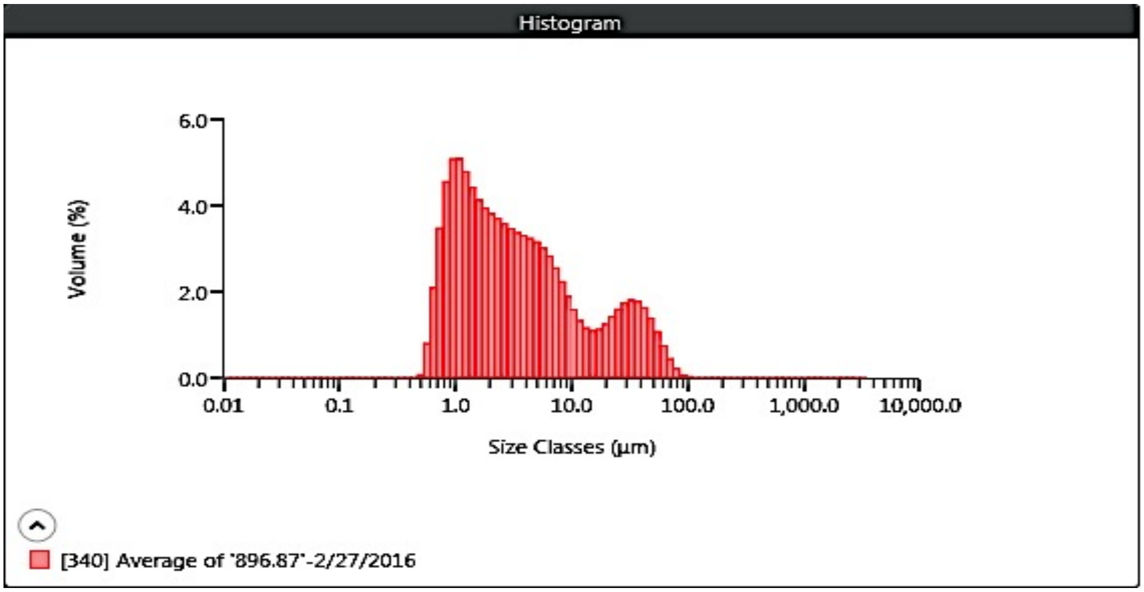

Result

Concentration	0.0012 %	**Span**	10.136
Uniformity	2.646	**Result Units**	Volume
Specific Surface Area	1151 m^2/kg	**Dv (10)**	0.848 µm
D [3,2]	2.00 µm	**Dv (50)**	2.79 µm
D [4,3]	8.79 µm	**Dv (90)**	29.2 µm
Volume Below (5) µm	65.14 %	**Mode**	0.992 µm
Volume Below (10) µm	78.81 %		
Volume Below (20) µm	**85.57 %**	**Volume In Range (500,1000) µm**	0.00 %
Volume In Range (5,20) µm	**20.43 %**	**Volume Above (1000) µm**	0.00 %
Volume In Range (20,200) µm	**14.43 %**		
Volume In Range (200,500) µm	0.00 %	**Volume In Range (1,2.5) µm**	30.43 %
Volume In Range (2.5,5) µm	18.25 %	**Volume In Range (5,10) µm**	13.67 %
D [3,3]	3.60 µm	**Kurtosis [3]**	6.802
Skew [3]	2.555		

Malvern Mastersizer 3000 LP Particle Size Analyzer

MAN 897.10

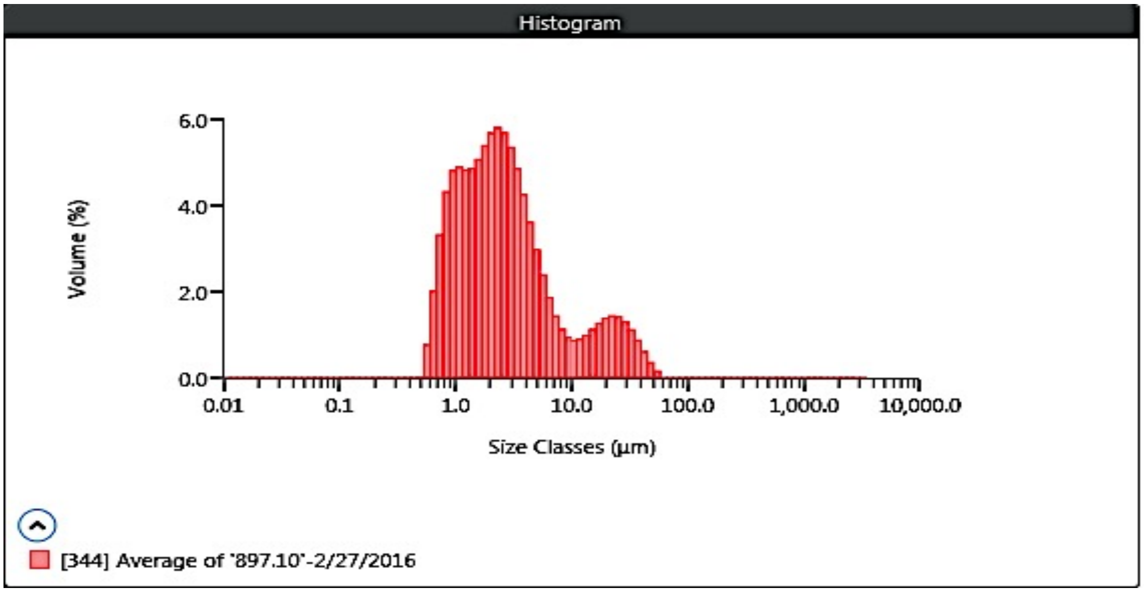

Result

Concentration	0.0028 %	**Span**	6.586
Uniformity	1.761	**Result Units**	Volume
Specific Surface Area	1235 m^2/kg	**Dv (10)**	0.861 μm
D [3,2]	1.87 μm	**Dv (50)**	2.33 μm
D [4,3]	5.45 μm	**Dv (90)**	16.2 μm
Volume Below (5) μm	77.60 %	**Mode**	2.27 μm
Volume Below (10) μm	86.37 %		
Volume Below (20) μm	92.13 %	**Volume In Range (500,1000) μm**	0.00 %
Volume In Range (5,20) μm	14.53 %	**Volume Above (1000) μm**	0.00 %
Volume In Range (20,200) μm	7.87 %		
Volume In Range (200,500) μm	0.00 %	**Volume In Range (1,2.5) μm**	37.62 %
Volume In Range (2.5,5) μm	24.38 %	**Volume In Range (5,10) μm**	8.77 %
D [3,3]	2.79 μm	**Kurtosis [3]**	8.627
Skew [3]	2.889		

Malvern Mastersizer 3000 LP Particle Size Analyzer

MAN 897.35

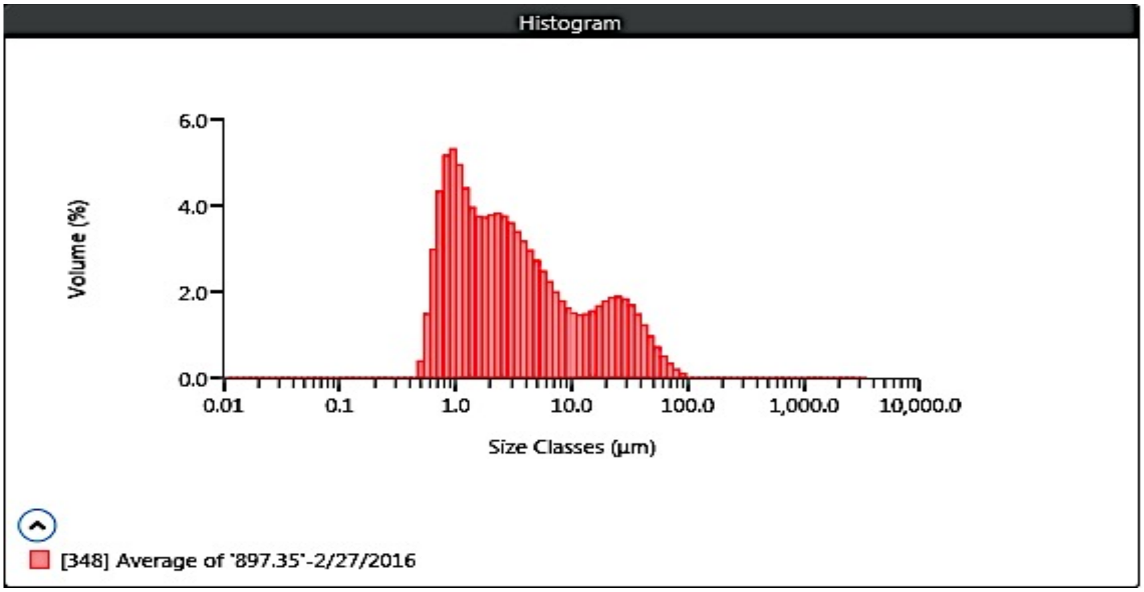

Result

Concentration	0.0020 %	**Span**	9.623
Uniformity	2.665	**Result Units**	Volume
Specific Surface Area	1245 m^2/kg	**Dv (10)**	0.783 µm
D [3,2]	1.85 µm	**Dv (50)**	2.58 µm
D [4,3]	8.17 µm	**Dv (90)**	25.6 µm
Volume Below (5) µm	66.88 %	**Mode**	0.905 µm
Volume Below (10) µm	77.99 %		
Volume Below (20) µm	**86.42 %**	**Volume In Range (500,1000) µm**	0.00 %
Volume In Range (5,20) µm	**19.55 %**	**Volume Above (1000) µm**	0.00000000000001 %
Volume In Range (20,200) µm	**13.58 %**		
Volume In Range (200,500) µm	0.00 %	**Volume In Range (1,2.5) µm**	29.03 %
Volume In Range (2.5,5) µm	17.81 %	**Volume In Range (5,10) µm**	11.11 %
D [3,3]	3.36 µm	**Kurtosis [3]**	8.170
Skew [3]	2.683		

Malvern Mastersizer 3000 LP Particle Size Analyzer

MAN 879.53 REP2

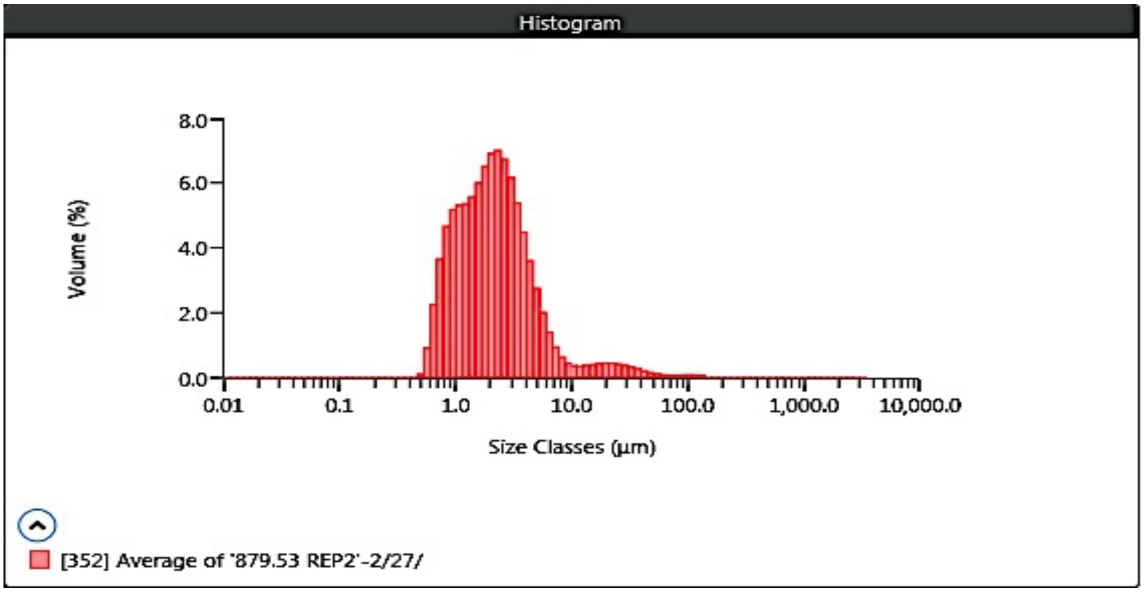

Result

Concentration	0.0032 %	**Span**	2.304
Uniformity	1.307	**Result Units**	Volume
Specific Surface Area	1382 m^2/kg	**Dv (10)**	0.833 µm
D [3,2]	1.67 µm	**Dv (50)**	2.02 µm
D [4,3]	3.89 µm	**Dv (90)**	5.50 µm
Volume Below (5) µm	88.27 %	**Mode**	2.20 µm
Volume Below (10) µm	94.67 %		
Volume Below (20) µm	**96.84 %**	**Volume In Range (500,1000) µm**	0.00 %
Volume In Range (5,20) µm	**8.57 %**	**Volume Above (1000) µm**	0.00 %
Volume In Range (20,200) µm	**3.16 %**		
Volume In Range (200,500) µm	0.00 %	**Volume In Range (1,2.5) µm**	44.26 %
Volume In Range (2.5,5) µm	26.72 %	**Volume In Range (5,10) µm**	6.40 %
D [3,3]	2.20 µm	**Kurtosis [3]**	88.252
Skew [3]	8.326		

Malvern Mastersizer 3000 LP Particle Size Analyzer

MAN 880.56 REP2

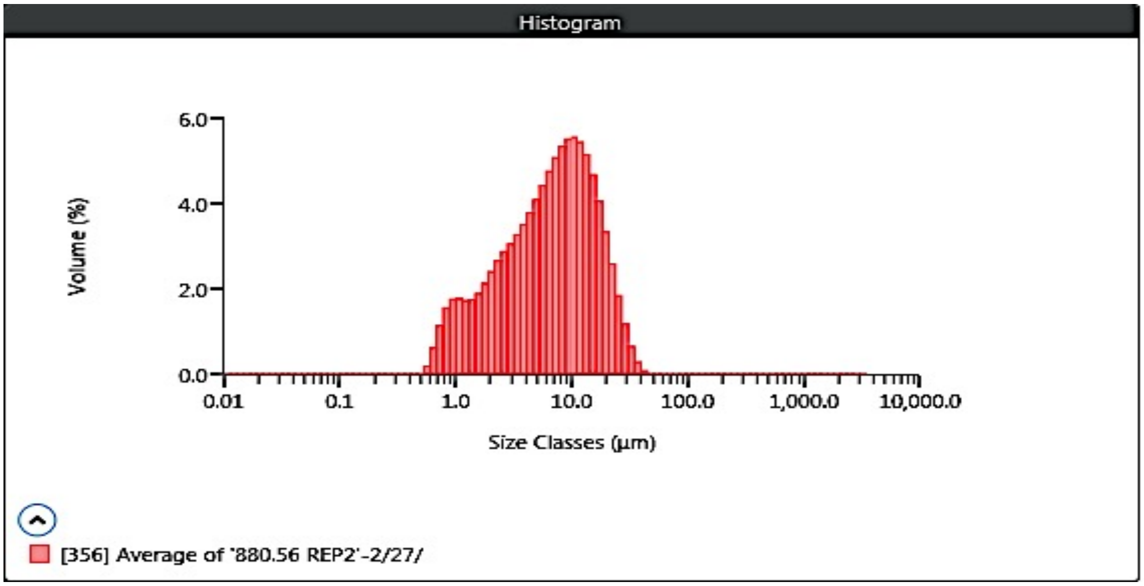

Result

Concentration	0.0050 %	**Span**	2.513
Uniformity	0.787	**Result Units**	Volume
Specific Surface Area	632.5 m²/kg	**Dv (10)**	1.41 μm
D [3,2]	3.65 μm	**Dv (50)**	6.85 μm
D [4,3]	8.68 μm	**Dv (90)**	18.6 μm
Volume Below (5) μm	38.76 %	**Mode**	10.2 μm
Volume Below (10) μm	65.81 %		
Volume Below (20) μm	**91.89 %**	**Volume In Range (500,1000) μm**	0.00 %
Volume In Range (5,20) μm	**53.13 %**	**Volume Above (1000) μm**	0.00000000000001 %
Volume In Range (20,200) μm	**8.11 %**		
Volume In Range (200,500) μm	0.00 %	**Volume In Range (1,2.5) μm**	14.84 %
Volume In Range (2.5,5) μm	18.58 %	**Volume In Range (5,10) μm**	27.05 %
D [3,3]	5.93 μm	**Kurtosis [3]**	1.596
Skew [3]	1.263		